Analysis of the Radiation Mechanisms in and Design of Tightly-Coupled Antenna Arrays

Terry Richard Vogler

Dissertation submitted to the faculty of the
Virginia Polytechnic Institute and State University
in partial fulfillment of the requirements for the degree of

Doctor of Philosophy
in
Electrical and Computer Engineering

William A. Davis, Chair
Warren L. Stutzman
Gary S. Brown
Luiz DaSilva
Yuriko Renardy

September 10th, 2010
Blacksburg, Virginia

Keywords: array, wideband, coupling, tuning

Analysis of the Radiation Mechanisms in and Design of Tightly-Coupled Antenna Arrays

Terry Richard Vogler

ABSTRACT

The objective of this research is to design well-tuned, wideband elements for thin planar or cylindrically conformal arrays of balanced elements fed over ground. These arrays have closely spaced elements to achieve wide bandwidths through mutual coupling. This dissertation develops two wideband designs in infinite, semi-infinite, and finite array configurations. The infinite array is best for element tuning. This research advances a concept of a distributed, parallel capacitance between elements and across feeds that must be mutually altered for tuning.

Semi-infinite techniques limit the problem space and determine the proper resistive loads to control the low-frequency array-guided surface wave (AGSW). The tight physical placement also forms a periodic structure that, along with the array boundary, launches a wave across the array surface. Options to suppress this surface wave are resistive loading and cylindrical conformations. AGSW control is necessary to achieve a maximum bandwidth, but lower radiation or aperture efficiency results. Conformation is shown to be an ineffective method for AGSW control alone.

The *Wrapped Bowtie* design emerges as a novel design offering nearly a 10:1 bandwidth as a finite array over ground. Some bandwidth comes from the losses in radiation efficiency, which is necessary to control the AGSW; however, its simulated VSWR < 3 bandwidth in an infinite array is 7.24:1 with full efficiency. Less than perfect efficiency is required to mitigate surface wave effects, unless bandwidth is to be compromised. That loss may be as radiation or aperture efficiency, but it is unavoidable if the infinite array bandwidth is to be maintained in finite array designs.

Lastly, this research articulates a development path for tightly-coupled arrays that extends in stages from infinite to semi-infinite, and thence finite layouts. Distinctions are explained and defended for the design focus at each stage. Element design, tuning, and initial feed design occur at the infinite array stage; AGSW suppression occurs at the semi-infinite stage; and design confirmation occurs only with the finite array.

ACKNOWLEDGEMENTS

I would like to thank Dr. Bill Davis for serving as my committee chairman, advisor, and lab manager these past five years. I have learned invaluable lessons and technical direction from him, and I hope to continue our relationship in the years ahead. I thank Drs. Warren Stutzman, Gary Brown, Luiz DaSilva, and Yuriko Renardy for serving on my committee and their professional advice. I wish also to acknowledge my friendship for Randall Nealy for our discussions and his guidance with test equipment.

In this past year of working at USCGA, my appreciation and thanks go to Drs. Richard Hartnett, Keith Gross, and Richard Freeman for their support and guidance. Small bits of encouragement do add up.

I am grateful for the advice, discussions, and camaraderie of my other graduate student friends: Taeyoung Yang, Kai Dietze, Guarav Joshi, Christian Hearn, Tyler Kramer, Jess Walker, Alex "Hot Plate" Young, Andrew Blischak, and Scott Bates. I would also like to thank my friends Diane Dorrell and Hakuin Rose, who made my time in Blacksburg a human and non-engineering experience. For their keen counsel and enduring friendship, I wish to thank John Pruitt and Sean Carroll. Lastly, my thanks go to my brother Tracy, his wife Leah, and Marc Thibault, who have traveled this Ph.D. road and could explain its twists and curves. As *PhD Comics* so well illustrates, earning a Ph.D. is a humorous and inhuman experience. I would have quit without all your support and guidance.

For their unwavering encouragement and assistance, I thank equally my parents, Richard and Wanda, and my Aunt Jean and Uncle Dan. I am at a loss for words for what you mean and have done over my entire life. And, as I grow older, I appreciate them in more profound ways. I love you all.

Above all, my thanks and love to my wife, Theresa. You have been supportive and flexible beyond words. You knew when to give me encouragement and when to throw down the gauntlet. Thank you for your insights, wit, and love, and for making me realize I would finish only when I decided I would.

TABLE OF CONTENTS

LIST OF FIGURES

Chapter 2

Chapter 3

Chapter 4

Chapter 5

Chapter 6

LIST OF TABLES

CHAPTER 1

Introduction

Many wideband applications require directive antenna patterns. Substantial directivity is possible using reflector antennas, horns, and traveling wave antennas. Increasing attention has focused on wideband planar arrays to support ultra-wideband (UWB) applications and frequency-agile radios. One method to achieve wide bandwidths is to closely space the array elements and promote strong mutual coupling between elements. This layout, in a way, extends the effective area of any one element beyond its physical size. This makes the physical area extend at least to the extents of the unit cell, which the element occupies within the array including the separations between elements, for cases of radiation and farther outward for cases of impedance. This mutual coupling allows the array elements to operate at frequencies where they would be electrically small as isolated elements. This dissertation refers to such arrays as being *tightly coupled*.

A limited amount of research is available on tightly-coupled arrays, with the bulk coming from Dr. Ben Munk at Ohio State, in collaboration with Harris Corporation. Some of that work relates to frequency-selective surfaces, and in places, it omits details on the design of tightly-coupled arrays for communications purposes. Limited element designs appear in the literature, and the bulk of research specifically addressing the mechanisms and designs for mid-sized arrays appears to be proprietary.

This dissertation considers a comprehensive investigation of planar and cylindrically conformal tightly-coupled arrays to expand past work and attempt to bring design concepts into practical use. The primary focuses of the research include tuning the array elements and placement over a ground plane for maximum bandwidth; explaining the variables or functions

related to bandwidth control; and mitigating a lower-frequency surface wave that negatively affects input impedance. These steps, in combination with others, detail and justify a design process for the future development of tightly-coupled arrays. The final chapter includes an overview of some construction details and concerns. This understanding will support the development of wideband arrays to meet specific applications.

1.1 Executive Summary

The research in this dissertation leads to two element designs for wideband tightly-coupled planar arrays. This research develops these element designs through their stages and demonstrates their performance. It makes distinctions between their performance in infinite, semi-infinite, and finite arrays. In the latter two, a low-frequency surface wave develops from the periodicity of the elements and finite nature of the array. This surface wave is extremely detrimental to the input impedance of elements within the array. Resistive loading and cylindrical conformation of the overall array both function to control this surface wave, but with impacts on radiation efficiency, pattern shape, and concurrently array gain.

This dissertation develops two designs. It explains the coupling mechanisms of one, the Rot 9 element, and argues its tuning as a distributed parallel capacitance. While the bandwidths achieved are not as wide as the other design explained below, the method of tuning offers insight into all other designs of tightly-coupled array elements. Because of their electrically small size as individual elements, the elements normally require additional capacitance. The gap between elements serves as one capacitor, and the region between the two sides of the feed serves as the second. The wider bandwidth of this design emerges only through adjustment to the feed region.

Many engineers revere the concept and definition of a 10:1 bandwidth. While such statements include impedance, pattern, and gain bandwidths, engineers rarely strictly define their aperture and/or radiation efficiency. The second design, the Wrapped Bowtie element, comes very close to the 10:1 bandwidth (10.77:1 on the more loaded, outer elements, and 8.85:1 overall) and has a ground plane underneath. The Wrapped Bowtie element is new and differs substantially from other tightly-coupled array designs. This research only hypothesizes on the reasons for its wide impedance bandwidth; in this physical layout, parallel and non-opposing currents development on each side of gaps between elements along the direction of the element

feeds. These currents are parallel across most of the operating bandwidth. This bandwidth far exceeds the bandwidth of all other designs within this dissertation. Unfortunately, this research does not provide a conclusive understanding of all its mechanisms, mostly because of the inability to test the hypothesis at this time and with the current body of literature.

The remaining chapters of the dissertation recommend and validate a design process for the design of similar wideband arrays. The design process adds value to the body of knowledge because of its clear presentation of how and where design factors influence array performance. Many of these factors are independent and the designer may tackle them in a sequential process. This process first relies heavily on infinite array techniques for initial element design and the development of the feed system, and on semi-infinite techniques to determine the effects and treatment of edge effects, including the low-frequency surface wave. The semi-infinite methods are more available computationally and with a smaller time burden than finite methods. The insights and designs from multiple, orthogonal semi-infinite designs transfer well to finite array designs. Finite array analyses offer confirmations of the design.

Lastly, this research presents some designs and restrictions to feeding elements in tightly-coupled arrays. Such wideband arrays are comprised of balanced elements, parallel over ground and requiring balanced feeds. If each element has a balanced source, feeding the array is manageable. Unbalanced sources are a different matter. The dominant limitation for these is the design of wideband, and volumetrically small, baluns. This dissertation introduces some balun options and but leaves them in the domain of others.

1.2 Dissertation Overview

This dissertation contains five substantive chapters. Chapters 2 and 3 present background information on the characterization of mutual coupling in arrays and numerical methods to solve those problems, respectively. This work forms the theoretical groundwork to reach and then explain the subsequent designs.

The front of Chapter 4 outlines other designs for tightly-coupled arrays from the literature. The next part of Chapter 4 presents a progression of element designs grown from different design motivations or concepts within infinite planar arrays. Two dominant designs emerge that continue forward into later chapters. The last of Chapter 4 articulates the effects of

ground, isolated element performance, and array scanning results on one or both of these dominant element designs.

Chapter 5 and 6 form the last of the dissertation. Chapter 5 advances the dominant designs from Chapter 4 using semi-infinite simulation techniques on arrays configured in both finite *H*-plane and finite *E*-plane layouts. These techniques are less computationally burdensome and allow for a good development of guidelines for finite array design. Chapter 5 develops details to control of the low frequency surface wave. First, though, Chapter 5 documents the effects of these waves and includes representations of the surface currents in the spectral domain. Lastly, Chapter 5 presents the effects of cylindrical conformation of the array and, separately, the performance limitations of *H*-plane scanning.

Chapter 6 extends the loading schemes from Chapter 5 unto finite arrays. It also includes cylindrically conformal and results. The remainder of Chapter 6 begins to consider the real and challenging issues of feeding these arrays. Divisions exist based on whether the sources have balanced or unbalanced output ports.

Chapter 7 presents a summary of the dissertation, articulates contributions to the body of knowledge, and recommends several tasks for further work.

CHAPTER 2

Coupling Mechanisms in Arrays

Early antenna engineers historically approached the design of an array by taking an antenna pattern and multiplying it by the array pattern. The array factor is the pattern solely stemming from the array shape and phasing between elements and, thus, is of isotropic sources. This is a first-order approach, but one that can work reasonably well if the influence of one element on another is not substantial. In one form, this implies that the (isolated) element impedance does not change as a result of the array into which it is placed, nor would the element pattern (i.e., the far-field radiation pattern of an array element radiating in the presence of the other array elements). When the influence of these effects is meaningful, engineers often lump them together as mutual coupling.

Perhaps from an inability to calculate the complete array process and to save money, engineers often design arrays with large element spacings to minimize the mutual coupling. This also has the benefit of maximizing array gain for a fixed number of elements, which saves on manufacturing costs. While mutual coupling is always present in arrays, it becomes much stronger when $d < 0.5\lambda$. If $d = 0.5\lambda$ is assumed to be the minimum spacing at the lowest frequency, wideband performance must be achieved by operating the array at higher frequencies. However, increasing frequency separates the elements electrically and eventually introduces grating lobes.

From a historical perspective, the narrowband nature of arrays often did not matter. Frequency licensing and limitations on the transmitter and receiver hardware point to narrowband applications. Wideband pulsed arrays, such as those used for electromagnetic pulse (EMP) testing, were an exception to this trend, but their use was not widespread. They also did not have the physical size limitations that many modern applications do. UWB radars, multiband communications systems, frequency agile radios, among others drive these modern applications. To achieve the bandwidth required of such applications, whether instantaneous or tunable, while avoiding grating lobes, engineers must let the minimum spacing requirement $d = 0.5\lambda$ pass into history or accept the complications of adopting space-tapered arrays.

As stated, mutual coupling becomes more of an issue when array elements are closer than $d = 0.5\lambda$. This chapter reviews some characterizations of mutual coupling, namely: impedance matrix, circuit model representations, and *S*-parameter coupling. This chapter reviews, relates, and contrasts these approaches. More importantly, this chapter makes an effort to explain the physical nature of this mutual coupling, regardless of how it is quantified or measured. This desire comes from the limitations that result from characterizing all interactions from an input-port perspective. If only the relationships at the ports are considered, there is no inherent understanding of how performance depends on the element shape. This chapter presents a review of surface wave phenomenology, namely the well-known substrate-guided surface wave and the less well-known array-guided surface wave. Both are important because of their impact on the design of wideband arrays. One needs to understand the nature of surface waves in order to counteract the effects properly.

Chapter 3 follows this treatment of the physical phenomenon with an overview of computational methods appropriate for modeling tightly-coupled arrays. Chapters 4-6 build on the theoretical background of this chapter and provide designs of wideband tightly-coupled planar arrays as designed using infinite, semi-infinite, and finite simulation methods.

Throughout this chapter and others, there are references to past work and restatements of derivations. For clarity, this chapter uses consistent notation and physical orientation of the arrays, unless otherwise stated. Since this dissertation addresses mostly planar arrays, the plane of that array is the *xy*-plane, with the surface normal $\hat{n}$ in the $+\hat{z}$ direction. Figure 2-1 shows this standard layout. For antennas designed for a single polarization, the elements have feeds

oriented in $\pm\hat{y}$, which defines an *E*-plane scan relative to $\pm\hat{y}$ and the *H*-plane scan relative to $\pm\hat{x}$, generally.

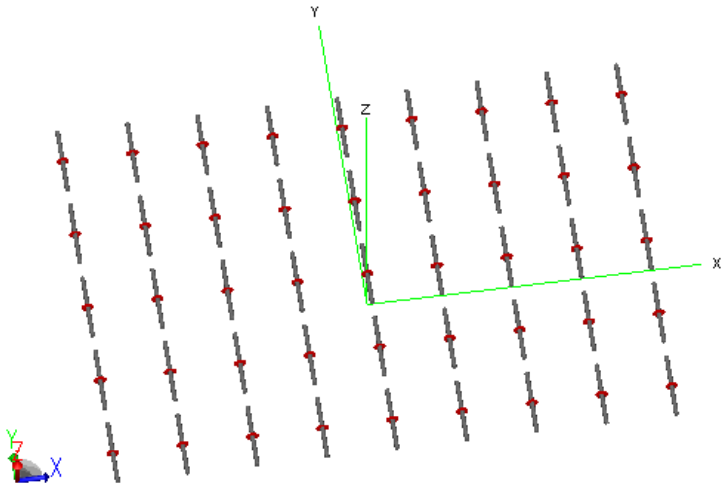

Figure 2-1 – Standard geometrical layout, shown via a 5×9 planar dipole array

2.1 Characterization of Coupling in Arrays

2.1.1 Mutual Impedance and Mutual Coupling

Determining the *mutual impedance* of elements in an array requires the measurement of the open-circuit voltage at each element when one element is driven; in other words, one element is excited with all other elements in open-circuit configurations [1]. Alternatively, the mutual admittance matrix may be calculated using short-circuited elements and then inverted to be the mutual impedance matrix. Mutual impedance differs from three other impedances discussed here: *isolated impedance*, *active impedance*, and *embedded impedance*. Isolated impedance is that of an array element with all other elements removed; and active impedance is that where all elements are in place and excited. (Some authors, such as Munk and Hansen, also refer to active impedance as *scan impedance* [2, 3].) Lastly, embedded impedance is the terminal impedance at one element when all others are terminated; these are usually in resistive loads and not excited. (The extension of these definitions to patterns and coupling do not track exactly, unfortunately.)

The measurement of each type of impedance requires a different array configuration and some change or limit to the physical definition of the array.

The earliest research on impedance coupling limited the problem to dipoles spaced at $\lambda/2$ and, if present, had a ground plane separated at $\lambda/4$. Carter [4] developed analytical formulations of the effects of scanning on mutual impedance in this geometry. He found that the impedance near the middle of a large array approached the infinite array solution. Engineers commonly employ this finding in its reverse form, where infinite array solutions have been used to model the interiors of large arrays. This approach (initially) ignores edge effects. The edge effects from the finite nature of an array cause distortions nearer to the array edges.

Allen, in early research on beam steered arrays [5], investigated the effects of mutual coupling in a planar array with a rectangular grid. (This dissertation considered no other grid layouts.) The antenna voltages and source currents on the i^{th} element are related by

$$v_i = \sum_j z_{ij} i_j \tag{1}$$

where z_{ij} is the mutual impedance between elements i and j. The well-known principle of *pattern multiplication* states that the array pattern is the product of the *isolated element pattern* (the performance of a single element in space) and the *array factor.*

Hannan [6] presents some limitations of mutual impedance measurements both from both the practical execution of the measurement and, separately, by what it excludes. Most operational array elements have a load attached, either as a source generator or a receive amplifier; measuring mutual coupling makes more practical sense than measuring mutual impedance. Mutual impedance does not capture any losses in the normally attached circuitry on an element. The difference in either case between a fully excited and attached feed structure and an attached but terminated feed structure is the definition of *mutual coupling*. Its effects are both on the pattern and impedance. (Such a configuration is different from the measurement of mutual impedance, wherein one element is excited and other elements are open-circuited.) The measurement of mutual coupling requires connecting the other elements to resistive terminations. The terminations become power absorbers but, as compared to an open-circuit element, typically make the terminated elements near resonant length, and re-radiation occurs. With this layout, Hannan [6] asked what is the trend in mutual coupling for planar-array antennas. Specifically, he

considered ones with substrates and substrate-guided surface waves (see Section 2.6.1 for further explanation). There are likenesses in such cases to surface waves in ground wave propagation (i.e., low and medium frequency propagation), which Collin [7] covers well. The realization for far distances is a field decay with mutual coupling of $1/r^2$ in planar arrays. As groundwave propagation is certainly more complicated than the asymptotic $1/r^2$ decay [8], the $1/r^2$ mutual coupling relationship in planar arrays is a first-order relationship. Unfortunately, for the coupling investigated in this author's research, asymptotic behavior is too coarse an estimation to be useful.

The mutual coupling is of great concern for direction-finding (DF) antenna arrays. It is a common application to represent a low limit of wideband performance. (The upper limit is at element-pair separations of $\lambda/2$ where phase differences are no longer unique.) Tight coupling between elements will distort the vectors that are necessary for the algorithm to resolve an angle of arrival with sum and difference signals. As expected, mutual coupling increases when the elements are more closely spaced but not monotonically with distance. When considering a wideband DF array, the lowest frequencies will be the most tightly coupled and, likewise, the incoming waves will have the minimum phase difference between elements. Mutual coupling is physically present in all DF elements, with varying levels across frequency. It may be removed algorithmically in the processor by the use of a static data lookup table developed during a manufacturer's calibration phase during production [9]. Later, in the discussion of *S*-parameters (Section 2.1.3), there is an equivalent realization to mutual coupling in direction finding. As the impedance match between antenna impedance and receiver reference impedance grows, more backscatter exists and the received power level declines. At the same time, mutual coupling between array element declines.

Gupta and Kseinski [10] derived the coupling matrix from a network perspective, including both self and mutual coupling, and related it to the impedance matrix. The impedance matrix is an intrinsic property of the antenna structure. They specifically describe the drastic effects of mutual coupling when the inter-element spacing $d < 0.5\lambda$. Their model used an *n*-terminal network plus one source network as shown in Figure 2-2.

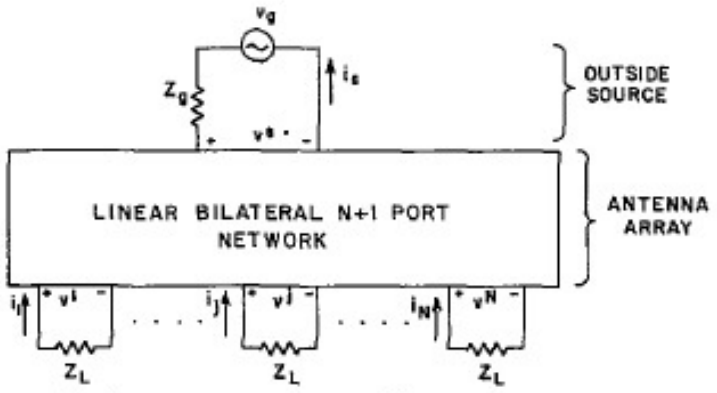

Fig. 2. Antenna array as a $N + 1$ terminal network.

Figure 2-2 – Antenna array as an *N*+1 terminal network (Fig. 2 of [10]. ©1983 IEEE. Reprinted with permission from IEEE.)

Each port of the array is terminated in a known load impedance Z_L, and the source generator has an open-circuit voltage v_g and internal impedance z_g. Employing Kirchoff relations for a plane-wave excitation, they expressed the array as

$$\begin{aligned} v^1 &= i_1 z_{11} + \ldots + i_j z_{ij} + \ldots + i_N z_{1N} + i_s z_{1s} \\ &\vdots \\ v^j &= i_1 z_{j1} + \ldots + i_j z_{ij} + \ldots + i_N z_{jN} + i_s z_{js} \\ &\vdots \\ v^N &= i_1 z_{N1} + \ldots + i_j z_{Nj} + \ldots + i_N z_{NN} + i_s z_{Ns} \end{aligned} \tag{2}$$

where i_s and z_{js} are the source current and impedance, z_{ij} is the mutual impedance between the ports of the array elements i and j.

If the feeds are all set as open circuits, $i_j = 0$ and (2) reduces to $v^j = z_{js} I_s$ for each element j. Separately, if each array element is terminated, this load Z_L can normalize each equation and relate the currents to the load impedance, $i_j = -v^j / Z_L$. These relationships reduce (2) to

$$\begin{bmatrix} 1+\frac{z_{11}}{Z_L} & \frac{z_{12}}{Z_L} & \cdots & \frac{z_{1n}}{Z_L} \\ \frac{z_{21}}{Z_L} & 1+\frac{z_{22}}{Z_L} & \cdots & \frac{z_{2n}}{Z_L} \\ \vdots & \vdots & \ddots & \vdots \\ \frac{z_{n1}}{Z_L} & \frac{z_{n2}}{Z_L} & \cdots & 1+\frac{z_{nn}}{Z_L} \end{bmatrix} \begin{bmatrix} v^1 \\ v^2 \\ \vdots \\ v^n \end{bmatrix} = \begin{bmatrix} v_{o1} \\ v_{o2} \\ \vdots \\ v_{on} \end{bmatrix} \tag{3}$$

or, more concisely, $[Z_0][V]=[V_o]$, where $[Z_0]$ denotes the normalized impedance matrix, $[V]$ denotes the element output (source) voltage, and $[V_o]$ denotes the open-circuit voltages at the terminals. As design changes reduce mutual coupling, $[Z_0]$ approaches a diagonal matrix. If all non-diagonal matrix elements are zero, no mutual coupling is present. The authors show further development and results for the effect of mutual coupling on adaptive arrays. They also illustrate the serious effects for small interelement spacing. They conclude with a treatment on adaptive arrays including transient responses, which are not the focus here.

Solving such matrices is not simple and requires several measurements with the array elements in different configurations. Su and Ling [11] present an approach using the full array pattern and an isolated element pattern to determine the coupling matrix. The "true" array pattern is then a modification of n isolated element patterns by a coupling matrix

$$[A_{true}]=[M][A_{theo}] \tag{4}$$

One can represent the coupling matrix $[M]$ and the stand-alone element pattern $[A_{theo}]$ for the i^{th} row as the stand-alone element $f_{iso}^{(i)}(\theta,\phi)$, adjusted for its position in the *xy*-plane as

$$a_i(\theta,\phi) = f_{iso}^{(i)}(\theta,\phi)e^{jkr_i} \tag{5}$$

where $r_i = x_i \sin\theta\cos\phi + y_i \sin\theta\sin\phi$. Su observed that the columnar stacking of $[Z]$ in (3) results in the active pattern matrix $[A_{true}]$ and that the open-circuit voltages $[V_o]$ can represent the stand-alone pattern matrix $[A_{theo}]$. This assumption results in $[M]=\left[Z^{-1}\right]=[Y]$. It is not a

rigorous solution but it works in an approximate sense. As Su states, it has been employed numerous times.

Friedlander and Weiss [12] present a comparable mutual coupling model to that provided by Gupta and Kseinski [10]. Their assumption requires the currents on the element not to change with scan angle. This effectively is a viewing of the average over all angles. If the current distribution on the element is independent of scan angle, the stand-alone element pattern is also independent of scan angle. This requirement typically holds true around the element resonant frequency, which emphasizes its use for simple resonant and narrowband antennas such as dipoles and patches. Su and Ling also extend (4) to other wire antennas by accounting for parasitic elements as separate but short-circuited array elements.

2.1.2 Circuit Model Representation

There is a small amount of literature on using circuit models to describe the coupling between elements in finite arrays. Lee and Chu [13] use block components, in a circuit form, to describe the admittance matrix of the array $[Y]$. The intent of this work was to develop a solution that was computationally less intensive than a full-wave solution and not having the limitations of infinite array techniques (see Section 2.4).

The normal electromotive force (EMF) or Method of Moments (MoM) formulation $[Z][I]=[V]$ is reformed to separate the isolated impedance of an isolated antenna element and the mutual impedance matrix

$$Z_{iso}([U]+[M])[I]=[V] \tag{6}$$

where $[U]$ is a unit or identity matrix and $[M]$ is the mutual impedance matrix $[Z]$ normalized by Z_{iso}. Assuming the self-impedance of physically matching elements is equal, which is only true in infinite arrays, the diagonal terms equal to zero. This makes the self-impedance of each element equal and Z_{iso} acts as an average isolated impedance. (If there is no mutual coupling, the concept of *pattern multiplication* becomes completely accurate.) This reformulation is possible since $Z_{iso} = z_{11} = z_{22} = \cdots = z_{nn}$. Once inverted, the reformed impedance matrix can be expressed

as a power series using the binomial expansion, using only a few terms, provided that the interelement spacing is not too close [13].

$$[Y]=[Z]^{-1}=[V]^{-1}[I]\simeq Y_{iso}\left([U]-\left[M^{1}\right]+\left[M^{2}\right]-\left[M^{3}\right]+\cdots\right) \tag{7}$$

where $\left[M^{2}\right]$ represents coupling from double bounces, $\left[M^{3}\right]$ represents triple bounces, and so forth, assuming $\left\|[M]\right\|<1$. The sign notation in (7) supports the physical interpretation of the paths shown in Figure 2-3. For example, in a linear dipole array, the direct coupling term represents coupling from +*x* currents on each j^{th} dipole onto the i^{th} dipole. These +*x* currents induce a –*x* current on the i^{th} dipole. For each additional bounce, the sign of this matrix flips. If elements are widely spaced, the influence of multiple scatterings (double, triple, etc. reflections in a physical-optics sense) will be less meaningful.

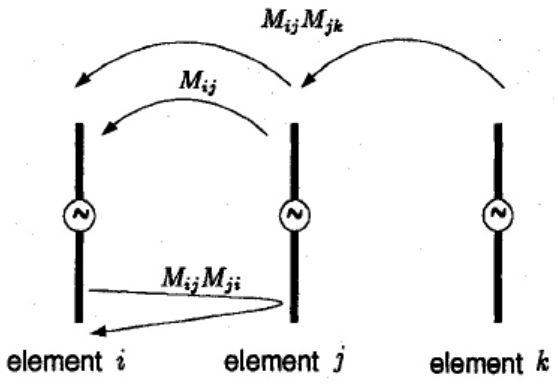

Figure 2-3 – Interpretation of the mutual coupling mechanism (Fig. 3 of [13]. ©1996 IEEE. Reprinted with permission from IEEE.)

Tighter inter-element spacing indicates higher mutual coupling and the need for higher-order terms. The viability of this approximation to tightly-coupled arrays with inter-element spacings down to $d=\lambda/20$ is unknown. Additionally, this representation suggests forcing terms $m_{ij}\to 0$ if elements are sufficiently separated. While this would reduce the computational burden, convergence of the solution may be problematic, and the approach may compromise accuracy. Reforming (6) and applying the binomial expansion, the admittance matrix becomes a series of coupling matrices

This observation is restated in a scattering sense for an arrangement of parallel cylinders. The scattering from any one cylinder becomes a superposition of the direct scattering component and the higher-order, multiple scattering components. For receive arrays, the isolated element admittance Y_{iso} relates to the direct scattering from an incident wave; $Y_i^{(1)}$ represents the contribution from the first bounce; and $Y_i^{(2)}$ represents the contribution from a double bounce. This presents an overall admittance on the element of

$$Y_{in}^{i} = Y_{iso} + Y_i^{(1)} + Y_i^{(2)} + Y_i^{(3)} + \ldots \tag{8}$$

Overall, this circuit model provides a good understanding of the effects of mutual coupling. Whether it is really a circuit model, a commonality is nonetheless present between mutual impedance, mutual coupling, and circuit method approaches.

2.1.3 Scattering Matrix Coupling and Effects on Gain

One way to represent the coupling between array elements and retain the phase lost in simple power measurements is through the *scattering matrix* $[S]$, commonly called *S*-parameters. *S*-parameters are coupling coefficients between ports, and the earlier relationships between two ports used voltage waves in the form

$$\begin{bmatrix} v_1^- \\ v_2^- \end{bmatrix} = \begin{bmatrix} s_{11} & s_{12} \\ s_{21} & s_{22} \end{bmatrix} \begin{bmatrix} v_1^+ \\ v_2^+ \end{bmatrix}$$
$$\left[V^-\right] = [S]\left[V^+\right] \tag{9}$$

where $\left[V^-\right]$ and $\left[V^+\right]$ represent reflected and incident voltages, respectively [14]. A specific element in an *n*-port network can be determined by

$$s_{ij} = \left.\frac{v_i^-}{v_j^+}\right|_{v_k^+ = 0 \; for \; k \neq j} \tag{10}$$

which states that the s_{ij} term is the measurement of the voltage on port i for a source voltage applied to port j. There should be no excitation on any port except j [15]. If all ports terminate

in reference loads, there will be no reflections. A reformation of the relationships allows for an observation of how *S*-parameters define all voltages reflected from (really, coming out of) any port i. A voltage port term v^i is the summation of incident and reflected voltages

$$\begin{aligned} v^i &= v_i^+ + v_i^- \\ &= v_i^+ + \sum_{j=1}^{n} s_{ij} v_i^+ \end{aligned} \tag{11}$$

Kurokawa [16] expressed *S*-parameters in terms of power waves instead of voltage waves. The square of the power wave then easily represents power flow. Assuming a real reference impedance Z_o, which is typical, he restated the voltages v_i^+ and v_i^- as power waves a_i and b_i flowing into and out of each i^{th} port, respectively

$$a_i = \frac{v_i^+ + z_i i_i}{2\sqrt{\left|\mathrm{Re}\{z_i\}\right|}},\ b_i = \frac{v_i^- - z_i^* i_i}{2\sqrt{\left|\mathrm{Re}\{z_i\}\right|}} \tag{12}$$

Like (10), he defined the *S*-parameter as a simple power wave relationship of the power waves flowing out of and into any port

$$s_{ij} = \frac{b_i}{a_j} \tag{13}$$

Applying the relationship of $v_i = z_L i_i$ for any port i, (12) and (13) reduce to the familiar form of the reflection coefficient

$$\Gamma = s_{ii} = \frac{Z_L - Z_i^*}{Z_L + Z_i} \tag{14}$$

As port representations, *S*-parameters have no explicit angular dependence. However, if two antennas are oriented with their main beams away from each other, the resulting s_{21} will be much different from when they point towards each other. While this description may indicate a common radio link layout, it also applies in arrays. Consider the difference between a collinear

array of dipole and a parallel array of dipoles, for example. The first are oriented in the pattern nulls of their neighbors, while the parallel elements lie where the dipole fields are strongest.

S-parameters capture all environmental effects between the ports in a system. If the environmental properties such as location and orientation of the antennas change, the resulting *S*-parameters will change. Losses exist in the element feeds unless the elements are purely orthogonal. A pair of infinitely thin cross-dipole antennas that have no cross-polarization can illustrate this. No power couples from one polarization to the other. However, this is purely ideal and theoretical. All real antennas have cross-polarization because they are not infinitely thin nor exist is a universe of their own. An overlap in element patterns in space implies cross-coupling between the corresponding feed ports [17]. With internal resistance in the element source generators, this cross coupling is lossy. Since real elements are not purely polarized, radiation from one element will couple into another, always. The array environment introduces asymmetries, and some of these lead to cross-polarization.

Within an array, mutual coupling from other elements affects every other element. Mutual coupling, reflection coefficients, and, of course, array size relate directly to the amount of gain reduction. As the array elements couple more, primarily by their separation but also their shape, the differences between an isolated development and a full (or infinite) array development grows increasingly. These relationships argue for the development of array element first in large or infinite arrays, where all mutual coupling is present for a given inter-element separation and element shape.

Ludwig [18] considers ideal coupling between two identical elements to simplify the explanations and shows the interrelationship between element pattern, mutual coupling, and passive reflections between elements. Below is a lengthy review of his work because the framework articulates the inter-element coupling in arrays. The derivation begins by considering the fields from two antennas and the radiation through a far-field surface S_3, as shown in Figure 2-4.

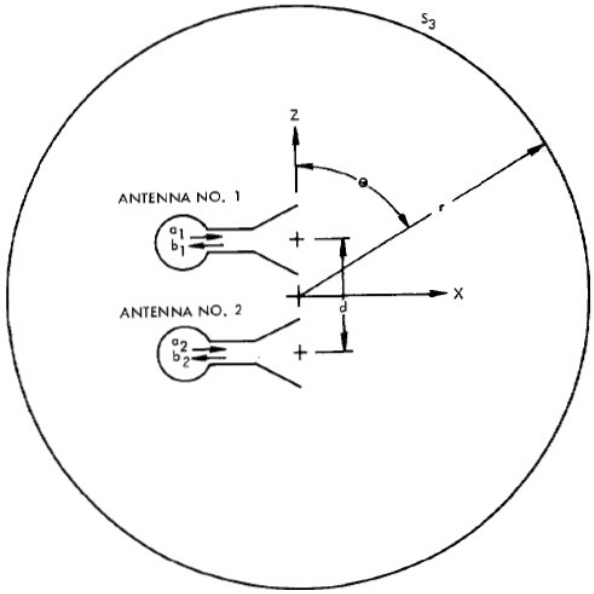

Figure 2-4 – Geometry of Ludwig's array (Fig. 1 of [18]. ©1976 IEEE. Reprinted with permission from IEEE.)

When Antenna 2 terminates in a reference load, the element electric field produced by Antenna 1 on surface S_3 with arbitrary polarization $\hat{i}$ is

$$\vec{E}_3(r,\theta,\phi) = b_3 \frac{e^{-jkr}}{r} f_3(\theta,\phi)\hat{i} \tag{15}$$

Likewise, when Antenna 1 terminates in a reference load, the electric field from Antenna 2 on its separate far-field surface S_4 with arbitrary polarization $\hat{j}$ is

$$\vec{E}_4(r,\theta,\phi) = b_4 \frac{e^{-jkr}}{r} f_4(\theta,\phi)\hat{j} \tag{16}$$

These fields summed produce a combined field

$$\vec{E}(r,\theta,\phi) = \frac{e^{-jkr}}{r}\left[b_3 f_3(\theta,\phi)\hat{i} + b_4 f_4(\theta,\phi)\hat{j}\right] \tag{17}$$

By normalizing the field patterns f_3 and f_4, they represent power patterns through

$$\frac{1}{2\eta_o}\int_{\Omega}\left|f_n(\theta,\phi)\right|^2 d\Omega = 1 \tag{18}$$

with the element of solid angle $d\Omega = \sin\theta d\theta d\phi$. If power flow between ports is considered, one can restate equation (17) following $\vec{S} = \frac{1}{2}\vec{E}\times\vec{H}^* = \frac{1}{2\eta_o r^2}\left|\vec{E}\right|^2 \hat{r}$ as

$$\vec{S} = \hat{r}\frac{1}{2\eta_o r^2}\left|b_3 f_3 + b_4 f_4\right|^2 \tag{19}$$

Applying (18) and integrating, the power flow through the far-field surface S_3 becomes

$$P_{rad} = \left|b_3\right|^2 + \left|b_4\right|^2 + 2\,\mathrm{Re}\left\{b_3 b_4^* \tau\right\} \tag{20}$$

where Ludwig defines τ as the beam-coupling factor

$$\tau = \frac{1}{2\eta_o}\int_{\Omega} f_3(\theta,\phi)\hat{i}\bullet f_4^*(\theta,\phi)\,\hat{j}d\Omega \tag{21}$$

The beam-coupling factor accounts for polarization differences between the fields, which is zero if the normalized field patterns are orthogonal. Using the principles of conservation of power and the power flow into and power out of each port, $\left|a_n^2\right|$ and $\left|b_n^2\right|$ respectively, all power can be described by

$$\begin{aligned}\left(\left|a_1^2\right| - \left|b_1^2\right|\right) + \left(\left|a_2^2\right| - \left|b_2^2\right|\right) &= P_{rad} \\ &= \left|b_3^2\right| + \left|b_4^2\right| + 2\,\mathrm{Re}\{b_3 b_4^* \tau\}\end{aligned} \tag{22}$$

Ludwig restates (22) using *S*-parameters in lieu of each port's field or power flow. Using modified scattering matrix parameters, where by definition $s_{32} = s_{41} = 0$,

$$
\begin{aligned}
b_1 &= s_{11}a_1 + s_{12}a_2 \\
b_2 &= s_{21}a_1 + s_{22}a_2 \\
b_3 &= s_{31}a_1 + s_{32}a_2 = s_{31}a_1 \\
b_4 &= s_{41}a_1 + s_{42}a_2 = s_{42}a_2 \\
\left(b_{rad} = b_3 + b_4 = s_{31}a_1 + s_{42}a_2\right)&
\end{aligned}
\tag{23}
$$

Equation (22) can be restated as

$$
\begin{aligned}
\left|a_1^2\right|\left(1-\left|s_{11}\right|^2-\left|s_{21}\right|^2-\left|s_{31}\right|^2\right)+\left|a_2^2\right|\left(1-\left|s_{12}\right|^2-\left|s_{22}\right|^2-\left|s_{42}\right|^2\right) \\
-2\,\mathrm{Re}\left\{a_1 a_2^*\left(s_{11}s_{12}^*+s_{21}s_{22}^*+s_{31}s_{42}^*\tau\right)\right\}=0
\end{aligned}
\tag{24}
$$

This form allows each parameters section to be restated as its own equation, independent of the source values a_1 and a_2. These three equations have further reduction. If the antennas are considered identical, $s_{11}=s_{22}$, and if the network media is linear isotropic, reciprocity holds that $s_{21}=s_{12}$ [14]. These are restated and reduced in (25) and (26) as only two equations, assuming no loss is present.

$$
1-\left|s_{11}\right|^2-\left|s_{21}\right|^2-\left|s_{31}\right|^2=0 \tag{25}
$$

$$
2\,\mathrm{Re}\left\{s_{11}s_{12}^*\right\}+\left|s_{31}\right|^2\tau=0 \tag{26}
$$

Equation (25) expresses the nature of the transmission from Antenna 1 or Antenna 2 into space (ports 3 or 4, respectively), which represent terminated closed-surface boundaries. Thus, s_{11} describes the reflection coefficient; s_{21} describes the coupling to Antenna 2; and s_{31} describes the radiation to the far field. Per (25), without losses anywhere (e.g., resistive loading, lossy substrates, or conductive losses), power is either reflected back to the source, into the termination of antenna 2, or radiated. If Antenna 2 is passively matched the same as Antenna 1, but both are excited, there is an infinite series of re-radiation between the antennas.

For a close-spaced antenna with a non-zero beam-coupling factor from (21) and with tuned identical antennas such that $s_{11}=s_{22}=0$, equation (26) expresses how there is no far-field power flow. All power flows from Antenna 1 into Antenna 2. Since this is intuitively wrong, this

means that τ is not constant. Instead, a perfect match on Antenna 2 will severely distort the antenna element pattern to push the main lobes in opposite directions to make $\tau = 0$. Ludwig simplifies the beam-coupling factor from (21) for the fundamental mode (omnidirectional in azimuth) to

$$\tau = \frac{\sin kd}{kd} \tag{27}$$

which shows that the beam coupling $\tau \to 1$ as element spacing $d \to 0$. Also, τ is positive until $d > \lambda/2$, where it shifts negative until $d = \lambda$. Then, it continues oscillation per its sinc function form. Figure 2 of [18] presents curves for different element patterns. Ludwig concludes that τ is not highly sensitive to element pattern beamwidth, but it is mostly driven by inter-element spacing. Through examples and (28), it is seen that far-field power flow is maximized when τ is minimized. This argues for the inter-element spacing to be $d = n\lambda/2$, where n is an integer multiple, in a linear array of azimuth omnidirectional antennas for maximized gain.

$$\left|s_{31}\right|^2_{\max} = \frac{1}{1+\left|\tau\right|} \tag{28}$$

An extension of this relationship accounts for any scan angle θ_o, by modifying the magnitude of the linear phase progression $\left|\psi\right| \to \tau\cos\psi$ for the main beam and extending the development of $\left|s_{31}\right|^2$ to array gain by equating it to radiation efficiency, $e_r = \frac{P_{radiated}}{P_{delivered}}$. Between two antennas in a link, the power coupling between two antennas is $\left|s_{21}\right|^2$ and is part of the radiated power. In the array sense, the power coupling is certainly within the near field of the network and not considered part of far-field coupling. For $\theta_o < 180^\circ$ and the network of two elements, the array gain is

$$\begin{aligned} G &= e_r D \\ &= \frac{P_{rad}}{P_{avail}} \frac{4\pi r^2 \left|\vec{S}\right|}{P_{rad}} = \frac{4\pi r^2}{P_{avail}} \frac{\left|b_3 f_3 + b_4 f_4\right|^2}{2\eta r^2} = \frac{2\pi}{\eta} \frac{\left|b_3 f_3 + b_4 f_4\right|^2}{P_{avail}} \end{aligned} \tag{29}$$

Substituting (23) and assuming identical element patterns $\left(f_3 = f_4\right)$, identical coupling from each antenna to its far-field $\left(s_{31} = s_{42}\right)$, and excitations of $a_1 = a_2^* = e^{j\delta/2}$ for $-\pi \le \delta \le 0$

$$\begin{aligned} G &= \frac{2\pi}{\eta}\frac{\left|s_{31}a_1 f_3 + s_{42}a_2 f_4\right|^2}{P_{avail}} \\ &= \frac{2\pi\left|s_{31}\right|^2\left|f_3\right|^2}{\eta}\frac{\left|a_1 + a_2\right|^2}{P_{avail}} = \frac{2\pi\left|s_{31}\right|^2\left|f_3\right|^2}{\eta}\frac{4}{P_{avail}} \end{aligned} \tag{30}$$

Assuming no impedance mismatch, $P_{delivered} = P_{available} = \left|a_1\right|^2 + \left|a_2\right|^2 = 2$

$$\begin{aligned} G &= \frac{2\pi\left|s_{31}\right|^2\left|f_3\right|^2}{\eta}\frac{4}{2} \\ &= \frac{4\pi\left|s_{31}\right|^2\left|f_3\right|^2}{\eta} \end{aligned} \tag{31}$$

Using (28),

$$G = 4\frac{1}{1+\tau\cos\theta}\frac{\left|f_3\right|^2}{\eta} = 2\frac{1}{1+\tau\cos\theta}D_{element} \tag{32}$$

where the element directivity is $\frac{2\pi\left|f_3\right|^2}{\eta}$. This representation further shows that any coupling between elements will reduce the array gain.

Ludwig expands the derivation already presented to cover when both antennas are transmitting to $\Gamma_1 = s_{11} + s_{12}\frac{a_2}{a_1}$ and $\Gamma_2 = s_{21}\frac{a_1}{a_2} + s_{22}$. These he defines as *active reflection coefficients* and are consistent with IEEE definitions [1], where all array elements are in place and excited. These relationships (28) and (29) can be reworked to include impedance mismatch, to determine the criteria for maximized array gain. This occurs when the combined power reflection coefficients (i.e., average for equivalent sources) are minimized. Assuming an array with zero ohmic losses,

$$\left[\frac{|\Gamma_1|^2+|\Gamma_2|^2}{2}\right]_{\min}=\frac{|\tau|-\tau\cos\theta^{\circ}}{1+|\tau|} \tag{33}$$

For $\tau=0$, the active reflection coefficients are minimized for all scan angles. This result makes intuitive sense if polarization alone is the driving factor of τ. For an interelement spacing $d<\lambda/2$ for omnidirectional patterns, the active reflection coefficients are minimized for the broadside angle ($\theta_o=0$) and diminish away from broadside. This result also makes physical sense.

One apparent extension of network models is beyond two elements. Takamizawa generalized the case for an array of *N* elements, using *N* + *M* ports [19]. The additional ports may be set $M=2$ to describe a common far-field boundary surface, capturing both orthogonal polarizations. (Conceivably, a third port could capture the third polarization in the near field, or for a case like ground wave propagation, where no far field exists.) As with Ludwig, the additional M ports describe the radiated power through an arbitrary surface.

The *S*-parameters in an *N*-port network include the impedance mismatches from each port source back to itself and to others. They therefore capture the power ratios between the available powers at each source port. If there is a complete mismatch at a port, no power will be coupled into another port (e.g., if $|s_{11}|^2=1$, $|s_{21}|^2+|s_{31}|^2=0$). However, (25) assumes no dissipative losses with the array. Takamizawa [19] points out that radiated power cannot be separated from ohmic losses in an *N*-port network description. These ohmic losses account for the difference between delivered and radiated power and argue for a modification of (25) to add another port that acts as a power sink. As such, he develops common antenna and array expressions using *S*-parameters, such as *realized gain.* Realized gain is defined as

$$\begin{aligned} G_{realized} &= \left(1-|\Gamma|^2\right)G \\ &= \left(1-|\Gamma|^2\right)e_r D \end{aligned} \tag{34}$$

where the reflection coefficient $\Gamma=(Z_L-Z_0)/(Z_L+Z_0)$ with Z_L as the load (antenna) impedance and Z_0 as the reference impedance. These terms are well known and applied regularly.

2.2 Arrays from Apertures

Aperture theory offers some additional insight into the effects of mutual coupling, at least as it applies to array gain. As with the impedance matrix, one may describe an element pattern or element gain in an isolated environment, but this performance changes when the element is included in an active array. Hannan [20] defined these two patterns as ideal pattern and element pattern, respectively. The development of these relationships will be from the array back to the element and relate directivity, gain, and realized gain.

2.2.1 Aperture Directivity

The ideal directivity for a circular aperture in the *xy*-plane is easily stated by

$$D_{ideal}(\theta) = \frac{4\pi A}{\lambda^2}\cos\theta \tag{35}$$

where A is the physical size of the array and no grating lobes exist (see Section 2.6.1). The $\cos\theta$ term accounts for variations in the projected area of the array in the direction of interest. As the *ideal* label implies, this serves as a fundamental upper limit to the directivity of an aperture, where maximization occurs at $\theta = 0$. For an $M \times N$ rectangular array, (35) can be restated using inter-element spacing $d_{x,y}$ as

$$\mathrm{D}_{ideal}(\theta,\phi) = \frac{4\pi(Md_xNd_y)}{\lambda_o^2}\cos\theta \tag{36}$$

This formulation has no ϕ variation but (36) considers all arrays to be equal and does not capture it. It also assumes a continuous aperture, although mathematically sub-divided into cells of $d_x \times d_y$. A distinction of a true aperture directivity from the ideal directivity needs some modification to (36). Allen [5] provided one simple modification by including an amplitude taper efficiency η_t in (36), which, because it includes losses, needs to be restated as gain

$$\begin{aligned} G &= G_{ideal}\eta_t \\ &= G_{cell}NM\eta_t \end{aligned} \tag{37}$$

In one sense, η_t acts as an average effect for all mutual coupling and array edge effects (see Section 2.5.1). This work is some of the first to describe the nature of the mutual impedance matrix and its role in distorting the otherwise straightforward performance of the array. In addition, the aperture directivity relates to the performance of each element within the array, and (37) breaks this apart, but still in an average sense. This formulation fails to capture a number of physical phenomena, including variations between elements, physical differences in location, and polarization.

2.2.2 Array and Element Efficiency

When considering arrays, one can separate the concepts of directivity, gain, and realized gain, and apply them to elements in summation to represent the entire array. Kahn [21] states flatly that the element efficiency quantifies all effects of mutual coupling in arrays. Relating the power relationships for the m^{th} element in an array to *S*-parameters illustrates this. First, he restates basic relationships in terms of powers available, delivered, and radiated as

$$\eta_m = \frac{P_{rad}^{(m)}}{P_{avail}^{(m)}} \tag{38}$$

If the available power does not radiate, it reflects or is absorbed, leading to a restatement of (38) as

$$\eta_m = 1 - \frac{P_{refl}^{(m)} + P_{abs}^{(m)}}{P_{avail}^{(m)}} \tag{39}$$

Breaking apart the total powers into element components following (23) where b_n is the power wave flowing out of each element, and a_m is the power wave flowing into each element, *S*-parameters may represent the element mismatch efficiency for each m^{th} element as

$$\begin{aligned} \eta_m &= 1 - \frac{\sum_{n=1}^{M\times N} |b_n|^2}{|a_m|^2} \\ &= 1 - \sum_{n=1}^{M\times N} \left|S_{mn}\right|^2 \end{aligned} \tag{40}$$

This form captures the power flow throughout the ports in the system, except for far-field radiation. If an additional port represents the far field, as Ludwig did [18], this form captures all power flow.

This element efficiency is the *realized gain*, divided by the *directive gain* $\eta_m = g_{realized}^{(m)} / d^{(m)}$. This form includes the presence of ohmic losses in the array and feed impedance mismatches. With the inclusion of the reciprocal relationship of $s_{mn} = s_{nm}$, one can reformulate and solve (40) by exciting each element successively with $a_m = a_0$ and measuring all reflected powers $|b_n|^2$. Less effectively, one can integrate the far-field pattern for each element sequentially.

The limits on aperture gain are the basis for quantifying bandwidth in wideband arrays. Often, gain, pattern, and impedance match (i.e., VSWR) are the target parameters for classifying bandwidth. With the wide bandwidths found in tightly-coupled arrays, the achievement of a consistent gain is not possible. The aperture electrical size alone dictates this restriction.

The previous relation (35) of maximum array gain to aperture theory is well known. Wasylkiwskyj and Kahn [21, 22] developed a reverse relationship to determine the minimum number of elements needed to achieve the maximum aperture gain, since the desire is to use the lowest number of elements. Using an average element efficiency $\bar{\eta} = \dfrac{1}{MN} \sum_{m=1}^{M \times N} \dfrac{g_{realized}^{(m)}}{d^{(m)}}$ for $M \times N$ elements, the average element efficiency relates to the maximum realized gain, averaged over 4π steradians.

$$MN\bar{\eta} = \sum_{m=1}^{M \times N} \frac{g_{realized}^{(m)}}{d^{(m)}} = \frac{1}{4\pi} \iint_{sphere} G_{realized\,\max} d\Omega \tag{41}$$

This can be easily restated to provide the lowest number of elements for a given gain, where $\bar{\eta} = 1$ provides the lowest bound. Equation (41) is not that different from (37), but it developed from another viewpoint.

2.2.3 Current Sheet

The concept of the current sheet is useful in distinguishing the continuous aperture (and its related equations) to an array of discrete elements. Dipole elements have an effective length and an effective area although they are physically linear. Wheeler [23] clearly states how scan angle affects element impedance using an infinite planar array. He conceived of parallel waveguides extending away from an infinite planar array. In developing this concept the waveguide boundaries, the walls in the *H*-plane (parallel to the elements) are open-circuited magnetic boundaries and the walls in the *E*-plane are short-circuited electric boundaries in order to maintain images as in an infinite array.

As the scan angle changes, the waveguides skew and reduce the cross-sectional area in each. For an effective element length l and inter-element spacing d, the input resistance relates to the free space impedance $\eta_0 = 377\Omega$ for a scan angle θ. The ratio (l/d) represents a transformation ratio between the antenna and free-space. Wheeler developed this relationship in [24] by first considering the dimensions of a rectangular waveguide of width a and height b, such that $R_{rad} = \eta_o b/a$. Wheeler developed the relationship between (b/a) and (l/d). Incorporating a $1/\cos\theta$ term adds a geometric correction to the aperture size when scanned off broadside. The resulting radiation resistance of the current sheet is

$$R_{rad} = \frac{\eta_0}{\cos\theta}\left(\frac{l}{d}\right)^2 \tag{42}$$

Additionally, there is a change to the amount of radiation in the beam direction. For dipoles, the normalized patterns are $F(\theta,\phi)^2 = 1$ in the *H*-plane, and $F(\theta,\phi)^2 = \cos^2\theta$ in the *E*-plane to stipulate the classic doughnut pattern. Adding these pattern terms into (42) yields a resistance relationship equal to (42) for *H*-plane scanning and $R_{rad} = \eta_o (l/d)^2$ for *E*-plane scanning. While a simple model, these relationships begin to illustrate how array scanning affects the input impedance on an array, and therefore also, its reflection coefficient and element efficiency.

2.3 Power Vector Coupling

This chapter has presented mutual impedance and *S*-parameters to allow for the experimental characterization of coupling between array elements. As these are port-based descriptions, they tend to obscure the mechanisms of direct power flow between array elements that the Poynting vector describes. The port-based methods lump all coupling power to the single location and do not explicitly describe the reactive near fields. The coupling coefficients also explain the loss of gain and impact on active impedance that stem from scanning the array to angle θ_o, ϕ_o in a planar array.

Maeda and Diament [25] explain that the Poynting-vector flows toward other source elements and not outwards in all cases. (This is an extension of Schantz [26, 27], who described the direction reversal of the Poynting-vector field near the source of a single dipole and defined a *causal surface* around a radiator where the normal component to the surface equals zeros, that is, where net power flow equals zero.) When one excites two parallel electric dipoles with a feed phase difference between them, an asymmetric Poynting vector is evident around the antennas. This power flow applies for time-averaged power flow. The inflow of power on the lagging antenna adjusts the net power flow of that antenna and affects its active impedance. This power flow occurs when the dipoles are very close together, e.g., $d = 0.016\lambda$ for the demonstration of the theory. A more practical separation of $d = \lambda/4$ is also considered, and as expected, the results show an overall decrease in the time-averaged power coupling from Dipole 1 into Dipole 2. As the fields flow into Dipole 2, the overall system radiation coming from Dipole 2 reduces. Results show that Dipole 2, lagging Dipole 1 in phase, radiates about $1/10^{th}$ the power of Dipole 1. The work of Maeda and Diament does not expand conceptual understanding of the mutual coupling between elements as much as it shows a distributed relationship between elements instead of simple port relationships.

2.4 Coupling in Infinite Arrays

Engineers have historically employed infinite array techniques to tackle the analysis of large arrays. The closest surrounding elements most strongly affect elements in arrays. If elements are sufficiently away from an array edge, they behave as though they are in an infinite array. As

such, infinite array techniques are useful in designing large arrays, but they naturally fail to capture all physical phenomena such as edge or end effects in infinite arrays.

Infinite array techniques rely on the periodicity of the elements in the array, followed by superposition, to reduce the complexity of the computational solution. Each array element exists within a unit cell, of arbitrary size but repeatable, and the boundary conditions for each unit cell match to the adjacent cell. The simplest unit cells are rectangular or square. Infinite array techniques only evaluate one cell, using boundary conditions, because every cell is the same, with the exception of a linear phase taper associated with beam steering.

The dominant method for analyzing infinite arrays involves Floquet theory, which expands the electromagnetic fields into a series of modes. (In its method of moments solution, FEKO© uses a modified form called the Periodic Boundary Condition.) Lower-order Floquet modes are more likely to propagate, while higher-order modes are cut-off and non-propagating, like in waveguides. The $m,n=0,0$ mode is always present, while modes $0,\pm1$ and $\pm1,0$ radiate only if grating lobes exist [28]. Stated in reverse, if no grating lobes are present, only the $m,n=0,0$ Floquet mode is present in infinite arrays. (Section 2.6.1 presents further details on Floquet modes.) Since the focus of this research is on tightly-coupled arrays, wherein the $d \le \lambda/2$, no grating lobes should be present. However, evanescent higher-order modes may exist within the array and affect impedance.

2.5 Coupling in Finite Arrays

Finite arrays are, of course, the concern of practical array designs. They are also the concern of this dissertation. The finite nature of arrays and the presence of array edges, introduces many interesting and disrupting behaviors in arrays. One distortion that exists across all frequencies comes from end or edge permutations. At certain frequencies (or certain inter-element spacings), there are additionally surface waves in finite arrays. A large portion of the literature on finite arrays, and especially the effects of edges, concern only dipoles, slots, or patches. The concept of the current sheet and the fundamental radiation patterns for electrically small and resonant antennas both support the use of these fundamental elements to describe effects in finite arrays.

For planar arrays, there are at least three different classes of elements: corner (vertex) elements, edge elements, and interior elements. This distinction means that the active impedance

and active element realized gain patterns vary between elements. This variation puts the active element pattern inside the summation, now limited to the $M \times N$ elements in the array, to define the normalized far-field pattern

$$F(\theta,\phi) = \sum_{n=1}^{M \times N} g_{ele}^{n}(\theta,\phi) i_n e^{-jkr_n} \tag{43}$$

where r_n is the arbitrary distance offset. The mutual coupling within the array directly affects each of the $M \times N$ element patterns.

This section should also note semi-infinite arrays. These arrays have been used in [29, 30], among many others, to reduce computational complexity while including edge effects. Chapter 5 also relies almost entirely on them. Some semi-infinite arrays, say in the xy-plane, are infinite in $\hat{x}$ and finite in $\hat{y}$. Others are infinite in $\hat{x}$ and $-\hat{y}$, and finite in $+\hat{y}$. Work with semi-infinite arrays in this dissertation is of the former type. This allows one to analyze *E*-plane and *H*-plane edge effects separately.

2.5.1 End Permutations

Distortions in finite arrays are the effect of the edge elements. As interelement coupling drops, the immediately adjacent elements have the dominant effect on any single element. For a periodically spaced rectangular planar array, an interior element has eight immediately adjacent elements and has reduced effects from ones farther separated. Still, differences are still present in such arrays since among the eight, two are *E*-plane oriented, two are *H*-plane oriented, and four are diagonally oriented. As a first-order approximation, one may consider all internal elements to be the same. Edge elements differ, however, because they lack three elements on one side. Likewise, corner elements only have three adjacent elements. Some modeling approaches [31, 32] for approximating large arrays rely on these geometric distinctions.

Hansen [33] presents simulation results for the input impedance of a semi-infinite array of resonant dipoles at an interelement spacing $d = \lambda / 2$ as the beam scanning is changed. The oscillations in active input impedance occur at all scan angles for an *E*-plane scan. The nature of the ringing is a function of the element shape, inter-element spacing, and the presence of any resistive loading, among possibly others. Hansen showed how they form of a standing wave and

how the period changes with the dipole radius. Thicker wires produced more substantial oscillations. Overall, the ringing reduces the effective area of the array because of imperfect phase coherence between elements, but it is typically not severe. Array gain in the presence of such effects can be close to the gain from a uniformly excited aperture.

These variations exhibit Gibbs phenomenon, just as in the Fourier approximation of a square wave, as shown in Figure 2-5. For a square wave approximation, the phenomenon stems from the approximation of a discontinuous function by a finite series of continuous sinusoids. The ringing shown by the Gibbs phenomenon would be similar to the current (or impedance) variations along the array. The greatest deviations (from an infinite array performance) are nearest to the edges, while the minimal deviations are in the center. This current ringing in a linear dipole array results from the discontinuous termination of currents at the end of the array (aperture), if fully articulated.

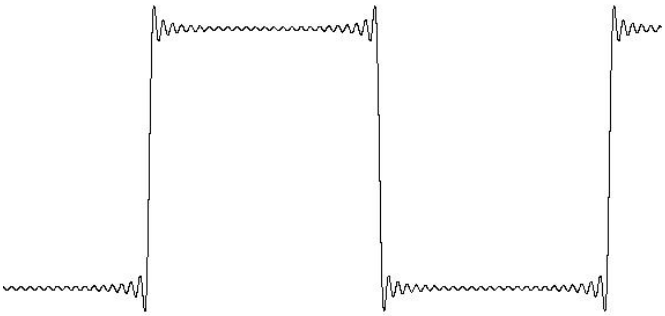

Figure 2-5 – Approximation of square wave with 25 Fourier series terms, showing Gibbs phenomenon

Craeye and Arts [34] explain the modulation in the currents or active impedances by the spatial sampling of the edge-diffracted wave. They consider a linear array of resonant half-wave dipoles with an inter-element separation $d = \lambda / 2$ and a spacing over a ground plane $h = \lambda / 4$. To differ from Hansen [33], they excite only the end element and observe the currents on the other 118 short-circuited elements. For $k = 2\pi / \lambda$, the current at the middle of each element short is

$$I_n = f(nd)\exp(-jnkd(1-\varsigma)) \tag{44}$$

where $f(nd)$ is the decaying complex envelope of the wave; n is the element index; and ς is a parameter phase correction term that accounts for phase velocity other than free space. This results in a monotonic decay away from the feed element, a nearly linear phase shift, and a phase velocity v slightly higher than c. One can estimate the parameter ϵ by subtracting the free-space phase shift between elements (180° at $d = \lambda / 2$) from the results. The phase difference between elements is greater for the thinner radius dipoles, and in both cases, the shifts are positive. This dictates that ϵ is positive. The higher phase velocity requires that any spatial sampling be increase beyond the standard Nyquist rate. There is speculation that the higher phase velocity is the result of the multiple reflections and radiations between the ground plane and the shorted dipole elements. Bekers *et al*. [35] found the same conclusion for more element shapes and spacings.

2.6 Surface Waves

Two different kinds of surface waves can exist along periodic structures. The more well-known type is the Substrate-Guided Surface Waves (SGSW), and a newer type of surface wave is termed the Array-Guided Surface Wave (AGSW).

A Substrate-Guided Surface Wave (SGSW) is a wave trapped within an array substrate because of the presence of a reactive boundary between the substrate and air [14]. The array may also trap the wave within the same region if a dielectric substrate is not present, because the presence of the array elements presents a reactive boundary to ground. The SGSW is normally present when the inter-element spacing is sufficiently large, along with the scan angle, to trap the wave. A critical angle must be reached to launch the wave, which thereafter the substrate traps it due to total internal reflection. This type of surface wave can occur in infinite array simulations. Therefore, it is not a function of the end permutations.

The second type of wave introduced by Munk *et al* [36] does not require a substrate or a ground plane. The array structure itself guides these surface waves, and hence are referred to as Array-Guided Surface Waves (AGSW). They can only exist in a finite periodic structure, implying the end permutations play an important role in their behavior. Additionally, these surface waves only occur when the inter-element spacing $d < \lambda / 2$.

The following sections discuss both types of surface waves in more detail. The SGSW is not applicable to the overall design of arrays in this dissertation. However, it is necessary to contrast it in detail to the AGSW, which will play an integral part in tightly-coupled array designs. This section concludes with a brief overview of the Yagi-Uda array and its ties to the AGSW.

2.6.1 Substrate-Guided Surface Waves (SGSW)

One assumption in (35) for aperture directivity is that no grating lobes are present. Grating lobes are secondary lobes of substantial size compared to the main lobe and form when phase spacing between elements is such that waves from all elements add together in phase in more than one direction [37]. If an array produces a plane wave in a direction with unit vector given by

$$\hat{s} = s_x \hat{x} + s_y \hat{y} + s_z \hat{z} \tag{45}$$

then, in general $s_x^2 + s_y^2 + s_z^2 = 1$. (Per standard orientations, $s_x = \sin\theta_s \cos\varphi_s$ and $s_y = \sin\theta_s \sin\varphi_s$ where θ_s and ϕ_s denote scan angles.) Real power transfer, i.e., real propagation, occurs when $s_z = \sqrt{1 - s_x^2 - s_y^2}$ is real. This requires the term $s_x^2 + s_y^2$ to lie within a circle in the s_x, s_y plane of radius 1 that defines *visible space*. That is, if $s_x^2 + s_y^2 < 1$, s_z is real and propagation occurs. Conversely, if $s_x^2 + s_y^2 \geq 1$, no propagation occurs, the region is considered invisible space, and the waves are evanescent. This formulation, however, only considers one propagating mode, namely Floquet modes $m, n = 0, 0$. The complete spectrum from a periodic structure in the *xy*-plane without dielectric is given by [38]

$$\hat{r} = \left(s_x + \frac{m\lambda}{d_x} \right) \hat{x} + \left(s_y + \frac{n\lambda}{d_y} \right) \hat{y} + s_z \hat{z} \tag{46}$$

As with the formulation in the s_x, s_y plane, there is a transition between propagating and evanescent modes when defined in the r_x, r_y plane

$$1 \le \left(s_x + \frac{m\lambda}{d_x} \right)^2 + \left(s_y + \frac{n\lambda}{d_y} \right)^2 \tag{47}$$

This chapter has assumed the square inter-element spacing $d = d_x = d_y = \lambda / 2$ many times. Applying it to (47), one can see the center of mode $1,0$ to be at $r_x = 2$. With the visible space radius limited to one, such spacing dictates that these circles not overlap (Figure 2-6). As d becomes less than $\lambda / 2$, the circles spread apart, and conversely, as d becomes larger, the circles of visible space begin to overlap. Once these circles overlap, grating lobes can appear in visible space depending on scan angle. If the elements are separated by λ or more, grating lobes will be present for a broadside angle $\theta = 0^\circ$ for the main beam [39].

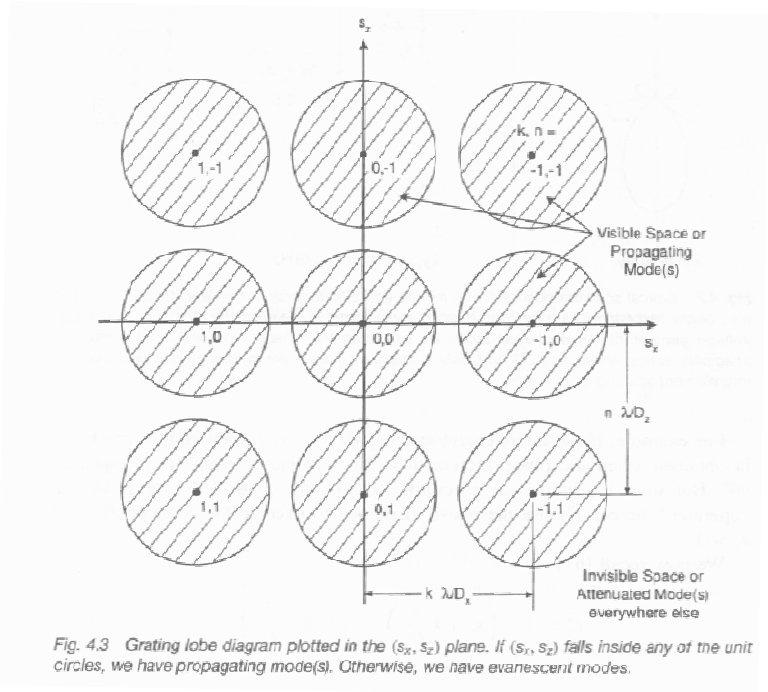

Fig. 4.3 Grating lobe diagram plotted in the (s_x, s_z) plane. If (s_x, s_z) falls inside any of the unit circles, we have propagating mode(s). Otherwise, we have evanescent modes.

Figure 2-6 – Occurrence of grating lobes as a function of scan angle and spacing (Fig. 4.3 of [2], reprinted with permission through subscription to the Copyright Clearance Center

While grating lobes are an obvious distortion to the array pattern, other concerns arise when $s_x^2 + s_y^2 \ge 1$, which is in invisible space. Here, Munk [2] considers the grating lobes to be trapped in the substrate. This surface wave will be called the Substrate-Guided Surface Wave (SGSW). Pozar and Schaubert [28] found that SGSW are trapped waves that can exist when the

array structure supports a slow wave, whether infinite or finite. Since a grounded dielectric slab supports a slow wave and they are commonly used, these configurations have been used in the development of much of this theory.

At certain scan angles, *scan blindness* can occur, and the array directs power only into a surface wave. This implicitly means that $R_{rad} \to 0$ and $|\Gamma| = 1$ when scan blindness occurs. This may occur because the scan angle is outside of visible space, as can happen with closely spaced elements and too large of inter-element phase progressions ψ. This condition results in an imaginary scan angle and offers a condition where no stationary phase exists at any observation angle [39]. One may consider this condition as a direct flowing of power from one element into another, which results in no power flow away from the array and a $|\Gamma| = 1$.

Scan blindness also means that the grating lobe is transitioning from invisible space to visible space, which occurs when elements are electrically far apart. If the array is infinite, there is no radiation carrying power away from the array. The closest modes that could overlap into the fundamental mode are directly in *H*-plane and *E*-plane scan directions (modes $\pm 1, 0$ and $0, \pm 1$, respectively). An inter-element space $d = \lambda_{eff} / 2$ and a scan angle $\theta = 90^{\circ}$ are the first conditions for scan blindness to occur, where the effective wavelength may differ from the free-space wavelength depending on the presence of substrates. In this dissertation, scan blindness resulting from grating lobes is of less importance because no substrates are present and the inter-element spacings $d_x = d_y$ are mostly below $\lambda_o / 2$. Scan blindness occurs when: 1) the wave number of the surface wave β_{sw} matches the wavenumber of the array; 2) the grid spacings d_x and d_y make the scan directions s_x and s_y lie within visible space; and 3) the TM or TE SGSW pole is not cancelled by a zero value of k_x or k_y respectively [28]. This understanding leads to

$$\begin{aligned} \beta^2 &= k_x^2 + k_y^2 \\ \beta_{SW}^2 &= \left(\frac{2\pi m}{d_x} + k s_x \right)^2 + \left(\frac{2\pi n}{d_y} + k s_y \right)^2 \end{aligned} \tag{48}$$

Normalizing (48), the form takes that of circles in the s_x, s_y-plane with origin offsets as in Figure 2-6 defined by m and n, which denote Floquet modes

$$\frac{\beta_{SW}^2}{k^2} = \left(\frac{m\lambda}{d_x} + s_x \right)^2 + \left(\frac{n\lambda}{d_y} + s_y \right)^2 \tag{49}$$

This form looks a lot like (47), but here two visible regions do not necessarily overlap (which would lead to grating lobes). An exact solution requires knowledge of the surface wave wavenumber. A common and basic example is a dipole array with $d_x = d_y = \lambda / 2$ scanned in the *H*-plane toward an end-fire condition. This array configuration results in $\beta_{SW}^2 = k^2$ and results in a trapped wave if the array is infinite.

The dominant SGSW is the TM_0 mode [40]. If the substrate thickness between the elements and the ground plane $h < \lambda_0 / 4\sqrt{\varepsilon_r - 1}$, only the TM_0 surface wave mode will exist. As the substrate becomes thicker, the SGSW becomes multi-modal as in waveguides. For rectangular gridded arrays, only the $(0,0)$, $(\pm 1,0)$, and $(0,\pm 1)$ Floquet modes couple to the TM_0 surface wave [40]. The last two mode sets have the TM_0 surface wave that extends into the visible space defined for the $(0,0)$ mode. If the array scans to an angle where it is coincidental with one of these TM_0 surface waves, scan blindness occurs.

2.6.2 Array Guided Surface Waves (AGSW)

Munk *et al.* [36] presented the concept of Array Guided Surface Waves (AGSW), although they acknowledge that these waves have been previously observed but without much study. The historical focus of past work involved Yagi-Uda antenna arrays [41-45]. The AGSW is distinctly different from the SGSW. It can only exist on finite arrays and only for the inter-element spacing $d < \lambda / 2$. At this spacing, SGSW and thus grating lobes are not possible.

AGSW are distinguishable by their phase velocity. As elements are more closely spaced, the phase surface velocity *v* drops [46]. The AGSW in planar arrays have different phase velocities than the phase velocities of Floquet currents. This causes interference between the AGSW and Floquet currents within a limited frequency/size range, resulting in wide variations in the current magnitude and input impedance. Additionally, the asymmetry in coupling of end elements results in changes to the currents, as compared to infinite currents. These surface waves

and end currents, in total, are responsible for larger side and back lobes in finite arrays, compared to the patterns of Floquet-only currents [36].

A linear array of dipoles allows for a basic example of the AGSW [47]. For thin dipole elements, the AGSW develops at frequencies about 20-30% below resonance if $d = \lambda_0 / 2$ and λ_0 is the wavelength at resonance of an isolated element. Figure 2-7 shows the geometry, excepting the perfect electrically conducting (PEC) ground plane that is below the array $(-\hat{z})$ and parallel to the dipole elements at $h = 0.4\lambda_o$.

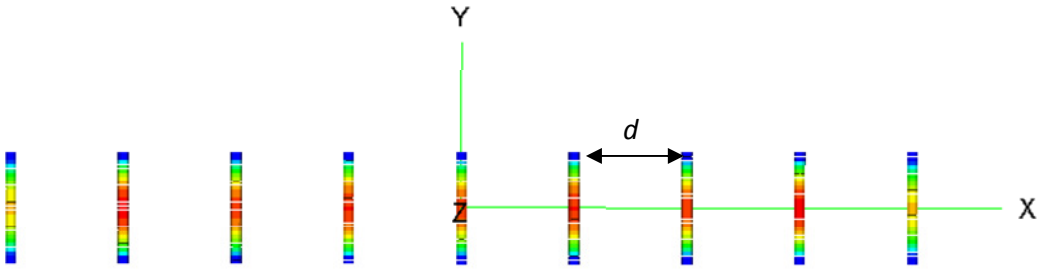

Figure 2-7 – Geometry of 9-Element λ/2 dipole array, with ground plane at *h*=0.4λ (not shown), showing currents

Figure 2-8 shows the input resistance of the center element for three array lengths; and, Figure 2-9 shows the reactance for the same. The "disruptions" in both R_{in} and X_{in} across frequency indicate frequency ranges where a good impedance match is not possible. If larger bandwidths of about 4:1 are desired, the AGSW are "unavoidable". They will exist within the bandwidth of such an array unless one takes steps to mitigate their presence or effects.

The concern for AGSW is that they substantially disrupt the active impedances of the elements. Depending on each location in the finite array, the element will experience widely different input impedances for a given frequency. These variations exhibit a periodic nature over the entire array structure. The launching of the wave itself is not as detrimental as the standing waves that the reflection from the edge of the array creates. These constructive and destructive combinations amplify the effects of the surface wave.

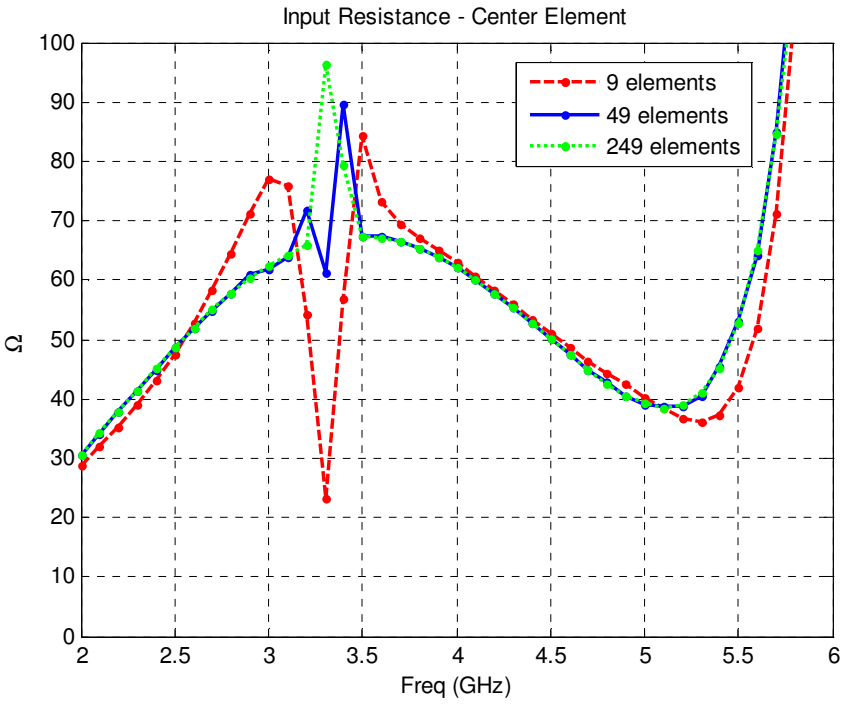

Figure 2-8 – Input resistance of center element of linear array of dipoles over PEC ground (as in Figure 2-7) for parallel arrays of 9, 49, and 249 elements [47]

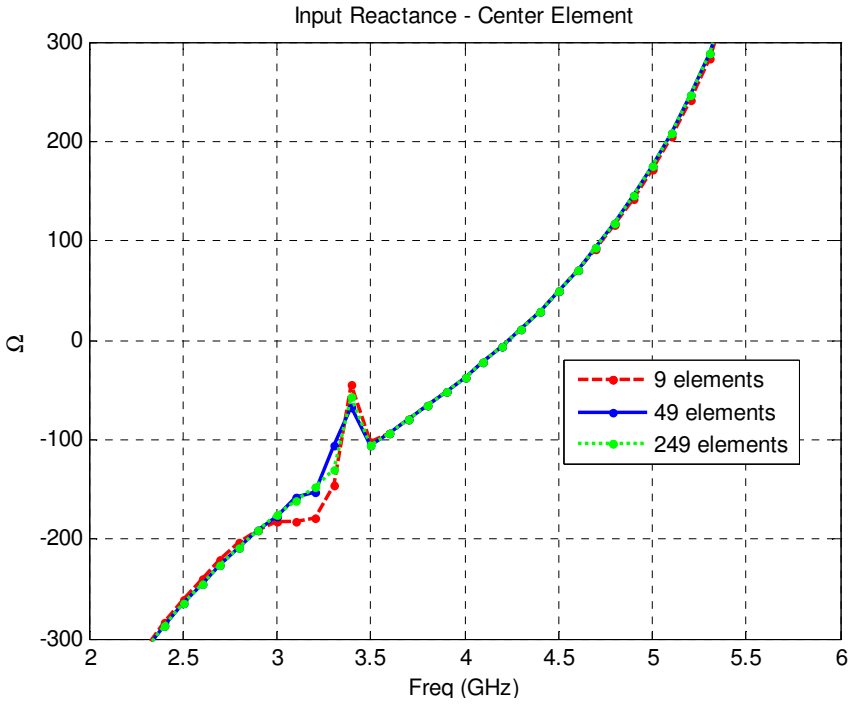

Figure 2-9 – Input reactance of center element of linear array of dipoles over PEC ground for parallel arrays of 9, 49, and 249 elements [47]

Plots, shown with real and imaginary axes, of the fields backscattered in the direction of an incident plane wave on tightly-coupled arrays have a tight loci of points across frequency when no AGSW is present [2, 36, 48]. When the array is analyzed over frequencies where the AGSW is present and no (or insufficient) suppression techniques are employed, the backscatter field values jump substantially between frequency points. A similar effect is evident in the input impedance across frequency.

Janning and Munk [49] explored the effects of array truncation using techniques based on Janning's dissertation [29]. If the Floquet currents $\left[I_{\text{Floquet}}\right]$ represent the currents for an infinite array (in all modes), the other currents present on a finite linear array $\vec{I}_{\text{Residual}}$ can be defined as

$$\left[I_{\text{Residual}}\right] \equiv \left[I_{\text{Total}}\right] - \left[I_{\text{Floquet}}\right] = \left[I_{\text{SW\_left}}\right] + \left[I_{\text{SW\_right}}\right] + \left[I_{\text{End}}\right] \tag{50}$$

Although the array is periodic, Floquet theory alone no longer describes its behavior; the edges at the truncation of the array are not periodic. When conditions allow, each source within the array launches and the array structure supports a surface wave traveling in all directions. For a linear array, this corresponds to equal left-going and right-going waves. A planar array of dipoles will launch surface waves in four directions, but the waves in two orthogonal directions will exhibit different propagation constants since the array structures are different.

2.6.2.1 AGSW Reflection and Excitation Coefficients

Janning and Munk [49] state that the AGSW is generated at one end of the array and propagates without loss (if no added resistive losses or conductive losses) until it reaches the other end.

Once it reaches the other end of the array, it reflects with a reflection coefficient $\Gamma(f)$. The reflection coefficient is independent of the array size or scan angle. A portion of the surface wave radiates away from the array, and one may consider this radiation to be the result of the end currents $\left[I_{\text{End}}\right]$. They are small compared to the other currents including the surface wave, and their radiation is typically not of much concern [36]. These currents are part of the end permutations described in Section 2.5.1 and indistinguishable from other end permutations. Since the similar surface wave travels in the opposite direction, an infinite summation of bounces is possible, if no loss is present. This is much like a standing wave on a transmission line.

For a plane wave incident on a semi-infinite array of parallel dipoles, the excitation develops left-going and right-going AGSW as Figure 2-10 shows. If the incidence angle is broadside, these two AGSW are equal. Thus, waves in both directions are a function of the array length and the angle of incidence. For a linear array in $\hat{x}$, $\phi_s = \{0^\circ, 180^\circ\}$.

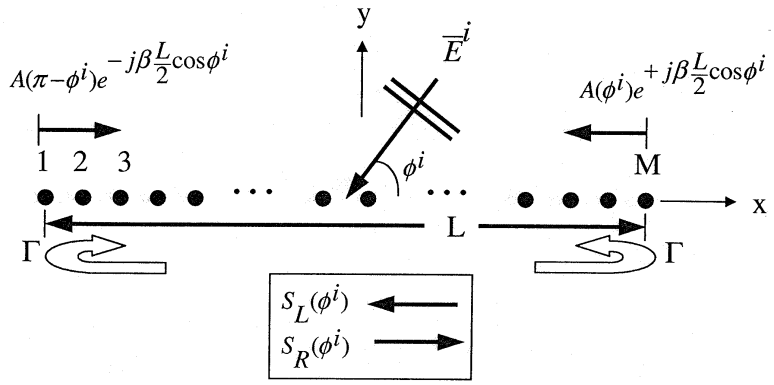

Figure 2-10 – Geometry showing Janning's development of the AGSW concept (Fig. 5 of [49]. ©2002 IEEE. Reprinted with permission from IEEE.)

Using Janning's terminology, the left-going surface wave is

$$\begin{aligned} S_L(\theta_s,\phi_s;L) = {} & A(\theta_s,\phi_s)e^{+jk(L/2)\sin\theta_s\cos\phi_s}\left[1+\gamma^2+\gamma^4+\cdots\right] \\ & +A(\theta_s,\phi_s)e^{-jk(L/2)\sin\theta_s\cos\phi_s}\left[\gamma+\gamma^3+\gamma^5+\cdots\right] \end{aligned} \tag{51}$$

where the overall length of the array $L=(M-1)d_x$ and $\gamma = \Gamma\exp(-j\beta s_{xo}L)$. The s_{xo} term is greater than one and represents the scan angle where the active impedance zero occurs in an infinite array. All even powers of γ come from bounces from the right edge of the array, and all odd powers are from the left edge of the array. The phase shift in the launching coefficient $A(\phi_s)$ follows this convention, as well. Reducing the geometric series in (51) yields

$$S_L(\theta_s,\phi_s;L) = \begin{pmatrix} A(\theta_s,\phi_s)e^{+jk(L/2)\sin\theta_s\cos\phi_s} + \\ \gamma A(\theta_s,\phi_s)e^{-jk(L/2)\sin\theta_s\cos\phi_s} \end{pmatrix}\left(\frac{1}{1-\gamma^2}\right) \tag{52}$$

Equivalently, one can express the symmetrical right-going surface wave as

$$S_R(\theta_s,\phi_s;L) = S_L(\theta_s,\pi-\phi_s;L)$$
$$= \left(A(\theta_s,\phi_s)e^{-j\beta(L/2)\sin\theta_s\cos\phi_s} + \gamma A(\theta_s,\phi_s)e^{+j\beta(L/2)\sin\theta_s\cos\phi_s}\right)\left(\frac{1}{1-\gamma^2}\right) \tag{53}$$

Two methods for determining $\Gamma(f)$ are presented in [49]. The first uses a broadside incident plane wave ($\theta_s = 0^\circ$) onto a semi-infinite array. This reduces (51) and (53) to equivalent forms in (54) where Γ and A are independent of the array size L.

$$\frac{1}{S_L(0;L)} = \frac{1}{S_R(0;L)} = \frac{1}{A(0)}(1-\Gamma e^{-j\beta s_{xo}L}) \tag{54}$$

Once Γ is solved, the angle of incidence can be varied to solve for the excitation coefficient $A(\theta,\phi)$ from the complex values of both surface waves.

The second method uses a semi-infinite array with only one Cartesian direction finite (like $+\hat{x}$). This technique compares calculations to the infinite Floquet wave solutions, and the difference defines the surface wave. Since there is only one edge, the reflection coefficient is isolated as the ratio of the surface wave approaching and leaving the finite edge. Conceptually, this approach is simpler, but it requires a specialized semi-infinite simulation program that is not commercially available.

2.6.2.2 Discrete, Spatial Fourier Transforms

Another method of viewing and analyzing the AGSW is to analyze the currents of the array in the discrete, spatial Fourier transform [29, 50]. Equation (55) defines that transform for a rectangular $M \times N$ periodic planar array in the *xy*-plane with interelement spacings d_x and d_y.

$$F(s_x,s_y) = \frac{1}{(2N+1)(2M+1)}\sum_{m=-M}^{M}\sum_{n=-N}^{N} I_{nm}e^{-jnks_x d_x}e^{-jmks_y d_y} \tag{55}$$

where all unique information to change the phase term from $-\pi \to \pi$ is contained within the range

$$\frac{-\lambda}{2d_x} < s_x \le \frac{\lambda}{2d_x} \text{ and } \frac{-\lambda}{2d_y} < s_y \le \frac{\lambda}{2d_y} \tag{56}$$

and the visible space (and also the Floquet currents) is limited to $|s_x| \leq 1$ and $|s_y| \leq 1$, which occurs for $d_{x,y} = \lambda/2$. Recall, the scan direction as $\hat{s} = s_x\hat{x} + s_y\hat{y} + s_z\hat{z}$ relates to the scan angles by $s_x = \sin\theta_s \cos\varphi_s$ and $s_y = \sin\theta_s \sin\varphi_s$.

Figure 2-11 (top) shows the terminal current magnitudes for a 49-element dipole array, matching the geometry of Figure 2-7. The effects of the array edge are clearly visible at both ends of the array. Figure 2-11 (bottom) shows the spatial discrete Fourier transform of this array. Since this 4 GHz analysis frequency is at resonance of the isolated element, there is one dominant mode, scanned to broadside (i.e., $s_x = 0$).

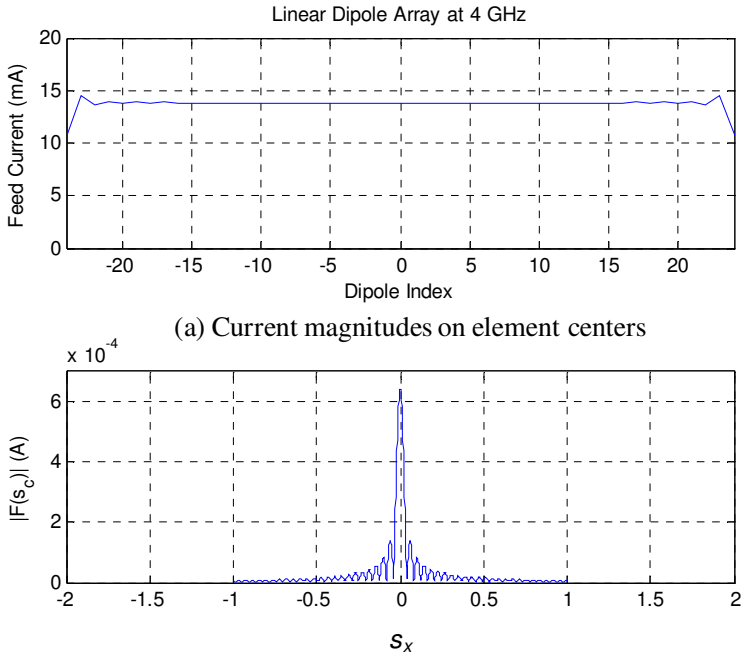

(a) Current magnitudes on element centers

(b) Fourier transform of (a)

Figure 2-11 – Near resonance behavior of linear array of 49 Dipoles over PEC ground: (a) discrete center currents; (b) discrete spatial Fourier transform of the currents

Figure 2-12 is a matching representation of the currents for the same geometry but at 3.4 GHz, about 15% below the isolated element resonance. As seen in Figure 2-8, this frequency lies in the middle of the range of impedance distortion. The box in the middle of Figure 2-12 (top) highlights the periodicity or standing wave nature of the AGSW, as represented in the currents on the center elements. It is clear in Figure 2-12 that two peaks lie outside the visible region that

extends to the contour direction $|s_c| \le 1$. Also, note that these peaks are smaller than the propagating mode at $s_c = 0$; there is still radiation at this frequency.

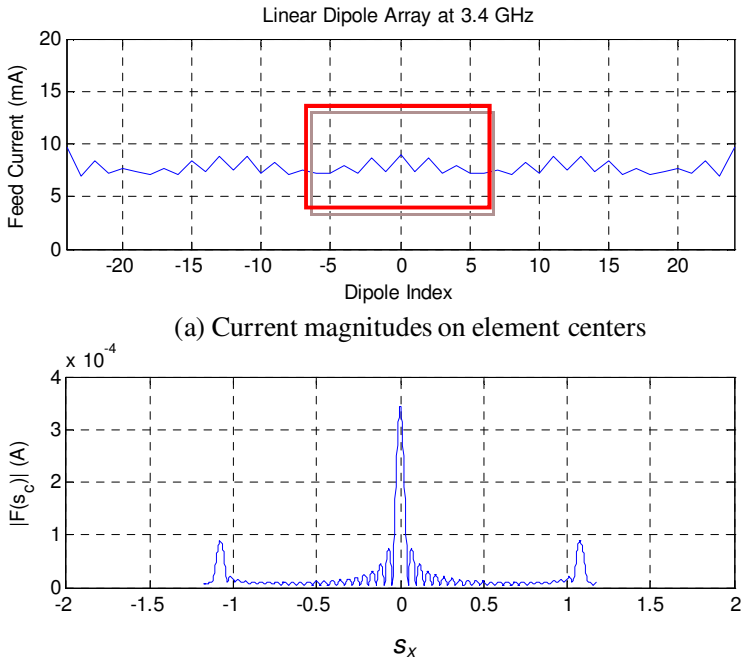

(a) Current magnitudes on element centers

(b) Fourier transform of (a)

Figure 2-12 – Near resonance behavior of linear array of 49 dipoles over PEC ground: (a) discrete center currents; (b) discrete spatial Fourier transform of the current

2.6.2.3 Rayleigh-Bloch Waves

In other disciplines, there are multiple names describing these same array guided surface waves, including *guided waves* in acoustics and *Rayleigh-Bloch waves* in fluids. In the latter, a linear series of cylinders is analyzed for an incoming ocean wave [51]. Thomson and Linton solve the two-dimensional Helmholtz equation and show how one can combine semi-infinite arrays to solve for long but finite arrays. The analogy in the latter would be an incoming plane wave on an array of shorted dipoles. They also observe many of the wave phenomena seen in antenna array, with a different vocabulary.

One interesting result of this work is how a small series of cylinders cannot fully exhibit the Rayleigh-Bloch surface wave, although all other necessary conditions exist. The literature on tightly-coupled antenna arrays has not articulated such a finding.

2.6.3 Yagi-Uda Antenna Array

A good initial look at the concepts of surface waves is to consider the Yagi-Uda antenna array. Substantial work has analyzed and optimized the Yagi-Uda design, and this section presents a historical overview. Yagi-Uda arrays do not have substrates, and the array elements guide the surface waves. The surface waves on Yagi-Uda arrays are present for inter-element spacing $d < \lambda / 2$ and for infinite Yagi-Uda arrays, as well, as defined by Sengupta [43]. However, the nature of a single excitation in an infinite Yagi-Uda array does introduce its own aperiodicity, and the infinite array may be better classified as a semi-infinite array.

The study of Yagi-Uda arrays is pertinent to the study of tightly-coupled arrays because it considers director elements of equal height, spacing, and radius. That is, they were mostly periodic, with the aperiodicities being the single reflector, the feed, and the array ends. The director and reflector elements can be considered short-circuited array elements and, more generally, as having altered feed loads. Figure 9 of [42] shows an interesting change in the maximum gain as a function of director spacing. Between 0.5λ and 0.4λ, the gain jumps from ~7 dB to ~13 dB for an array of length $L = 6\lambda$. This transition is in line with the concept of tightly-coupled arrays and AGSW. The alignment of the surface wave and the main radiation, since this is end fire, may occlude the overall effects of the surface wave. The edge reflection of the AGSW is the major problem, but the Yagi-Uda array is optimized to radiate from that edge.

Ehrenspeck and Poehler [42] introduced the concept of the surface wave along the array structure to explain the interrelationships between performance parameters in the Yagi-Uda antenna. Instead of defining performance based on height, diameter, reflector spacing, and director spacing, Ehrenspeck and Poehler related gain only to the phase velocity along the array. This simplified the design problem space and allowed for the use of optimization routines.

Sengupta [43] considered the infinite Yagi-Uda array structure and presented a wide range of results for different element heights, radii, and spacing d while keeping these parameters uniform within any given array. He first applied a transmission line analogy to the array, which is comparable to a corrugated waveguide. Looking into the corrugation, the input impedance appears reactive [52] as is needed for the SGSW. This leads to the development of an expression for the phase velocity for an infinite array structure extending along the array axis $\hat{x}$

$$v = \left(1 + \frac{x}{2kdX}\right)c \tag{57}$$

where v is the phase velocity, c is the speed of light, d the inter-element spacing, and X is the parallel reactance between elements. Some results of this first-level approximation are that the phase velocity will be slow ($v < c$) for capacitive loading and fast ($v > c$) for inductive loading. In addition, the surface wave will propagate unattenuated if the array has no ohmic losses.

Several features of this relationship to phase velocity are supported in findings by Sengupta [43]. Shorter elements are more capacitive due to their current distributions. The phase velocity drops with tighter interelement spacing and larger element radii. Both increase the interelement capacitance and are physically intuitive. A larger radius requires a shorter element length to achieve resonance. Conversely, as the element radius goes to zero $v \to c$, meaning that the array disappears, leaving free space propagation.

Serracchioli [44] calculated the phase velocity for long end-fire uniform dipole arrays. This formulation considered an external source at the end of the linear array, and this form comes closer to the more modern formulations of tightly-coupled arrays. As compared to (2) where elements are open-circuited, if all elements are short-circuited, the feed voltage at a general zeroeth element can be written as

$$V_0 = v_s + \sum_n i_n z_{0n} = 0 \tag{58}$$

where v_s is the direct contribution of the source, i_n is the current on the n^{th} element, and z_{on} is the mutual impedance between the n^{th} and 0^{th} element. If the array is sufficiently long, the direct effect of v_s is marginal and dropped in this formulation. This forces i_n to be in the form of $i_n = i_0 \exp(-jnkd)$. Reworking these relationships for an infinite array allows the relationship to be restated as

$$\sum_{-\infty}^{+\infty} z_{0n} \exp(-jnkd) = 0 \tag{59}$$

This expression shows that solutions exist for positive-traveling $+k$ and negative-traveling $-k$ waves with a phase factor between elements of $\exp(-jnkd)$. Since the trapped wave is a slow wave and if $d \le \lambda/2$, the limitations are $k < k_x < \pi/d$ for $k > 0$ and $-\pi/d < k_x < k$ for $k < 0$.

2.7 Summary

Many aspects of array design and wave phenomenology affect the mutual coupling in arrays. Various forms may express the concept of mutual coupling, and this chapter has reviewed several, including impedance coupling and *S*-parameters. This chapter has presented some methods and background supporting the evaluation of arrays. Later chapters will use aperture theory and spectral-domain methods. The emphasis in all cases has been to explain physical phenomena in array coupling, versus computational methods, while admittedly this distinction sometimes grays. Chapter 3 offers a brief treatment of computational methods and are valuable in rounding out a full review of the literature on tightly-coupled arrays.

While much research of mutual coupling indicates the role of the element, the literature has compared few specifics. Chapters 4-6 present designs and analyses for wideband arrays. Additionally, these chapters present the role and limitations of a ground plane. The chapters strive to develop sound, wideband element designs and design details needed to complete the construction of a tightly-coupled array.

2.8 References

[1] IEEE, "IEEE standard definitions of terms for antennas," *IEEE Std 145-1993,* 1993.

[2] B. A. Munk, *Finite Antenna Arrays and FSS*. Hoboken, NJ: Wiley-Interscience, 2003.

[3] R. C. Hansen, "Comments on 'The active element pattern'," *Antennas and Propagation, IEEE Transactions on,* vol. 43, p. 634, 1995.

[4] P. Carter, Jr., "Mutual impedance effects in large beam scanning arrays," *Antennas and Propagation, IRE Transactions on,* vol. 8, pp. 276-285, 1960.

[5] J. Allen, "Gain and impedance variation in scanned dipole arrays," *Antennas and Propagation, IRE Transactions on,* vol. 10, pp. 566-572, 1962.

[6] P. Hannan, "The ultimate decay of mutual coupling in a planar array antenna," *Antennas and Propagation, IEEE Transactions on,* vol. 14, pp. 246-248, 1966.

[7] R. E. Collin, "Hertzian dipole radiating over a lossy earth or sea: some early and late 20th-century controversies," *Antennas and Propagation Magazine, IEEE,* vol. 46, pp. 64-79, 2004.

[8] T. R. Vogler, *et al.*, "Improvements on MF Ground Wave Antennas for the Global Maritime Distress and Safety System (GMDSS)," in *Proceedings of the 2007 Antenna Applications Symposium*, Allerton Park, Monticello, IL, 2007, p. 29.
[9] C. Roller, "Effects of mutual coupling on super-resolution DF in linear arrays," 1992, pp. 257-260.
[10] I. Gupta and A. Ksienski, "Effect of mutual coupling on the performance of adaptive arrays," *Antennas and Propagation, IEEE Transactions on,* vol. 31, pp. 785-791, 1983.
[11] T. Su and H. Ling, "On modeling mutual coupling in antenna arrays using the coupling matrix," *Microwave and Optical Technology Letters,* vol. 28, pp. 231-237, 2001.
[12] B. Friedlander and A. J. Weiss, "Direction finding in the presence of mutual coupling," *Antennas and Propagation, IEEE Transactions on,* vol. 39, pp. 273-284, 1991.
[13] K.-C. Lee and T.-H. Chu, "A circuit model for mutual coupling analysis of a finite antenna array," *Electromagnetic Compatibility, IEEE Transactions on,* vol. 38, pp. 483-489, 1996.
[14] R. Harrington, *Time-Harmonic Electromagnetic Fields*. New York: Wiley-IEEE Press 2001.
[15] D. M. Pozar, *Microwave engineering*, 3rd ed. Hoboken, NJ: J. Wiley, 2005.
[16] K. Kurokawa, "Power Waves and the Scattering Matrix," *Microwave Theory and Techniques, IEEE Transactions on,* vol. 13, pp. 194-202, 1965.
[17] S. Stein, "On cross coupling in multiple-beam antennas," *Antennas and Propagation, IEEE Transactions on [legacy, pre - 1988],* vol. 10, pp. 548-557, 1962.
[18] A. Ludwig, "Mutual coupling, gain and directivity of an array of two identical antennas," *Antennas and Propagation, IEEE Transactions on,* vol. 24, pp. 837-841, 1976.
[19] K. Takamizawa, "Analysis of Highly Coupled Wideband Antenna Arrays Using Scattering Parameter Network Models," Ph.D. Dissertation, Bradley Dept. of Electrical and Computer Engineering, Virginia Tech, Blacksburg, VA, 2001.
[20] P. Hannan, "The element-gain paradox for a phased-array antenna," *Antennas and Propagation, IEEE Transactions on,* vol. 12, pp. 423-433, 1964.
[21] W. K. Kahn, "Element Efficiency: A Unifying Concept for Array Antennas," *Antennas and Propagation Magazine, IEEE,* vol. 49, pp. 48-56, 2007.
[22] W. Wasylkiwskyj and W. Kahn, "Efficiency as a measure of size of a phased-array antenna," *Antennas and Propagation, IEEE Transactions on,* vol. 21, pp. 879-884, 1973.
[23] H. Wheeler, "Simple relations derived fom a phased-array antenna made of an infinite current sheet," *Antennas and Propagation, IEEE Transactions on [legacy, pre - 1988],* vol. 13, pp. 506-514, 1965.
[24] H. A. Wheeler, "The Radiation Resistance of an Antenna in an Infinite Array or Waveguide," *Proceedings of the IRE,* vol. 36, pp. 478-487, 1948.
[25] S. Maeda and P. Diament, "Power flow between adjacent electric dipoles," *Antennas and Propagation Magazine, IEEE,* vol. 44, pp. 68-76, 2002.
[26] H. G. Schantz, "The flow of electromagnetic energy in the decay of an electric dipole," *American Journal of Physics,* vol. 63, pp. 513-520, 1995.
[27] H. Schantz, *The Art and Science of Ultrawideband Antennas*. Boston: Artech House, 2005.
[28] D. Pozar and D. Schaubert, "Scan blindness in infinite phased arrays of printed dipoles," *Antennas and Propagation, IEEE Transactions on,* vol. 32, pp. 602-610, 1984.

[29] D. S. Janning, "Surface Waves in Arrays of Finite Extent," Ph.D. Dissertation, Dept. of Electrical and Computer Engineering, The Ohio State University, Columbus, OH, 2000.
[30] J. B. Pryor, "Suppression of surface waves on arrays of finite extent," M.S. Thesis, Dept. of Electrical and Computer Engineering, The Ohio State University, Columbus, Ohio, 2000.
[31] S. J. Franson and R. W. Ziolkowski, "Method of Simulation of Closely Spaced, Finite, Periodic, Radiating or Reflecting Structures, Including Metamaterials," presented at the 22nd Annual Review of Progress in Applied Computational Electromagnetics, Miami, FL, 2003.
[32] D. F. Kelley, "Relationships between active element patterns and mutual impedance matrices in phased array antennas," in *IEEE Antennas and Propagation Society International Symposium*, 2002, pp. 524-527.
[33] R. C. Hansen, "Anomalous edge effects in finite arrays," *Antennas and Propagation, IEEE Transactions on,* vol. 47, pp. 549-554, 1999.
[34] C. Craeye and M. Arts, "Modulated oscillations appearing in the scan impedance of a finite phased array," *Antennas and Propagation, IEEE Transactions on,* vol. 51, pp. 2504-2506, 2003.
[35] D. J. Bekers*, et al.*, "Eigencurrent analysis of resonant behavior in finite antenna arrays," *Microwave Theory and Techniques, IEEE Transactions on,* vol. 54, pp. 2821-2829, 2006.
[36] B. A. Munk*, et al.*, "Scattering from surface waves on finite FSS," *Antennas and Propagation, IEEE Transactions on,* vol. 49, pp. 1782-1793, 2001.
[37] W. H. Von Aulock, "Properties of Phased Arrays," *Proceedings of the IRE,* vol. 48, pp. 1715-1727, 1960.
[38] B. Munk, *Frequency Selective Surfaces: Theory and Design*. New York: Wiley-Interscience, 2000.
[39] W. Stutzman and G. Thiele, *Antenna Theory and Design*, 2nd ed. New York: John Wiley & Sons, Inc., 1998.
[40] D. Pozar and D. Schaubert, "Analysis of an infinite array of rectangular microstrip patches with idealized probe feeds," *Antennas and Propagation, IEEE Transactions on,* vol. 32, pp. 1101-1107, 1984.
[41] D. M. Pozar, "Beam Transmission Of Ultra Short Waves: An Introduction To The Classic Paper By H. Yagi," *Proceedings of the IEEE,* vol. 85, pp. 1857-1863, 1997.
[42] H. Ehrenspeck and H. Poehler, "A new method for obtaining maximum gain from yagi antennas," *Antennas and Propagation, IRE Transactions on,* vol. 7, pp. 379-386, 1959.
[43] D. Sengupta, "On the phase velocity of wave propagation along an infinite yagi structure," *Antennas and Propagation, IRE Transactions on,* vol. 7, pp. 234-239, 1959.
[44] F. Serracchioli and C. Levis, "The calculated phase velocity of long end-fire uniform dipole arrays," *Antennas and Propagation, IRE Transactions on,* vol. 7, pp. 424-434, 1959.
[45] R. Mailloux, "Excitation of a surface wave along an infinite yagi-uda array," *Antennas and Propagation, IEEE Transactions on,* vol. 13, pp. 719-724, 1965.
[46] J. Richmond and R. Garbacz, "Surface waves on periodic array of imperfectly conducting vertical dipoles over the flat earth," *Antennas and Propagation, IEEE Transactions on [legacy, pre - 1988],* vol. 27, pp. 783-787, 1979.

[47] T. R. Vogler and W. Davis, "Surface Waves in Medium-Sized, Tightly Coupled Planar Arrays," presented at the USNC-USRI National Radio Science Meeting, Boulder, CO, 2009.
[48] J. B. Pryor, "On ohmic losses in frequency selective surfaces at near-infrared wavelengths " Ph.D. Dissertation, Dept. of Electrical and Computer Engineering, The Ohio State University, Columbus, OH, 2003.
[49] D. S. Janning and B. A. Munk, "Effects of surface waves on the currents of truncated periodic arrays," *Antennas and Propagation, IEEE Transactions on,* vol. 50, pp. 1254-1265, 2002.
[50] O. A. Civi*, et al.*, "Surface waves on a finite planar dipole array in free space," in *Antennas and Propagation Society International Symposium, 2002. IEEE*, 2002, pp. 78-81 vol.2.
[51] I. Thompson*, et al.*, "A new approximation method for scattering by long finite arrays," *Quarterly Journal Mechanics of Applied Math,* vol. 61, pp. 333-352, 2008.
[52] R. F. Harrington, *Time-harmonic electromagnetic fields*. New York,: McGraw-Hill, 1961.

CHAPTER 3

Simulation Methods for Tightly-Coupled Arrays

Research into tightly-coupled arrays has been progressing since the early 1990s and has relationships to frequency selective surfaces (FSS). During the same period, computing power has increased exponentially. There is a substantial treatment in the literature on the numerical methods to model infinite arrays. A little less is available on how to truncate infinite arrays to represent finite arrays. However, a review of this research and the underlying techniques is part of a necessary treatment on the subject. Although this chapter may have some sections similar to the sections of Chapter 2, the intent here is to focus on the mathematical or processing techniques rather than the underlying physical phenomena.

Some techniques described herein require the use of specialized codes developed over years. This chapter presents overviews of these codes or methods to give breadth to the subject of modeling large arrays. Other techniques are manipulations, or extensions, of standard commercial electromagnetics codes.

This chapter starts with a review of specific, infinite-array simulation techniques and then moves into a discussion of semi-infinite array techniques. It then presents a quick review of compressions techniques, primarily the multi-level fast multipole method (MLFMM). Time-domain techniques are briefly summarized for their applicability to the design and analysis of tightly-coupled arrays. A large amount of research in the literature covers asymptotic techniques for large arrays. These align well with the trends of the physical phenomena detailed in Chapter 2, but they may not have exact pertinence in this or future work because of the great advances in cheap computing resources. These asymptotic techniques are an interesting piece of history in

electromagnetics and, by illustrating what they do not capture, help emphasize these details. The chapter concludes with a presentation of aperture theory and element efficiency. The chapter presents a review of some post-processing techniques and concludes with an assessment of the validity of finite array techniques.

3.1 Infinite Array Techniques

Infinite array techniques have substantial value for their overall simplicity and quick solution times. Since all elements are comparable, with the only difference being a phase shift, the number of unknowns is substantially smaller. Infinite array methods are desirable for these reasons, but they are not realistic. The lack of finite boundaries prohibits the observation of certain surface-wave and edge effects in arrays. Chapter 2 discussed these phenomena.

Past dissertations at Virginia Tech developed infinite array techniques. Lapean *et al*. [1, 2] formulated a Floquet infinite array solution using the Method of Moments (MoM) as the underlying solution method. It is entitled Analysis Software for Infinite Arrays (ASIA). (There are several implementations of infinite MoM solutions, including the Periodic Moment Method (PMM) code from Ohio State in 1983 [3].) ASIA uses an equivalent, indirect form of the Green's function using modal field functions. The infinite array was in the *xy*-plane, with *unit cell* dimensions $d_{x,y}$ respectively. The propagation vector of a scanned plane wave equals

$$\begin{aligned}\vec{k} &= k_x\hat{x} + k_y\hat{y} + k_z\hat{z} \\ &= k\sin\theta\cos\phi\hat{x} + k\sin\theta\sin\phi\hat{y} + k\cos\theta\hat{z} \\ &= \vec{k}_\rho + \vec{k}_z\end{aligned} \tag{1}$$

The fields in the unit cell are expanded by Floquet modes m,n in TE^z and TM^z with transverse and longitudinal wave numbers so that

$$\vec{k}_\rho = \left(ks_x + \frac{2\pi m}{d_x}\right)\hat{x} + \left(ks_y + \frac{2\pi n}{d_y}\right)\hat{y} \tag{2}$$

where $k_z = \sqrt{\varepsilon_r \mu_r k^2 - |\vec{k}_{planar}|^2}$ includes definitions for both an air and any dielectric (substrate) medium. The beam steering angle θ_s, ϕ_s is defined by $\hat{s} = s_x \hat{x} + s_y \hat{y} + s_z \hat{z}$, where $s_x = \sin\theta_s \cos\varphi_s$ and $s_y = \sin\theta_s \sin\varphi_s$. The application of Floquet current and voltage modes then solves for the MoM impedance matrix. If the inter-element spacing $d < \lambda/2$, only a single Floquet mode $m, n = 0, 0$ radiates.

In Section 2.2.4 of his dissertation [2], Lapean reviews the structure of the Floquet MoM formulation at length. He describes three different ways to apply Floquet analysis to the radiating element in the unit cell and surveys the literature. These are single whole-domain basis function descriptions, multiple whole-domain descriptions, and multiple sub-domain descriptions. The first is lacking because it ignores any mutual coupling within the unit cell and because only a single basis function is used, leading to inaccuracies. The second technique, using multiple whole-domain basis functions, has limited application to simple geometries like linear dipoles or slots. In addition, although it can be accurate, the overall accuracy depends more on the type of basis function used and may inaccurately capture current distributions on the elements. Lastly, sub-domain basis functions allow for a full characterization of arbitrarily shaped radiating elements and may employ many different forms without the loss of generality. ASIA employs sub-domain basis functions, as does FEKO®. With the improvements in computing power, there is and will continue to be less need for whole-domain basis functions.

Buxton [4] developed a second infinite array technique using Finite Difference Time Domain (FDTD). Her code analyzed finite and infinite foursquare antenna arrays. As with normal FDTD, infinite FDTD requires well-defined absorbing boundary conditions. Since the array is infinite, the fields must match at the boundary of the unit cell. In a 2-D infinite array in the *xy*-plane, equations (3) and (4) define the magnetic and electric field boundary conditions, respectively,

$$\begin{aligned} H_z(d_x, j, k) &= H_z(0, j, k) \\ H_y(d_x, j, k) &= H_y(0, j, k) \\ H_z(i, d_y, k) &= H_z(i, 0, k) \\ H_x(i, d_y, k) &= H_x(i, 0, k) \end{aligned} \tag{3}$$

$$
\begin{aligned}
E_z(0, j, k) &= E_z(d_x, j, k) \\
E_y(0, j, k) &= E_y(d_x, j, k) \\
E_z(i, 0, k) &= E_z(i, d_y, k) \\
E_x(i, 0, k) &= E_x(i, d_y, k)
\end{aligned}
\tag{4}
$$

where i, j, k are the indices of $\hat{x}, \hat{y}, \hat{z}$, and d_x, d_y define the extents of the unit cell. The terminal currents and voltages within the unit cell are found by

$$
I(t, x_i, y_j, z_k) = \oint_C \vec{H}(t, x_i, y_j, z_k) \cdot d\vec{l} \tag{5}
$$

and

$$
V(t, x_i, y_j, z_k) = -\int_C \vec{E}(t, x_i, y_j, z_k) \cdot d\vec{l} \tag{6}
$$

3.1.1 Periodic Boundary Condition

The implementation used primarily in this dissertation is the Periodic Boundary Condition (PBC) implementation in the frequency domain. This solution has been implemented in FEKO® [5], starting with Suite 5.4 for 1-D or 2-D periodic structures. This section restates some of its details below. A clear and close reading of [6] and Section 4 of [7] is recommended to implement such a feature.

The fields from the infinite array are summations over the infinite 2-D plane of the fields from one unit cell, with a phase shift applied through the exponent [6]. The PBC implementation in FEKO® allows for the geometric structure to extend to the end of the unit cell and repeat into the adjacent cell, by the use of a half basis function. The spatial translation is accomplished by the general function

$$
f(\vec{r}) = \sum_{m,n=-\infty}^{\infty} f_0(\vec{r} - \vec{\rho}_{mn}) e^{-jk_\rho \rho_{mn}} \tag{7}
$$

where the translation vector of the lattice $\vec{\rho}_{mn} = m\hat{x} + n\hat{y}$ reflects the phase shift in the exponent. Likewise, the 2-D periodic Green's Function (GF) is an extension of the free-space Green's function G_0

$$G(\vec{r} - \vec{r}') = \sum_{m,n} G_0(\vec{r} - \vec{r}' - \vec{\rho}_{mn}) e^{-j\vec{k}\cdot\vec{\rho}_{mn}} \tag{8}$$

In free space, the Poisson 2D modal formulation transforms G_0 to the spectral domain as

$$G_0 = \frac{e^{-jkR}}{4\pi R} \rightleftarrows \tilde{G}_0 = \frac{e^{-\gamma|z-z'|}}{2\gamma} \tag{9}$$

where $\gamma = \sqrt{k_x^2 + k_y^2 - k^2}$. Applying (9) to (8), a Green's function that solves the infinite images of the boundary conditions is

$$G(\vec{r} - \vec{r}') = \frac{1}{4\pi} \sum_{m,n} \frac{e^{-jkR_{mn}}}{R_{mn}} e^{-j\vec{k}\cdot\vec{\rho}_{mn}} \tag{10}$$

Equation (10) is slowly converging because of the infinite summation. FEKO® [8] uses the Ewald transformation [6] to remove this singularity

$$\frac{e^{-jkR}}{R} = \frac{2}{\sqrt{\pi}} \int_0^{\infty} \exp\left(-R^2\xi^2 + \frac{k^2}{4\xi^2} \right) d\xi \tag{11}$$

where ξ is a complex variable and the integration path is selected to make the integrand bounded as $\xi \to 0$ and decay as $\xi \to \infty$.

The Ewald transformation is a form of the Poisson summation and is a method of representing a periodic function in one domain as discrete samples in the other domain [6], [7]. By applying (11) to (10) and splitting the integral into two ranges from $0 \to E$ and $E \to \infty$, separate spectral and spatial components emerge that both converge rapidly.

$$G(\vec{r}-\vec{r}') = \frac{1}{4\pi}\sum_{m,n} e^{-j\vec{k}\cdot\vec{\rho}_{mn}} \frac{2}{\sqrt{\pi}} \int_0^E \exp\left(-R_{mn}^2\xi^2 + \frac{k^2}{4\xi^2}\right) d\xi + \frac{1}{4\pi}\sum_{m,n} e^{-j\vec{k}\cdot\vec{\rho}_{mn}} \frac{2}{\sqrt{\pi}} \int_E^\infty \exp\left(-R_{mn}^2\xi^2 + \frac{k^2}{4\xi^2}\right) d\xi \tag{12}$$

with the application of the Poisson 2-D summation formula

$$\int_r^\infty \exp\left(-p^2\xi^2 + \frac{q^2}{4\xi^2}\right) d\xi = \frac{\sqrt{\pi}}{4p}\left(e^{-jpq}\operatorname{erfc}\left(pr - j\frac{q}{2r}\right) + e^{jpq}\operatorname{erfc}\left(pr + j\frac{q}{2r}\right)\right) \tag{13}$$

removes the integral and allows a fast-converging solution to (12). The optimal break point for E for a 2D orthogonal lattice is given by $E = \sqrt{\pi}/d$, unless the size of the unit cell becomes so large with respect to λ that the Ewald transformation becomes unstable. This occurred in studies in Section 4.2.9 of [7] for an inter-element separation $d = 5.5\lambda$. This instability should not be of a concern using FEKO® because of the limitation of the cell size to about $d = \lambda/2$.

3.2 Semi-Infinite (Finite-by-Infinite) Array Techniques

Semi-infinite array techniques capture and distinguish edge effects in a single dimension $\hat{x}$ or $\hat{y}$, without the computational burden of finite array solutions. Since this solution has a single finite dimension, any presence of the array guided surface waves (AGSW) is a function of only the finite dimension. In some more specialized codes, such as SPLAT (Scattering from a Periodic Linear Array of Thin wire elements) [9] at Ohio State, it is possible to limit a finite edge to only one Cartesian direction like $+\hat{x}$ instead of $\pm\hat{x}$. This allows only one wave to exist on the array surface and prevent multiple bounces between sides, which can occlude an understanding of the wave phenomena. These solutions need no geometric series to represent multiple bounces between array edges. While such tools are beneficial, they were not available during this research. The dominant simulation method in this work was FEKO®, where a 1D PBC defines a semi-infinite array.

Beyond isolating edge effects to one edge, semi-infinite techniques can act as steps in solving large finite array problems. Munk *et al.* [10] describe a simple approach to using finite and one-direction semi-infinite array techniques to model a finite array. Floquet techniques solve

the currents for the infinite array. Outside the extent of the desired finite array, one may subtract the currents from multiple semi-infinite array solutions to truncate the infinite array. This removes the currents from outside the finite boundaries and impresses the residual edge currents within the finite range from all sides. Figure 3-1 illustrates this concept, which can be stated mathematically as

$$I^{\infty,x} \simeq I^{\infty} - I^{-x} - I^{+x}$$
$$I^{\infty,y} \simeq I^{\infty} - I^{+y} - I^{-y} \tag{14}$$

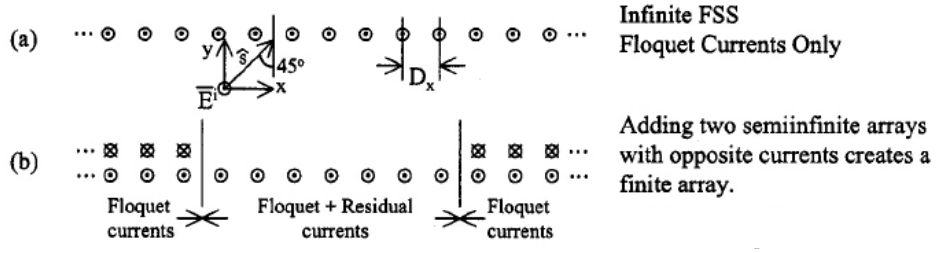

Figure 3-1 – Construction of finite array using infinite and semi-infinite techniques (Fig. 4.5 (a) & (b) of [3], reprinted with permission through subscription to the Copyright Clearance Center)

Separately, Craeye and Dardenne [11] describe an approach for planar arrays, which subtracts semi-infinite results in two dimensions. For an array in the *xy*-plane, the currents can be explained as

$$I \simeq I^{\infty} - I^{-x} - I^{+x} - I^{+y} - I^{-y} \tag{15}$$

This approach increases errors near the corners since it does not offer a full treatment of the corner with concurrent 2D truncations. To correct this error, the truncation technique described above estimates the currents on the corner element with the error from a small solution applied. This leads to the pattern from the corner element being described as

$$f_{corner} \simeq f_{corner}^{trunc} + \left(f_{corner}^{exact} - f_{corner}^{trunc} \right)_{small} \tag{16}$$

Craeye *et al*. [12] investigated the effects of array truncation on tapered slot antenna arrays that contained no dielectrics and had connections connected at the unit cell. For an array infinite in only one dimension, the Free-Space Green's Function can be limited to a 2D form

$$\frac{e^{-jkR}}{4\pi R} \rightarrow \frac{1}{4jd}\sum_{n=-\infty}^{\infty} e^{-jk_n x} H_0^{(2)}(\gamma_n R) \tag{17}$$

$$\gamma_n^2 = k^2 - k_n^2 = k^2 - \left(\frac{\psi_x}{d} + n\frac{2\pi}{d}\right)^2 \tag{18}$$

where n is the Floquet mode in the infinite direction; R is the distance from the infinite array axis; $k = 2\pi/\lambda$; d is the inter-element spacing in the infinite direction; and ψ_x is the phase shift in the infinite direction. This formulation is intriguing because it reduces the 3-D problem to a 2-D problem. The series in (17) converges fast for R larger than a few tenths of a wavelength.

The impedance plots of [12] show an interesting point that is not discussed. At low frequencies, the MoM finite and semi-infinite approximation show negative element input resistances. The included infinite array solutions never show a negative input impedance. This effect was seen in past work with foursquare antenna arrays [13] and attributed to strong surface wave coupling from one source into another. In addition, the errors diminished with increased frequency. This is effectively due to an increase in the electrical size of the array and an increased separation of elements from edge effects.

3.3 Semi-Infinite and Infinite Array Truncation

Several techniques are available to semi-infinite and infinite array solutions to account for the truncation effects in finite arrays. Considering a planar rectangular array, the interior elements typically exhibit consistent current distributions with possibly different phases. If the interior elements are solved using infinite array techniques, Floquet currents alone can often represent them adequately. One can ignore the effects of truncation at the edges, which is the historical approach for very large arrays. They can also be approximated by special fringe integral equations [14] or high-frequency techniques. Since tightly-coupled arrays have an inter-element spacing $d < \lambda/2$, it is suitable to represent the far-field radiation pattern by only one radiating Floquet mode $(m,n = 0,0)$ and one edge-diffracted field from each edge [7]. Several high-frequency techniques are available to represent the edge-diffracted field, including Physical Theory of Diffraction (PTD), Uniform Theory of Diffraction (UTD), and extensions of these. Because these work with infinite array techniques, one can consider these hybrid techniques.

An early development for analyzing large arrays was presented by Ishimaru et al. [15] as the Finite, Periodic-Structure Method. This method accounts for the truncation effects on an infinite-array solution using a finite window. Mathematically, this window acts as a pulse function and is the size of the desired outer limits of a finite array. This method solves the input impedance of a finite dipole array with progressive phasing by assuming that currents on each element are identical, except for weighting coefficients. The linear nature of the solution forces the phase shift between elements to match the infinite array solution. Forcing the currents from discrete array elements into a continuous current distribution across the aperture uses the Poisson sum formula and sets the weighting coefficients. Separately, the application of the spatial Fourier transform expresses the impedance matrix $[Z]$. See [15] for a full derivation. This approach is essentially a convolution between the infinite array and the aperture distribution, and some refer to it as a windowing scheme. The mathematical truncation, as with the physical truncation in a finite array, produces Gibbsean ringing at the edges (see Section 2.5.1). Although this captures some edge effects, there is no evidence that this technique has shown evidence of the AGSW. Because of its approach, the author does not believe it will without some other compensation. An application of this method to a large patch antenna array is presented in [16].

Skrivervik and Mosig [17] developed an extension to the windowing technique to account for non-periodicities, non-linear phase shifts, and multilayer printed arrays. This method is a form of infinite array truncation because it assumes as a starting point that the current distributions on all elements are identical. Stating the integral equation plus windowing in the space domain, instead of the spectral domain, with dyadic finite-array Green's functions provides common current distributions. The use of the space domain allows one integral equation to be solved for each element, making it of order $O(N)$ for CPU time. This technique is only slightly more computationally intensive that the spectral-domain windowing, but it allows for non-periodic analysis including failed elements. It is much faster than a full wave solution, which requires CPU time of $O(N^3)$. Sommerfeld integrals solve the finite array Green's function, thus eliminating the use of Floquet waves.

Craeye *et al*. [18, 19] covered truncation of interconnected tapered slot arrays; Figure 3-2 shows the geometry. Due to the 3-D rapidly varying current distributions on these elements, the windowing approaches of [15, 16] are not considered sufficient. Coupling is especially strong in these designs because elements are physically interconnected (allowing a DC current flow). The

differences in the element patterns from center element to edge element is as large as 5 dB for this array. This does not lead to an overall reduction in the array directivity. As some elements have their element pattern reduced, others are increased. Three main points from this research are applicable within this dissertation: the effects tend to average out as the main beam scans from broadside; the main beam and first side lobes remain mostly unaffected by the finite extents of the array; and effects may vary in different directions due to the antenna shape and interconnections. The variations tend to oscillate around the infinite array solution, with the greatest variations occurring at large scan angles.

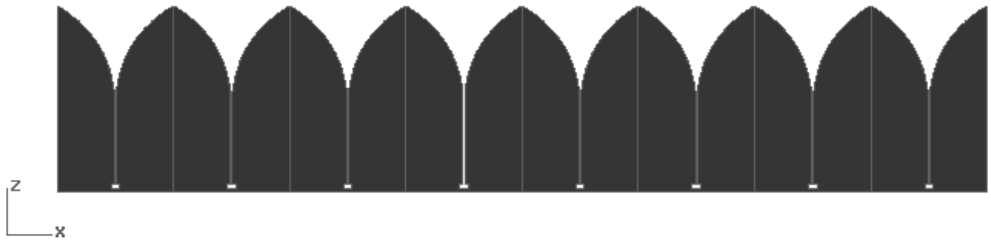

Figure 3-2 – Geometry of a 1x8 interconnected tapered slot array

A large number of papers [20-25] from researchers at the University of Siena, together with Felsen, focus on the asymptotic representations of the edge currents on large arrays. The asymptotic formulation reduces the solution to a limited number of propagating and evanescent Floquet-wave modes. To these, they add additional diffracted fields. Fringe integral equations expand the unknown edge currents to represent the diffraction. Corner (i.e., vertex) elements act as point diffractions and radiate spherical space waves or cylindrical surface waves. The edge elements will act as line diffractions and radiate conical space waves or planar surface waves. A rectangular array can thus be approximately by as few as nine current components. A spectral-domain formulation represents the fields radiated from elementary dipoles as a superposition of continuous source distributions from truncated Floquet waves, across the entire array. If the observation point is away from the array, asymptotic techniques are sufficient because evanescent and diffracted fields are negligible. This technique is more efficient than solving for the fields directly from each array element contribution.

3.4 Techniques to Compress the Number of Unknowns

This section carries a strange title, but it encompasses a number of implementations to reduce the computation and memory requirements of a full-wave Method of Moment solution by using fast iterative methods. The two dominant techniques are the Fast Multipole Method (FMM), which also exists with multilevel structures, and the Discrete Fast Fourier Transform (DFFT) techniques. The DFFT techniques rely on sub-domain basis functions (i.e., macro-basis functions) to reduce the number of unknowns.

A method for reducing the computational burden is to assume the current distributions on elements fit a certain form. Infinite array solutions provide these forms. However, this approach captures no edge effects. In [18], Craeye *et al*. solved a semi-infinite planar array explicitly and extracting the currents from its first outer two elements to capture the edge effects. Thereafter, being interior elements and less varying, a linear combination of six standard current distributions solved each element. This expansion means each element uses six whole-element basis functions instead of the hundreds of sub-domain basis functions that would be necessary with standard MoM for these electrically large antennas. Additionally, spatially iterative techniques solve two successive antenna elements, while the new solution is kept for only the first of the two antennas. This solution is shown empirically to require only a few iterative steps across the array to achieve a 10^{-3} accuracy [18].

FEKO® implements a Multi-Level, Fast Multipole Method (MLFMM), as do several other commercial codes, such as WIPL-D® and CST Microwave Studio®. For uniform expansion functions, MoM treats each unknown in the problem set equally, resulting in an $O(N^2)$ memory to store the impedance matrix and $O(N^3)$ in CPU-time to solve. With large arrays, especially ones with element surfaces (vs. wires) and dielectrics, the memory and computational burden grow quickly. For example, a 5×5 Foursquare array, which occupies a nearly maximum amount of the aperture area with conducting surfaces, uses 7050 basis functions with standard $\lambda_{\min}/10$ meshing. A solution to this array is tractable using full MoM computations, but it is especially burdensome when considering a wide range of frequencies. Arrays in this dissertation have a minimum target of a 4:1 bandwidth; typically simulations in Chapters 4-6 cover 1-12 GHz.

Coifman *et al*. [26] provide a succinct (they call it “pedestrian”) overview of MLFMM, which appears from [27] to be close to the implementation used in FEKO®. The process divides

the N basis functions into M localized groups. A good choice for the parameter is $M \sim \sqrt{N}$. The minimized sphere that can enclose an entire group identifies that group. A sparse matrix is constructed for the paired basis function between the centers of these group spheres if they lie within about a distance λ of each other. An expansion of the Free-Space Green's Function called the Transformation matrix solves all other regions that are not nearby. This expansion relates locations x, x' through a primary vector $\vec{X}$ and perturbation $\vec{d}$ per

$$\frac{e^{-jk\left|\vec{X}+\vec{d}\right|}}{4\pi\left|\vec{X}+\vec{d}\right|} = \frac{-jk}{4\pi}\int d^2\hat{k}e^{-j\vec{k}\cdot\vec{d}}\sum_{l=0}(-j)^l(2l+1)h_l^{(1)}\left(kX\right)P_l\left(\hat{k}\cdot\hat{X}\right) \tag{19}$$

where $\left|\vec{X}\right| > \left|\vec{d}\right|$, j_l is a spherical Bessel function of the first kind, $h_l^{(1)}$ is a spherical Hankel function of the first kind, and P_l is a Legendre polynomial. This expanded kernel relates the Fourier components of the field around each group from sources that are not nearby. The MLFMM solution uses standard MoM for interactions near sources. For a single level Fast Multipole Method, the M groups of distant elements change the MoM memory burden from $O(N^2) \to O(NM)$ and, if chosen properly, $M \cong \sqrt{N}$. This leads to an overall order of the algorithm of $O(N^{3/2})$.

In FEKO®, level zero would define the entire computational space. Each level is subdivided three-dimensionally into a maximum of eight sub-cubes [27]. Level 1 defines the first division. The algorithm continues to divide the cubes across multiple levels until the side of the cube is about $\lambda/4$. Multiple unknowns are aggregated to a single point, translated to another point, and disaggregated to approximate an overall free-space Green's function per (19). A MLFMM solution can reduce the computational memory burden from $O(N^2)$ to $O(N\log N)$ and the CPU-time from $O(N^3)$ to $O(N\log^2 N)$. MLFMM, as implemented in FEKO®, is a poor solution for arrays with overall small extents because of the minimum cube sub-division of $\lambda/4$. For instance, an 8×4 finite array at its lower operating frequencies may only be 0.8λ wide. The $\lambda/4$-cube is too crude to such an array. It is better suited for medium to large arrays, and perhaps more for linear than planar arrays since larger physical separations are possible for a given number of elements. The large array size needed to test MLFMM unfortunately makes it

difficult to solve the same array in another full wave method. In a further sense in [5] and [8], Van Tonder and Jackobus used MLFMM solutions for arrays of 11×11 and 51×51 elements to verify results from their newer infinite array solutions (PBC). Deviations between the two results are typically in the back lobes of the patterns; and the main and first side lobes typically match well. Since edge diffraction strongly affects the back lobes, which would be missing from the PBC infinite solution, that finding is reasonable.

Figure 3-3 shows a close match between the currents from a full MoM solution and an MLFMM solution for a linear array of 49 parallel dipoles without scanning [28]. At resonance (4.2 GHz), the currents are nearly identical. Where the AGSW is present (2.7 GHz), the error is more apparent but the AGSW effects are certainly visible. MLFMM results for both frequencies appear to meet the accuracy needs of an intermediate step in the design process.

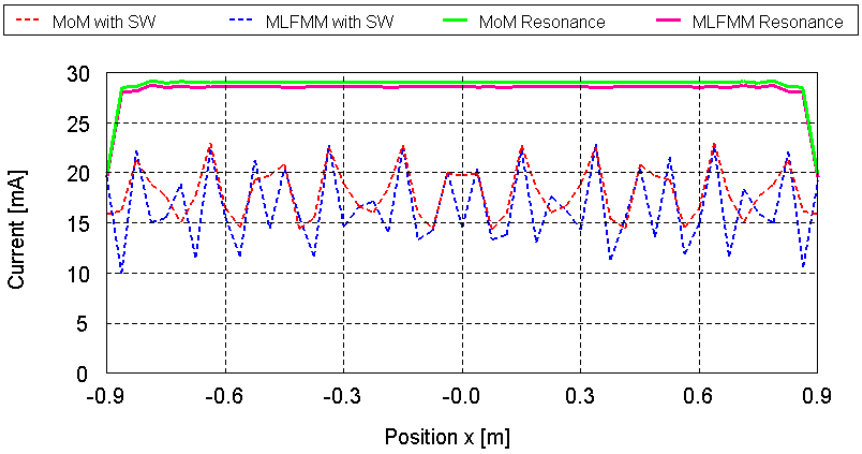

Figure 3-3 – Center-element currents for linear array of 49 parallel dipoles

3.5 Time-Domain Techniques

Time-domain techniques have some value in understanding the wave phenomenology in arrays. Boryssenko *et al.* [29] analyzed a connected array of Vivaldi antennas (1×10 *E*-plane connected, similar to what shown in Figure 3-2) by using the time-domain integral equation (TDIE). A pulse source together with time gating allows one to limit the number of edge reflections. Their results found that two reflections from edges are sufficient to characterize the embedded input

impedance[1] on the center array element, when compared to the full time (infinite) sequence. This is likely due to the resistive loading present in the terminations. Little other radiation of the surface wave occurs, except at aperiodicities such as the array boundary. Using only one edge reflection produced substantial errors. Such results will be invariably dependent on the nature of the element. Time-domain techniques also allow for an easy calculation of the complex propagation constant $k = \beta - j\alpha$ in the array via an FFT, assuming only one mode exists. The same authors [12] compare time-domain and frequency-domain techniques for the same connected Vivaldi array configuration. The authors conclude full frequency-domain solutions are suitable for smaller arrays (e.g., 4×4), time-domain solutions for medium arrays (e.g., 10×10), and infinite array solutions for larger arrays (e.g., 20×20). Reference [12] does not consider the use of MLFMM techniques. This assessment also does not account for the changing level of computational power.

3.6 Small-to-Large Array Extension Techniques

The section presents a few finite array techniques that, in general, rely on modeling a smaller array or element pairs, categorizing the spatial nature, and extending the results to approximate larger arrays. In some sense, it is exactly opposite from using infinite array techniques for finite solutions. These solutions are available to use in nearly any commercial EM code. They can be implemented outside of the software package (i.e., quasi-post-processed), without modifying source codes. Therefore, these are perhaps the simplest techniques available to estimate large arrays.

Craeye *et al*. [30] present a waveform extrapolation method where one element in a linear array is excited and the rest are terminated. First, a small linear array of $N_2 + 1$ elements is excited at the middle element. Another solution is made for a linear array of N_1 elements where $2N_1 \approx N_2$. They then extract the reflected wave distortions from the ends of the array. The difference in the currents between the two arrays up to the N_1 element defines the reflected currents. This assumes that the end reflection effects are not meaningful on the larger array at the

[1] The embedded impedance entails exciting only a single element while terminating all others.

N_1 point, effectively at the ¼th or ¾th point in the larger array. The third step expands the size of the linear array using the power law for amplitude and increments of the phase velocity from the small array solution. They re-center this result and truncate it to the physical limits of the array. To this last, they reapply the extracted waves representing the reflected waves. This process matches very well to the presented full-wave solutions. However, it is not clear how well this can model a fully active receiving or transmitting array. The impedance matrix could be expanded to approximate a full impedance matrix, but [30] did not address the accuracy of the results.

The feko.info web site [31] provides guidance on modeling large arrays that use the active element pattern for each element in a 3×3 array. There, the FEKO® staff calculated the far-field radiation pattern for each element individually, while all other eight elements are terminated with matched loads. Franson and Ziolkowski [32] describe a comparable technique for modeling large arrays. As opposed to using the far-field pattern, they use the near-field results at the unit cell boundary for each element in a 3×3 array, and because each element is not fully symmetric, they evaluate all nine array positions. In both of the aforementioned cases, the patterns or near-field cells become building blocks for a larger rectangular array. All interior elements in the large array use the center element of the 3×3 array. Each corner uses the corner element of the smaller array, and this approach expands the edge elements to all the respective edge elements in the larger array.

The resulting far-field patterns match fairly well to a MLFMM solution from FEKO® [33]. This approach was not exhaustive and only considered patch antenna geometries. These patches used a unit-cell layout with $d = \lambda / 2$, and [33] only presented results for a single frequency. It is likely a quick and easy solution, whose error grows with more complicated mutual coupling.

According to [32], by its geometry, the near-field unit cell approach only includes the mutual coupling from the nearest neighbors. Each unit cell actually has a varying inclusion of effects from its neighbors. As illustrated in Figure 3-4, only nearest neighbors surround the center element, while the left corner sees first and second nearest neighbors as well as the edge. In hypothesizing about the performance of this approach, the corner element is likely a more accurate representation than the center element. It includes two nearest neighbors in the same configuration it occurs in a larger array. One might take multiple small simulations using this method to consistently capture the same number of nearest neighbors. Following this, the active

element pattern from the middle element of a 5×5 array can repeat to form all interior elements in a larger array.

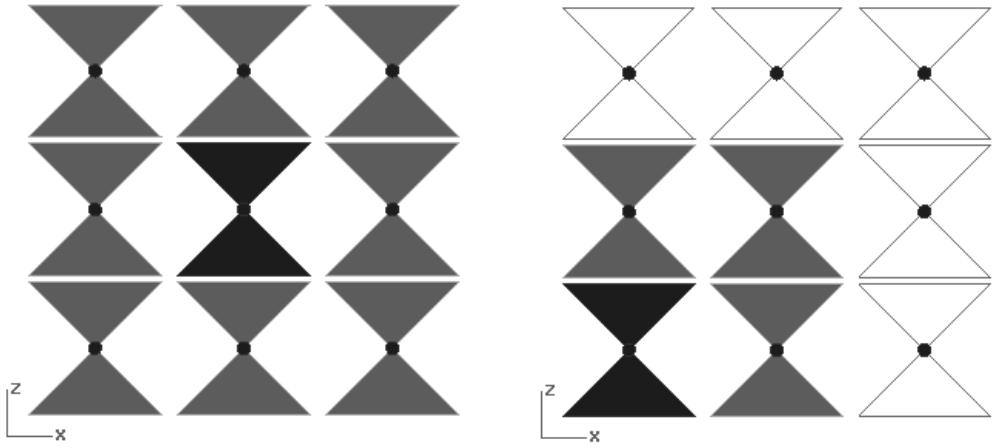

(a) (b)

Figure 3-4 – Geometry of 3x3 array: (a) center element showing ring of eight nearest neighbors; (b) corner element showing partial ring of nearest and second nearest neighbors

As the elements are brought close together, in the case of [32] for metamaterials at separations of $d=\lambda/10$, the need to consider mutual coupling from more neighbors is necessary. There is an expected convergence of the electric far-field pattern as more neighbors are considered. The authors of [32] reconstruct a computer model of a 10×10 array of resonant capacitively loaded loops from only center elements; these elements come from the center element in simulations of smaller arrays of increasing size. Zero neighbors would mean a 10×10 array constructed from an isolated element; the one-neighbor array would come from the center element of a 3×3 array, and so forth, until the four-neighbor array is reconstructed from the center element of a 9×9 array. Figure 5 of [32] shows the normalized E-field patterns for these $0\rightarrow4$ neighbor arrays. From weakest to strongest, using $\{1, 2, 0, 3, 4\}$ neighbors produces increasing gains, with the three-neighbor peak at about 97% of the four-neighbor peak. These results show a reasonable convergence at four neighbors and possibly three. The element geometry and electrical spacing, here being tight, directly affect this number. The ability to capture additional number of neighbors becomes computationally difficult, although one could make comparisons to infinite PBC and MLFMM solutions.

3.7 Validation of FEKO® as a Suitable Computational Tool

Since the majority of work in this dissertation stems from computational results from FEKO®, it is valuable and necessary to state some comparable work that validates its suitability to solve the currents in tightly-coupled array.

The strongest work is from Van Tolder [8] that considers the validity of FEKO® to solve for the reflection coefficients of a frequency selective surface (FSS) of Jerusalem crosses using the 2D Periodic Boundary Conditions (PBC). In [8], the reflection coefficient is compared to the solutions from Stevanovic *et al* [6] which uses a space-domain integral-equation method. For the Jerusalem cross, a unit cell of 15.2 mm is used for analysis over a frequency range of 3-11 GHz. The size of this unit cell used throughout Chapter 4 (in 2D) and Chapter 5 (in 1D) of this dissertation is $d_x = d_y = 15$ mm for the frequency range 1-12 GHz. While not exact, this range is closely comparable and shows the PBC to be a good computational solution for infinite and semi-infinite arrays.

The author also found additional agreement of results, such as at which frequencies the AGSW develops relative to the isolated element impedance, using arrays of parallel dipole elements in [28]. These results agree with Munk and Janning's separate, simulated solutions using SPLAT (an Ohio State code) for plane waves incident on parallel dipole arrays [3, 34].

3.8 Summary

This chapter has presented an overview of several techniques for modeling large arrays. There are many nuances and limitations to these presented techniques, as all approximate full-wave techniques. Advances in computing power have rendered some methods less valuable. Others required substantial development to be available for use in this research. However, both groups illustrate the history of this area of electromagnetics and some simplified representations of the complex array phenomenon.

The emphasis of this dissertation is to present new designs for tightly-coupled arrays and to give a clear understanding to their physical behavior. In this light, it is not necessary, and it would probably be detrimental, to focus too widely on the implementation of computational methods. The design process will employ a certain set of methods and perhaps develop additional tools or methods to analyze those designs. These methods are a means to an end.

3.9 References

[1] J. W. LaPean, *et al.*, "A computational tool for large planar phased arrays-ASIA," in *Antennas and Propagation Society International Symposium, 1996. AP-S. Digest*, 1996, pp. 822-825 vol.2.

[2] J. W. LaPean, "Analysis of Infinite Arrays of Arbitrarily Shaped Planar Radiating Elements Using a Floquet Mode Based method of Moments Approach," Ph.D. Dissertation, Bradley Dept. of Electrical and Computer Engineering, Virginia Tech, Blacksburg, VA, 1996.

[3] B. A. Munk, *Finite Antenna Arrays and FSS*. Hoboken, NJ: Wiley-Interscience, 2003.

[4] C. G. Buxton, "Design of a Broadband Array Using the Foursquare Radiating Element," Ph.D. Dissertation, Bradley Dept. of Electrical and Computer Engineering, Virginia Tech, Blacksburg, VA, 2001.

[5] EMSS. (accessed 09/16/2008, *Analysis of periodic structures in FEKO*. Available: http://www.feko.info/feko-product-info/technical/special-module-and-feature-articles/analyzing-periodic-structures

[6] I. Stevanovic, *et al.*, "Integral-Equation Analysis of 3-D Metallic Objects Arranged in 2-D Lattices Using the Ewald Transformation," *Microwave Theory and Techniques, IEEE Transactions on,* vol. 54, pp. 3688-3697, 2006.

[7] R. E. Jorgenson, *et al.*, "Analysis of electromagnetic scattering by nearly periodic structures: an LDRD report," SAND2006-6833, 2006.

[8] J. van Tonder and U. Jakobus, "Infinite Periodic Boundaries in FEKO," presented at the 25th International Review of Progress in Applied Computational Electromagnetics (ACES), Monterey, CA, 2009.

[9] J. M. Usoff and B. A. Munk, "Edge effects of truncated periodic surfaces of thin wire elements," *Antennas and Propagation, IEEE Transactions on,* vol. 42, pp. 946-953, 1994.

[10] B. A. Munk, *et al.*, "Scattering from surface waves on finite FSS," *Antennas and Propagation, IEEE Transactions on,* vol. 49, pp. 1782-1793, 2001.

[11] C. Craeye and X. Dardenne, "Element pattern analysis of wide-band arrays with the help of a finite-by-infinite array approach," *Antennas and Propagation, IEEE Transactions on,* vol. 54, pp. 519-526, 2006.

[12] C. Craeye, *et al.*, "Computation of truncation effects in broadband tapered-slot phased arrays using efficient frequency-domain and time-domain approaches," in *Antennas and Propagation, 2003. (ICAP 2003). Twelfth International Conference on (Conf. Publ. No. 491)*, 2003, pp. 445-448 vol.2.

[13] T. R. Vogler and W. Davis, "Parasitic Modifications to the Finite, Foursquare Antenna Array," presented at the USNC-USRI National Radio Science Meeting, Boulder, CO, Jan 2008.

[14] A. Neto, *et al.*, "A truncated Floquet wave diffraction method for the full-wave analysis of large phased arrays .II. Generalization to 3-D cases," *Antennas and Propagation, IEEE Transactions on,* vol. 48, pp. 601-611, 2000.

[15] A. Ishimaru, *et al.*, "Finite periodic structure approach to large scanning array problems," *Antennas and Propagation, IEEE Transactions on,* vol. 33, pp. 1213-1220, 1985.

[16] A. K. Skrivervik and J. R. Mosig, "Finite phased array of microstrip patch antennas: the infinite array approach," *Antennas and Propagation, IEEE Transactions on,* vol. 40, pp. 579-582, 1992.
[17] A. K. Skrivervik and J. R. Mosig, "Analysis of printed array antennas," *Antennas and Propagation, IEEE Transactions on,* vol. 45, pp. 1411-1418, 1997.
[18] C. Craeye*, et al.*, "Computation of finite array effects in the framework of the Square Kilometer Array project," in *Antennas and Propagation, 2001. Eleventh International Conference on (IEE Conf. Publ. No. 480)*, 2001, pp. 298-301 vol.1.
[19] C. Craeye and X. Dardenne, "Efficient computation of the polarization characteristics of infinite and finite arrays of tapered-slot antennas," in *Phased Array Systems and Technology, 2003. IEEE International Symposium on*, 2003, pp. 377-382.
[20] M. Albani*, et al.*, "An overview of the truncated Floquet wave diffraction theory," in *Antennas and Propagation Society International Symposium 2006, IEEE*, 2006, pp. 1237-1240.
[21] A. Cucini*, et al.*, "Truncated Floquet wave full-wave (T(FW)/sup 2/) analysis of large periodic arrays of rectangular waveguides," *Antennas and Propagation, IEEE Transactions on,* vol. 51, pp. 1373-1385, 2003.
[22] F. Capolino*, et al.*, "Frequency-domain Green's function for a planar periodic semi-infinite phased array, Part I. Truncated Floquet wave formulation," *Antennas and Propagation, IEEE Transactions on,* vol. 48, pp. 67-74, 2000.
[23] F. Capolino*, et al.*, "Frequency-domain Green's function for a planar periodic semi-infinite phased array, Part II. Diffracted wave phenomenology," *Antennas and Propagation, IEEE Transactions on,* vol. 48, pp. 75-85, 2000.
[24] F. Capolino*, et al.*, "Asymptotic high-frequency Green's function for a planar phased sectoral array of dipoles," *Radio Science,* vol. 35, pp. 579-593, March-April 2000.
[25] E. Martini*, et al.*, "Array interaction with complex platforms," in *IEEE Antennas and Propagation Society International Symposium*, 2005, pp. 163-166.
[26] R. Coifman*, et al.*, "The fast multipole method for the wave equation: a pedestrian prescription," *Antennas and Propagation Magazine, IEEE,* vol. 35, pp. 7-12, 1993.
[27] J. J. van Tonder and U. Jakobus, "Fast multipole solution of metallic and dielectric scattering problems in FEKO," in *Wireless Communications and Applied Computational Electromagnetics, IEEE/ACES International Conference on*, 2005, pp. 511-514.
[28] T. R. Vogler and W. Davis, "Surface Waves in Medium-Sized, Tightly Coupled Planar Arrays," presented at the USNC-USRI National Radio Science Meeting, Boulder, CO, Jan 2009.
[29] A. O. Boryssenko*, et al.*, "A wave-based model for mutual coupling and truncation in finite tapered-slot phased arrays," in *Antennas and Propagation Society International Symposium, 2003. IEEE*, 2003, pp. 11-14 vol.4.
[30] C. Craeye*, et al.*, "Wave propagation and coupling in linear arrays with application to the analysis of large arrays," *Antennas and Propagation, IEEE Transactions on,* vol. 54, pp. 1971-1978, 2006.
[31] EMSS. (2008, Sep 16). *Analysis of periodic structures in FEKO*. Available: http://www.feko.info/feko-product-info/technical/special-module-and-feature-articles/analyzing-periodic-structures
[32] S. J. Franson and R. W. Ziolkowski, "Method of Simulation of Closely Spaced, Finite, Periodic, Radiating or Reflecting Structures, Including Metamaterials," presented at the

22nd Annual Review of Progress in Applied Computational Electromagnetics, Miami, FL, 2003.

[33] EMSS. (accessed 3/5/2008, *Large Array Modeling - A Microstrip Case Study*. Available: http://www.feko.info/knowledge-base/application-notes/large-array-modelling-microstrip-example/

[34] D. S. Janning and B. A. Munk, "Effects of surface waves on the currents of truncated periodic arrays," *Antennas and Propagation, IEEE Transactions on,* vol. 50, pp. 1254-1265, 2002.

CHAPTER 4

Designs of Infinite Planar Tightly-Coupled Arrays

The previous two chapters outlined the physical phenomenon and computational methods available for the design and analysis of tightly-coupled arrays. Up to this point, this dissertation has presented very little on the array design process or on the designs themselves. This chapter will present several designs and layout a process for the overall development of a tightly-coupled array. First, this chapter presents an overview of past planar array and tightly-coupled array designs from the literature. Supported from the background of the previous chapters, this chapter assesses new design options and the approach to their development. This chapter presents several array designs evaluated with the Periodic Boundary Condition (PBC) found within FEKO®. The emphasis is on tightly-coupled planar arrays over perfect electrically conducting (PEC) ground planes. Chapter 5 will expand on these designs using semi-infinite techniques, which allows for the investigation of the array-guided surface wave (AGSW) in one dimension. Chapter 6 incorporates the totality of Chapters 4 and 5 and presents finite array designs and analysis.

Some design constraints for the element designs in tightly-coupled arrays need to be stated. The literature presents many of the constraints, but the intention here is to define more clearly a design process. That two designs emerge for continued analyses is secondary. Many antenna engineers, and certainly as taught in the undergraduate level, consider arrays as extensions or multiples of single antenna designs, which capture the benefits of beamforming. Here, the arrays are designs from an array perspective from the beginning using infinite array techniques. Designing the elements in an infinite array accounts for all mutual coupling effects present in arrays, but it lacks the ability to capture any array edge effects. These effects are

generally negative in nature, but the compensation methods are in many ways common to all tightly-coupled arrays. Research suggests that later stages in the design sequence can provide sufficient solutions to array truncations. These solutions are primarily through the application of loading to mitigate edge effects (reflection or diffraction) and to suppress the AGSW.

4.1 Influence of Ground Plane

As the ground plane is common to all these designs, a solid foundation to planar arrays first requires an understanding of ground effects on those arrays. A typical and historical understanding of the spacing between elements and the ground plane has $h = \lambda / 4$. The notion of narrowband antennas drives this concept. For example, a horizontal dipole over ground has the double travel distance for fields to ground, plus a 180° phase shift on the metallic ground, which combine in phase to increase the system gain. This concept often extends beyond narrowband antennas and a $\lambda / 4$ spacing is set for the middle of the operating frequency band. This approach is not completely wrong or misguided, but it does not work well for wideband antennas. It is a common misconception that antennas spaced closer to the ground plane have severe pattern and impedance distortions. The overall impact of following this misconception is to limit the bandwidth of wideband antennas and arrays. These limitations stem from pattern effects at the higher frequencies.

There is really no optimal spacing for a wideband array over ground [1]. There are merely two limits; near $h = 0$ and near $h = \lambda / 2$, with harmonic distances of $N\lambda / 2$. Near $h = 0$, the ground plane shorts the electric currents (and fields) to ground as per PEC boundary conditions. This is evident in the drop of the input resistance of the element as it nears the ground. However, the pattern shape barely changes. Near a separation distance of $h = \lambda / 2$, the pattern develops a null in the direction of the array broadside ($+\hat{z}$ following the standard geometry of an array in the *xy*-plane). Figure 4-1 shows these effects for patterns. The pattern at broadside pulls in by 6 dB at a spacing of 0.44λ. If the target is a 4:1 bandwidth, the spacing at the lower frequency becomes 0.1λ. This range may shift lower, as well, if less array gain is acceptable.

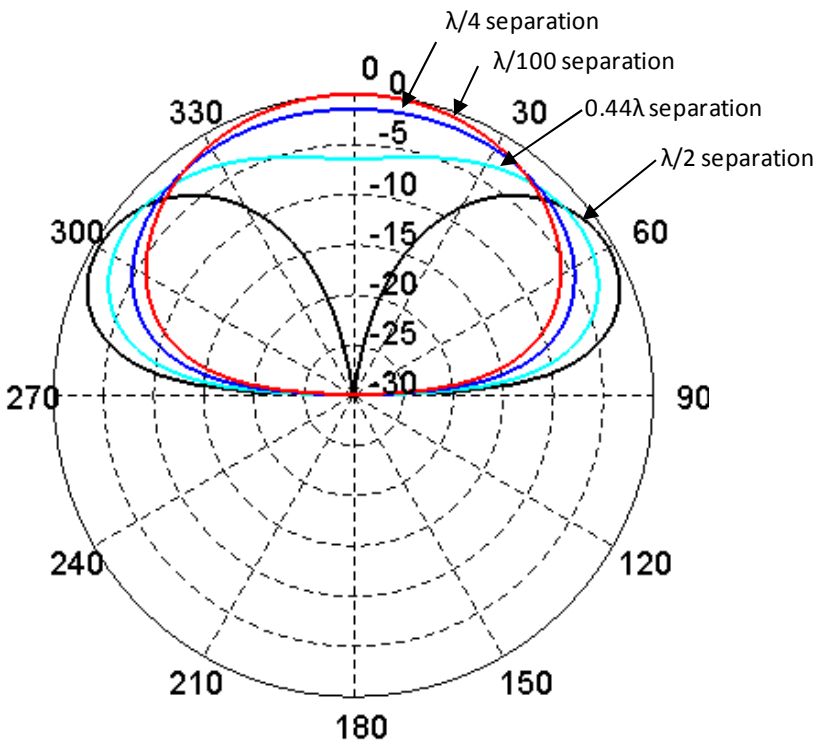

Figure 4-1 – Normalized far-field patterns for a horizontal dipole over infinite PEC ground

A PEC ground plane appears to be inductive at a short electrical distance and thus low frequencies. As frequency and the electrical distance increase, the ground plane varies slowly into a capacitive surface. As a PEC without loss, the impedance appears as an arc on the outer right side of the Smith Chart and is defined by

$$Z_{GND} = jR_o \tan\left(kh / \cos\theta\right) \tag{1}$$

The separation h is the perpendicular distance to ground, to keep it consistent with physical measurements described elsewhere. If the array main beam scans from the normal direction, the $1/\cos\theta$ term in (1) corrects for the distance to the ground plane. Latter sections address how the antenna or array impedance interacts with the ground impedance. For an isolated half-wavelength horizontal dipole, Figure 4-2 shows the change in impedance as its distance from ground increases; these graphs were calculated using FEKO®.

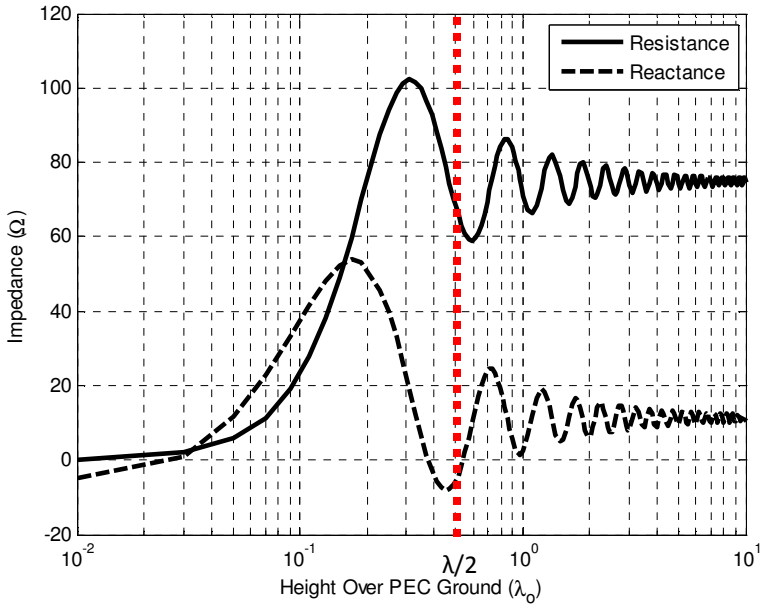

Figure 4-2 – Input impedance of a horizontal λ/2 dipole over an infinite PEC, calculated using FEKO® MoM

Because of the oscillatory nature of the impedance and the largest changes occurring between $0.1\lambda \rightarrow 0.5\lambda$, where there tightly-coupled array designs will be spaced, the concept of a tapered ground plane has some value. Suh [2] presented the concept and results for a tuning plate with the Foursquare and fourpoint antennas (not arrays). This plate is located under the feed section of the antenna and is responsible for improving the higher frequency performance. Suh, however, does not explain the mechanism that allows for this bandwidth expansion. This plate may function as a partial sleeve and as part of a discontinuous, ground plane. The location of the tuning plate is very close to the feed. Assuming an $\epsilon_r = \epsilon_{r,eff} = 2.33$, the tuning plate lies a maximum electrical distance from the element (at the highest frequency) of 0.053λ. The plate is at distances of 0.787 mm from the element compared to the distance to the ground plane of 8.71 mm. For the better-performing Fourpoint antenna, the tuning plate increases the upper frequency from $10.1 \rightarrow 13.3$ GHz, while leaving the low frequency of 5.8 GHz unchanged. Section 4.5.4.2 presents an infinite array design that considers a flat ground plane, but with elements tapered in $+\hat{z}$, affecting a tapered ground. Its electric distance, however, is a maximum 0.3λ and a minimum 0.063λ over the impedance bandwidth of the infinite array. This is fundamentally different than Suh's tuning plate concept.

4.2 Element Designs in Planar Arrays

Engineers understand the need and applications of planar arrays well. Without belaboring their value, it is safe to say that they are not an obscure facet of antenna engineering. There are several types of planar arrays in use including open-ended waveguides, tapered-slot arrays, patch arrays, and dipole and slot arrays, with several derivations of each type. There is also a limited use of ultra-wideband or frequency independent elements for planar arrays, specifically spirals. All produce patterns that are broadside to the plane of the array, but physically they have varying limitations. In all, there is an effective ground plane below the array elements, i.e., in the opposite direction of the desired radiation direction. This distinguishes planar arrays from an array of monopoles or a monopole Yagi-Uda array, for example.

Open-ended waveguides (or horns) and tapered-slot arrays require a substantial depth and are not suitable for low-profile applications. The feed networks for open-ended waveguides are substantially complicated and likewise expensive to manufacture. (Slotted waveguides can have less depth, but the slot spacing and phase control typically limit bandwidth.) The size aspects of waveguides forces their application into either very large arrays or high frequency applications, primarily for radar systems. These arrays exhibit moderate bandwidths. A similar comment applies to tapered-slot arrays, e.g., Vivaldi arrays. Tapered-slot arrays are very desirable for their bandwidth, which can approach 9:1 [3]. While not necessarily implemented as such, isolated elements typically show a maximum gain when the radiation slot is 6.5λ in length [4]. The array feed network requires additional physical depth, and it typically includes microstrip and coaxial transmission lines.

Patch elements are a favorite choice for planar arrays. They are cost effective to manufacture; loading by a dielectric substrate can minimize their physical size; and their unbalanced structure allows for a relatively easy feed network. A probe or microstrip transmission line typically feeds patch elements. However, the radiation mechanisms of patches lead them to be very narrowband. The fringing fields on the sides of the patch and the 180° phase shift across the $\lambda/2$ surface of the patch are responsible for the antenna radiation [5]. This physical limitation restricts the bandwidth to a few percent, and overall, they are a poor choice for wideband array applications, even when considering the benefits of mutual coupling [1].

When using planar UWB antennas as elements in an array, it is important to consider the overall application. The tightly-coupled array designs sought in this work are planar and have elements placed parallel over a ground plane. With this in mind, some benefits and restrictions of UWB antennas will be addressed using a traditional spiral antenna as the example. The radiation regions within a spiral antenna vary outwardly from the center depending on the frequency. The higher frequencies radiate first when the first resonant diameter or slot is reached, and lower frequencies radiate farther along the spiral. Now consider the presence of a ground plane. Given a fixed separation from the ground plane, it should be set according to the highest frequency at $h = 0.4\lambda_{small}$. If the frequency range were limited to approximately a 4:1 bandwidth, the minimum electrical separation would occur at around $h = 0.1\lambda_{large}$. (This is comparable to the relationship for simple dipoles over ground discussed in Section 4.1.) The inability to keep the distance to ground at $h = \lambda/4$ across the entire frequency range discounts the use of spirals with a ground plane, and such designs often use absorber between the antenna and ground [6].

The impedance looking at the ground varies gradually over this frequency range from inductive to capacitive with increasing frequency and is almost entirely reactive[1]. Munk explains this relationship well in Section 6.3 of [1]. Without a ground, a UWB antenna changes rapidly about the reference point within a tight (low) VSWR circle on a Smith Chart. This causes the system impedance to oscillate between where the antenna and ground plane reactively cancel each other, to where they do not. This observation argues against using UWB elements in such an array layout. However, the extent of control offered by properly choosing the UWB element and limiting its bandwidth to manage these effects are unknown.

The other limitation, and comparable discussion, is the inter-element spacing. Again, with an inter-element spacing $d = \lambda/2$ at the highest frequency to avoid grating lobes at all scan angles, the lower frequencies are electrically closer together, at about $d = \lambda/8$. A layout of normally sized spirals that minimizes gaps between elements still dictates an inter-element separation of $d \sim 2\lambda$ at the highest frequencies[2]. Since $d > \lambda$, grating lobes are always present

[1] If the ground is a PEC, its impedance is purely reactive.

[2] The operative and most important words of this explanation on the spiral are "normally sized". The next section reviews existing designs and shows that once the concept of "normally sized" disappears, wideband arrays emerge.

regardless of scan angle. The results from [7] for a Wideband Array With Variable Element Sizes (WAVES) show the growth of sidelobes when elements become electrically separated.

The last class of elements for tightly-coupled planar arrays has shapes derived from dipole elements, and by duality, variations of slot radiators. These can have many shapes, but their fundamental properties are that they are balanced antenna structures and resonant at about $\lambda/2$ in length when isolated. There are a number of extensions between these two fundamental designs, including the long slot and others of a UWB nature. For UWB elements in a tightly-coupled array, the overall length is sized to be about the highest operating frequency if isolated; conversely, in single-element UWB designs, the largest physical length radiates the lowest frequency. Several methods have been applied to widen the bandwidth of these types of antennas (e.g., fat dipole, sleeve dipole, and folded dipoles), but they typically range between 10-30% bandwidth. Much wider bandwidths are possible in tightly-coupled arrays even with basic element shapes, implying untuned or un-optimized elements. Electrically short elements allow for a tight electrical spacing in an array. This tight inter-element spacing leads to increased input resistance for each element and yields an effective increase in bandwidth.

4.3 Tightly-coupled arrays Designs

In the range of publications on arrays, few address tightly-coupled arrays, and several other designs strive to reduce mutual coupling between elements. (This is done primarily by disrupting any surface wave in the substrate using an effective cavity with a rim, such as in [8], which is accomplished using a fence of vias.) This section presents a brief review of tightly-coupled planar arrays. There are several fundamental similarities between these following designs. In all designs, the mutual coupling between elements is responsible for enhancing the array bandwidth, not reducing it.

Taylor, Munk, and Durham at Ohio State and Harris Corp. developed a wideband planar array around 2003 with fat dipole elements [9]. This design has become known as the Current Sheet array. Pryor in his thesis [10] and Janning in papers and his dissertation [11, 12] supported this development. Munk documented a substantial portion of the technical background in two books [1, 13] and states in [13] that an array of dipoles and a ground plane can be designed to

have a 4:1 bandwidth defined by a VSWR < 2[3]. Impedance matching layers in front of the array elements (a "superstrate") add additional bandwidth for their designs. These can extend the bandwidth to greater than 7:1.

Several engineers at Georgia Tech Research Institute (GTRI) between 2001 and 2006 used fragmented elements [14] to achieve a measured 12:1 bandwidth with no ground plane present and an 8:1 bandwidth with a ground plane present [15]. These designs emerged from genetic algorithms and used pixel structural features. Unfortunately, this reduces one's ability to interpret and conceptualize the optimized designs.

More recently, Neto and Lee, *et al*. with Raytheon have developed and analyzed a set of tightly-coupled arrays that use long slot apertures [16-18]. Periodically spaced dipoles, or loops depending on one's interpretation, feed these slots. They are effectively multi-layer structures, but are still overall thin, and achieve bandwidths around 5:1 without ground plane loading. Newer designs report a 10:1 bandwidth [19] and a 22:1 bandwidth [20]. All designs use long slots to produce a TEM radiation mode across the gap. The lower cut-off frequency is therefore a function of the slot length and may conflict with other desired design features.

Because of its development at Virginia Tech, the last tightly-coupled array this section reviews is the Foursquare array. Nealy holds the patent for the Foursquare element array from 1999 [21]. Dissertations followed by Buxton [22] in 2001 and Takamizawa [23] in 2002 at Virginia Tech and expanded the modeling methods and conceptual contexts of the Foursquare array. These works reported bandwidths of 1.8:1. There are many similarities of the Foursquare array to the Current Sheet array and the Long Slot arrays. Suh [2] further developed and tuned the Foursquare antenna into the Fourpoint antenna, but this development was as an individual antenna. Up to this point, the Foursquare array has not achieved the large bandwidths reported for the others.

4.3.1 (Harris) Dipole/Current Sheet Array (CSA)

The Current Sheet Array (CSA) arises because of similarities to Wheeler's current sheet antenna [24]. It refers to the work from Ohio State and the Harris Corporation. Although there are

[3] Because of the clumsiness of stating VSWR < 2 or VSWR < 3 repeatedly, this dissertation adopts a simple notation of S2 bandwidth or S3 bandwidth, respectively.

certainly many, the well-published design [1, 9, 25-27] uses fat dipoles, with inter-digital (finger) capacitors between elements. The array elements are configured in a linear form for a single polarization (such as in Figure 4-3) or in an orthogonal lattice for circular or dual polarization.

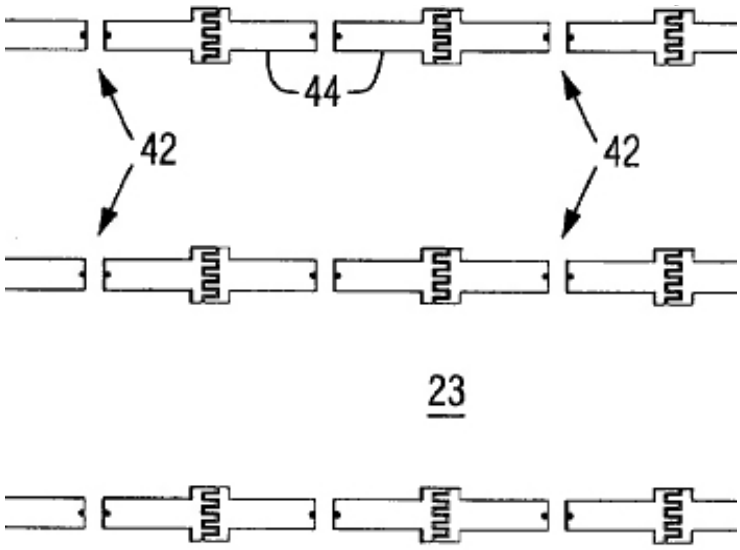

Figure 4-3 – Harris Current Sheet Array (CSA) for a single polarization [9]

The dipole elements do not occupy much of the unit cell for each element, and the physical configuration of a dual/circularly polarized layout is relatively simple. The CSA design matches a fair amount with the concepts described previously in Chapters 2 and 3 about behaviors in tightly-coupled arrays. The inter-element spacing is at $d = \lambda / 2$ at the highest frequency. Because the elements extend and interlace with the adjacent element, the element length is longer than the inter-element spacing. This design feature increases the capacitance and complements a reduction in the natural inductance resulting from the short length of the element. Because both components change with frequency, a wideband match is possible. Figure 4-4 shows a circuit model for this mutual coupling behavior.

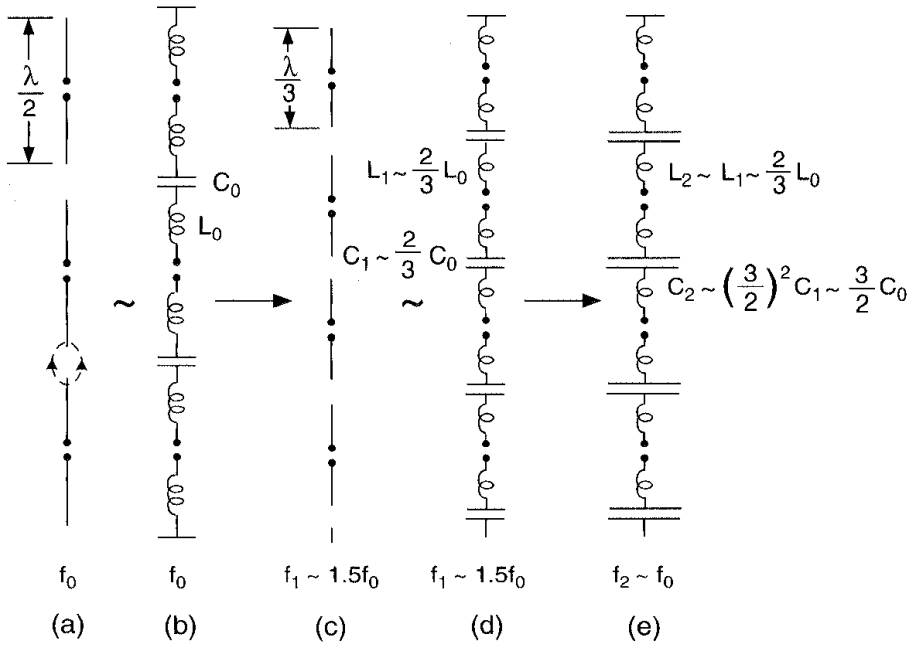

Fig. 6.18 Self-impedance of a short dipole is indeed capacitive. However, it contains no "big bad capacitance." In fact, a dipole is comprised of an inductive wire L_0 near its terminals and a capacitance C_0 at the tips. Thus, if L_0 is reduced, C_0 must be increased to maintain resonance. Any conclusion to the contrary is based on voodoo physics. This figure explains why the capacitance between dipole tips must be increased if the dipoles are shortened and the resonance frequency is to be maintained.

Figure 4-4 – Circuit model of short dipole array (Fig 6.18 of [1], reprinted with permission through subscription to the Copyright Clearance Center)

McCann [28, 29] and a Harris patent [30] present comparable designs using slots. This section will only briefly mention the slot arrays because the dipole designs characterize them by duality. Both are meant to approximate Wheeler's theoretical *current sheet* described in Section 2.2.3 [24]. Opposite to the dipole, the slot has a natural capacitance. The inter-digital structure at the end of the element in the slot design creates a meandering line between elements, whereas it creates a meandering slot in the CSA. This line creates a series inductance between elements and provides for a wideband match and field continuity. In either the slot or dipole arrays, the general linear nature of the element helps achieve a low cross-polarization of less than -30 dB across the operating bandwidth [25]. The slot is preferred in some cases for its element pattern at high scan angles; the far-field pattern does not pull in near the PEC ground plane because radiation comes from magnetic currents. The admittance on a slot array also matches the impedance of the dual dipole array in free space. However, the ground impedance is the same for both dipole and slot arrays. For an *impedance* Smith Chart, the impedance looking into the ground shifts along the

extent (since there is no loss) from inductive to capacitive with increasing frequency. For an *admittance* Smith Chart, the ground traces from capacitive to inductive, thus appearing rotated 180°. Both dipole and slot arrays are parallel over the ground plane. The CSA over ground yields an input impedance with a crossing loop on the Smith Chart; the slot array over ground results in a smooth line [29]. The loop in the CSA of dipoles results in expanded operating bandwidth and is evident in the designs presented later in this chapter.

In both the dipole and slot designs, the spacing to the ground plane is at $h \sim 0.4\lambda$ of the isolated element resonance and $h \sim 0.1\lambda$ at the lowest frequency [26]. Both designs can have one or several dielectric layers added above the front of the array, as shown in Figure 4-5. This addition changes the impedance seen by the element or slot to something less than $\eta_o = 377\Omega$ and puts a lower impedance in parallel with the ground plane, which allows for large increase in the bandwidth. Measurements for a finite array with an S3[4] bandwidth exceeding 9:1 (2-18 GHz) were presented in [25]. This array had the spacing to ground of $h \sim 0.05\lambda$ at the lowest frequency.

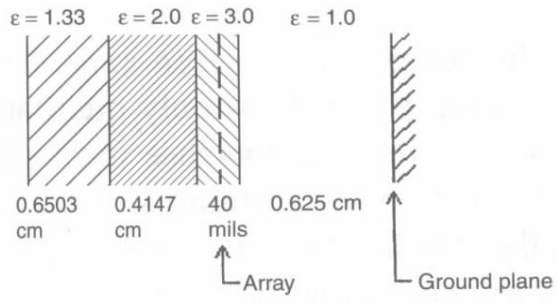

Figure 4-5 – Side view of an example CSA dipole array with substrate and superstrates (Fig 6.12 of [1], reprinted with permission through subscription to the Copyright Clearance Center)

The CSA designs have features to mitigate the impedance variations from AGSW. Chapters 5 and 6 present exact techniques, but in short, the design relies on a ring of several terminated elements to suppress the AGSW. Some earlier prototype designs used only the center 4×4 and 8×8 elements, where the remainder of the 28×28 element array was resistively terminated, although this termination region was admittedly larger than necessary [26]. The

[4] S3 denotes a VSWR < 3 bandwidth.

design development used the OSU Periodic Moment Method (PMM) code to simulate infinite array structures. OSU engineers used CST Microwave Studio® and Ansoft HFSS® to model finite structures [25]. This dissertation uses a similar design approach with FEKO®.

4.3.2 (GTRI) Fragmented Array

The fragmented array is a creation of researchers at Georgia Tech and the Georgia Tech Research Institute (GTRI), as patented in [31], and Steyskal *et al*. [32, 33] have expanded it to other applications and smaller arrays. The various fragmented array designs use pixilated structures with a set number of pixels for a given element, and a genetic algorithm (GA) determines if the pixel is a conducting shape or empty. This is a binary design decision for each pixel in the array element. The genetic algorithm optimizes the element design in the layout of an infinite array, using Floquet theory and in the presence of mutual coupling.

The GTRI designs use square pixels [15] and small plus shapes [31] as the conducting elements (see Figure 4-6). The "empties" are simply the dielectric substrate. The pixel size is $\lambda/20$ at the highest design frequency, which argues that the pixel shape would have little or no impact. The employed design solution uses a combination of a reduced resolution genetic algorithm as the first stage and a hill-climb algorithm as the second stage [15]. For the 31×31 pixel element totaling 2^{961} variations, the GA uses 40 genes to develop large-scale characterization, while the hill-climb (stochastic) algorithm uses all 961 variants to refine the solution. Hill climbing takes the GA solution and iterates it through small changes. If the change results in an improvement to the scoring (optimization) criteria, the genetic algorithm keeps the change. When it finds no more improvements, the algorithm terminates. Linearly polarized element use a single feed, while circularly polarized elements may use one or two feeds. The circular polarization designs are symmetrical along both axes.

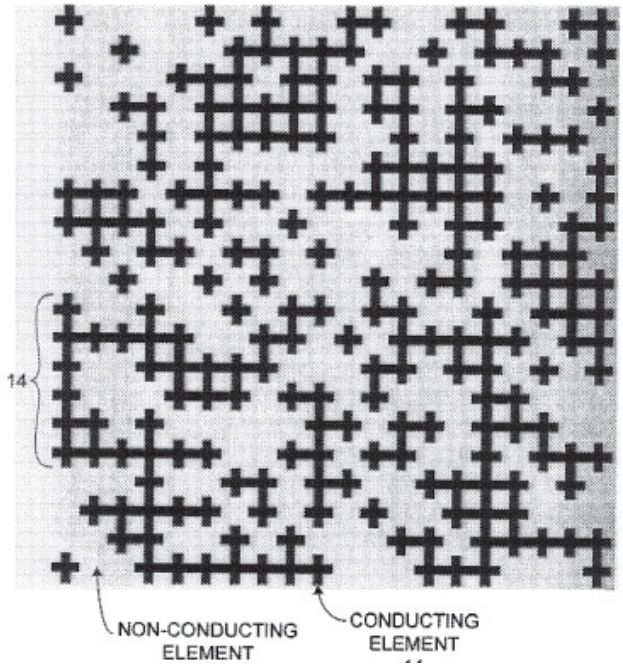

Figure 4-6 – Fragmented aperture array element [31]

As in any antenna, the longer electrical connections between pixels are responsible for the lower frequency performance (along with mutual coupling between elements). The overall aperture size dictates the lowest usable frequency, at approximately λ/3 for the side of a square aperture. The element characteristics appear to dominate the high-frequency limit, although once the inter-element feed spacing exceeds $\lambda/2$, grating lobes will appear as a function of the scan angle. The arrays described in [15] are mostly without a ground plane. Measurements for these show bandwidths of 12:1 for linear polarization and 8:1 for dual linear polarization. This work only briefly considers the inclusion of a ground plane, and it advances *as necessary* the concept of separating the array from the ground at $h = \lambda/4$ at the mid-frequency. The ground plane and this separation reduced the bandwidth, as defined by gain, to 8:1. Overall, the inclusion of the ground plane effects is lacking, along with the lack of specific impedance data.

4.3.3 (Raytheon) Long Slot Array

Lee *et al.* [34] designed an array using Vivaldi-like elements, that are shorter than conventional elements. One variation known as the "bunny-ear" array features dual tapers (inside slot and outside) and does not interconnect elements (see Figure 3-2). Both element designs have much

shorter slots than typical tapered-slot antennas. Alterations near the element feed improved some problems with Vivaldi arrays at lower frequencies, although [34] provides few details on the feed of the element and the dimensions. The interesting part of these elements is that they have poor efficiency at low frequencies when isolated and are not especially wideband near resonance. However, when the element is electrically small, it radiates only the fundamental TM_{01} mode. This detail means that the taper is, in most of the operating band, functioning only as an impedance match of the array element. These elements exhibit a bandwidth of 5:1 when used in a tightly-coupled array, however, and the same principles explain its performance improvement as with the CSA (see Section 4.3.1). These principles rely on the deviation from how elements are "normally sized", as indicted in Section 4.2. The presence and role of a ground plane in such designs, however, are not clear.

The above array designs were introduced because the engineers (Lee, Livingston, and Koenig) nearly concurrently developed the long slot array design for VHF and UHF frequencies [35]. They cited the lack of bandwidth in other dipole and patch designs and the not-so-low-profile nature of a tapered-slot array. (At 100 MHz, the array depth would be at least 75 cm.) The long slot array uses a continuous, long slot of the maximum width of the array to support a TEM wave mode. The TEM modes have no low frequency cut-off in an infinitely long slot [36] and would form a plane wave following Huygens principle [37]. These slots accommodate a continuous current sheet (described in [16, 17]) when radiating TEM modes. The length of the slot determines the low frequency performance when sized at about $\lambda/4$, provided no ground plane is present [38]. The separation between slots sets the upper frequency limit in one of the dimensions of the array aperture. The feed spacing sets the upper frequency limit in the other aperture dimension. As with the other designs, feeds are set to have $d < \lambda/2$ at the highest operating frequency in order to prevent the development of grating lobes. Figure 4-7 shows the geometry of the long slot array.

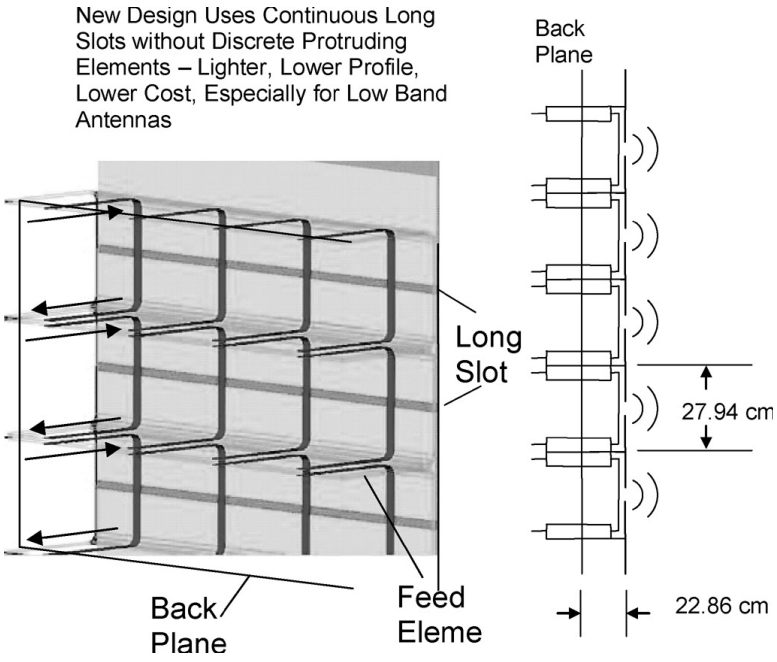

Fig. 1. Back side of a long slot array, with each slot fed by an array of feed elements spaced at the "Nyquist" interval (half wave length at high end of the band).

Figure 4-7 – Geometry of Long Slot array (Fig. 1 of [18]. © 2006 IEEE. Reprinted, with permission, from IEEE and the author.)

Half-loops feed the long slot at Nyquist intervals (i.e., feed spacing $d = \lambda / 2$ at the highest operating frequency) with the center of the half-loop aligned orthogonally to and behind the gap. There are similarities again to the dipole array concerning element spacing. The half-loops do not connect to the ground plane, but pass through and are interconnected through transformers, which work to transform the signal from a nominal 50-Ohm feed to the impedance seen through the long slot. Without a dielectric matching layer, this is nominally 377 Ohms. Figure 4-8 shows a circuit model of this design. The opposite current flow from the adjacent element counteracts the current flow on the half-loop normal to the array surface. This produces a set of split, balanced ("push-pull") feed lines for each element and acts partially as a balun along with the transformer. The only exception occurs at the array edges where no complementary feed is present.

The slot length and the feed interval together set the long slot array bandwidth. The overall bandwidth can be considered to be the ratio of lower wavelength to the upper wavelength, roughly $2N$, where N is the number of feeds along the slot [38]. This can allow for incredible bandwidths. Simulations including the balun showed a 60:1 bandwidth when no ground plane was present [18]. This design used a parallel line feed behind the slot (like the

outline of a rectangle) instead of a thin wire. This improved the array bandwidth, presumably by creating a more continuous current in the slot. The parallel feed lines on each element also increase the frequency when grating lobes appear. Putting two wires in parallel across the slot but on the same feed divides the current in the slot in half. This design then needs a transformer from 50 Ohms to 188 Ohms, which allows for a lower profile design.

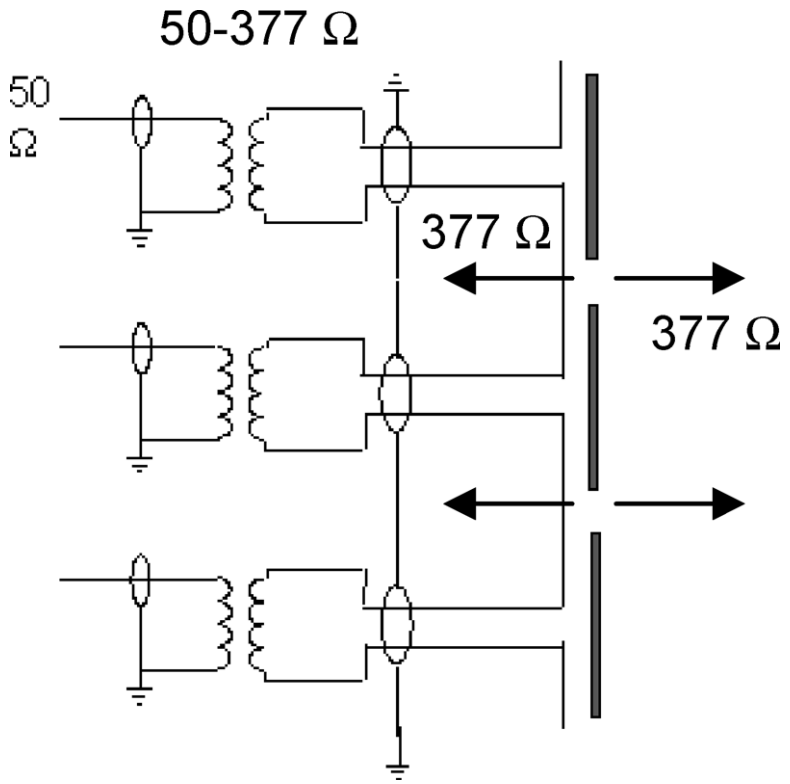

Fig. 2. Equivalent circuit of the long slot with transforming balun to match input (50 Ohm) impedance.

Figure 4-8 – Feed model of Long Slot array (Fig. 2 of [18]. © 2006 IEEE. Reprinted, with permission, from IEEE and the author.)

While these reported bandwidths are astounding, the introduction of a ground plane limited the bandwidth to 4:1 (150-600 MHz) for a ground plane separation of 23 cm. This put the separation at $h \sim \lambda/8$ at 150 MHz and $h \sim \lambda/2$ at 600 MHz. The gain results approaching 600 MHz begin to drop away from the aperture maximum (Figure 14 of [18]). This drop may be due to some losses in the feed structure and transformer (balun), but some effects of $h \to \lambda/2$ may be at play.

The severe restrictions on bandwidth with the gap present showed a clear need to mitigate the disturbances from the ground plane. A later design [19] used ferrite loading with an air gap,

which was possible because of the desired frequency range of 200-2000 MHz, where ferrites are not overly lossy. The ferrite loading decreased the ground plane gap to $h \sim \lambda/20$, as well. Ferrites make the ground approximate a magnetic conductor, but it also adds about 2 dB of loss. A follow-on design expanded the bandwidth to 22:1 by using electromagnetic band gaps (EBG) and a ferrite ground plane in a hybrid form [20]. The EBG functions at frequencies higher than what ferrite loading alone can improve. For example, the ferrite range in the second design in [20] covers 170 MHz to 1.39 GHz, while the EBG range covers 1.39 GHz to 3.8 GHz. This EBG is a mushroom structure on a substrate with a PEC backing, PEC patches on top, and vias connecting them. This EBG structure creates parallel inductances and capacitances and establishes a high impedance surface at resonance. If the ground structure begins to appear to have a 377-Ohm impedance for a field incident on it, the disturbance from the ground becomes minimal ($\Gamma \to 0$). Additionally, the phase of the reflection shifts to $\pm 90^{\circ}$ (orthogonal) and is non-interfering as compared to a reflection from a PEC ground.

4.3.4 (Virginia Tech) Foursquare Array

The final tightly-coupled array presented in this review is the Foursquare array. The typical Foursquare antenna array has inter-element spacing $d \sim \lambda/2$ of the single element resonant size. Figure 4-9 shows a 5×5 example of the Foursquare array. Note the overall coverage of the array aperture by conducting elements, and note the limited gaps between and within elements (between squares surrounding the same feed).

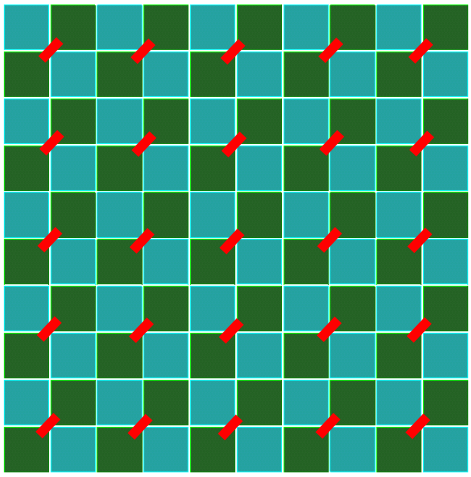

Figure 4-9 – 5x5 Foursquare array with diagonally fed squares

Although one could limit the scan range, it is best to consider a maximum scan range and force the inter-element spacing to be $d \le \lambda / 2$ at the highest operating frequency. (A $d = 0.6\lambda$ spacing will prevent grating lobes through a $\pm 60^{\circ}$ scan volume.) Being balanced, one may view the Foursquare element as a dipole structure, perhaps specifically as a sleeve dipole with the top-left and bottom-right parasitic squares (for a single polarization feed) acting as the sleeve. This behavior is evident in the behavior of the isolated Foursquare element.

4.3.4.1 Isolated Foursquare Element

The Foursquare antenna is a balanced-feed antenna, and although it appears to be the collection of four microstrip patches, the radiation comes from currents on the surface. The radiating currents are not fringe currents, and the Foursquare antenna does not require a ground plane or substrate to operate and thus is not related to microstrip antennas. There are a number of possible feed layouts in this antenna. The most common is a single or dual diagonal feed. In the dual-feed layout, the engineer usually seeks circular polarization. In either, because of the orthogonal nature of the geometry and the circular feed phasing, the other pair of squares act as parasitic patches. Dual polarization is also possible, although the literature does not define as clearly the role of the other/parasitic squares if the orthogonal pairs are in phase. For this isolated element discussion, the geometry of Figure 4-10 applies, where no ground plane is present.

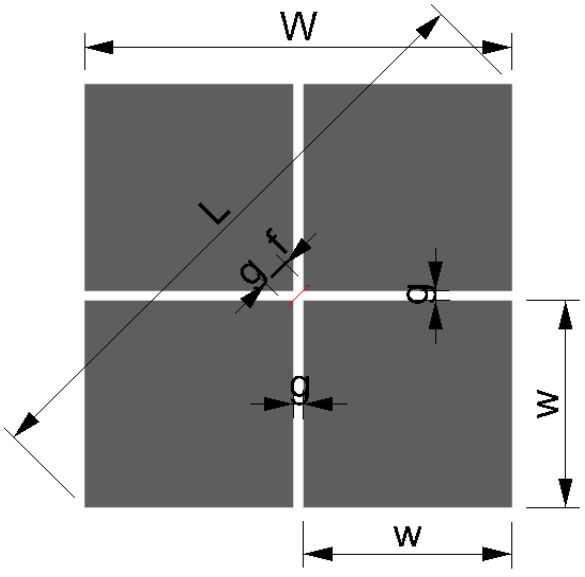

Dimension	Length (mm)
W	20.73
L	14.66
w	7.16
g	0.34
g_f	0.98

Figure 4-10 – Geometry of isolated Foursquare element

The feed and presence of the ground plane both affect the development of currents on the isolated Foursquare element. In many ways, the locations of radiation are unclearly tied to frequency. However, an interesting observation is the nature of the currents on the parasitic squares. At nearly every frequency around the 5 GHz match for this antenna, the currents on the parasitic elements rotate circularly around the edge of the square. Near the feed region, these currents are opposite the currents from the driven squares. This distribution is clearly evident in Figure 4-11, where the arrows show the direction and, by color, the magnitude of the instantaneous currents. This current reversal, by duality, argues for radiation coming from an equivalent magnetic current in the slot gap. The width of the gaps between the four squares plays a role in the mutual coupling from the driven to the parasitic elements and affects the bandwidth of the Foursquare antenna.

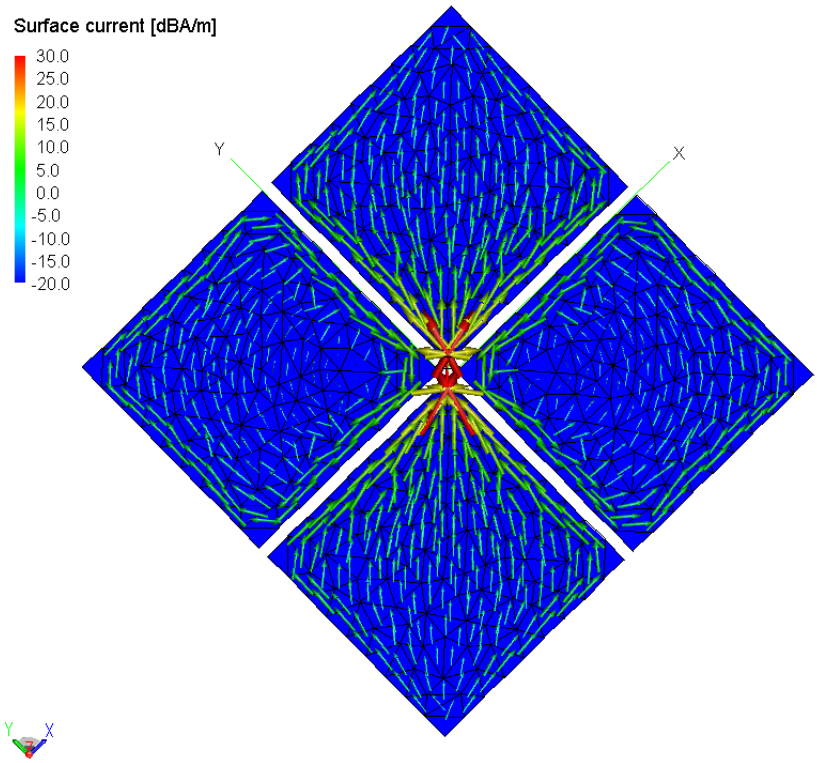

Figure 4-11 – Foursquare element, center frequency (f_c) currents

4.3.4.2 Infinite Foursquare Array

Buxton [22] found that the control of the impedance bandwidth is a function of the gap at the feed g_f and independently the gap between elements g. She presented a limited number of variations of the separation between elements, heights, and element spacings. In these, the inter-square separations, lengths, and dielectric thickness remained the same. The best bandwidth achieved for an infinite Foursquare array was 58% (or, 1.82:1) for Geometry V (see Table 8.1 of [22]). Across the five geometry variations presented, the one factor that most significantly affected bandwidth was a reduction in the distance to the ground plane (her Geometry III). The widest bandwidth geometry, Geometry V, was distinguished from Geometry I (37% bandwidth) and Geometry IV (39%) by having a $g = 2.5$ mm spacing between Foursquare elements (not between squares), as compared to 0.5 and 1.0 mm, respectively. This put the inter-element gaps at $G = 10g$.

In the work below, a scaled duplicate of the above Geometry V was simulated in FEKO®, which uses the Periodic Boundary Condition described in Section 3.1.1, but the input impedance results are substantially different than reported previously in [22]. This discrepancy may be the unclear definitions of the bandwidth, the lack of a substrate in the FEKO® model, or different accuracies in the methods. Since this design is merely the beginning, an explanation of the differences is less important than improving the design. From FEKO®, the calculated S3 bandwidth is 3.46:1 for $Z_o = 100$ Ohms. When observing the input impedance on the Smith Chart, the impedance loop resulting from the interaction with the ground plane is clearly visible. The thick line backing the entire trace in Figure 4-12 denotes the matched S3 range from 2.4-8.4 GHz for $Z_o = 100$ Ohms, in which the impedance is completely capacitive. Structural alterations are necessary to better tune this design.

These results may show the limiting factor to most Foursquare analyses to date. By keeping with the square shapes and only altering the inter-element and inter-square spacings, the Foursquare design lacks enough freedom to optimize its impedance match. The use of the Smith Chart in such designs offers the clearest presentation of the input impedance and allows for the quickest interpretations.

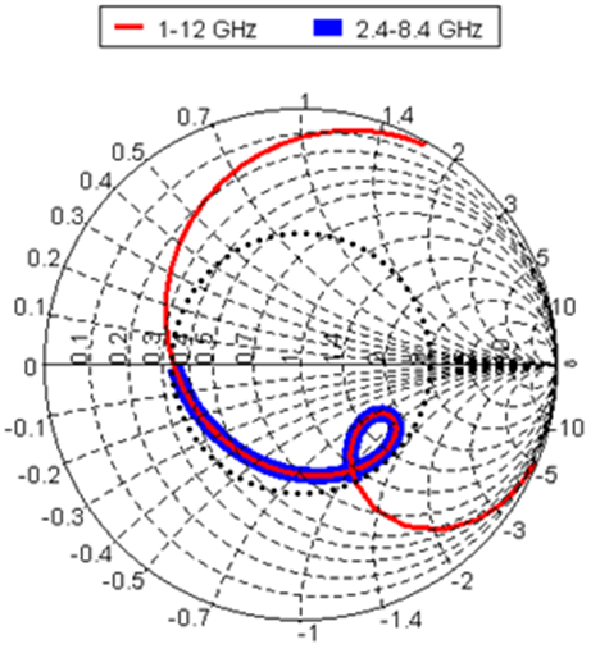

Figure 4-12 – Input impedance of infinite Foursquare array (VSWR < 3 boundary (S3 bandwidth) shown as dotted line)

4.3.4.3 Finite Foursquare Array

The isolated Foursquare element can offer some basic estimates about the finite Foursquare array performance. A frequency range for 2-3 GHz, or a 1.5:1 bandwidth, is to be expected, but the tight coupling when placed into a tight array would expand the bandwidth sufficiently. With details in Table 7.1 of [22], Buxton calculated the far-field patterns of a 3×3 Foursquare array using FDTD. The resonances and element patterns for the 3×3 array are significantly different from those of an isolated element. Simulations using FEKO® without a ground plane for both a 3×3 and a 5×5 Foursquare array confirmed that this small array size is still capable of supporting an AGSW. Figure 4-13 shows the geometry and element numbering of the 3×3 Foursquare array, and Figure 4-14 shows the active input resistances for the first five unique elements. The input resistances alone are sufficient to show the presence of the AGSW, as discussed in Chapter 2, especially if a negative resistance is present.

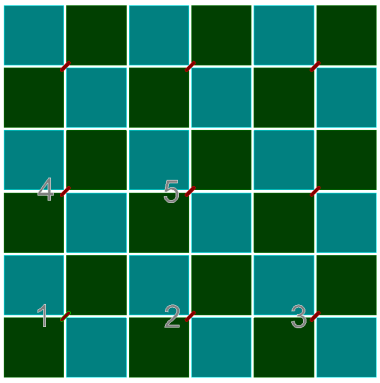

Dimension	Length (mm)
W	21.59
L	30.53
w	10.54
g_{square}	0.51
$g_{element}$	0.51
g_f	1.44
$W_{x,array}$= $W_{y,array}$	65.79

Figure 4-13 – 3x3 Foursquare array geometry

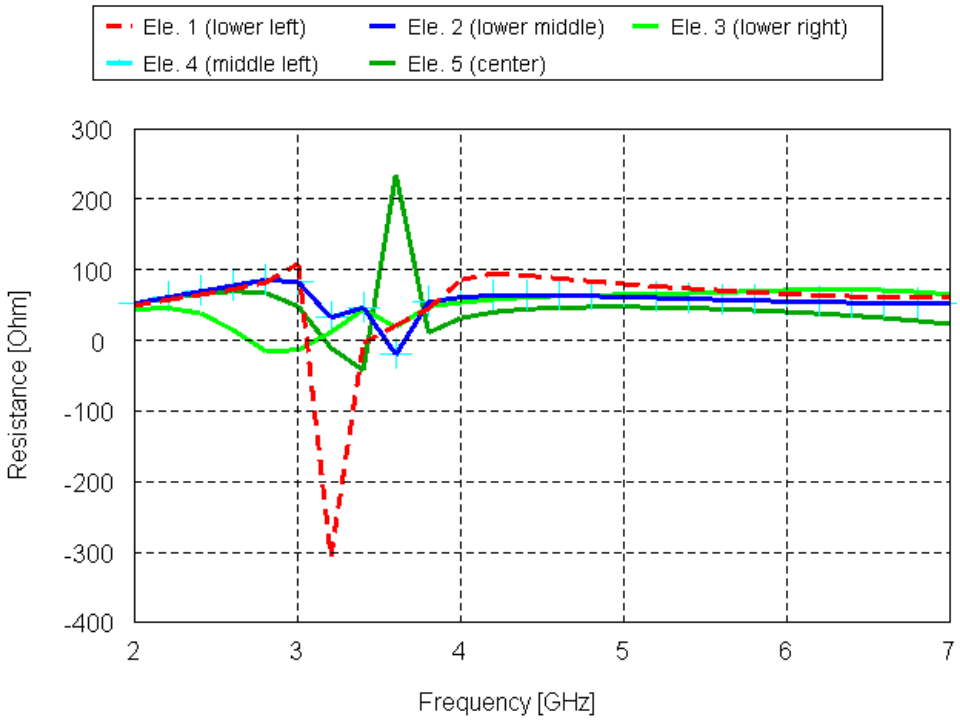

Figure 4-14 – Active input resistance of 3x3 Foursquare array of Figure 4-13

Another interesting observation in Buxton's results [22] is the comparison of the active input impedance between the infinite array solution and the 3×3 array solution. The infinite array resonance is lower, at roughly 80% of the 3×3 solution. This is significant because it supports the interpretation that mutual coupling in tightly-coupled arrays extends substantially past the first neighboring element, at least for this element design. The maximum mutual coupling would be present in an infinite array, but with only a 3×3 array, the mutual coupling is

limited to less than one neighbor on average. This follows the results from Franson and Ziolkowski [39], as discussed in Section 3.6, that suggests considering 3 or 4 neighboring rings of elements to account for all mutual coupling.

One way to view this extension of the element effectively beyond its physical size is through the embedded currents. This requires one element to be excited while all others are terminated. Here, only the center element is excited (between the bottom-left and top-right squares) while all others are terminated in 50-Ohm resistors. Figure 4-15 shows the average surface currents in dBA/m for the array at 3.6 GHz, which is the resonance of the center element in this configuration. No ground plane is present. The single center element is highlighted by a red dashed square, and strong currents clearly extend past the single element. This initial result is presented without equivalent representations for other designs. It is unclear what interpretations can be made when viewing current magnitude alone; phase is certainly needed to offer a conclusive result. This approach is a method for further development with designs tuned for wider bandwidth performance.

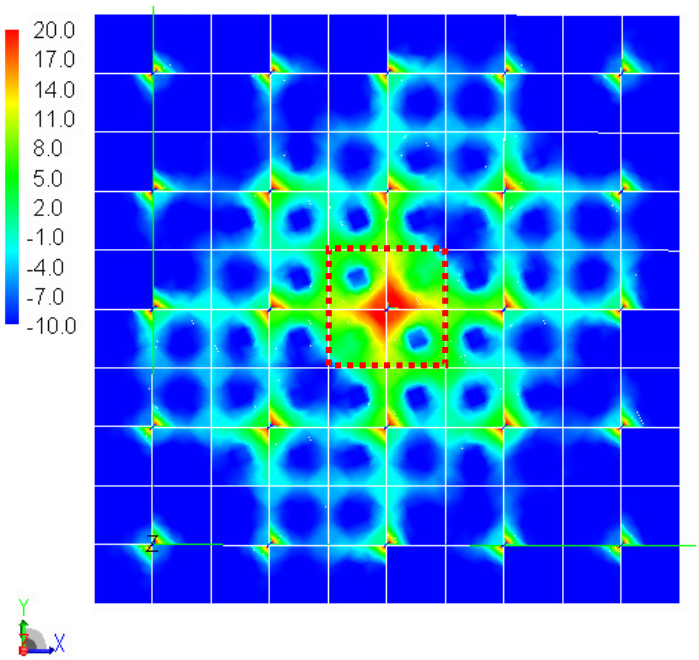

Figure 4-15 – Embedded currents on the 5x5 Foursquare array of Figure 4-8 at its resonance of 3.6 GHz without ground plane present. Inter-element spacing *d*=15 mm.

Takamizawa [23] demonstrated his *S*-parameter model on the same 3×3 Foursquare array. In tests, 180° hybrid couplers and power dividers fed the elements. Takamizawa used the

active antenna patterns and active element *S*-parameters to determine the mutual coupling between each element. He then superimposed these element patterns to develop the full array pattern. These compared well to measurements of the fully excited array. The finite Foursquare array has the same disrupting edge effects and AGSW that affect other tightly-coupled arrays. Figure 4-16 illustrates a 5×5 Foursquare array where all elements are equally excited as an example of the irregular current distribution across the array where, at 26% below resonance, the AGSW is present. At 15% below resonance and higher, as Figure 4-17 shows, only minor edge disturbances are observable, particularly on the aperture vertices.

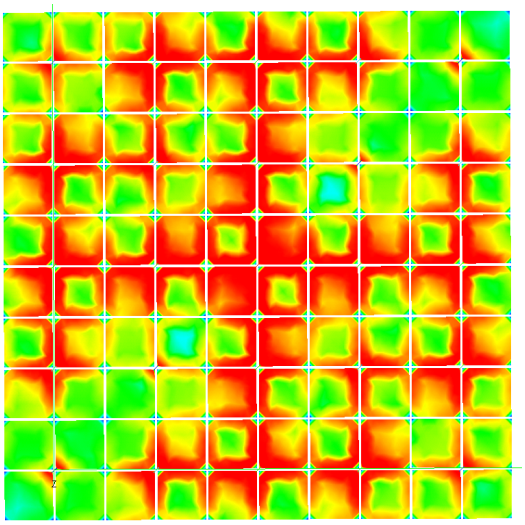

Figure 4-16 – 5x5 Foursquare array currents at 26% below resonance (*f* = 3.4 GHz)

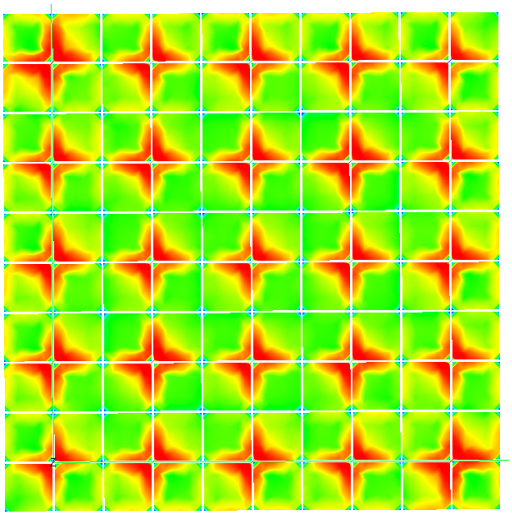

Figure 4-17 – 5x5 Foursquare array currents at 15% below resonance (*f* = 4.0 GHz)

Because of its tight coupling, the Foursquare array has the potential to force a negative input resistance on specific elements. Simulations of a 5×5 Foursquare array showed a negative active resistance at about 25% below the resonant frequency of the element without a ground plane present. Figure 4-18 shows the input impedance of the center element with all elements excited equally and no elements loaded; and Figure 4-19 shows a close-up of the currents on the center element. The colors are scaled to accentuate the reversal in the current flow on the center element, and the center element is clearly pointing out of phase of the other elements (since all are equally fed). At this frequency of 3.4 GHz, the inter-element spacing puts the four neighboring elements at ~λ/4, with the physical structure of the inter-element gap providing a direct coupling path between each. As evident in Figure 4-16, the nature of the AGSW distortion is dependent on the element location within the array.

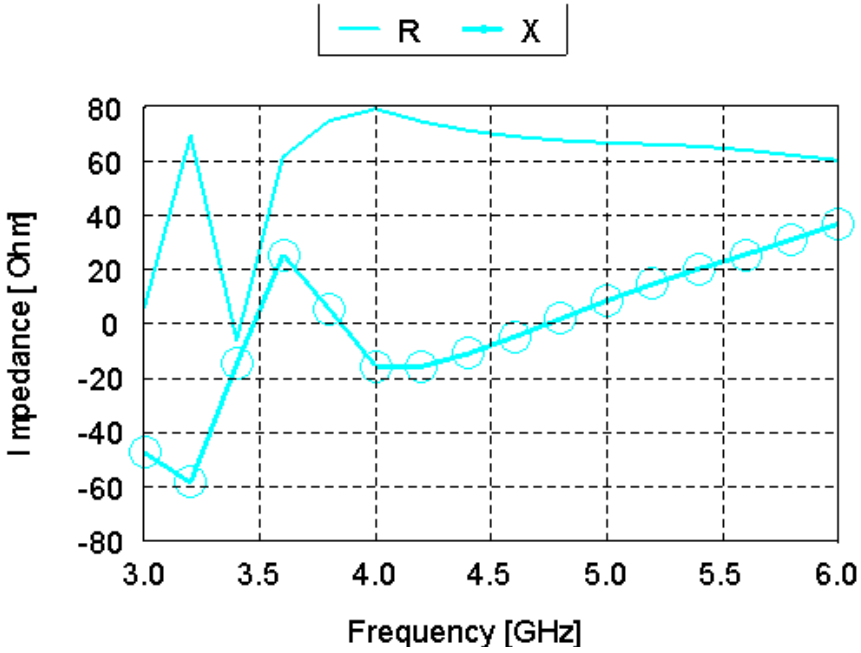

Figure 4-18 – Center element input impedance of 5x5 Foursquare array of Figure 4-16 without ground

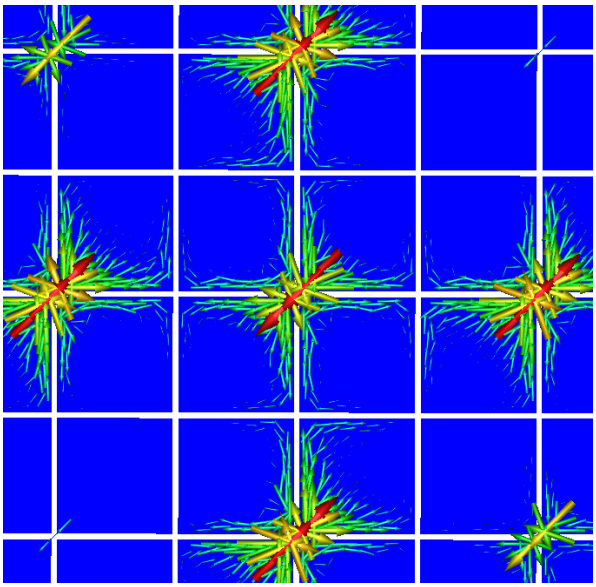

Figure 4-19 – Instantaneous currents (as arrows) at center element of a 5x5 Foursquare array of Figure 4-16, 26% below resonance (f = 3.4 GHz) with all elements excited but unloaded

4.4 Assessment of Element Characteristics

The designs presented in Section 4.3 above have several characteristics in common. Primarily, their isolated elements all have moderately narrow bandwidths, regardless of the ground plane. No ultra-wideband designs are in this set. To achieve a target bandwidth of 4:1, the bandwidth range has an upper bound near the resonance of the isolated element. Therefore, the lower frequency limit must occur on an electrically small element, at an approximate length of $(\lambda/2)/4 = \lambda/8$.

Since electrically small elements, in their limit, function predominantly as dipoles with a fundamental TM_{01} radiation mode, the expected active element pattern will be that of a dipole, *in general.* Design enhancements beyond simple dipoles are primarily to improve the input impedance of the elements and compensate for the mutual coupling effects of the array on the element. Shape alterations to the element influence the AGSW and move its location in frequency. The designs presented below and expanded in the following chapters are shown to be incapable to relocating the AGSW frequencies to outside the frequency range otherwise seen in the infinite array. Perhaps some limited application has an unused section of frequency between

two other bands, and a specialized design can adjust the AGSW to occur in this range. Otherwise, some technique must mitigate or suppress the AGSW distortions.

Bandwidths beyond 4:1 or 5:1 are possible through the use of impedance loading either in front of the array [26] or loading the ground plane with ferrites or EBG structures [19, 20, 26]. These appear to be independent of the array design. In other words, it appears sufficiently viable to first design the array in the presence of a ground plane, mitigate the AGSW effects, and subsequently choose a method comparable to the two mentioned to widen the bandwidth, if desired. Such bandwidth enhancements in this last step are outside the scope of this dissertation.

4.5 Element Designs

Following the presentation of past designs of tightly-coupled arrays, the remainder of this Chapter 4 presents new designs or designs used to illustrate some of the described phenomenology. The focus is on infinite wideband arrays, but this section wraps some basic finite structures with basic feeds into the presentation. All infinite array solutions come from FEKO® and use the periodic boundary condition (PBC). While certainly some designs exhibit superlative bandwidth performance, this section presents a limited progression of designs as a way of explaining the coupling and tuning insights and processes used. These include variations to the infinite dipole array, long-slot array, and Foursquare array, in some sense. Modifications to increase the circular polarization bandwidth are also considered.

4.5.1 Variations of Infinite Dipole Arrays

Infinite array designs start with a basic, fat dipole in a 2D periodic boundary. The unit cell has width $d_x = d_y = 15$ mm on each side, which provides a $d_x = d_y = \lambda/2$ sizing for 10 GHz. This sizing is consistent for all designs going forward. The geometries show a natural progression to achieve a higher capacitance in the input impedance, as is expected since the elements are electrically small. The initial element shape in Figure 4-20 is tapered at the feed to allow an orthogonal element to fit. (The square indicates the unit cell in the infinite array.) An edge current is applied at the middle of the dipole, and the element spacing from ground is $h = 12\,\text{mm}$, or $0.4\lambda_{10\text{GHz}}$. The edge of the dipole in all cases was $g_{cell} = 0.15$ mm from the unit cell, yielding

a $g = 0.3$ mm gap between infinite elements, for an overall element length $w_y = 14.7$ mm (0.49λ at 10 GHz). The widest section of the element is $w_x = 3$ mm.

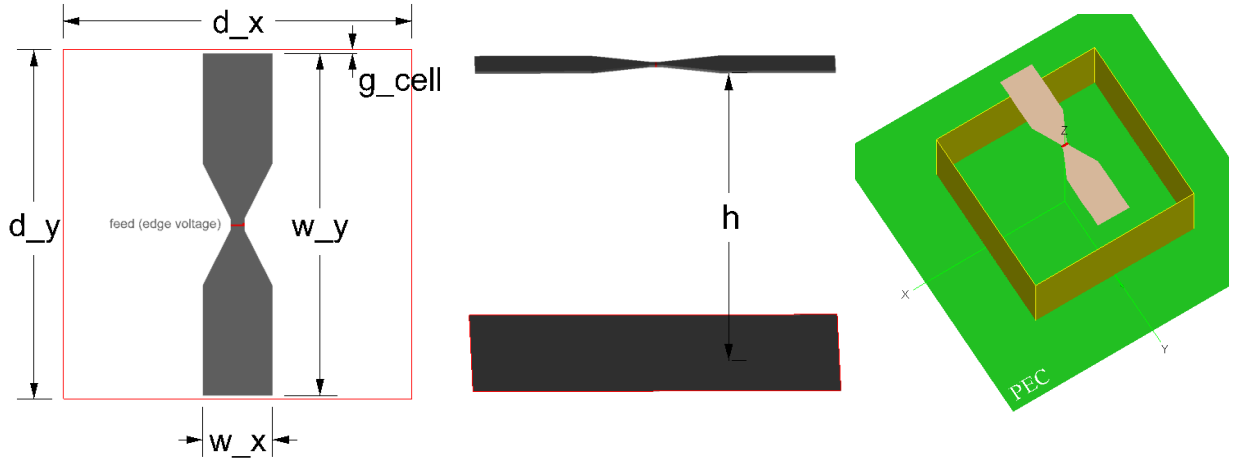

Figure 4-20 – Initial Dipole element design: (a) top-down view with unit cell, (b) side view with ground plane, and (c) isometric view from PostFEKO® with unit cell and PEC ground

The initial design achieves an S3 bandwidth of 2.55:1 (4-10.2 GHz for a $Z_o = 150\,\Omega$), but looking at the impedance Smith Chart in Figure 4-21, it is apparent that more capacitance is required as with the recreated Foursquare design of Section 4.3.4.2. The loop seen in Figure 4-12 does not develop in this design, and this is indicative of its lower bandwidth.

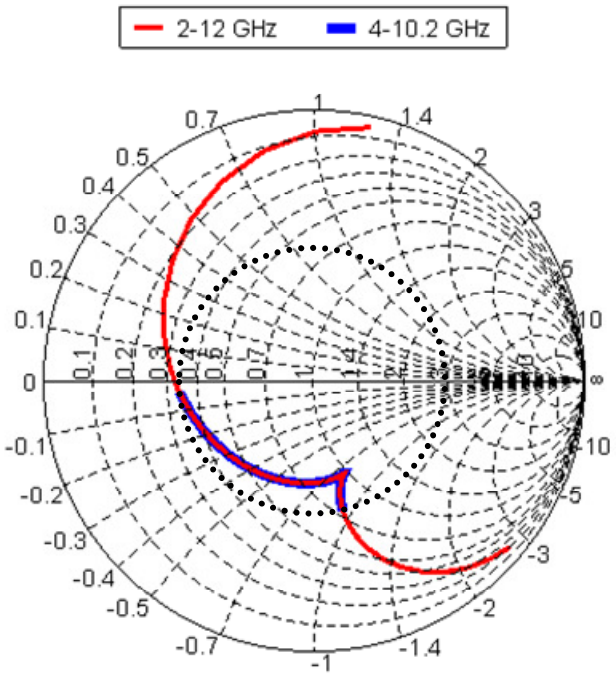

Figure 4-21 – Input impedance for Initial Dipole element design of Figure 4-20

Expanding w_x where it abuts the adjacent element to $w_x = 7$ mm and leaving $w_2 = 3$ mm as before, as Figure 4-22 shows, seeks to increase the element capacitance. A $Z_o = 150\,\Omega$ yields an S3 bandwidth of 3.85:1. These tabs move the input reactance closer to zero and, with the ground plane effects present, develop the "loop" seen on the Smith Chart in Figure 4-23. Optimally, the crossover of this loop would lie on the real axis of the Smith Chart. An additional 75 Ohms reactance would achieve this.

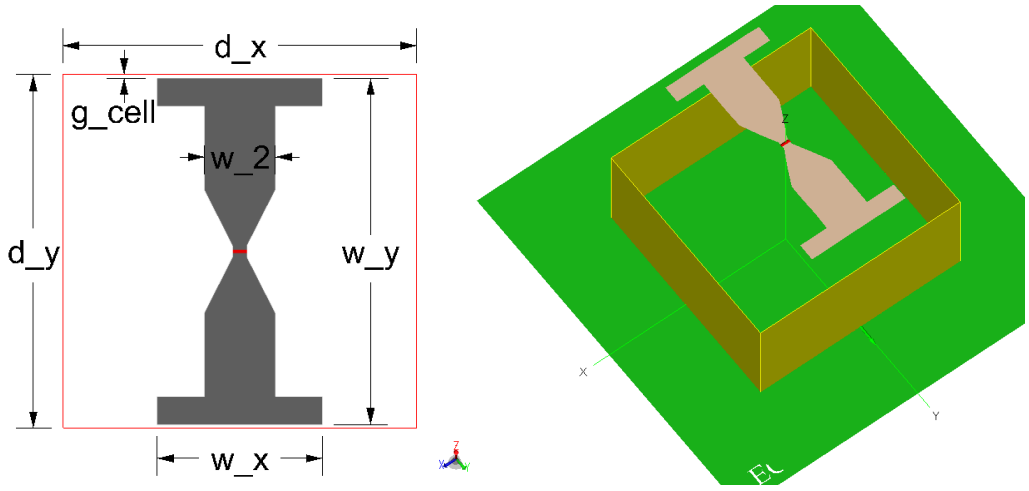

(a) (b)

Figure 4-22 – Modification 1 to dipole element design (a) top-down dimensions and (b) isometric view from PostFEKO®

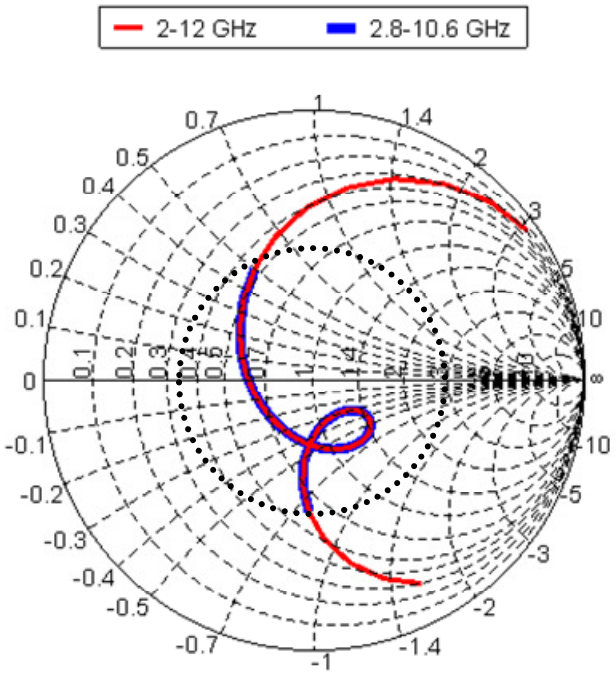

Figure 4-23 – Input impedance for Modification 1 design of Figure 4-22

While Modification 1 (adding end tabs as shown in Figure 4-22) does not yet achieve a perfect match, widening the edge can only increase the capacitance so much. As is done with the CSA, inter-digital shapes can increase capacitance. This would closely approach the OSU design detailed previously in Section 4.3.1. Modification 2 considers the importance of the original

element width, shown in Figure 4-24, where w_2 narrows from $3 \rightarrow 1$ mm and w_x remains at 7 mm. This modification both increases the capacitance and the resistance to use a reference impedance $Z_o = 200\,\Omega$. This increase would normally indicate the presence of higher mutual coupling and higher bandwidth, but Modification 2 does not achieve as a wide a bandwidth as Modification 1 (an S3 bandwidth of 3.72:1). Some of the changes in the trace on the Smith Chart of Figure 4-25 are worth noting, however. The lower end of the bandwidth has not changed, but the upper frequency range has declined. This appears to result from the loss of the taper near the element feed. A further narrowing of the dipole width w_2 from $1 \rightarrow 0.6$ mm (not shown) increases the reference impedance to 300 Ohms and reduces the S3 bandwidth to 3.51:1. Mostly, the upper frequency range is affected.

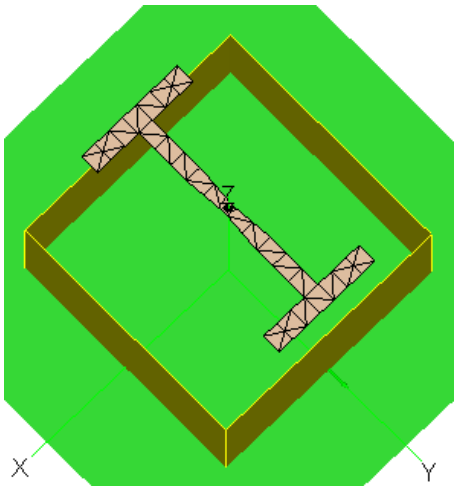

Figure 4-24 – Modification 2 to dipole element design, with w_2 = 1 mm

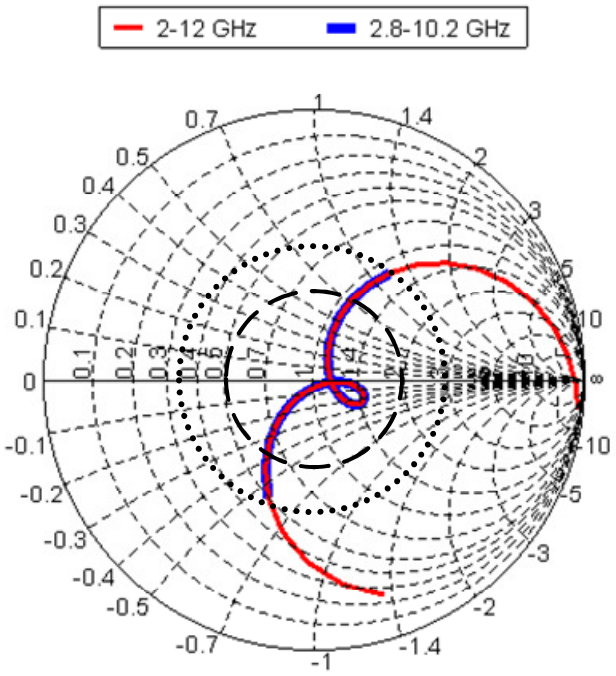

Figure 4-25 – Input impedance for Modification 2 design of Figure 4-24, showing VSWR = 2 (S2) and VSWR = 3 (S3) boundary circles

A final modification to the fat dipole element (seen in Figure 4-26) is considered. This widens the dipole section to approach that of a bow-tie shape and expand the taper. As expected, the input resistance falls with this geometry to use a $Z_o = 150\,\Omega$ reference impedance and results in nearly the same bandwidth of 3.70:1. There is hardly a noticeable change in performance, but differently, this design results in a shift upward of the S3 frequency range at both ends of the frequency range. The overall shape on the Smith Chart of Figure 4-27, as compared to Figure 4-25, shows a flatter reactance but an increasing resistance.

The findings of these designs are not fully complete. No design achieved a superlative impedance match, but the four designs do point to the element regions that are responsible for matching at different frequencies. However, this section will conclude with the Modification 3 design where $w_x = 7$ mm. It is a worry that derivations of the dipole design will inevitably lead to a repeat of the (Harris) Current Sheet Array design (Section 4.3.1).

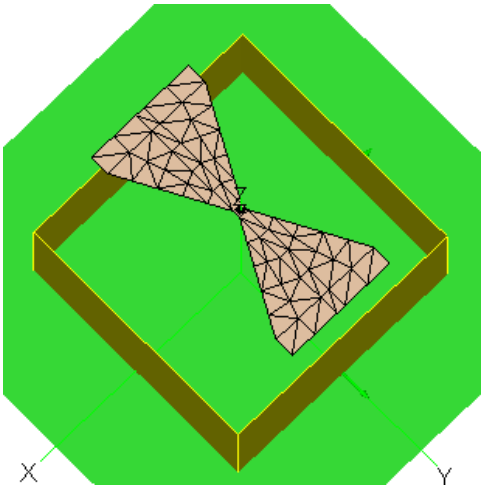

Figure 4-26 – Modification 3 to dipole element design

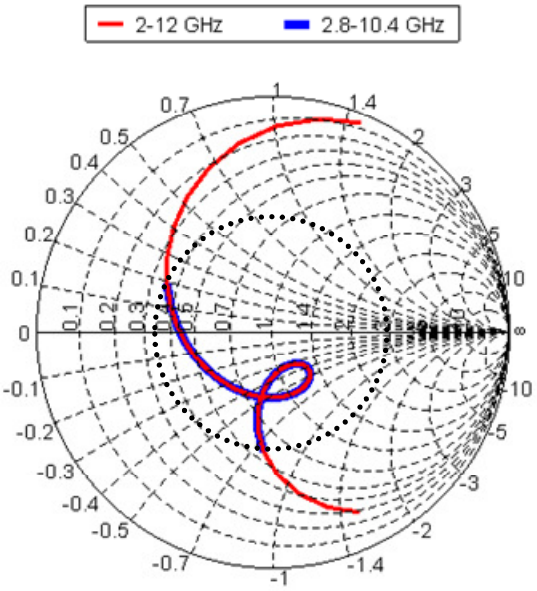

Figure 4-27 – Input impedance for Modification 3 design of Figure 4-26

4.5.2 Variations of Infinite Long-Slot Arrays

Some of the author's designs first explored using finite techniques in [40] showed the effects of widening dipole elements in an array of linear elements in the *H*-plane. Once the width extends fully to the unit cell, the elements form an infinitely long slot. This differs from the (Raytheon) Long Slot array, however, since the feed is directly across the slot in this case, whereas the former design entails a half-loop behind the slot. In the below simulations, the unit cell of

$d_x = d_y = 15$ mm and the ground-plane separation of $h = 12$ mm, as shown in Figure 4-20, remain unchanged. All designs use infinite array techniques and have a ground plane present. With no AGSW present in infinite arrays, the focus of the work is on tuning the designs first.

In the finite analyses, elements with $w_x < 0.5\lambda$ width exhibited problems from the AGSW, but the long slot did not within the impedance bandwidth of the array. The input reactance became noticeably more level for a width $w_x = 0.25\lambda_{10\text{GHz}} = 7.5$ mm and a feed gap $w_{feed} = 0.5$ mm; w_y remains at 14.7 mm [40]. Figure 4-29 shows the input impedance for three element widths $w_x = \{0.25, 0.375, 0.48\}\lambda$ at 10 GHz alongside each other for comparison. As the element is widened, bandwidth increases from 3.12:1 for a $Z_o = 75\ \Omega$, to 3.64:1 and 3.70:1 with $Z_o = 50\ \Omega$, respectively. A full extension of the width to the sides of the unit cell only marginally affects the bandwidth, but this signifies an infinitely long slot, or "gap", with periodic feeds across. In all cases mentioned, the element needs more capacitance, and some other fundamental change in the design is necessary.

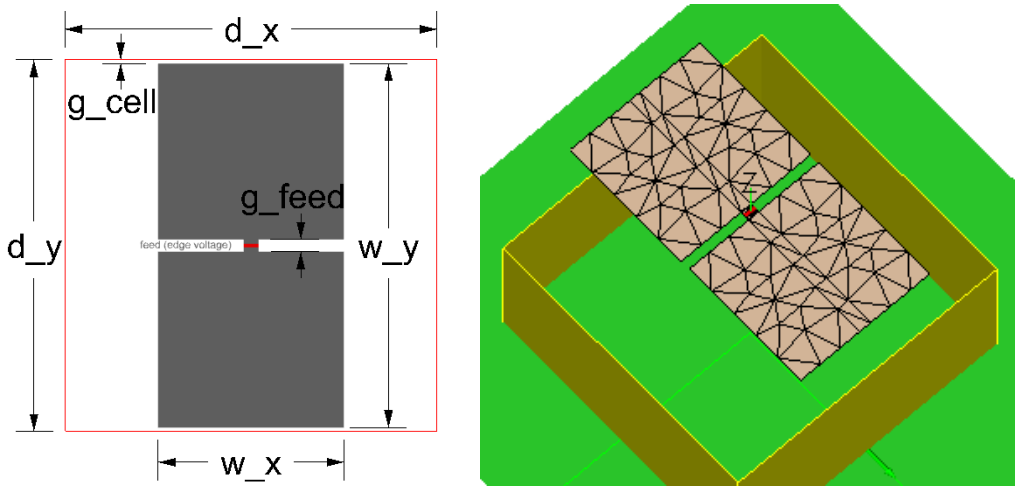

(a) (b)

Figure 4-28 – Slot 1 element design (a) top-down dimensions and (b) isometric view from PostFEKO®. Height over ground *h*=12 mm.

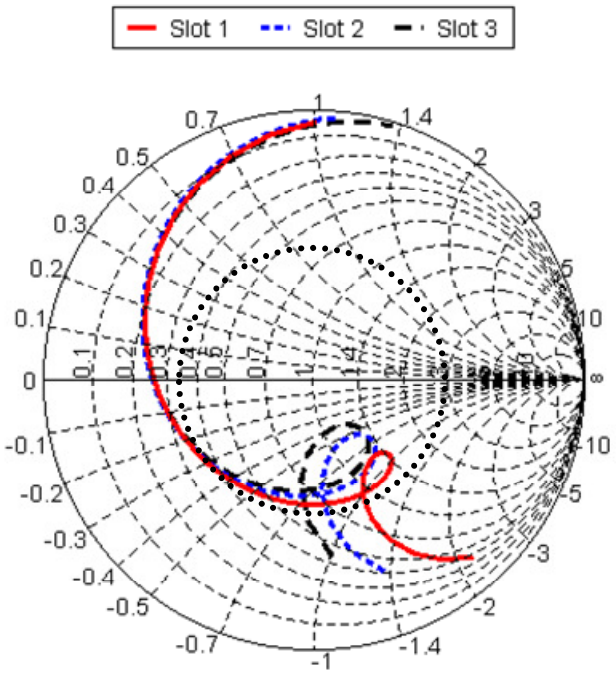

Figure 4-29 – Input impedance for the Slot 1-3 designs of Figure 4-28

One may view the fundamentals of these designs as one capacitive gap between the positive and negative sections of a single element and secondly capacitive gaps between the elements on their outer edges in the *E*-plane. Viewing these as series, but distributed, capacitances, a reduction is one should increase the overall capacitance at the element feed. A widening of the gap at the slot region is the only option, as the ability to change the outer edge is limited. The lesser effect at the element edge may be from the lower currents found there.

Feed gaps widths $g_{feed} = \{1, 2, 3, 4\}$ mm were simulated and yielded S3 bandwidths of 3.97:1 (50-Ω ref.), 4.10:1 (50-Ω ref.), 4.21:1 (100-Ω ref.), and, 4.36:1 (100-Ω ref.) as the Slot 8 design below. One lesson learned from the fat dipole designs is the need for a taper near the feed region. The Slot 9 design smoothes out the abrupt transition in Slot 8 but keeps the feed gap $g_{feed} = 4$ mm. Figure 4-30 shows both geometries. The result is an improvement at the upper operating frequency to $f_u = 9.45$ GHz and a slight improvement in the bandwidth to 4.44:1 with $Z_o = 100\ \Omega$. Figure 4-31 shows the two impedances. The improvement at the upper frequency using the Slot 9 design ties the feed region to the higher frequency performance. When viewed as an isolated element, this design detail would be electrically small and have little meaning.

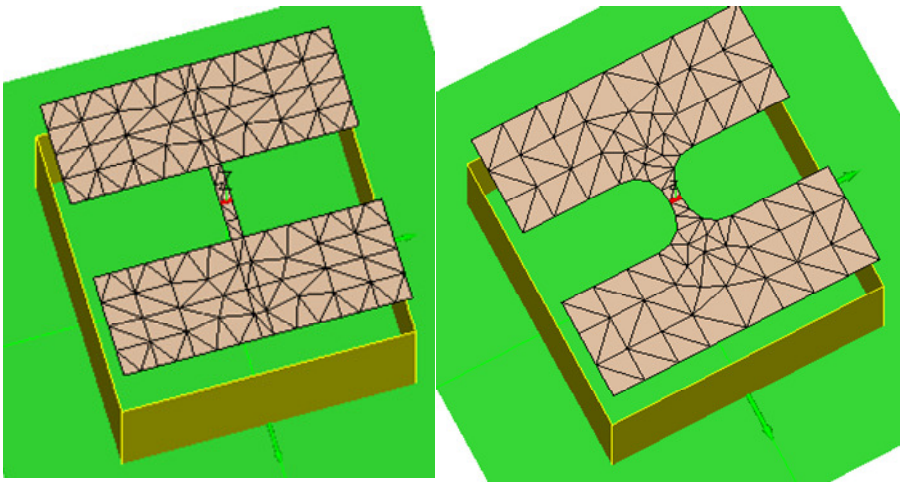

(a) (b)

Figure 4-30 – (a) Slot 8 and (b) Slot 9 element designs, with g_{feed} = 4 mm

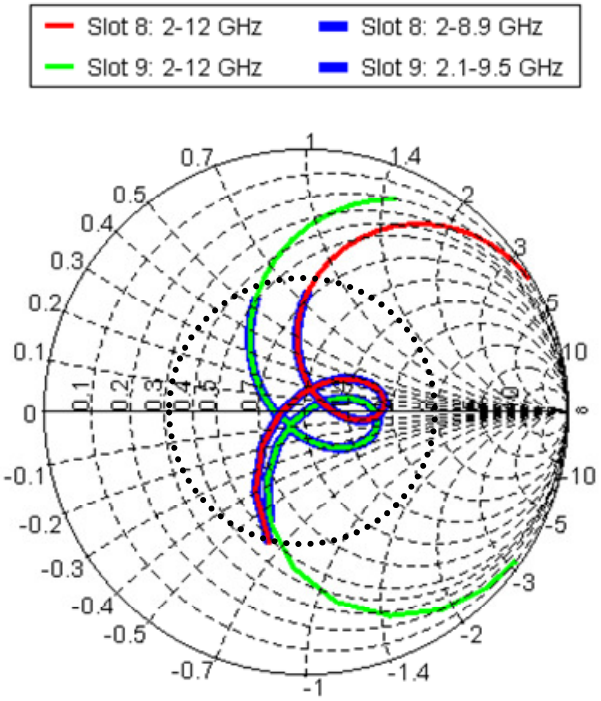

Figure 4-31 – Input impedance for Slot 8 and Slot 9 of Figure 4-30

4.5.3 Variations of Infinite Foursquare Element Designs

The Foursquare array designs start from the design presented in Section 4.3.4.2, which used the scaled dimensions from Buxton's best performing design [22]. Analyzed with the same unit cell

of $d_x \times d_y = 15 \times 15$ mm and a ground plane separation $h = 12$ mm, the starting Foursquare design of Figure 4-10 with a ground spaced at $h = 12$ mm produced an S3 bandwidth of 3.46:1. This design uses an intra-square spacing of $g = 0.34$ mm and an intra-element gap of $g_{element} = 2g_{cell} = 0.34$ mm.

The first variations considered two alternate gap distances that had the overall effect of reducing the bandwidth. Removing the inter-element gap ($g_{element} \to 0$) is notably a terrible choice and behaves in no way like the designs of the previous section. (It becomes simply like a narrowband dipole.) However, as previously shown, the original Foursquare design is not optimally tuned. The main problem may be a lack of the needed degrees of freedom in the geometry to properly tune the element within the infinite array. If the squares must remain square (to be called a "Foursquare"), only the gaps can be adjusted. The designer can optimize the separation to the ground plane, but this applies commonly to all designs. Alternative heights h from 6-14 mm in 2-mm increments yield some improvement; a ground separation of $h = 8$ mm resulted in the best bandwidth.

4.5.3.1 Foursquare Parasitic Modifications

One avenue to vary the Foursquare design is to use an asymmetry between the driven and parasitic elements, which immediately limits any design to a single polarization. The author explored such variations in [41] for finite arrays, and these were meant to shift the onset of a negative resistance downward in a 5×5 array. It is now clear that AGSW cause the negative input resistance. Alterations to the array shape simply shift the frequency where the AGSWs occur.

An extension beyond [41] is the diamond array. The geometry extends to the edge of the unit cell ($d_x \times d_y = 15 \times 15$ mm), and one must "reassemble" it in a repetitive pattern to visualize the shape of a cut diamond. Figure 4-32 shows equivalent representations, where the unit cells are matching in size. The left (a) is the shape within the unit cell, and the right (b) is how it appears as a single element in a larger array. The infinite diamond array achieves an impressive S3 bandwidth of 6.25:1 for $Z_o = 125\ \Omega$ (see Figure 4-34). The longer length along the element edge here explains to some extent the drop in the lower frequency to $f_L = 1.5$ GHz. This places

the largest element dimension (across the middle diamond bevels) at $L = 23.2$ mm, or 0.11λ at $f_L = 1.5$ GHz. The gaps $g = g_{element} = 0.34$ mm as in the initial Foursquare array design of Figure 4-10. As with the previous designs, the feed in FEKO® uses an edge voltage between the bottom-left and top-right halves of the Diamond element. Overall, the input impedance was slightly capacitive.

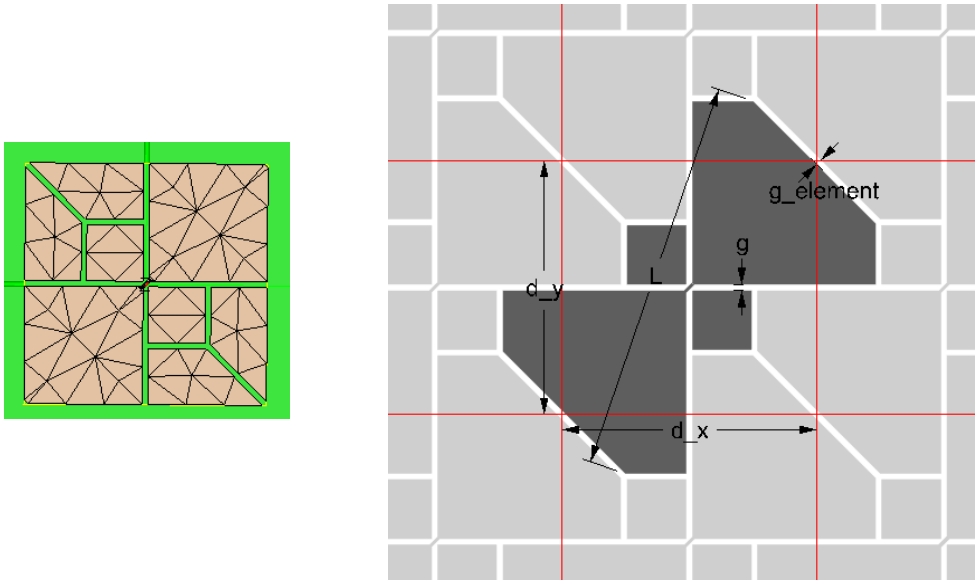

(a) (b)

Figure 4-32 – Diamond element design where (a) is a PostFEKO® representation within a single unit cell; and (b) is an "unwrapped" element with multiple unit cells shown. Height over ground *h*=12 mm.

Using similar approaches already presented, the top of the diamond element was widened to improve the input reactance. Since no meaningful empty space exists in this design, any widening of the diamond element results in a concurrent reduction in the size of the parasitic elements. In subsequent designs, as the parasitic elements became smaller, the bandwidth improves until the parasitic elements are completely removed. The parasitic elements appear to play no significant role. Figure 4-33 shows the resulting geometry which is an interwoven, or wrapped, bowtie array. The S3 bandwidth of the infinite Wrapped Bowtie array is 7.24:1 for a $Z_o = 125\ \Omega$ reference impedance, with a frequency range from 1.31-9.49 GHz. In the designs so far presented and others to come, the designs come from a seed design. Shape alterations at their outer and inner (near feed) areas adjust the reactance to make it undulate around $X_{in} = 0$.

Clearly, the loop on the Smith Chart in Figure 4-34 is much larger than other designs presented. One can see that over a large portion of the bandwidth the VSWR is between two and three.

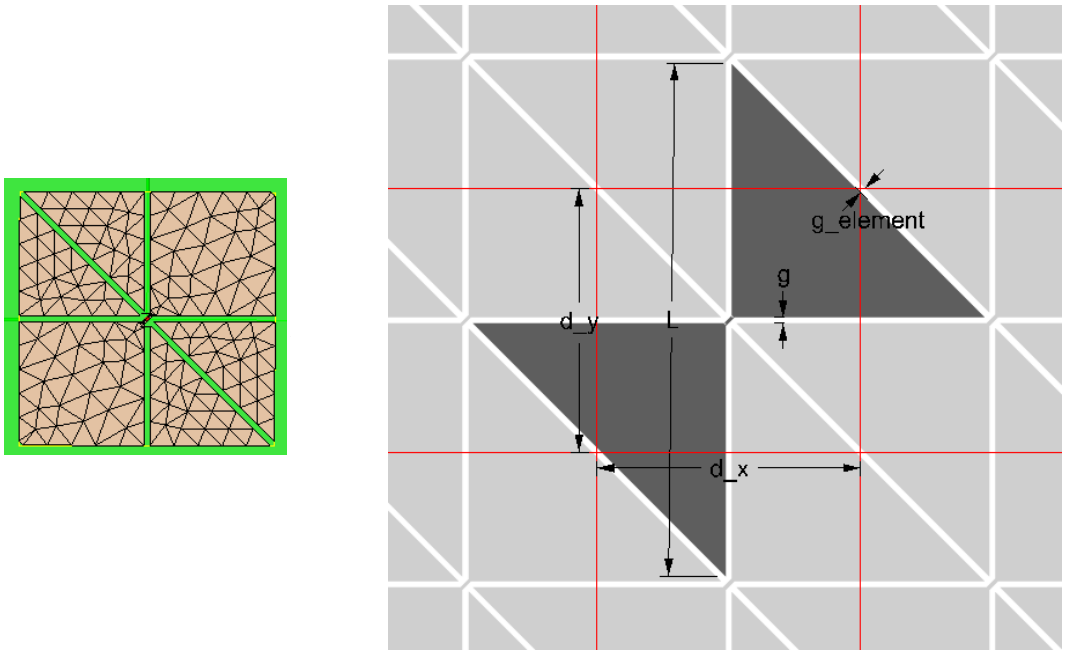

(a) (b)

Figure 4-33 – Geometry of the Wrapped Bowtie array where (a) is a PostFEKO® representation within a single unit cell; and (b) is an "unwrapped" element with multiple unit cells shown. Height over ground *h*=12 mm.

One realization from the process is the need to reduce the capacitance near the feed in most designs. This Wrapped Bowtie design differs somewhat, although it did show the value of extending the edge section as compared to the Diamond Array to adjust the tuning. The space near the feed it filled and no optimization step occurred for the feed region. Still, the Wrapped Bowtie array achieves the largest bandwidth of any infinite array design in this dissertation. (When placed into a finite array, this design obviously cannot be fully realizable at the array edges and may require a larger number of elements to exhibit all its traits.) One hypothesis is that the currents between elements are more continuous across the inter-element gaps and across many frequencies align between elements to form nearly a true current sheet. This appears at many frequencies, although not all. Figure 4-35 shows a representative example of the electric surface currents on the element at 7 GHz. These parallel currents differ from those on the initial Foursquare array, as shown in Figure 4-11, which has currents on the parasitic elements that circulate.

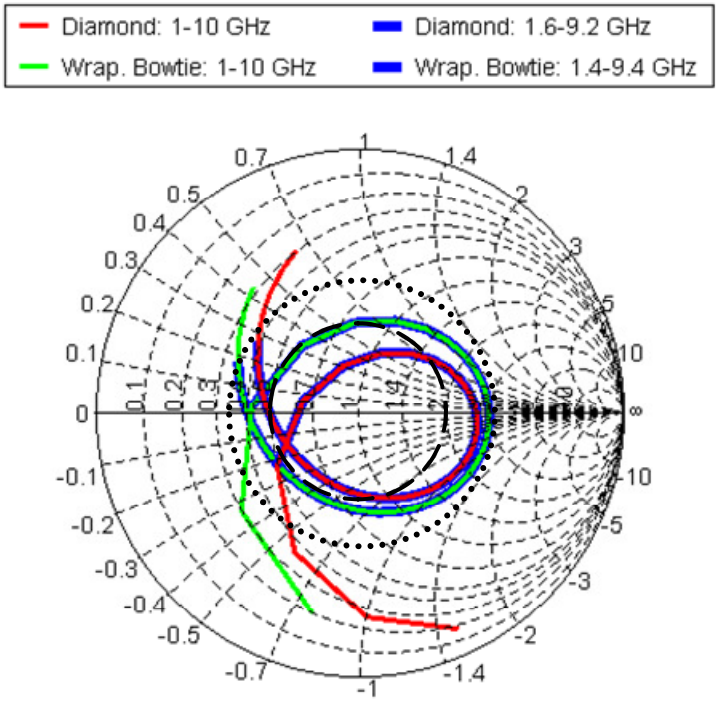

Figure 4-34 – Input impedance for the Diamond and Wrapped Bowtie designs of Figure 4-32 and Figure 4-33, respectively

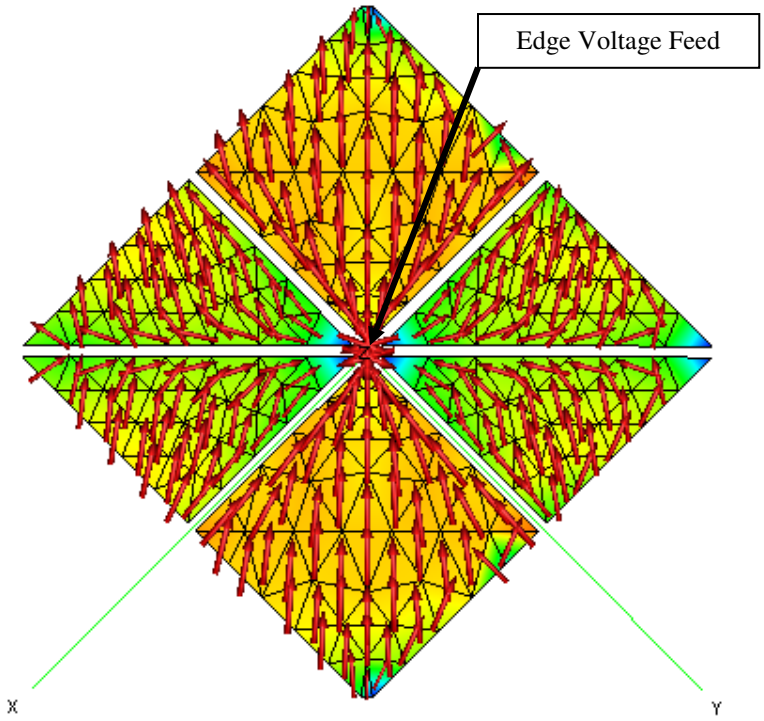

Figure 4-35 – Currents on Wrapped Bowtie of Figure 4-33 at 7 GHz

4.5.3.2 Rotated Foursquare Variations

A second, new degree of freedom in the Foursquare design is to rotate it 45° while keeping the unit cell unchanged. This rotation means the appropriate scaling down in the element size. Interestingly, scaling down the element size to 70% of the original results in an increase in the element resonance of only 8%.

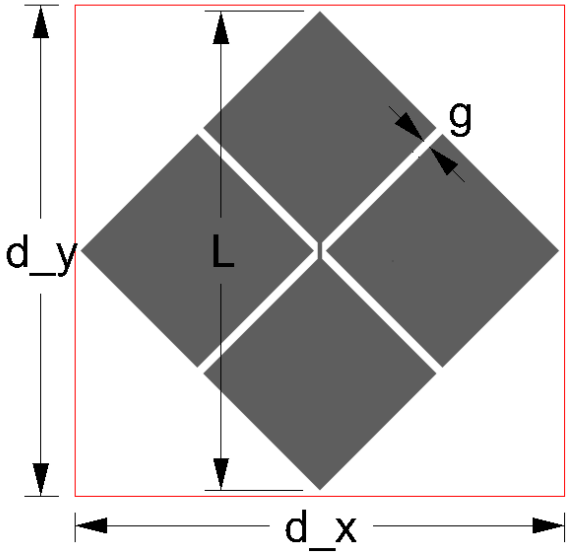

Dimension	Length (mm)
d_x	15
d_y	15
L	14.66
g	0.24
h	12

Figure 4-36 – Geometry of rotated Foursquare array

As with other designs thus far presented, this design requires more capacitance. Following past design approaches, the engineer can reduce the capacitance near the feed or between elements. The first modification, named Rot 2 and shown in Figure 4-37 with $w_x = 7.16$ mm, achieves an S3 bandwidth of 3.42:1 for a $Z_o = 100\ \Omega$. Rot 3 (not shown) uses a 50% wider intra-square gap g and achieves a 3.5:1 bandwidth, with the slight improvement solely at the upper end of the frequency band. This increase of the intra-square gap is a reduction in the influence of the parasitic elements. Following this idea, the Rot 4 design removes the parasitic elements entirely. This achieves an S3 bandwidth of 3.77:1 for $Z_o = 100\ \Omega$, but overall the reactance is still capacitive in much of the band. (See Figure 4-39.)

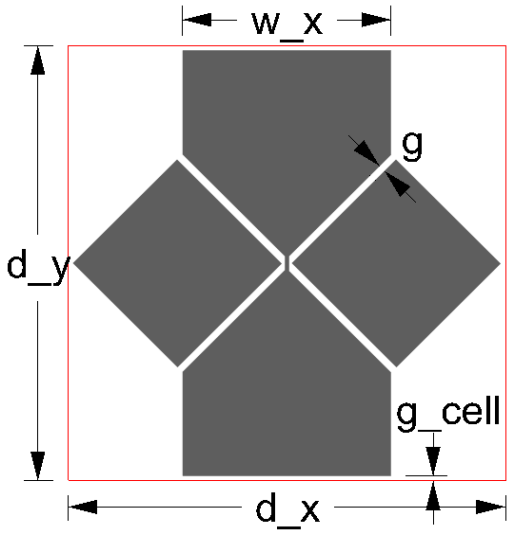

Dimension	Length (mm)
d_x	15
d_y	15
w_x	7.16
g	0.24
g_{cell}	0.17
h	12

Figure 4-37 – Rot 2 Element Design (Rot 4 design removes the parasitic elements).

The next geometric extension Rot 5 is a full bowtie element, without parasitic elements present, and not wrapped as shown in Figure 4-38(a). Normally, a bowtie antenna is exceptionally wideband, perhaps UWB. The radiation mechanism for an isolated bowtie antenna is from its λ/2 overall length at f_L and then from smaller regions of the continuous slot as frequency increases. The Rot 5 element is longer than the Rot 2-4 designs and achieves better low frequency performance. In this infinite array, it is an electrically small element throughout its operating band. This begs the question then, of what importance is the linear tapered slot around the feed of the Rot 5 design? Thus, the bowtie geometry yields to a trimmed geometry as Figure 4-38 shows and achieves an improved bandwidth.

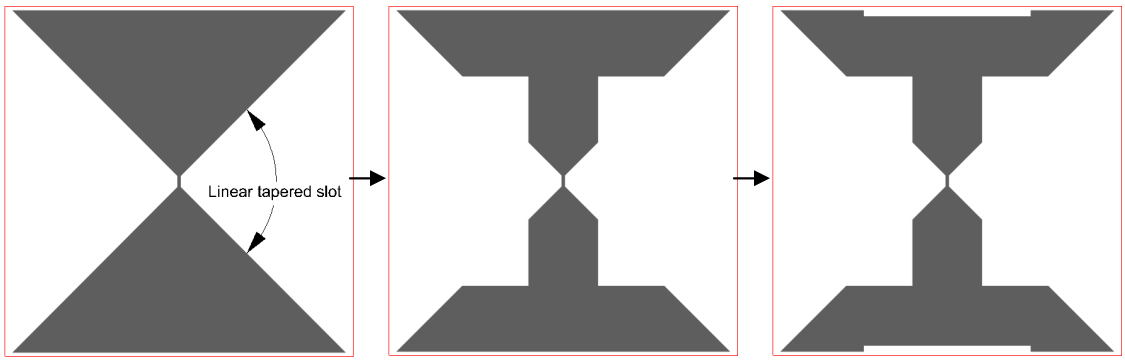

(a) (b) (c)

Figure 4-38 – Design progression from (a) Rot 5 to (b) Rot 6 and (c) Rot 7

The S3 bandwidth for the Rot 7 design is 4.64:1 for $Z_o = 150\ \Omega$. Additionally, for the first time, the Rot 7 design achieved a wide S2 bandwidth increase to 3.94:1 for $Z_o = 150\ \Omega$ (or 4.18:1 for $Z_o = 125\ \Omega$). Figure 4-39 shows a comparison of input impedances for the Rot 4 and Rot 7 designs, using $Z_o = 100\ \Omega$ and $Z_o = 150\ \Omega$, respectively. The Rot 7 design has increased input resistance, typically associated with wider bandwidths, as well as a more balanced reactance that undulates around $X_{in} = 0$. This results in the loop in Figure 4-39 being centered on the real axis. Admittedly, any bandwidth above 10 GHz will have the potential of developing grating lobes because $d > \lambda / 2$. Since this shape only occupies two pie quadrants of the unit cell, it is a starting design for the development of a circularly polarized array.

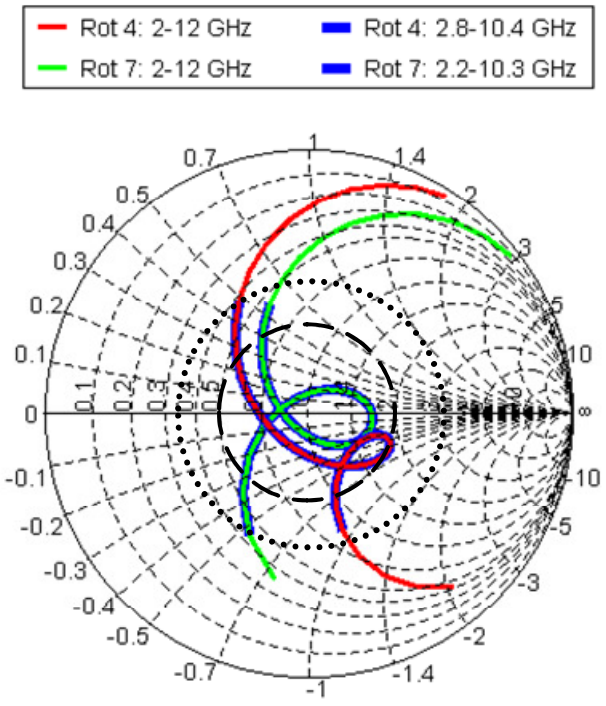

Figure 4-39 – Input impedance for Rot 4 and Rot 7 designs of Figure 4-37 and Figure 4-38(c), respectively

4.5.4 Infinite Circular Polarization Designs

This section takes two approaches. One is to expand the Rot 7 design found for linear polarization into a dual- or circular-polarization (CP) design. The other is to modify the basic Foursquare design directly to improve its CP performance. Because of some improved

performance from their starting points, the resulting designs are later then retooled back to linear polarization designs. Additionally, this section considers changes to the ground plane separation.

4.5.4.1 Rot 7 for Circular Polarization

The Rot 7 design is the starting point for developing a circularly or dual-polarized array design. Analyses use a geometrically rotated element and a 90° lagging phase feed to create a left-hand circularly polarized (LHCP) antenna array. Since patterns are not overly meaningful in infinite array simulations, only the impedance match is considered. Figure 4-40 shows the geometry named Dual 1, along with the unit cell. Because these simulations use induced edge voltages and those edges between positive and negative element sides are planar, the rotated element has a vertical offset of 0.1 mm. This slight alteration may require a later compensation.

The initial results show a limitation in the bandwidth as compared to the single polarization. The introduction of new physical structures of the element explains this bandwidth reduction. Whereas the Rot 7 design produces an S3 bandwidth of 4.64:1 with $Z_o = 125\ \Omega$, exciting dual polarizations limits the bandwidth to a S3 LHCP bandwidth is 2.99:1. The operating band is 2.25-6.73 GHz and shows limitations at the upper frequency range. Dual 1 is excited with two orthogonal edge voltages at the center of the element. These performance data represent a single port in the element, but there is good agreement between the two ports. Overall, there is a lack of capacitance in the element design.

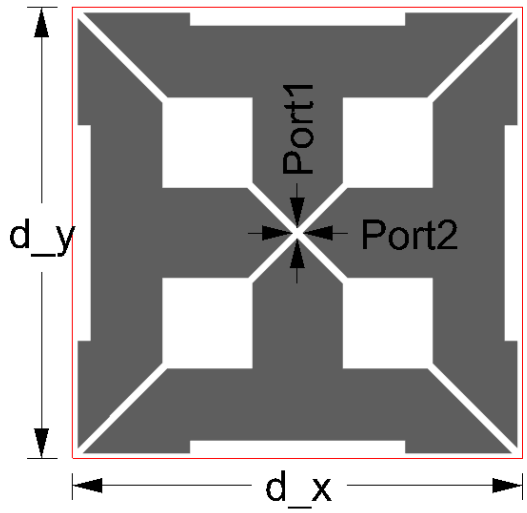

Figure 4-40 – Dual 1 element design

The Dual 1 design was altered along two main degrees of freedom: the connection area between elements at the corner of the unit cell and the configuration near the feed. Some parametric iteration led to the emergence of the Dual 8 design, and Figure 4-41 shows a slight curvature in the slot. The Dual 8 design achieved an S3 bandwidth of 3.57:1 for $Z_o = 100\ \Omega$. As an important observation, the replacement of the curvature along the slot with a straight line limited bandwidth.

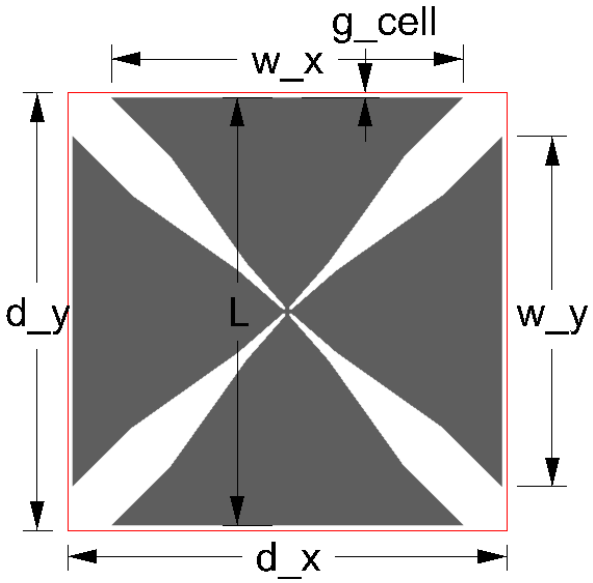

Dimension	Length (mm)
d_x	15
d_y	15
L	14.66
w_x	12.0
w_y	12.0
g_{cell}	0.17
h	12

Figure 4-41 – Dual 8 element design

Following the concept of a curved edge, Figure 4-42 shows the resulting Dual 14 design. It achieves an S3 bandwidth of 4.40:1 for $Z_o = 100\ \Omega$, ranging from 2.11-9.28 GHz. Figure 4-43 shows the input impedance. This design required an extension of w_x and w_y and a very close spacing g_{cell} to the unit cell. This spacing results in an inter-element gap $g_{element} = 2g_{cell} = 0.1$ mm for this array sizing, which may be problematic to manufacture at these frequencies. Although the impedance loop is not centered on the real axis of the Smith Chart, this design proved difficult to adjust further. Further adjustments to the length typically shifted the frequency range but did not expand the bandwidth measurably.

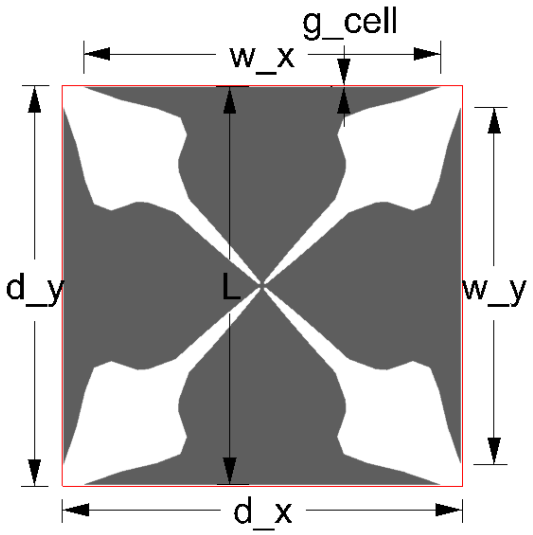

Dimension	Length (mm)
d_x	15
d_y	15
L	14.9
w_x	13.38
w_y	13.38
g_{cell}	0.05
h	12

Figure 4-42 – Dual 14 element design

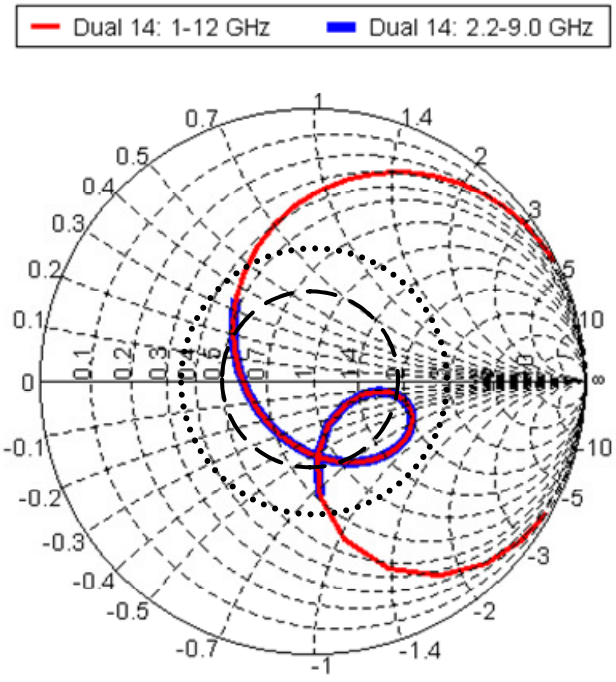

Figure 4-43 – Input impedance for Dual 14 (single port) of Figure 4-42

The progression from the Dual 8 design to the Dual 14 design shows the area near the feed region to control mostly the upper frequency performance. This fits with other work in this chapter. If the gaps become smaller, the lower frequency range is slightly affected, but the upper frequency drops substantially. The overall length and inter-element capacitance dominate the low

frequency range. If viewed as a single, isolated element, especially as a UWB antenna, these regions should be obvious. The lowest frequencies radiate from the entire structure, and the higher frequencies radiate from near the feed region. However, these designs are not sized in this manner. Here, the main axis length L of Dual 14 ranges from 0.1λ to 0.46λ across its operating bandwidth.

4.5.4.2 Modified Foursquare Design for Circular Polarization

Recall that for the single polarization case, the initial design achieved an S3 bandwidth of 3.46:1 for $Z_o = 100\ \Omega$. One recurring observation in tuning these designs is the need to reduce the capacitance near the feed. The FSQ_B design simply widens the gap around the feed g_{feed}, as seen in Figure 4-44, to confirm this trend. This design did not expand the bandwidth, but the location of the loop on the Smith Chart clearly moves to be on the real axis. Figure 4-45 shows the input impedance of the initial Foursquare and FSQ_B designs for comparison.

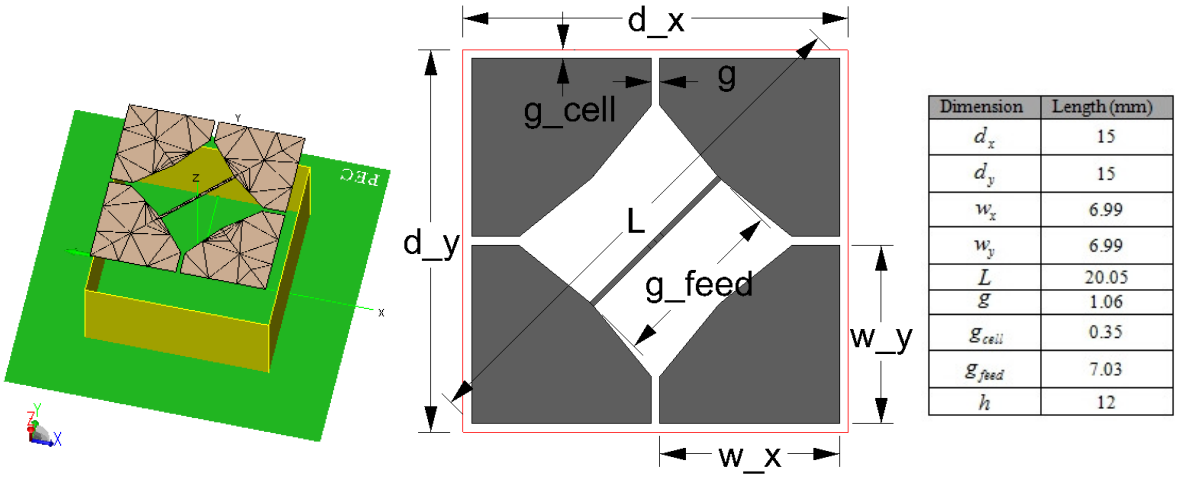

Dimension	Length (mm)
d_x	15
d_y	15
w_x	6.99
w_y	6.99
L	20.05
g	1.06
g_{cell}	0.35
g_{feed}	7.03
h	12

Figure 4-44 – FSQ_B element design, shown for single polarization: (a) isometric view from PostFEKO®; and (b) top-down view with dimensions

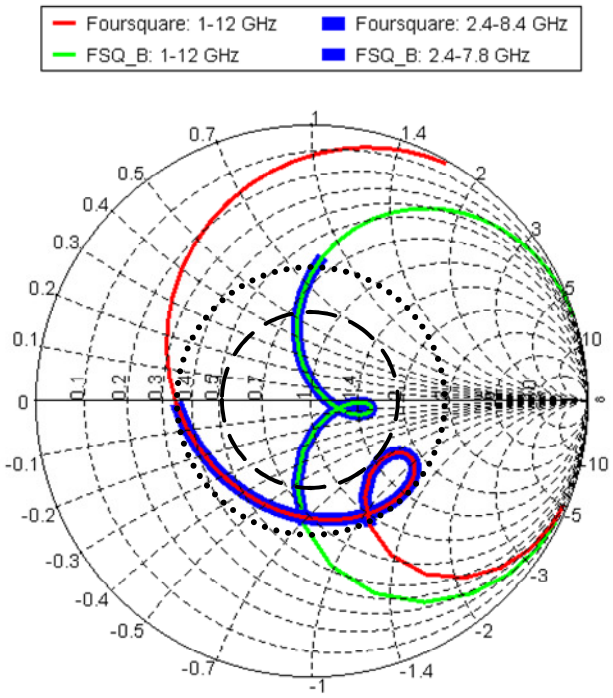

Figure 4-45 – Input impedances of the initial Foursquare array of Figure 4-10 and the FSQ_B array of Figure 4-44

The loss in the bandwidth in the FSQ_B design is at the upper frequency range. As with the slot designs, a tapering near the feed as seen in Figure 4-46 improves the bandwidth. The FSQ_D design results in an S3 bandwidth of 4.12:1 with a frequency range from 2.24-9.22 GHz and a $Z_o = 200\ \Omega$.

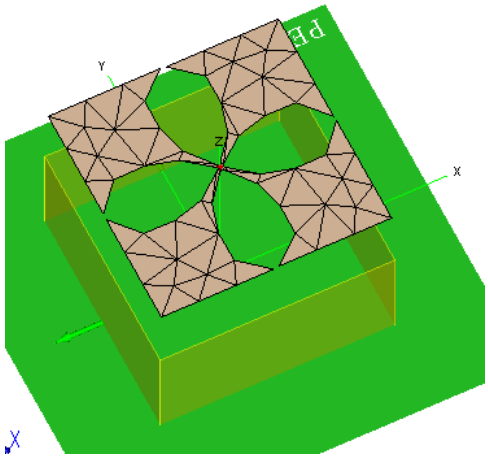

Figure 4-46 – FSQ_D element design

As with all designs in this section, the spacing to ground is $h = 12$ mm. To advance this design, this section next considers some adjustments to the spacing from ground. Figure 4-47 shows the input impedance for an alternative spacing of $h = 9.9$ mm compared to that for a $h = 12$ mm spacing. The overall S3 bandwidth only slightly improves to 4.17:1 with $Z_o = 200\ \Omega$, but the important result is the shift in the frequency range. The initial range of 2.24-9.22 GHz shifted upward to 2.45-10.22 GHz.

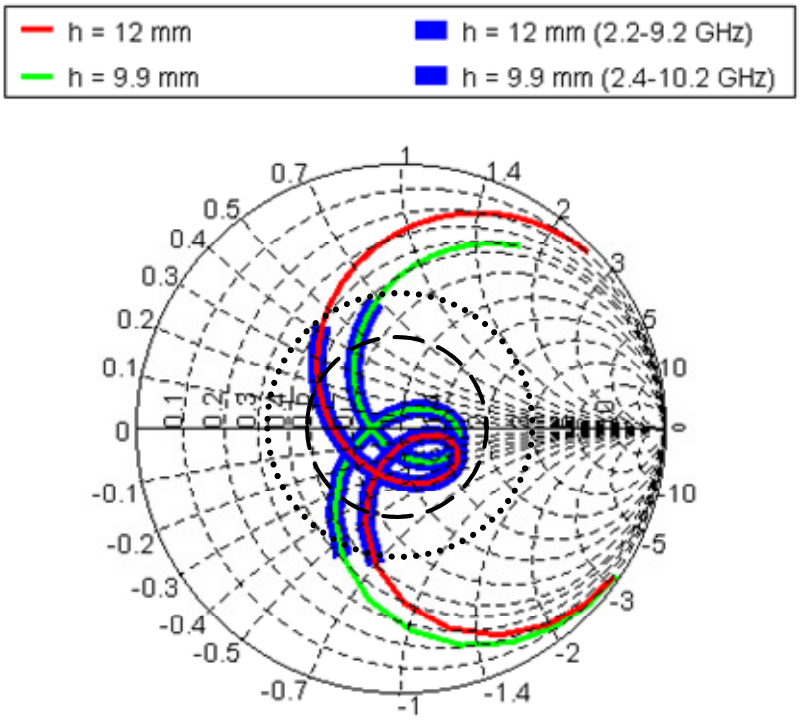

Figure 4-47 – Input impedances of FSQ_D design of Figure 4-46 for both *h*=9.9 and *h*=12 mm

The changes evident at the higher and lower frequencies for these two separations suggest some value to using a variable separation to ground along the element. A linear, vertical taper (not shown) from a center at $h = 9.9$ mm to the edge at $h = 12$ mm produces an S3 bandwidth of 4.34:1, ranging from 2.3-10.0 GHz. These results show a compromise between the two constant separation distances. Seeking to extend both ends of the frequency range, the next design shown in Figure 4-48 adds an exponential taper in $+\hat{z}$ from the center of the element. This design has $h = 10.5$ mm, a 16° angular rise, and a 1.5 exponential on the half-element radial distance (i.e., $r^{1.5}\tan 16^\circ$). This places the tip of the element at $z_{\max} = 20.08$ mm from ground. This taper increases the length of the element and, unsurprisingly, shifts the frequency range

downward. However, it also results in an increased S3 bandwidth to 4.85:1, ranging from 1.80-8.73 GHz, for a $Z_o = 200\ \Omega$. Figure 4-49 presents the input impedance for both the linearly and exponentially sloped elements. While deviating from a purely planar design, such designs may yet be within certain application tolerances.

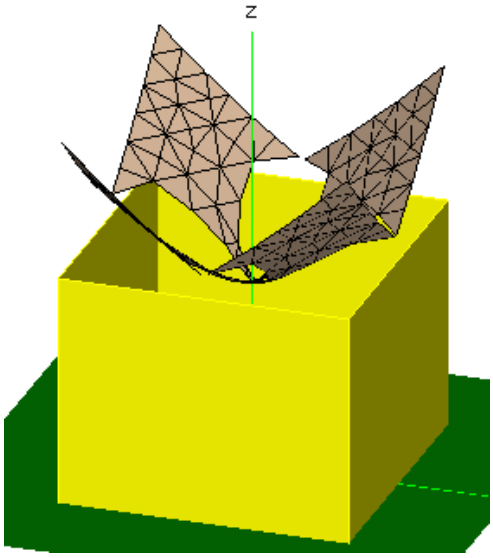

Figure 4-48 –Geometry of exponential tapered design with unit cell

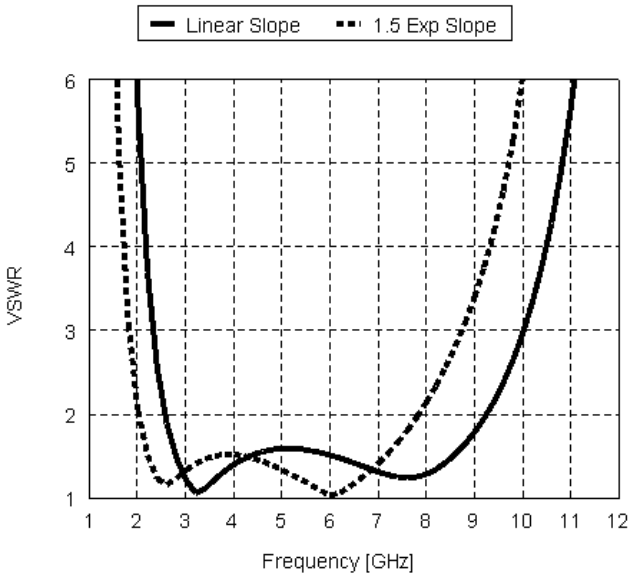

Figure 4-49 –VSWR of FSQ_D design with linear and exponential element tapers

4.5.5 Readdressing the Single Polarization Design

The terminal Dual 14 design for circular polarization has a substantially different S3 bandwidth of 4.4:1 from its dual Rot 7 starting point of 2.99:1. This section reconsiders the Dual 14 design for a linearly polarized array. Its removal (i.e., only half the Dual 14 design) results in an S3 bandwidth of 5.08:1, from 2.1-10.67 GHz, for $Z_o = 100\ \Omega$. Compared to the Dual 14 design, all bandwidth improvement occurs at the higher frequencies. With the orthogonal element removed, the mutual coupling effects change appreciably.

After observing a capacitive shift at the lower frequencies, w_x was extended to become the Rot 9 design of Figure 4-50. This expanded the S3 bandwidth slightly to 5.23:1 for the same $Z_o = 100\ \Omega$. Figure 4-51 shows how the impedance loop effect from the presence of the ground plane is nearly on the real axis of the Smith Chart. The larger size of the loop also shows that this is the best performing design in terms of S3 bandwidth, except for the less conventional Wrapped Bowtie design.

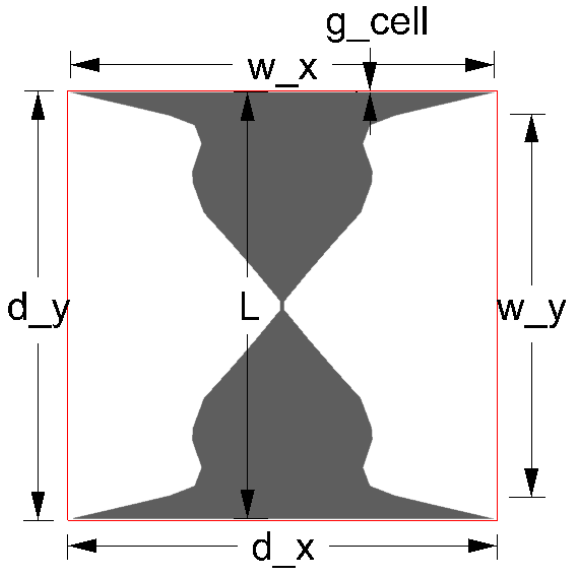

Dimension	Length (mm)
d_x	15
d_y	15
L	14.9
w_x	14.8
g_{cell}	0.05
h	12

Figure 4-50 – Rot 9 element design

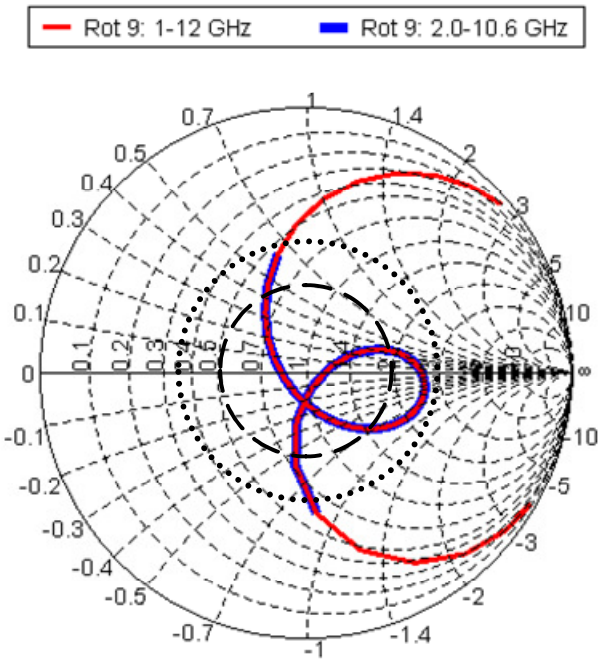

Figure 4-51 – Input impedance for the Rot 9 infinite array of Figure 4-50

4.5.6 Adjustments to Ground Plane Separation for the Rot 9 Infinite Array

Alterations to the height of the element over ground will tune the input impedance, as the ground plane appears purely reactive and tuning is primary an adjustment to negative reactance. Although this and the remaining analyses with the Rot 9 element use an $h = 12$ mm, a height of $h = 11$ mm aligns the center of the loop in the Smith Chart on the real axis. A height of 9 mm, however, results in the largest bandwidth. Figure 4-52 shows the changes to the input impedance for separations of 9, 11, and 12 mm. The crossover point of the loop moves along a line of nearly equal resistance, with the ground plane acting in a purely reactive fashion. Munk [1] details this relationship, but its use as a tuning mechanism is underemphasized. Further design details such as element supports and substrates, even of a low dielectric constant, will affect the exact tuning. An exact tuning is not necessarily important at this stage of the design as much as an understanding of the mechanisms.

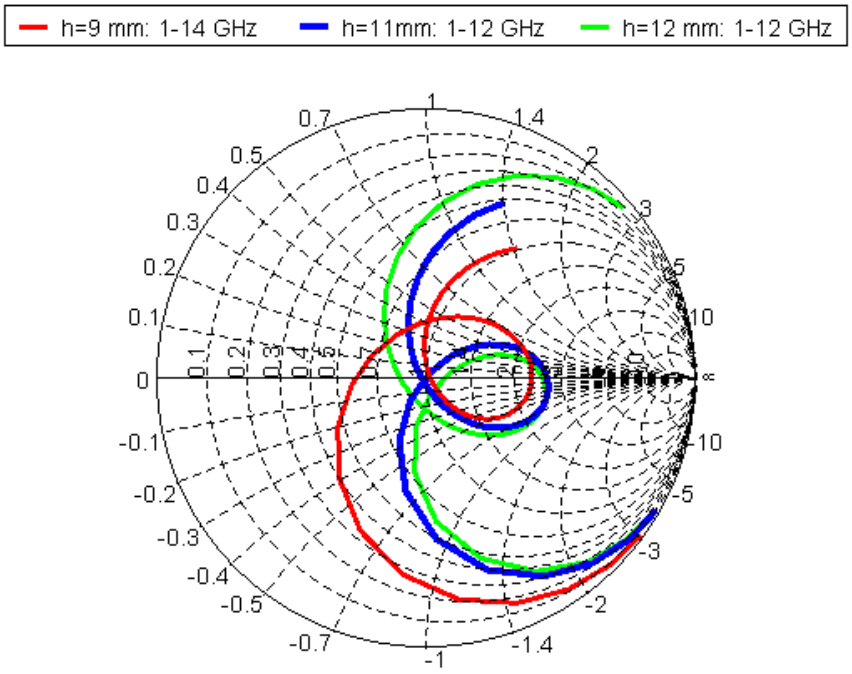

Figure 4-52 – Input impedances for the Rot 9 infinite array for ground separations *h*=9, *h*=11, and *h*=12 mm

Table 4-1 lists the changes to the minimum and maximum S3 bandwidth frequencies for varying heights over ground. Note that the widest bandwidth at $h = 9$ mm is also the closest electrical height to ground at f_L.

Table 4-1 – Summary of effects of height over ground

Heights over Ground	S3 Bandwidth	f_L (GHz)	Height at f_L	f_u (GHz)	Z_o
0.2λ /6 mm	4.61	4.04	0.0808λ	18.65	200
0.3λ /9 mm	5.55	2.47	0.0741λ	13.72	150
0.37λ /11 mm	5.35	2.14	0.0785λ	11.46	100
0.4λ /12 mm	5.23	2.04	0.0816λ	10.67	100
0.5λ /15 mm	4.73	1.87	0.0935λ	8.86	100

4.5.7 Summary of Infinite Array Designs

Table 4-2 – Summary of infinite array designs

Name	Shown in	S3 Bandwidth	f_L (GHz)	f_u (GHz)	Length parallel to feed (λ_L)	h (λ_L)	Z_o
Dipole Variations	**Linear Polarization**						
Initial Dipole	Figure 4-20	2.55	4.00	10.20	0.196	0.160	150
Modification 1	Figure 4-22	3.85	2.80	10.60	0.137	0.112	150
Modification 2	Figure 4-24	3.72	2.74	10.20	0.134	0.110	200
Modification 3	Figure 4-26	3.70	2.81	10.41	0.138	0.112	150
Long-Slot Variations	**Linear Polarization**						
Slot 1	Figure 4-28	3.12	2.96	9.24	0.145	0.118	75
Slot 2	Figure 4-28	3.64	2.54	9.24	0.124	0.102	50
Slot 3	Figure 4-28	3.70	2.28	8.43	0.112	0.091	50
Slot 8	Figure 4-30	4.36	2.04	8.90	0.100	0.082	100
Slot 9	Figure 4-30	4.44	2.13	9.45	0.104	0.085	100
Foursquare Variations	**Linear Polarization**						
Initial	Figure 4-10	3.46	2.45	8.47	0.169	0.090	100
Diamond	Figure 4-32	6.25	1.49	9.31	0.104	0.060	125
Wrapped Bowtie	Figure 4-33	7.24	1.31	9.49	0.091	0.052	125
Rot 2	Figure 4-37	3.42	2.81	9.61	0.137	0.112	100
Rot 4	Figure 4-37	3.77	2.75	10.38	0.134	0.110	100
Rot 7	Figure 4-38(c)	4.64	2.23	10.33	0.109	0.089	150
Rot 9	Figure 4-50	5.23	2.04	10.67	0.101	0.082	100
Foursquare Variations	**Circular Polarization**						
Dual 1	Figure 4-40	2.99	2.25	6.73	0.110	0.090	125
Dual 8	Figure 4-41	3.57	2.42	8.63	0.118	0.097	100
Dual 14	Figure 4-42	4.40	2.11	9.28	0.105	0.084	100
FSQ_B	Figure 4-44	3.31	2.33	7.72	0.157	0.093	100
FSQ_D (h = 12 mm)	Figure 4-46	4.12	2.24	9.22	0.155	0.090	200
FSQ_D (h = 9.9 mm)	Figure 4-46	4.17	2.45	10.22	0.169	0.098	200
FSQ_D (linear taper)	Not shown	4.34	2.30	10.00	0.164	0.092	200
FSQ_D (exp. taper)	Figure 4-48	4.85	1.80	8.73	0.173	0.072	200

4.6 No Ground Plane

Section 4.1 discussed the effects of the ground plane, and the ground plane is a realistic part of any planar array design. Most infinite array designs presented in this chapter are over an infinite PEC ground plane with spacing $h = 12$ mm. It is worth considering, however, the effects of the ground quantitatively on the designs presented. Based on the S3 bandwidth, this section evaluates the two best performing linear-polarization designs: the Wrapped Bowtie array and the Rot 9 array. Generally, engineers view the ground plane as a limiting factor to the bandwidth of the array.

4.6.1 Rot 9 Infinite Array Design, No Ground

The input impedance and VSWR for the Rot 9 infinite array show clearly the influence of the ground. The S3 bandwidth with a ground is 5.20:1, while without a ground it is 7.25:1 (see Figure 4-53). The bandwidth expansion is primarily at the upper frequencies ($f_{max} = 17.4$ GHz), where grating lobes occur without significant scanning. A loop still develops with no ground and may be the result of the curvatures along the element edge.

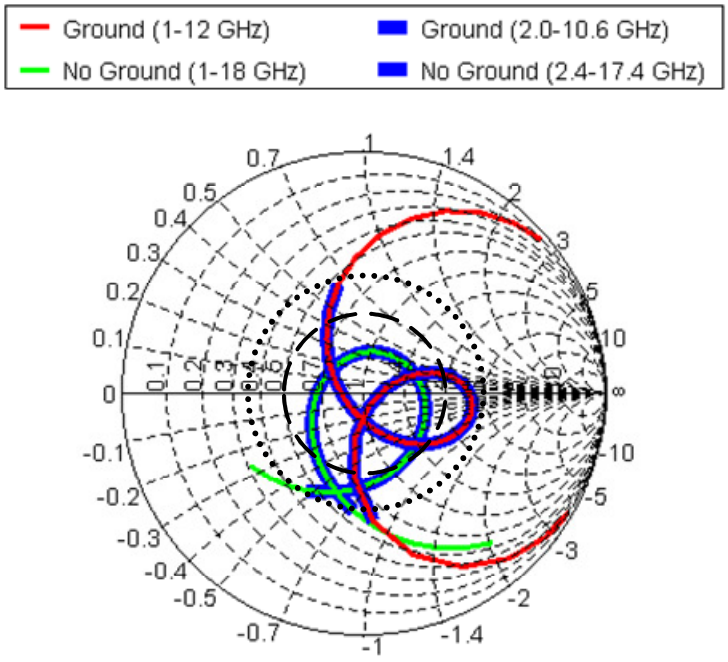

Figure 4-53 – Input impedances for the Rot 9 design of Figure 4-50, with and without a PEC ground plane

4.6.2 Wrapped Bowtie Infinite Array Design, No Ground

The input impedance and VSWR for the Wrapped Bowtie infinite array show clearly the influence of the ground. The S3 bandwidth with a ground is 7.25:1, while without a ground it is ~14:1. The bandwidth expansion is primarily at the upper frequencies, but it is interesting to note that the highest resistance within the S3 bandwidth is at the lowest frequencies, where it is also the most capacitive. The presence of the ground unquestionable diminishes the bandwidth of this array. It is interesting to note that the lower frequency point for both cases is the same, but a clear explanation is not immediately available.

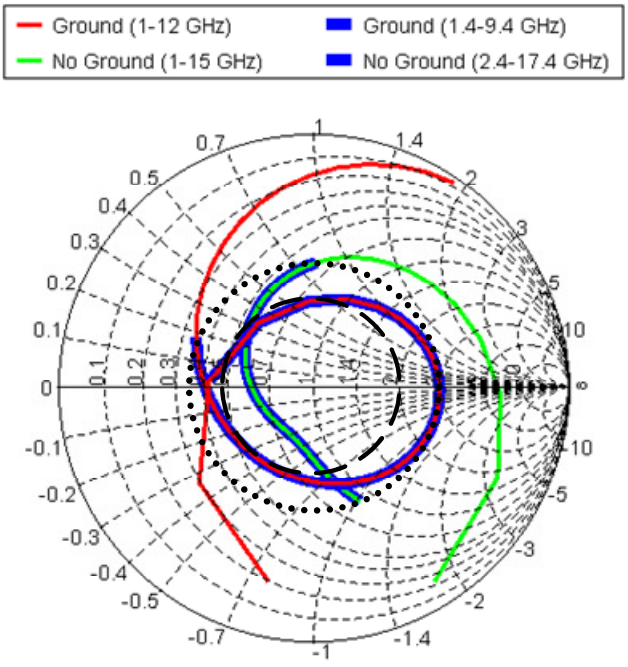

Figure 4-54 – Input impedances for the Wrapped Bowtie design of Figure 4-33, with and without PEC ground plane

4.7 Evaluation as Isolated Elements

The strong mutual coupling in the arrays presented from other researchers and the new designs are responsible for the wide bandwidths achieved. It binds the element to its nearest neighbors and effectively extends it beyond its physical size. The larger effective size provides the bandwidth extension downward in frequency. As a final check of these effects, this section evaluates the two leading linear-polarization designs (Rot 9 and Wrapped Bowtie) as single elements. These designs include backing ground planes, since that aspect is mostly an independent function on the antenna. The results are not surprising, but they are worth documenting. For comparison, the figures show the isolated element results alongside the infinite array results. Neither isolated antenna exhibits the bandwidth found in the corresponding infinite array. The isolated element has at least a 3:1 impedance bandwidth, but the frequency range covers the 12.5 GHz frequency where $h = 12\,\text{mm} = \lambda/2$ and a large null in the normal direction forms. This limits the S3 and pattern bandwidth to less than 2:1, whereas the infinite Rot 9 array exhibits a 5.23:1 S3 bandwidth.

The Rot 9 antenna from Figure 4-50, as a single isolated element, shows an input impedance that looks classically like an electrically small antenna over ground. The input resistance rises to only 25 Ohms when the element is $\lambda/4$ long near 5 GHz.

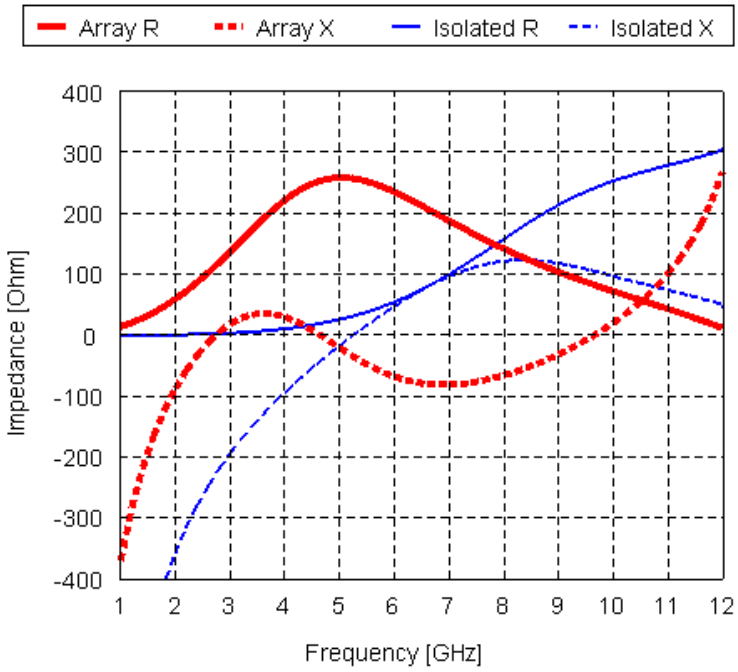

Figure 4-55 – Input impedance of the infinite Rot 9 array of Figure 4-50 and isolated Rot 9 antenna over a PEC ground

The Wrapped Bowtie from Figure 4-33, as a single isolated element, is no longer wrapped. It is simply a single bowtie antenna over an infinite PEC ground plane that extends beyond the unit cell. The results are comparable to a wideband antenna above about 8 GHz, but at the lower frequencies, the isolated antenna appears simply to be electrically small, with low resistance and a largely capacitive reactance. As with the isolated Rot 9 design, the isolated Wrapped Bowtie design forms a large null at 12.5 GHz where $h = 12\,\text{mm} = \lambda/2$. Taking the pattern and S3 bandwidths into account, the isolated Wrapped Bowtie element achieves under a 2:1 bandwidth, whereas the infinite Wrapped Bowtie array exhibited a 7.24:1 S3 bandwidth.

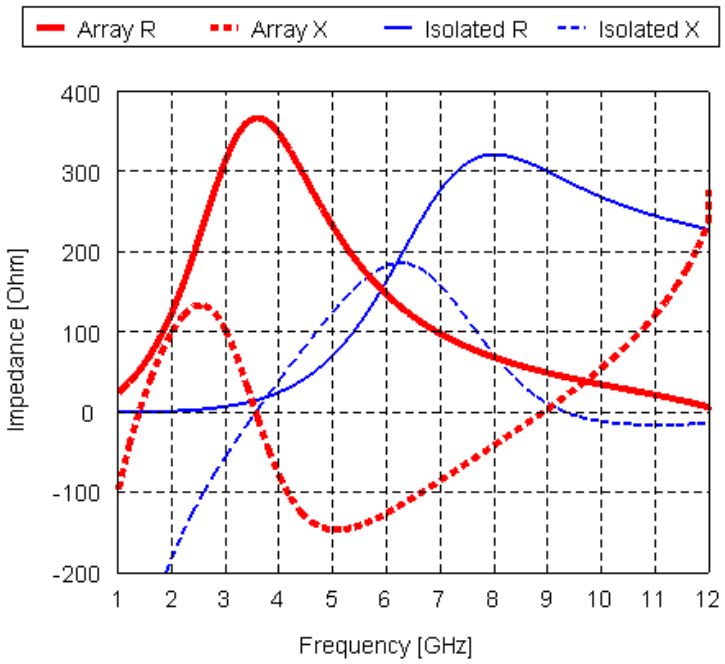

Figure 4-56 – Input impedance of the infinite Wrapped Bowtie array of Figure 4-33 and isolated Wrapped Bowtie antenna over a PEC ground

4.8 Infinite Array Scanning

For its performance as a linearly polarized antenna, this section considers both *H*-plane and *E*-plane scanning of the infinite Rot 9 array as shown in Figure 4-50, where inter-element spacing $d = 15$ mm. FEKO® allows for far-field patterns to be calculated as multiples of radiation from a single cell in the infinite array solution. The far-field patterns are for a 1×8 array for *H*-plane scanning and an 8×1 array for *E*-plane scanning. Array scanning has several benefits and expands the usability of arrays. Different phase progressions ψ are required across frequency as the electrical inter-element spacing changes. Figure 4-57 shows the required inter-element phase progression $\psi = kd\sin\theta$ for a desired scan angle θ_o. Scanning at an increment higher than the red line, which indicates a scan on the array surface at $\theta_o = 90^\circ$, forces the beam into invisible space. Likewise, if a grating lobe begins to transition from invisible space to visible space, the grating lobe may interfere and also force a condition of scan blindness where $R_{rad} \to 0$ and $|\Gamma| = 1$, as discussed in Section 2.6.1.

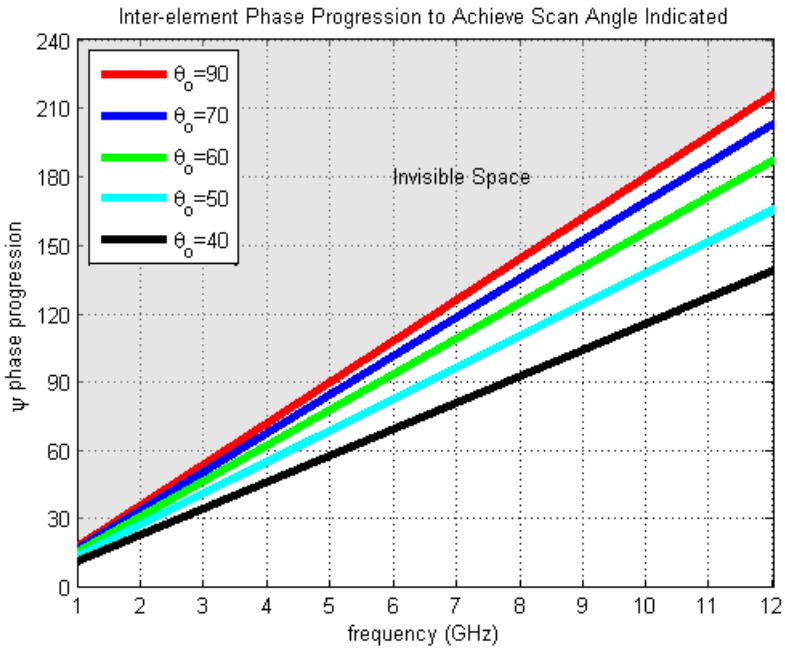

Figure 4-57 – Phase progressions ψ for various scan angles θ_o per $\psi = kd\sin\theta_o$, where $d = d_x = 15$ mm

4.8.1 *H*-plane Scanning in the Infinite Rot 9 Array

Following the scan progressions of Figure 4-57, the Rot 9 array was phased to steer the main beam in the intended directions of $\theta_o = \{40^\circ, 50^\circ, 60^\circ, 70^\circ\}$ for $\phi_o = \{0^\circ, 180^\circ\}$. The variable phase progression ψ across frequency keeps the main beam in visible space and comes close to the intended scan angle θ_o. The presence of the ground plane distorts the angle upwards somewhat, especially at higher scan angles. This error is evident in the array at mid-band at 5 GHz and when the inter-element spacing $d_x = d_y = \lambda/2$ at 10 GHz, in Figure 4-58 and Figure 4-59, respectively. For the 70-degree scan at 10 GHz, the appearance of a grating lobe is becoming evident as the back lobe grows.

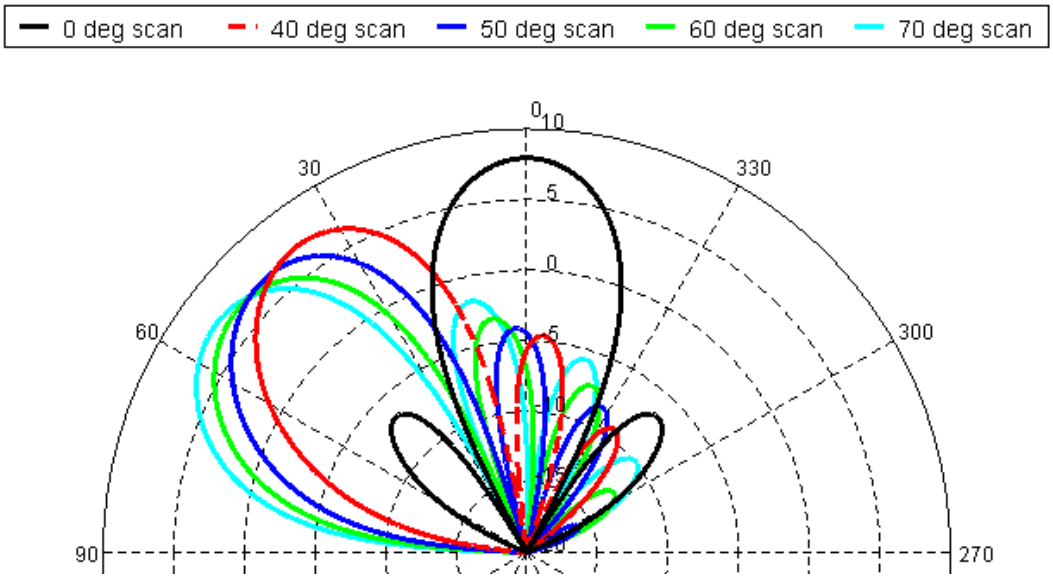

Figure 4-58 – *H*-plane scan pattern of the Rot 9 infinite array of Figure 4-50, expanded to 1x8 elements, at 5 GHz for θ_o = {0, 40, 50, 60, 70}° and d_x = 15 mm

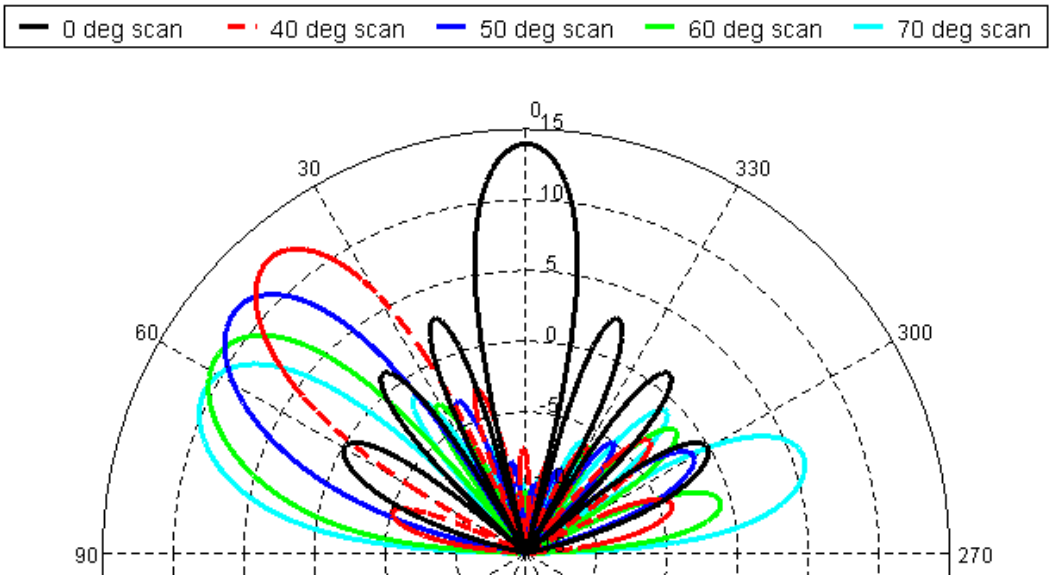

Figure 4-59 – *H*-plane scan pattern of the Rot 9 infinite array of Figure 4-50, expanded to 1x8 elements, at 10 GHz for θ_o = {0, 40, 50, 60, 70}° and d_x = 15 mm

This approach of varying the phase progression ψ with frequency shows how scanning to a given angle θ_o and $\phi_o = \{0^\circ, 180^\circ\}$ limits the bandwidth of the antenna. As the array scans from broadside, both the input resistance and input reactance show increased magnitudes, as seen in Figure 4-60 and Figure 4-61. Because a single element radiates only a fundamental dipole

mode in this array, this relationship trends to $1/\cos\theta$ for *H*-plane scans (increasing with scan angle) as Wheeler describes [24]. Scan blindness is evident in the input resistance (Figure 4-60) where $R_{in}=0$, as well as at frequencies where R_{in} dips abruptly. This dip, instead of reaching $R_{in}=0$ and although tightly sampled in frequency, indicates an increasingly diminished effect of scan blindness with scan angle θ_o. See Table 4-3 for a tabulation of scan blindness locations in the *H*-plane scans and comparisons to those in *E*-plane scans. In the 40- and 50-degree scans, the location of scan blindness is clearly tied to the upper operating frequency, and it therefore limits the array bandwidth.

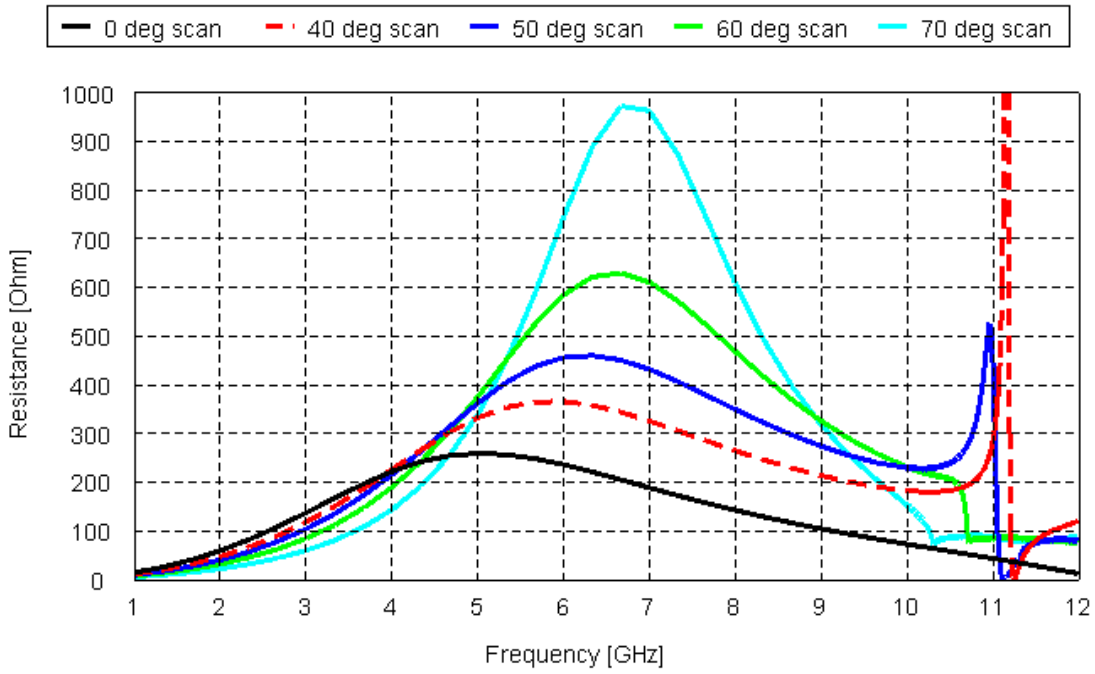

Figure 4-60 – Input resistance for *H*-plane scan of Rot 9 infinite array of Figure 4-50 for scan angles θ_o = {0, 40, 50, 60, 70}° and d_x = 15 mm

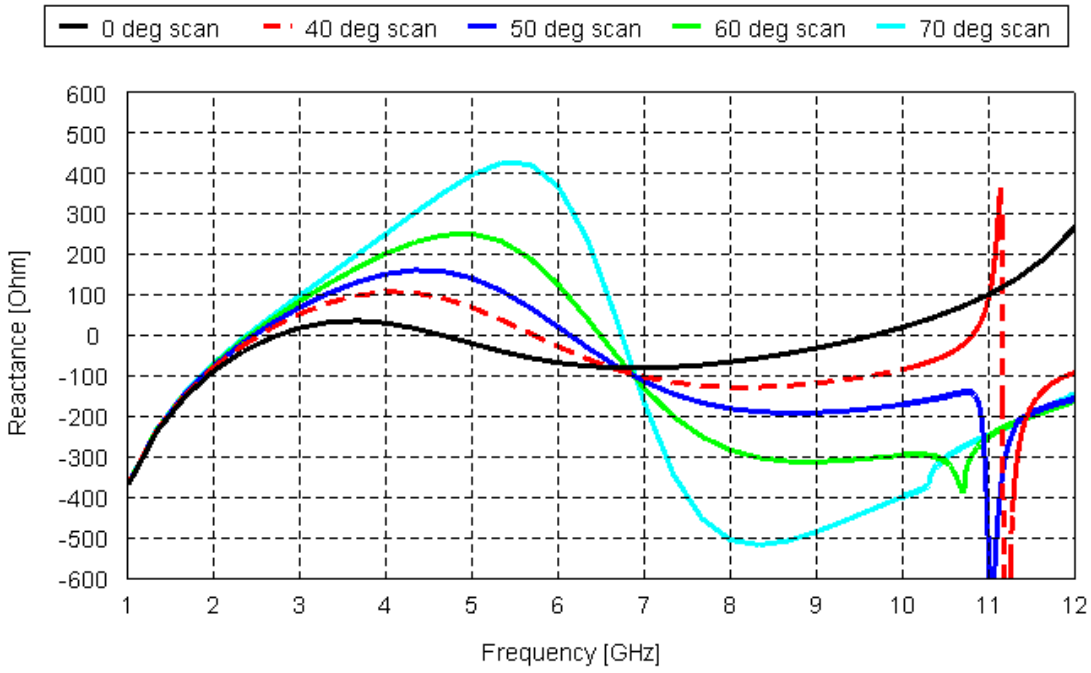

Figure 4-61 – Input reactance for *H*-plane scan of Rot 9 infinite array of Figure 4-50 for scan angles θ_o = {0, 40, 50, 60, 70}° and d_x = 15 mm

Scanning from broadside increases the input impedance of the element as its fields couple more tightly to the array surface. Likewise, the reactance develops larger maximum and minimum values are the fields become asymmetric in $\pm\hat{x}$, the direction of the *H*-plane scan. Both real and imaginary changes in the input impedance lead to an overall reduction in the bandwidth. The VSWR for these five scan angles is shown in Figure 4-62, with various reference impedances, although this variation with scan angle θ_o has some practical limitations. Therefore, the VSWR results are repeated in Figure 4-63 for a constant $Z_o = 100$ Ohms of the broadside scan. In either case of the reference impedance, the S3 bandwidths are substantially limited. See Table 4-3 for a tabulation of bandwidths possible.

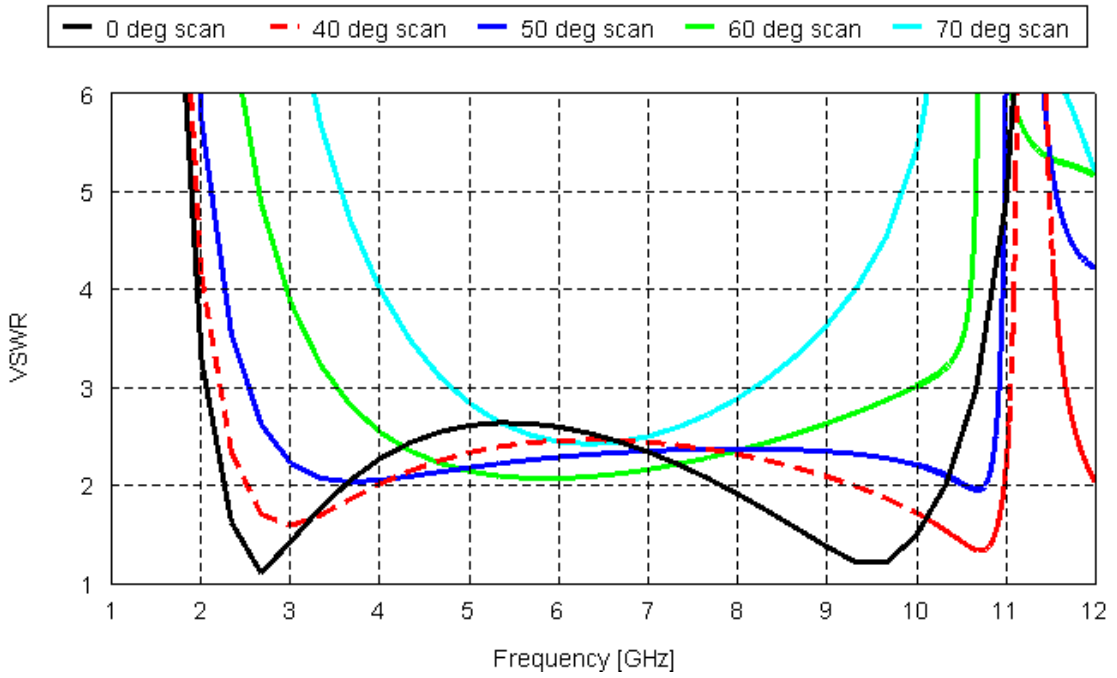

Figure 4-62 – VSWR for *H*-plane scan of Rot 9 infinite array for scan angles θ_o = {0, 40, 50, 60, 70}° and d_x = 15 mm. Reference impedances Z_o= {100, 150, 200, 300, 400} Ohms, respectively.

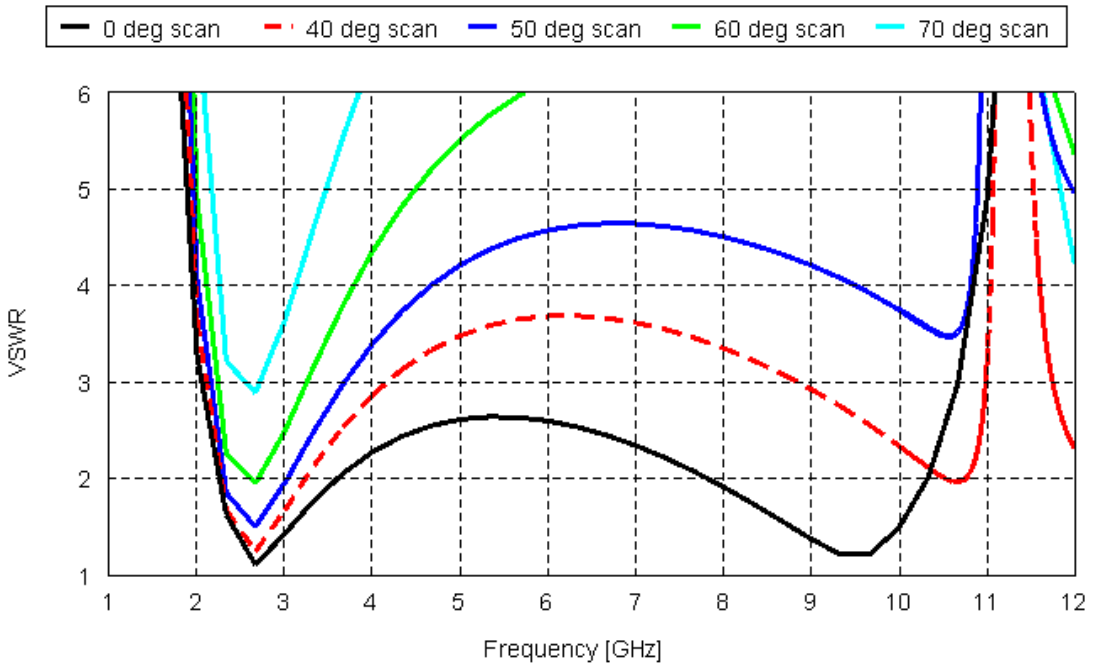

Figure 4-63 – VSWR for *H*-plane scan of Rot 9 infinite array for scan angles θ_o = {0, 40, 50, 60, 70}° and d_x = 15 mm. Reference impedances are constant at Z_o = 100 Ohms.

4.8.2 *E*-plane Scanning in the Infinite Rot 9 Array

Following the scan progressions of Figure 4-57, as with the *H*-plane scans, the Rot 9 array was phased to steer the main beam in the intended directions of $\theta_o = \{40^\circ, 50^\circ, 60^\circ, 70^\circ\}$ for $\phi_o = \{90^\circ, 270^\circ\}$. The variable phase progression ψ across frequency keeps the main beam in visible space and comes close to the intended scan angle θ_o, although with less accuracy than the *H*-plane scan. The presence of the ground plane distorts the angle upwards somewhat, especially at higher scan angles. The large capacitance and, therefore, charge between elements in the *E*-plane scan is likely the cause of the increased deviation in the scan angle. This error is evident in the array at mid-band at 5 GHz and when the inter-element spacing $d_x = d_y = \lambda/2$ at 10 GHz, in Figure 4-64 and Figure 4-65, respectively.

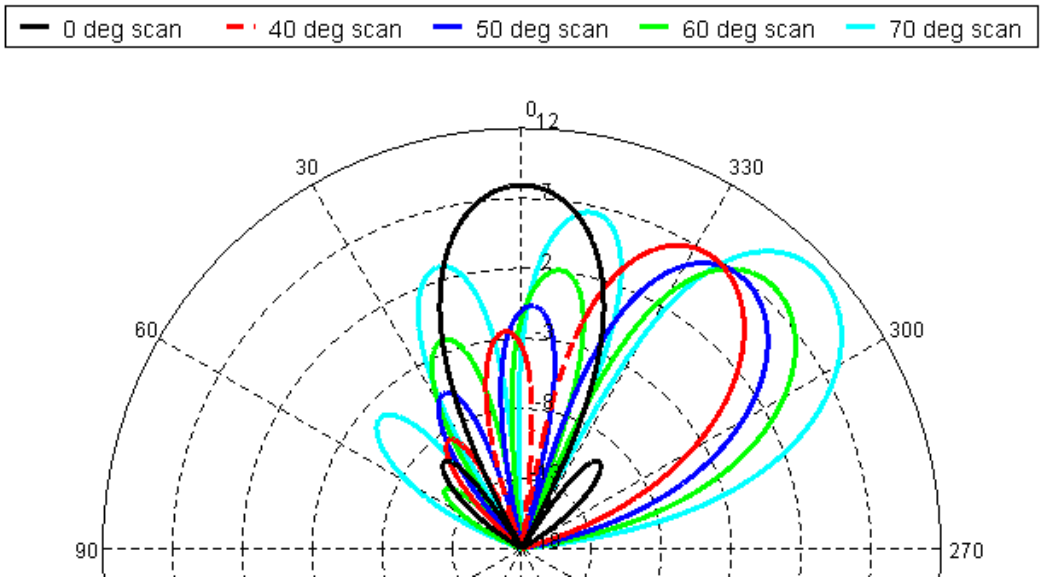

Figure 4-64 – *E*-plane scan pattern of the Rot 9 infinite array of Figure 4-50, expanded to 8x1 elements, at 5 GHz for θ_o = {0, 40, 50, 60, 70}°, ϕ={and d_x = 15 mm

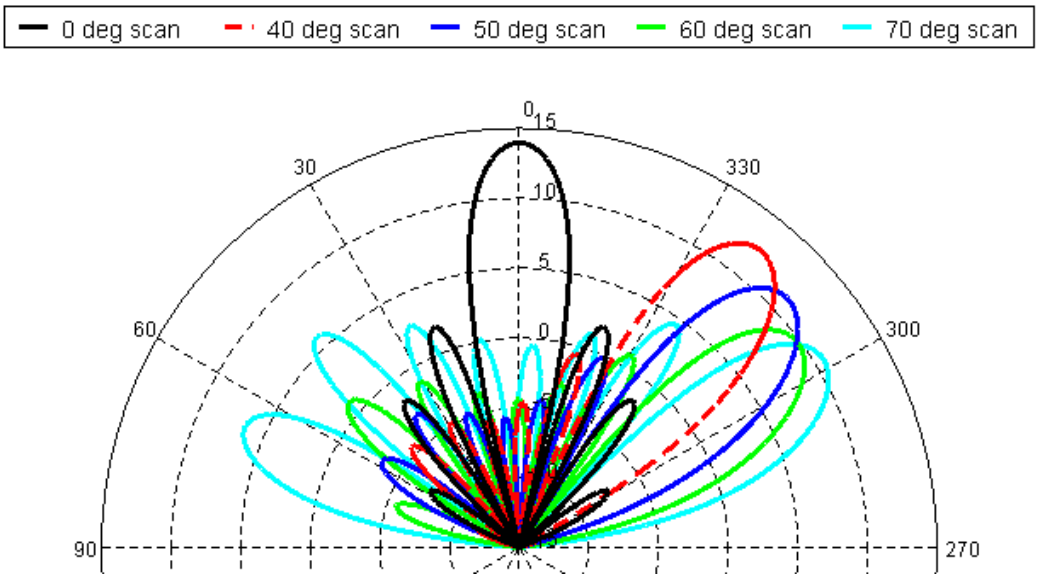

Figure 4-65 – *E*-plane scan pattern of the Rot 9 infinite array of Figure 4-50, expanded to 8x1 elements, at 10 GHz for θ_o = {0, 40, 50, 60, 70}° and d_x = 15 mm

This approach of varying the phase progression ψ with frequency shows how scanning to a given angle θ_o and $\phi_o = \{90^\circ, 270^\circ\}$ limits the bandwidth of the antenna. As the array scans from broadside, the input resistance shows a decrease in magnitude, as seen in Figure 4-66. Because a single element radiates only a fundamental dipole mode in this array, this relationship trends to $\cos\theta$ for *H*-plane scans (increasing with scan angle) as Wheeler describes [24]. Conversely, the input reactance of Figure 4-67 becomes more linear and appears to have less influence from the ground plane, which without scanning causes a slow oscillation about $X_{in} = 0$ Ohms. Scan blindness is not as evident in the input resistance (Figure 4-66) for the E-plane scan. The input resistance does not equal zero ($R_{in} \neq 0$), but abrupt changes are evident for $\theta_o = \{50, 60, 70\}^\circ$ scans. See Table 4-3 for a tabulation of scan blindness locations in the *E*-plane scans.

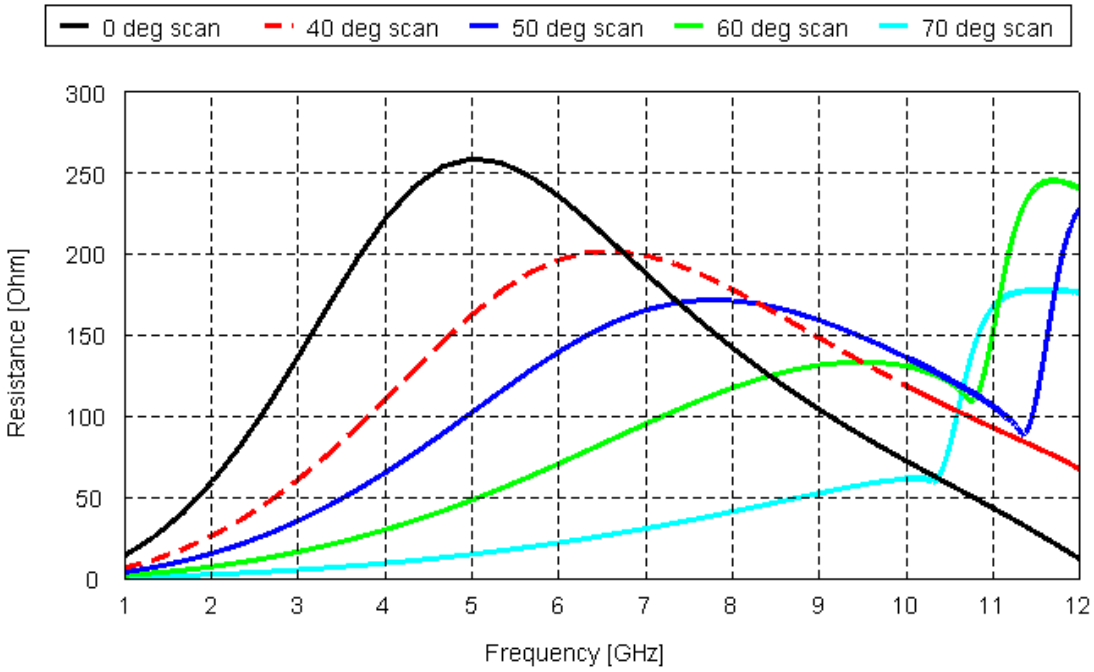

Figure 4-66 – Input resistance for *E*-plane scan of Rot 9 infinite array of Figure 4-50 for scan angles θ_o = {0, 40, 50, 60, 70}° and d_y = 15 mm

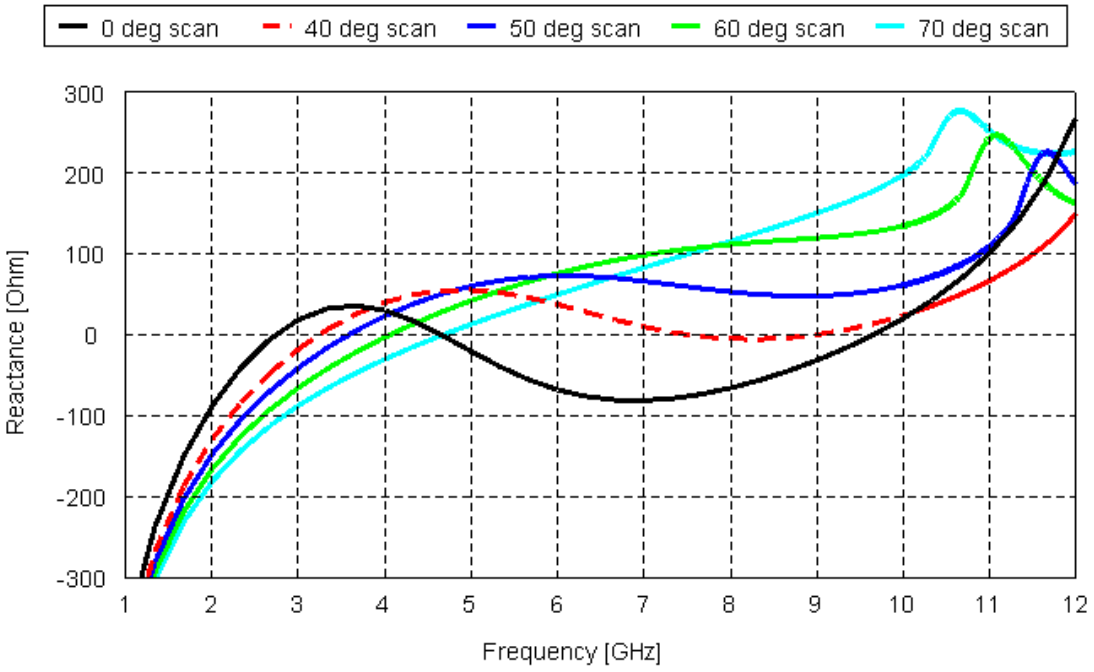

Figure 4-67 – Input reactance for *E*-plane scan of Rot 9 infinite array of Figure 4-50 for scan angles θ_o = {0, 40, 50, 60, 70}° and d_y = 15 mm

The changes in input impedance with the E-plane scan does not argue for increasing the reference impedance with scan angle. As such, Figure 4-68 presents the VSWR for the aforementioned scan angles using a constant $Z_o = 100$ Ohms. Scanning in the E-plane limits the bandwidth, like in the H-plane scan case, but a greater than 2:1 bandwidth is still available for the 60-degree scan. Table 4-3 summarizes the bandwidth results.

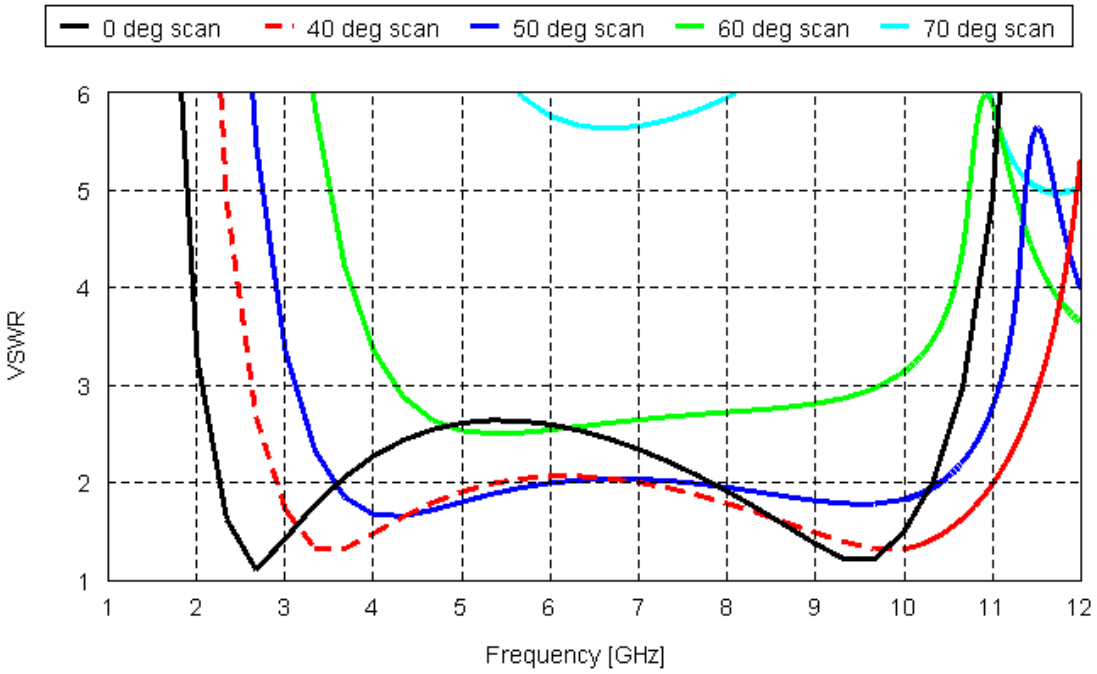

Figure 4-68 – VSWR for *E*-plane scan of Rot 9 infinite array for scan angles θ_o = {0, 40, 50, 60, 70}°, d_y = 15 mm, and Z_o = 100 Ohms for all angles.

4.8.3 Comparison of *H*-plane and *E*-plane Scanning in the Infinite Rot 9 Array

Table 4-3 summarizes data presented graphically from Figure 4-58 to Figure 4-68.

Table 4-3 – Comparison of *H*-plane and *E*-plane Scanning in the Infinite Rot 9 Array

Design Scan Angle θ_o (deg)	**Freq. of scan blindness** (GHz)	**Z_o** (Ω)	**S3 Band-width**	**S3 Band-width Z_o =100**	**D_{max} (dBi) at 5 GHz** (Note 1)	**First SLL** (dB)	**θ of D_{max}** (deg)	**D_{max} (dBi) at 10 GHz** (Note 1)	**First SLL** (dB)	**θ of D_{max}** (deg)
H-plane Scan (1x8 infinite elements)										
0	>12	100	5.23	5.23	7.9	-14.6	0	14.0	-11.1	0
40	11.26	150	4.98	1.97	7.1	-11.7	36	12.6	-15.6	41
50	11.13	200	4.30	1.74	6.8	-11.0	43	11.8	-15.0	50
60	10.70	300	2.84	1.47	6.7	-10	49	11.0	-13.7	58
70	10.31	400	1.71	1.16	7.3	-9.2	53	10.6	-12.0	63
E-plane Scan (8x1 infinite elements)										
0	>12			5.23	7.9	-17.7	0	14.0	-12.0	0
40	>12			4.35	7.0	-9.3	33	12.5	-9.3	39
50	11.35			3.54	6.9	-7.7	39	11.3	-7.7	47
60	10.76			2.30	8.0	-6.0	44	9.8	-6.0	54
70	10.33			-	11.0	-4.5	47	10.7	-4.5	58

Note 1: Using 1x8 elements for H-plane scans and 8x1 elements for E-plane scans, where the elements are multiples of the single element radiation in an infinite array solution

4.9 Summary of Design Methodology

The use of infinite array techniques, namely the Periodic Boundary Condition (PBC) in FEKO®, has been useful in developing wideband array designs with a relatively low computational burden. In this chapter, such techniques employed no phase shift in most cases and dictated that each element be the same[5]. Although they do not capture the edge effects and finite surface wave effects, infinite array techniques are extremely valuable for their speed and accuracy of the remaining design aspects. The design hypothesis moving into the next chapters is that design modifications to handle edge effects and array guided surface waves exist mostly independent of the element design.

The literature has illustrated that applying wideband element designs to tightly-coupled arrays is problematic. The presence of the ground is too far separated if the separation $h = \lambda / 4$

[5] The author's research in [40] with finite dipole arrays showed that alterations to the element shapes were not beneficial to stop the AGSW and limited bandwidth overall. A tapered increase in dipole length only served to shift the operating band such that a small frequency range was common to all elements.

at the center frequency, and this spacing will lead to pattern nulls at the upper frequencies. Using wideband elements also means inter-element spacings larger than $d > \lambda / 2$ at higher frequencies, leading to grating lobes. In short, electrically small to resonant-sized elements are a fundamental requirement in tightly-coupled arrays.

This chapter has presented the leading designs in tightly-coupled arrays and illustrated the development process for two new leading designs for infinite tightly-coupled arrays over a conducting ground plane. These, the Rot 9 and Wrapped Bowtie element designs, achieve VSWR < 3 impedance bandwidths of 5.23:1 and 7.24:1, respectively, in infinite array layouts. Table 4-2 summarized these and other progressive designs leading to them. These element designs attain a length of approximately $\lambda / 2$ at their upper frequency limits.

Because of these size limitations, the overarching task in the design is impedance tuning. The need was to shift the capacitive reactance upward, especially at the lower frequencies. A wide and tight capacitive gap to the adjacent cell and concurrently a reduced capacitance near the feed region mostly provided such tuning. In designs like the Foursquare array, this is difficult because of the lack of element width on each side of an inter-element gap (it is a point) and minimal degrees of freedom. Tuning and adjustments may improve operation at the upper frequency range. For a single polarization, parasitic elements appear to be detrimental as viewed from impedance, once the element is nearly optimized. This is likely due to the increased capacitance near the feed regions.

The chapter rounds out these two element designs by comparing their performance with and without a ground plane. From these comparisons, the guidance is clear. Engineers should clearly design tightly-coupled arrays with ground present from their earliest stages. The results without ground offer little direct insight for predicting the performance with a ground plane present. There are substantial differences in the performance of an element in an array versus when isolated, and comparably but not at as severe, a level of difference exists for the array without a ground plane as with one.

The design guidelines combined and evaluated over the many pages in this chapter are summarized in the below list. This chapter has consistently applied, and can now concisely state, these design steps.

1. Choose the operating frequency, VSWR requirement, and notionally choose a reference impedance Z_o
2. Select the desired polarization (linear or dual/circular)
3. Begin using infinite array techniques
4. Set the unit cell to be around $\lambda/2$ at the highest desired frequency
5. Set the ground plane spacing to be around 0.4λ at the highest operating frequency
6. Select a basic element design to meet the requirements, such as a dipole
7. Tune the element design, considering both feed region and inter-element factors.
8. Repeat until the design meets the appropriate resonance and impedance match for the given requirements. The center of the loop on the Smith Chart will typically lie on or close to the real axis on a Smith Chart. Alter the reference impedance as necessary.
9. Advance into semi-infinite array techniques to determine methods to control the array-guided surface wave (AGSW).
10. Move into finite array designs to complete design and confirm AGSW suppression techniques.

4.10 References

[1] B. A. Munk, *Finite Antenna Arrays and FSS*. Hoboken, NJ: Wiley-Interscience, 2003.

[2] S.-Y. Suh, "A comprehensive investigation of new planar wideband antennas," Ph.D. Dissertation, Bradley Dept. of Electrical and Computer Engineering, Blacksburg, Va., 2002.

[3] C. Craeye and X. Dardenne, "Efficient computation of the polarization characteristics of infinite and finite arrays of tapered-slot antennas," in *Phased Array Systems and Technology, 2003. IEEE International Symposium on*, 2003, pp. 377-382.

[4] W. Davis and T. R. Vogler, "Ultra-Wideband Antenna (UWBA) For Electronic Attack Aircraft (N06-040)," Virginia Tech, Blacksburg, VA10/06/2006 2006.

[5] W. Stutzman and G. Thiele, *Antenna Theory and Design*, 2nd ed. New York: John Wiley & Sons, Inc., 1998.

[6] D. W. Smith and P. E. Mayes, "Spiral antennas over a ground plane," in *Antennas and Propagation Society International Symposium, 1992. AP-S. 1992 Digest. Held in Conjuction with: URSI Radio Science Meeting and Nuclear EMP Meeting., IEEE*, 1992, pp. 2093-2096 vol.4.

[7] D. Shively and W. Stutzman, "Wideband planar arrays with variable element sizes," in *Antennas and Propagation Society International Symposium, 1989. AP-S. Digest*, 1989, pp. 154-157 vol.1.

[8] T. Teshirogi, *et al.*, "Wideband, high-gain printed antenna for uwb automotive radar," in *Antennas and Propagation Society International Symposium, 2007 IEEE*, 2007, pp. 3868-3871.
[9] R. C. Taylor, *et al.*, "Wideband phased array antenna and associated methods," US Patent #6512487, 2003.
[10] J. B. Pryor, "Suppression of surface waves on arrays of finite extent," M.S. Thesis, Dept. of Electrical and Computer Engineering, The Ohio State University, Columbus, Ohio, 2000.
[11] D. S. Janning, "Surface Waves in Arrays of Finite Extent," Ph.D. Dissertation, Dept. of Electrical and Computer Engineering, The Ohio State University, Columbus, OH, 2000.
[12] D. S. Janning and B. A. Munk, "Effects of surface waves on the currents of truncated periodic arrays," *Antennas and Propagation, IEEE Transactions on,* vol. 50, pp. 1254-1265, 2002.
[13] B. Munk, *Frequency Selective Surfaces: Theory and Design*. New York: Wiley-Interscience, 2000.
[14] J. Toon. (2006, 01/30/2007). 100-to-1 Bandwidth: New planar design allows fabrication of ultra-wideband, phased-array antennas. *physorg.com*. Available: www.physorg.com/news66491924.html
[15] P. Friederich, *et al.*, "A New Class of Broadband Planar Apertures," in *Proceedings of the 2001 Antenna Applications Symposium*, Allerton Park, Monticello, IL, 2001, pp. 561-587.
[16] A. Neto and J. J. Lee, "'Infinite Bandwidth' Long Slot Array Antenna," *Antennas and Wireless Propagation Letters, IEEE,* vol. 4, pp. 75-78, 2005.
[17] A. Neto and J. J. Lee, "Ultrawide-Band Properties of Long Slot Arrays," *Antennas and Propagation, IEEE Transactions on,* vol. 54, pp. 534-543, 2006.
[18] J. J. Lee, *et al.*, "Compact Light Weight UHF Arrays Using Long Slot Apertures," *Antennas and Propagation, IEEE Transactions on,* vol. 54, pp. 2009-2015, 2006.
[19] J. J. Lee, *et al.*, "A low profile 10:1 (200-2000 MHz) wide band long slot array," in *Antennas and Propagation Society International Symposium, 2008. AP-S 2008. IEEE*, 2008, pp. 1-4.
[20] J. M. Bell, *et al.*, "Ultrawideband Hybrid EBG/Ferrite Ground Plane for Low-Profile Array Antennas," *Antennas and Propagation, IEEE Transactions on,* vol. 55, pp. 4-12, 2007.
[21] J. R. Nealy, "Foursquare antenna radiating element," US Patent #5926137, 1999.
[22] C. G. Buxton, "Design of a Broadband Array Using the Foursquare Radiating Element," Ph.D. Dissertation, Bradley Dept. of Electrical and Computer Engineering, Virginia Tech, Blacksburg, VA, 2001.
[23] K. Takamizawa, "Analysis of Highly Coupled Wideband Antenna Arrays Using Scattering Parameter Network Models," Ph.D. Dissertation, Bradley Dept. of Electrical and Computer Engineering, Virginia Tech, Blacksburg, VA, 2001.
[24] H. Wheeler, "Simple relations derived fom a phased-array antenna made of an infinite current sheet," *Antennas and Propagation, IEEE Transactions on [legacy, pre - 1988],* vol. 13, pp. 506-514, 1965.
[25] M. Jones and J. Rawnick, "A New Approach to Broadband Array Design using Tightly Coupled Elements," in *IEEE Military Communications Conference*, 2007, pp. 1-7.

[26] B. Munk, *et al.*, "A low-profile broadband phased array antenna," in *IEEE Antennas and Propagation Society International Symposium*, 2003, pp. 448-451.
[27] W. F. Croswell, *et al.*, "Phased array antenna with edge elements and associated methods," US Patent #6876336, 2005.
[28] J. F. McCann, *et al.*, "An array of slot elements for wide scan angles and large bandwidth," in *IEEE Antennas and Propagation Society International Symposium*, 2006, pp. 3027-3030.
[29] J. F. McCann, "On the design of large bandwidth arrays of slot elements with wide scan angle capabilities," M.S. Thesis, Dept. of Electrical and Computer Engineering, The Ohio State University, 2006.
[30] T. E. Durham, *et al.*, "Wideband slotted phased array antenna and associated methods," US Patent #6977623, 2005.
[31] J. G. Maloney, *et al.*, "Fragmented aperture antennas and broadband antenna ground planes," US Patent #6323809, 2001.
[32] B. Thors, *et al.*, "Broad-band fragmented aperture phased array element design using genetic algorithms," *Antennas and Propagation, IEEE Transactions on,* vol. 53, pp. 3280-3287, 2005.
[33] H. Steyskal and D. Hanna, "Design aspects of fragmented patch elements for phased arrays," in *IEEE Antennas and Propagation Society International Symposium*, 2007, pp. 141-144.
[34] J. J. Lee, *et al.*, "A low-profile wide-band (5:1) dual-pol array," *Antennas and Wireless Propagation Letters, IEEE,* vol. 2, pp. 46-49, 2003.
[35] J. J. Lee, *et al.*, "Wide band long slot array antennas," in *IEEE Antennas and Propagation Society International Symposium*, 2003, pp. 452-455.
[36] A. Neto and J. J. Lee, "Reply to Dr. Hansen's comments on 'Infinite bandwidth' long slot array antenna," *Antennas and Wireless Propagation Letters, IEEE,* vol. 4, p. 497, 2005.
[37] E. C. Jordan and K. G. Balmain, *Electromagnetic Waves and Radiating Systems*, 2nd ed. Englewood Cliffs, NJ: Prentice-Hall, 1968.
[38] R. C. Hansen, "Comments on 'Infinite Bandwidth Long Slot Array Antenna'," *Antennas and Wireless Propagation Letters, IEEE,* vol. 4, p. 497, 2005.
[39] S. J. Franson and R. W. Ziolkowski, "Method of Simulation of Closely Spaced, Finite, Periodic, Radiating or Reflecting Structures, Including Metamaterials," presented at the 22nd Annual Review of Progress in Applied Computational Electromagnetics, Miami, FL, 2003.
[40] T. R. Vogler and W. Davis, "Surface Waves in Medium-Sized, Tightly Coupled Planar Arrays," presented at the USNC-USRI National Radio Science Meeting, Boulder, CO, 2009.
[41] T. R. Vogler and W. Davis, "Parasitic Modifications to the Finite, Foursquare Antenna Array," presented at the USNC-USRI National Radio Science Meeting, Boulder, CO, 2008.

CHAPTER 5

Designs of Semi-Infinite Tightly-Coupled Arrays

Chapter 4 presented the development and designs for numerous infinite tightly-coupled arrays. It related the designs to their impedance bandwidths and their interaction with a backing ground plane. These infinite-array techniques are beneficial because of their relatively low computational burden, but infinite-array simulations do not capture several physical phenomena that occur in real, finite arrays. As detailed in Chapters 2 and 3, the asymmetry of array boundaries affects tightly-coupled arrays through edge currents and, at certain frequencies, the array-guided surface wave (AGSW) currents. Infinite techniques do not capture these effects.

Chapter 5 predominantly tackles the issues arising from array boundaries and the AGSW, and their distortions to the active impedance across the array. Compensation for the AGSW relies on adding real loading to the array, and semi-infinite techniques allow for this development without the computational burden of finite array simulations. Semi-infinite array designs are still computationally manageable and are an intermediate step to finite array designs. Within FEKO®, these semi-infinite array analyses use the periodic boundary condition (PBC), but they are limited to one dimension. (The infinite array simulations used the PBC in two dimensions.) Semi-infinite means finite in one dimension, say finite in $\hat{x}$ and infinite in $\hat{y}$, if the array lies predominantly in the *xy*-plane. As in the infinite array analysis, the $\hat{z}$ direction is finite and $+\hat{z}$ is typically the direction normal $\hat{n}$ to the array face.

This chapter analyzes the leading designs from Chapter 4: the Rot 9 and the Wrapped Bowtie elements. Finite directions of both $\hat{x}$ and $\hat{y}$ are separately considered for the Rot 9

design. Since the feed in the infinite Wrapped Bowtie array was oriented diagonally between $\hat{x}$ and $\hat{y}$, this chapter rotates its geometry to consider strictly *E*-plane and *H*-plane finite dimensions. This chapter considers both unloaded and loaded forms of these array designs, with spatial Fourier analyses of the AGSW, and considerations for the impact of radiation efficiency and far-field radiation patterns. Different coupling and, by extension, different edge effects are expected when the finite limit is parallel or perpendicular to the feed direction. Additionally, this chapter investigates a conformed array as a method to radiate off some power of the AGSW, which would reduce the loading requirements otherwise needed.

Lastly, this chapter presents some work on array scanning with the Rot 9 design. Scanning results from Chapter 4 left questions regarding source impedances (and their effect on input impedance) and the verification of far-field radiation at low frequencies, where R_{in} became very small in infinite array scanning. Chapter 6 carries forward the designs from this chapter with finite limits in the direction of the scan and considers several issues with feeding the array.

5.1 AGSW Suppression Methods

Section 2.6.2 detailed the nature of the array-guided surface wave (AGSW) and the use of the Discrete Fast Fourier Transform (DFFT) to analyze it. The author's previous work [1] with finite arrays explored methods to control the AGSW, with the initial hypothesis that the element shapes could sufficiently disrupt the AGSW. Modifications to the element design can shift the frequency where the AGSW appears, but it was not clear that the degrees of freedom in the design can shift the AGSW to outside any reasonably wideband frequency range. Continued work in [2] considered finite arrays of dipole variations in a parallel feed arrangement. (Figure 2-3 shows this geometry.) This work contained several options to suppress or control the AGSW including: tapering the lengths of elements along the array, inserting randomness into the placement of the elements away from center in their periodic (unit) cells, and altering the array size. None of these methods proved to have substantial value over a large frequency range. The first enacted different resonant points within the array, and while possibly providing a radiation region in different portions of the array across a wide frequency band, it came without the directivity benefits of arrays. The insertion of randomness appeared to create weaker periodicities but did not show a meaningful improvement to the active element impedances

across the array. Alterations to the array length produced no meaningful distinctions and matches the descriptions of edge effects and the AGSW detailed in Chapter 2. The AGSW is not a function of the array size, and it acts mostly like a standing wave on the array. The only exception is the need to have an array large enough, with its dependencies on mutual coupling, to support the wave. While a two or three element array may not support an AGSW, a 3×3 Foursquare array is sufficiently large and had sufficient mutual coupling to support the AGSW.

The only meaningful way found to suppress the AGSW in a planar array is through the inclusion of loss in the design. Previously cited work by Pryor, Munk, and Janning [3-5] support the idea that the introduction of ohmic losses into the array is the main method to control the AGSW. These losses may be distributed, such as from lossy conductors or dielectric materials, or by loading the elements in series with resistors. Part of this latter option could include source generator resistance in arrays where each element has an independent feed.

Another method to controlling or dissipating the AGSW involves conforming the array from a strictly planar shape. As Pryor [3] showed for radiation backscattering, conforming the array along the direction of the AGSW allows some of the energy in the AGSW to radiate away from the array surface much in the same way as the creeping wave in the Uniform Theory of Diffraction (UTD) techniques. This radiation removes real power in the same way resistive loading does. Section 5.6 investigates how effective such a technique is for active arrays, and specifically the Rot 9 design. By conforming the array and ground plane (where the separation to ground remains the $h=12\,\text{mm}$ used in Chapter 4), less resistive loading can be expected to control the AGSW. However, conforming concurrently widens the beamwidth, and the peak gain drops. An evaluation considers the overall effects from both loading and conforming approaches to determine if conforming has any practical value. For practical and application reasons, all conforming presented is cylindrical in the *H*-plane (i.e., the array is flat along lines in $\hat{y}$ and conformed in $\hat{x}$).

Whatever technique is chosen, trade-offs arise. The inclusion of loss will reduce the radiation efficiency e_r and require changes in the feed design to match a changed input resistance. Conforming will widen the beamwidth of the main lobe and reduce the array gain. Depending on the extent of either, these may be acceptable, but they will be design dependent. Each design in this chapter includes evaluations of these compromises.

Later sections advance the Rot 9 and Wrapped Bowties semi-infinite arrays for analysis of the AGSW, other edge effects, and their compensation methods. This chapter presents arrays finite in the *H*-plane for each element design first, followed by arrays finite in the *E*-plane. For each, this chapter presents a progression of loading and its effects on the AGSW, as well as the impacts on efficiency and comparison to the aperture gain limit.

5.2 Rot 9 *H*-Plane Finite Array

Figure 5-1 shows the geometry of the semi-infinite Rot 9 array, finite in $\hat{x}$ or the *H*-plane. As in Chapter 4, an infinite PEC ground plane is located behind this array (in the view shown, below) at a distance $h = 12\,\text{mm}$. Although not shown, the periodic boundaries remain 15 mm apart. The Rot 9 element has a length of 14.9 mm.

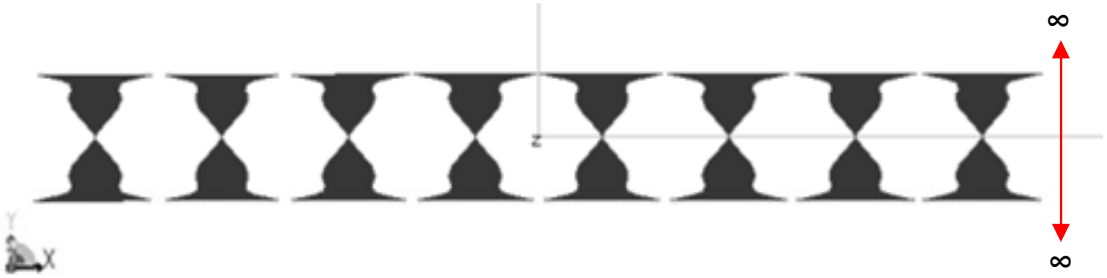

Figure 5-1 – Geometry of the eight-element Rot 9 semi-infinite array (element 1 is on the left, to element 8 on the right)

With all elements modeled as PEC surfaces and excited in phase, the AGSW is visible in the input impedance in Figure 5-2. Array sizes from one to twenty elements in the finite dimension illustrated no meaningful or definitive impacts due to size. The AGSW is present for an array as small as three elements in the finite direction. Small arrays may not exhibit some other behaviors that occur in infinite arrays. One is the behavior of the center element and how it approaches the infinite array solution. Semi-infinite arrays with an increasing number of elements in the finite direction offer some guidance on how many elements make the array sufficiently large. Figure 5-2 and Figure 5-3 show the input resistance and reactance, respectively, for the center element of the infinite, 3-element, 5-element, and 7-element Rot 9 semi-infinite arrays in the orientation of Figure 5-1. Excepting the AGSW effects between 2.4-3.4 GHz, both the 5-element and 7-element arrays come close to the infinite array impedance,

while the mutual coupling in the smaller, 3-element array is not sufficient to approach the input impedance of an infinite array. For consistency, the arrays in this chapter going forward all have eight elements in the finite direction.

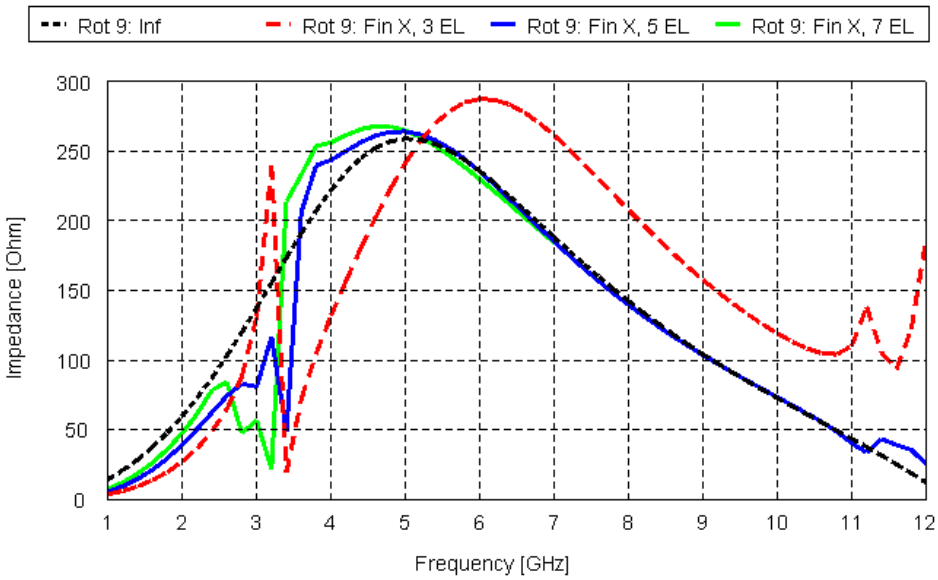

Figure 5-2 – Input resistance for infinite and center elements of 3-, 5-, and 7-element semi-infinite arrays, all elements unloaded at broadside scan

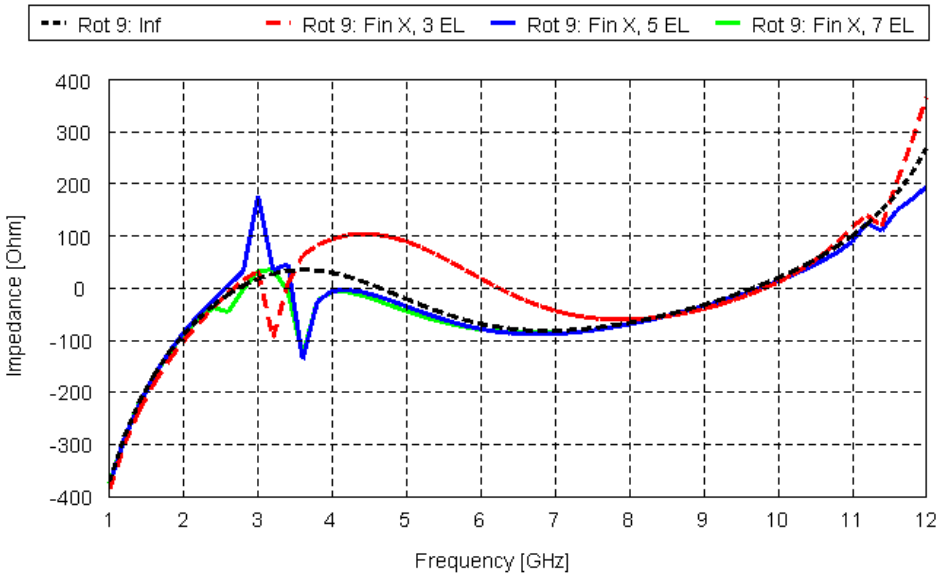

Figure 5-3 – Input reactance for infinite and center elements of 3-, 5-, and 7-element semi-infinite arrays, all elements unloaded at broadside scan

5.2.1 The Unloaded Array

This section documents the behavior of an eight-element semi-infinite array, finite in the *H*-plane direction. The first condition to observe is for the unloaded array, which means there are no additive losses to the elements in the array. Loads can be resistive, reactive, or complex, and they can be intended additions to the element or part of an internal source impedance. They are mean to control the AGSW.

Although Chapter 4 relied heavily upon Smith Charts, they become hard to comprehend when the AGSW is present. Input impedance or VSWR is therefore used. As seen in Figure 5-4, the AGSW is present between 2.4-3.7 GHz, with different impacts and frequencies depending on the element. The behavior of elements in the array differs with element number in the finite direction, although it is symmetrical about the center if the array has no phase shift. With the exception of this frequency region, the input resistance on all interior elements is generally the same, and the end element, Element 1, shows the largest deviation from the center element impedance. Element 2 shows some minor differences also between 3.8-4.8 GHz. As discussed in Chapters 3 and 4, a negative input resistance is observable on Elements 2-4, and Element 1 is as low as 0.1 Ohm. Not surprisingly, these distortions to the input impedance limit the bandwidth substantially. The upper frequency, as seen in Figure 5-5 is unchanged, but the lower frequency increased from 2.04 to 3.58 GHz. The S3 bandwidth decreased from 5.23:1 to 2.98:1.

One difference from past findings [2-5] is the frequency where the AGSW exists. In these works, the AGSW exists 20-30% below resonance (or where the inter-element spacing $d = \lambda / 2$, here 10 GHz.), for example between 7-8 GHz. In the Rot 9 semi-infinite array, the AGSW occurs at 63-76% below resonance between 2.4-3.7 GHz (at 24-37% of resonance). It is tempting to consider this result to be the result of tighter mutual coupling between elements. If so, the AGSW would affect the Wrapped Bowtie semi-infinite array, which as an infinite array exhibited an even larger bandwidth, at a lower frequency. At this time, it is not entirely clear why the AGSW occurs at the frequencies it does.

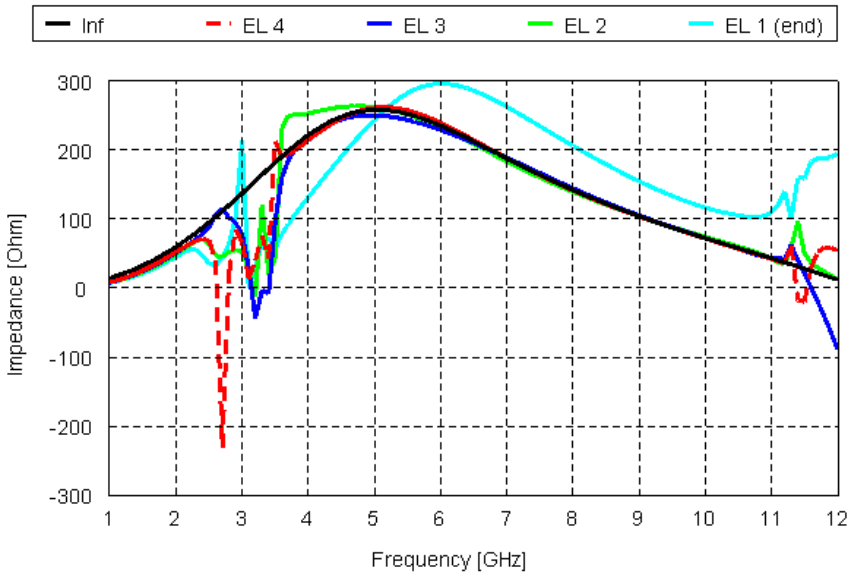

Figure 5-4 – Input Resistance at elements 1-4 on the eight-element Rot 9 semi-infinite array, finite in *H*-plane, unloaded and at broadside scan

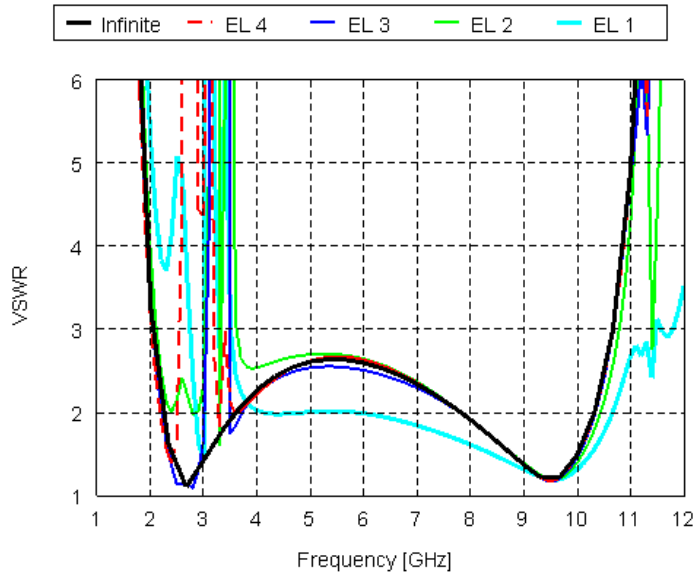

Figure 5-5 – VSWR at elements 1-4 on the eight-element Rot 9 semi-infinite array, finite in the *H*-plane, unloaded and at broadside scan[1]

[1] $Z_o = \{150,100,100,100,100,100,100,150\}$ Ohms on elements 1-8 across the array.

Applied spatially, a discrete fast Fourier transform (DFFT) of the currents at the element feeds across the array also illustrates the AGSW. Plots of the magnitude of the element feed currents and their Fourier transformers, padded for smoothness, are shown below in Figures 5-6 to 5-17 for the frequencies 2.0, 2.4 3.2, 3.9, 10.0, and 11.5 GHz. These frequencies show some interesting properties. Additionally, each frequency section provides its corresponding far-field pattern to display how the AGSW has little noticeable effect on that pattern. The patterns are from only the eight elements shown. All eight elements, and by extension all in the infinite direction, are equally fed and phased (to broadside) with edge voltages.

2 GHz

The spatial and spectral domains of the currents at 2 GHz are well behaved. This frequency is below the onset of the AGSW. Recall, visible space exists for $|s_c| \leq 1$. In addition, note the slight change in the current amplitude across the array and, of course, its symmetry.

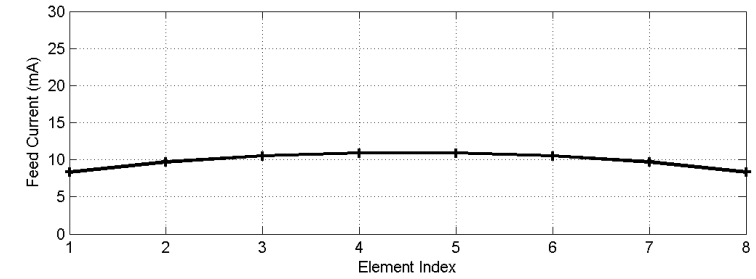

(a) Current magnitudes on element centers

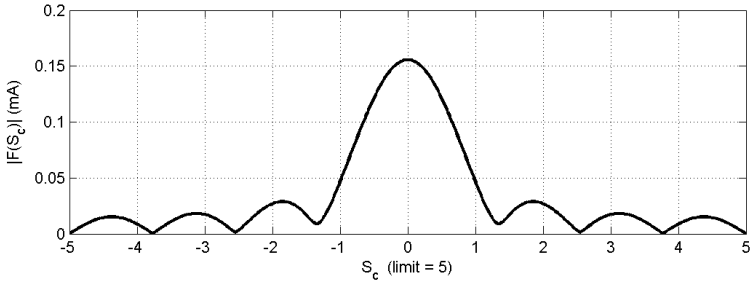

(b) Fourier transform of (a)

Figure 5-6 – Currents on eight-element Rot 9 semi-infinite array at 2 GHz

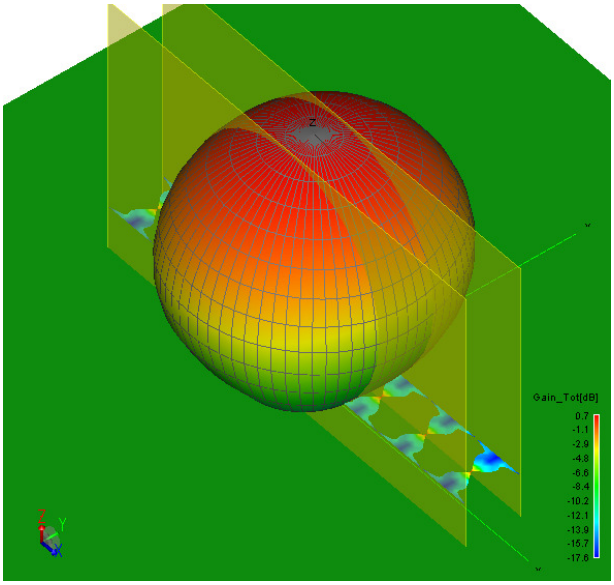

Figure 5-7 – Far-field pattern of the Rot 9 semi-infinite array at 2 GHz

2.4 GHz

The spatial domains of the currents at 2.4 GHz appear to be fairly well behaved, but the first side lobes in the spectral domain are increased and merged with the main lobe. This indicates the onset of the AGSW.

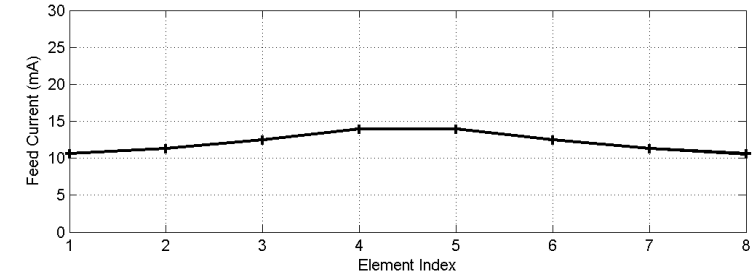

(a) Current magnitudes on element centers

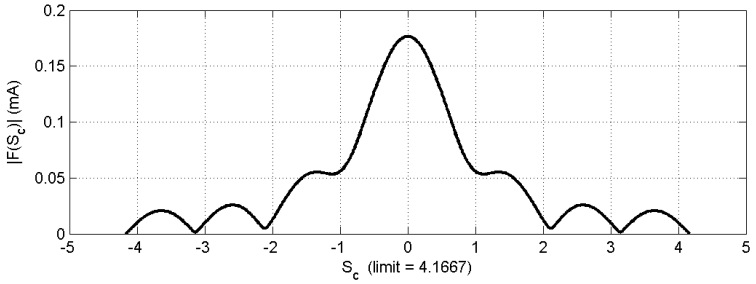

(b) Fourier transform of (a)

Figure 5-8 – Currents on eight-element Rot 9 semi-infinite array at 2.4 GHz

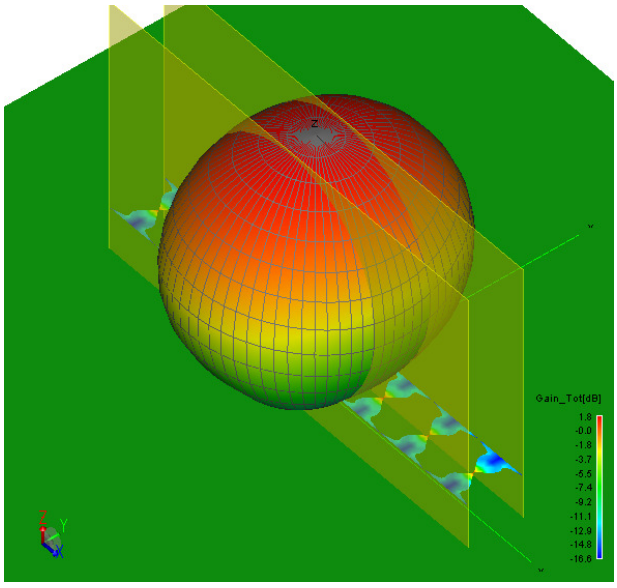

Figure 5-9 – Far-field pattern of the Rot 9 semi-infinite array at 2.4 GHz

3.2 GHz

At 3.2 GHz, the AGSW is near its strongest. Large variations in the current magnitude between elements are evident. In the spectral domain, more currents are located in the invisible region than in the visible region. The symmetry of the two main peaks at $S_c = \pm 1.8$ indicate both the left- and right-traveling surface waves (likewise $-\hat{x}$ and $+\hat{x}$).

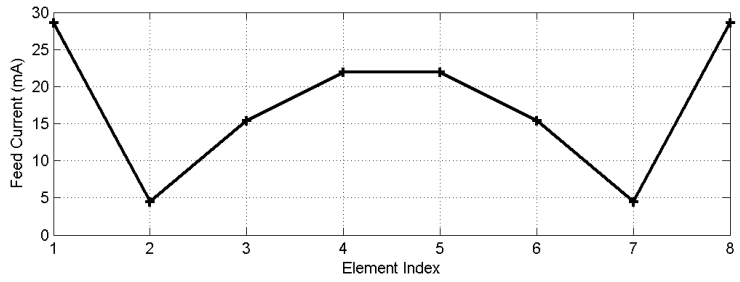

(a) Current magnitudes on element centers

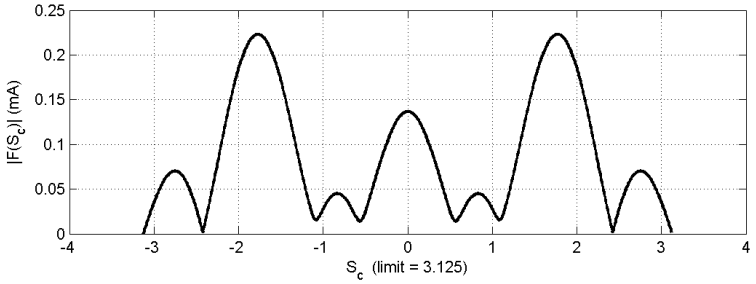

(b) Fourier transform of (a)

Figure 5-10 – Currents on eight-element Rot 9 semi-infinite array at 3.2 GHz

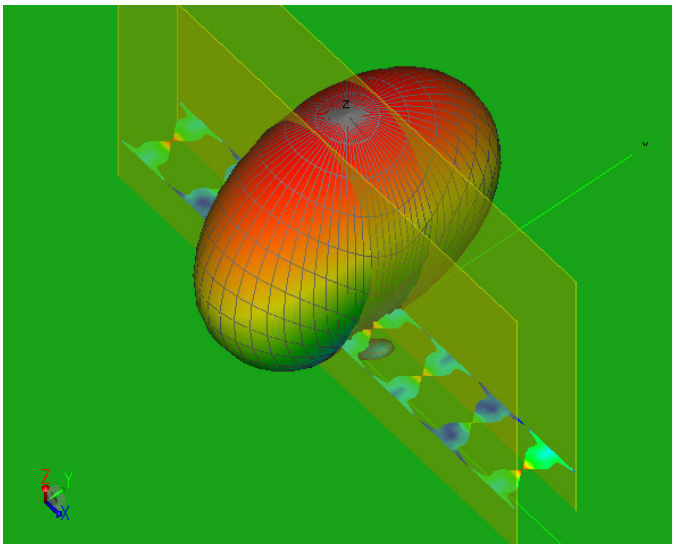

Figure 5-11 – Far-field pattern of the Rot 9 semi-infinite array at 3.2 GHz

3.9 GHz

At 3.9 GHz, the AGSW is no longer evident. Note the reduction in the limit of invisible space as frequency increases. With some minor changes to the exact shapes of the current distribution across the array, such results are evident from 3.9 GHz up to and past 10 GHz. With increased frequency, the beamwidth narrows, as expected.

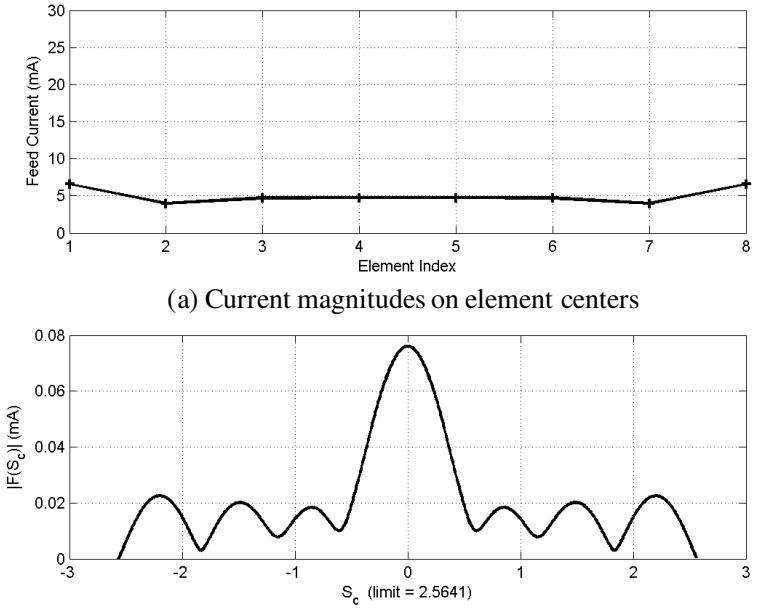

(a) Current magnitudes on element centers

(b) Fourier transform of (a)

Figure 5-12 – Currents on eight-element Rot 9 semi-infinite array at 3.9 GHz

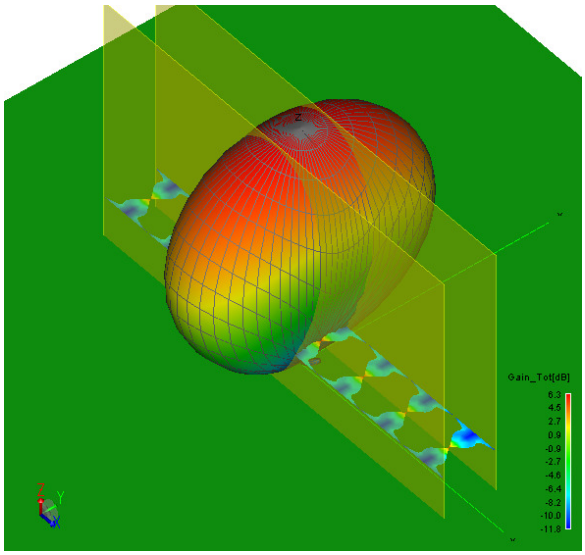

Figure 5-13 – Far-field pattern of the Rot 9 semi-infinite array at 3.9 GHz

10 GHz

The results for 10 GHz are presented simply to show that at this spacing, all currents are now located within visible space, since the inter-element spacing $d = \lambda / 2$ occurs at 10 GHz. The pattern has started to show some effects of cancelation from the ground image. The gain at $\theta = 0^{\circ}$ is -1 dB of $G_{\max}$.

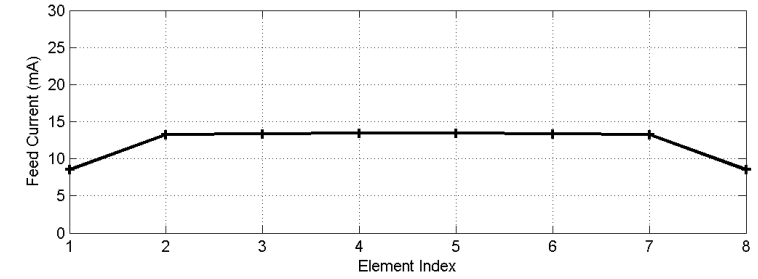

(a) Current magnitudes on element centers

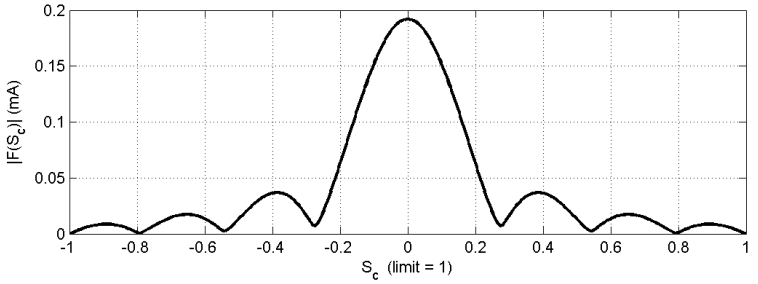

(b) Fourier transform of (a)

Figure 5-14 – Currents on eight-element Rot 9 semi-infinite array at 10 GHz

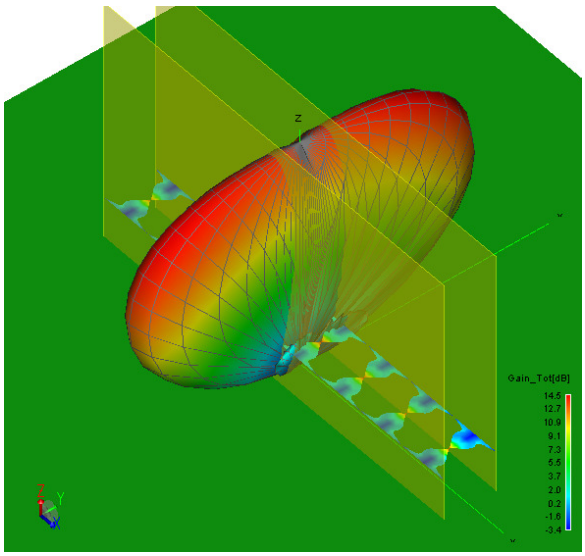

Figure 5-15 – Far-field pattern of the Rot 9 semi-infinite array at 10 GHz

11.5 GHz

From the results in Figure 5-4 and Figure 5-5, some distortion is evident between 11-12 GHz. Although outside the operating region of this array (at least its infinite form), the DFFT technique proves useful in showing the presence of a visible grating lobe. Figure 5-17 shows a clear illustration of its presence.

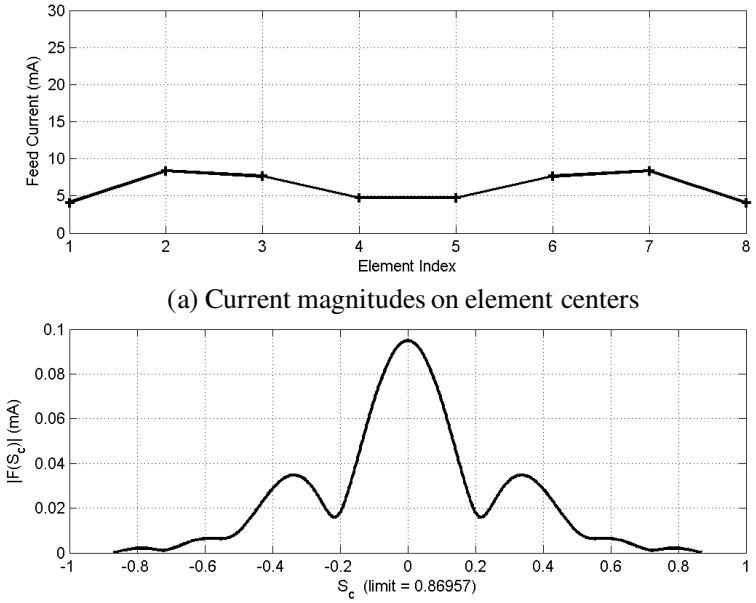

(a) Current magnitudes on element centers

(b) Fourier transform of (a)

Figure 5-16 – Currents on eight-element Rot 9 semi-infinite array at 11.5 GHz

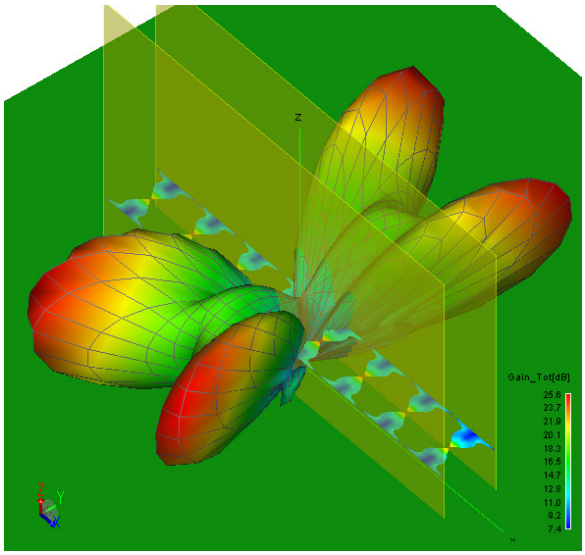

Figure 5-17 – Far-field pattern of the Rot 9 semi-infinite array at 11.5 GHz

5.2.2 Suppression of the AGSW

As laid out in Section 5.1, the dominant method to suppress the AGSW is to introduce ohmic losses into the array. Also in [2], the addition of a load equal to the characteristic impedance of the antenna appeared to provide the best suppression of the AGSW. Recall, the reference impedance of the infinite Rot 9 array is 100 Ohms. A series of simulations, and guidance from [3], indicated the need to taper the loads approaching the edge element up to the characteristic impedance. Figure 5-18 and Table 5-1 detail the loadings applied.

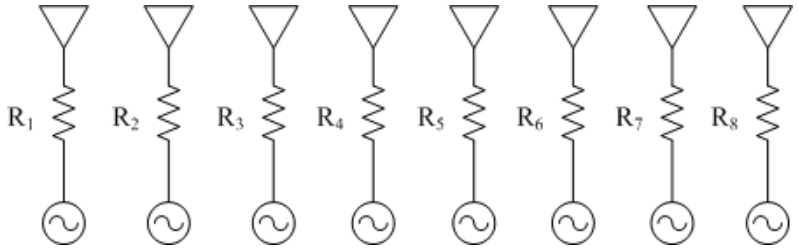

Figure 5-18 – Block diagram of element loads in finite direction

Table 5-1 – Loadings on the *H*-plane finite Rot 9 array across the finite dimension $\hat{x}$

Name	R_1	R_2	R_3	R_4	R_5	R_6	R_7	R_8
Unloaded	0	0	0	0	0	0	0	0
Load02	100	0	0	0	0	0	0	100
Load03	100	50	0	0	0	0	50	100
Load04	200	100	50	0	0	50	100	200
Load05	100	50	25	0	0	25	50	100

In observing the loading effects on the input resistance of Element 4 (center), Figure 5-19 shows that either Load04 or Load05 the AGSW sufficiently suppress the AGSW. The frequency range is limited to the region where the AGSW occurs in the unloaded array. A similar smoothing of the input resistance happens on Elements 1-3 due to the series resistance, although the element input resistance diverges from the infinite array solution.

The Load04 array diverges from the other schemes and jumps to a 200-Ohm load on the end elements. Its load is generally a scaled increase upward. Load05 is a return to the initial tapering progression, and it functions sufficiently, but not perfectly, to suppress the AGSW. However, the Load05 array at its best frequency seen in Figure 5-20 has $e_r = 88\%$, versus an $e_r = 81\%$ for the Load04 array.

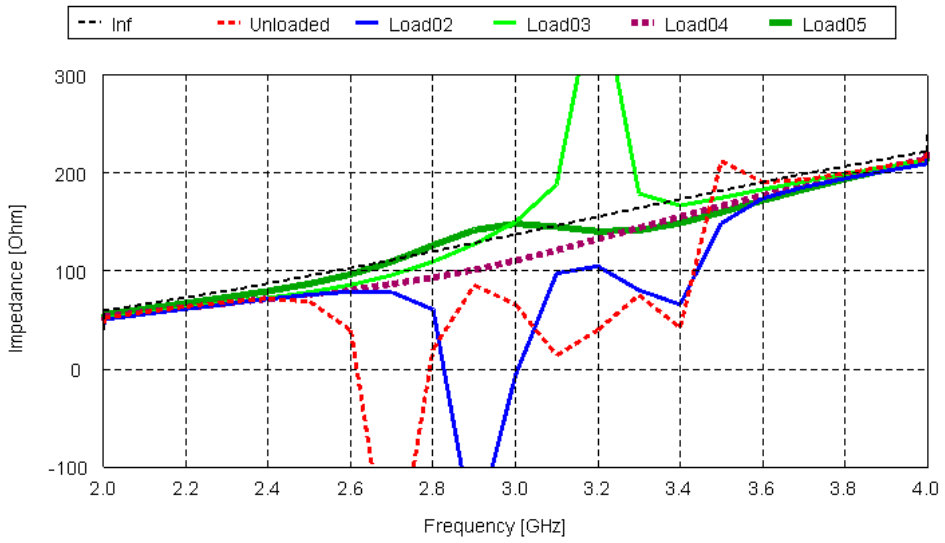

Figure 5-19 – Input impedance on center element 4 of the *H*-plane finite Rot 9 array of eight elements under various loads

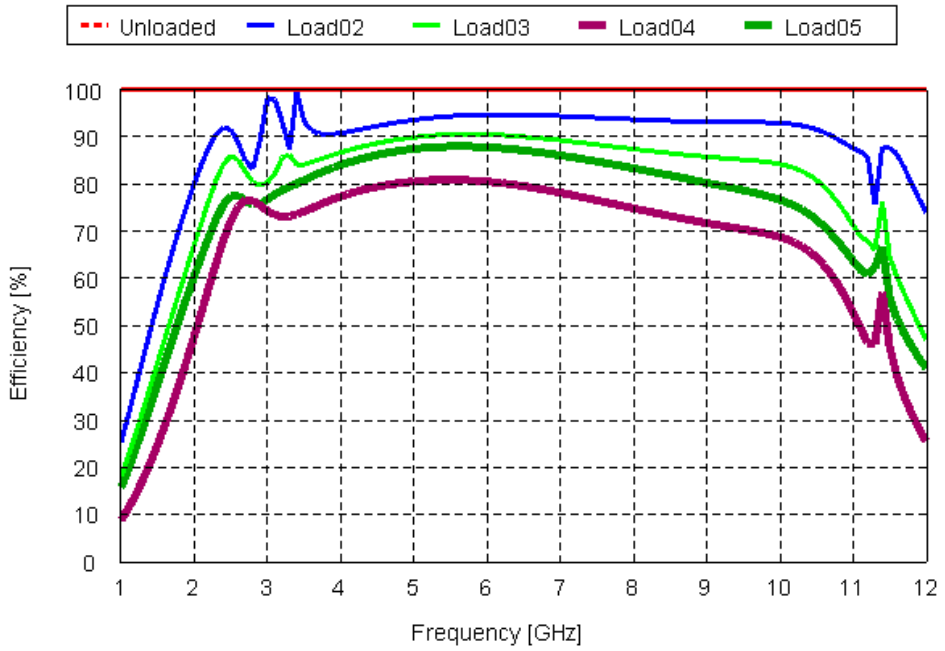

Figure 5-20 – Radiation efficiency of *H*-plane finite Rot 9 arrays for various loads

As a last check of the suppression of the AGSW, the DFFT for 2.3-3.7 GHz in 0.1 GHz steps are overlaid. This is the region where the AGSW was strongest in the unloaded array. In the Figure 5-21 (top), the lobes outside the visible region are clearly present in the unloaded array. In the Load05 array (bottom), the AGSW is no longer meaningfully large.

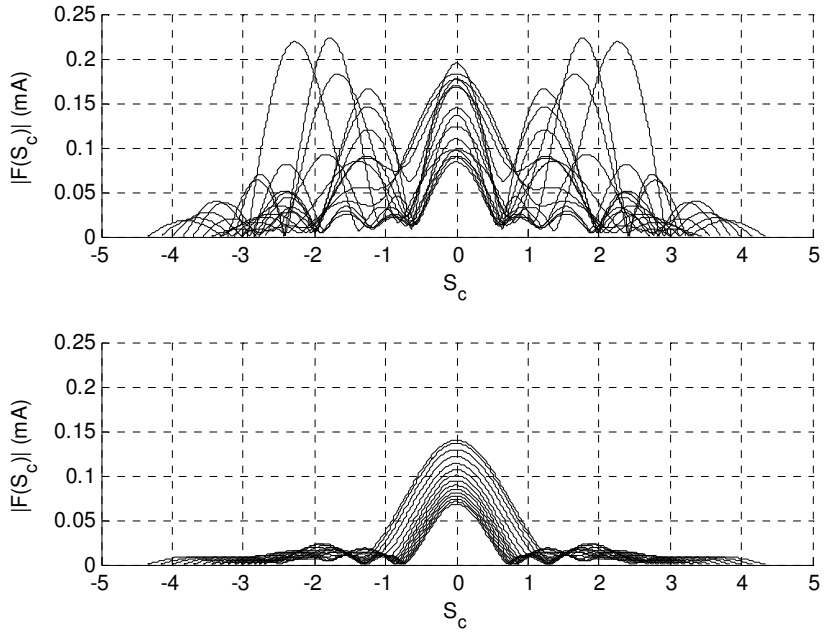

Figure 5-21 – Overlaid spectral domain of unloaded array (top) and Load05 array (bottom) in region of AGSW (2.3-3.7 GHz)

The Load05 pattern results in a S3 bandwidth that nearly matches the infinite bandwidth solution, being 5.22:1 and ranging from 2.06-10.75 GHz. The unloaded center elements had the narrowest bandwidth, while the loaded Elements 1-3 exhibited wider bandwidths. Figure 5-22 shows the VSWR for each element, along with the infinite array VSWR. The reference impedances require modification to account for the series resistance and are $Z_o = \{250, 150, 125, 100, 100, 125, 150, 250\}$ Ohms across the array.

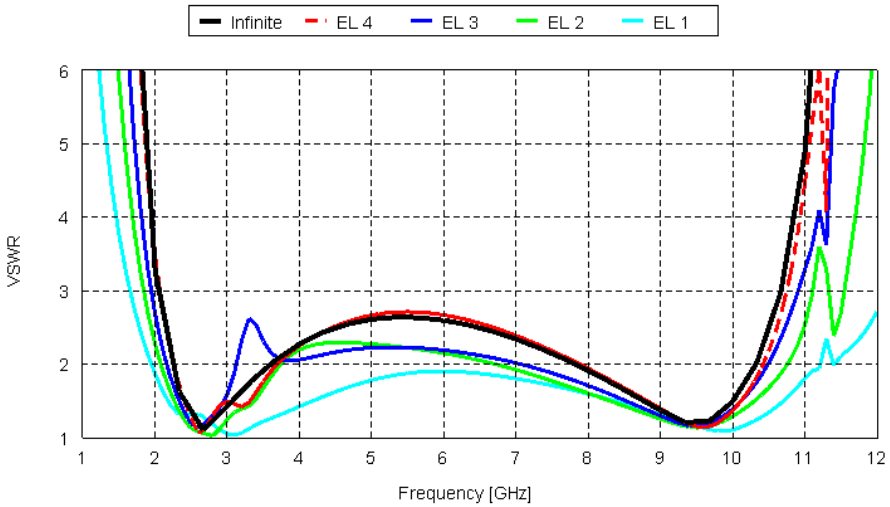

Figure 5-22 – VSWR on elements 1-4 of Load05, *H*-plane finite Rot 9 array

There is certainly a trade-off in this design between efficiency and impedance control. One question not yet answered is how the gain of this array compares with its aperture limit (see Section 2.2). Using an area of eight times the unit cell ($8\times15\times15$ mm^2), Figure 5-23 shows the $+\hat{z}$ array gain for the uniform aperture against the eight shown elements of both the unloaded array and the Load05 array. At the low frequencies, the lower efficiency is the cause of the divergence from aperture gain; at the higher frequencies, the pattern distortion stemming from the ground plane reflection is the cause. Within the operating band, the largest difference is at the upper frequency of 10.75 GHz, where a 2.3 dB difference occurs.

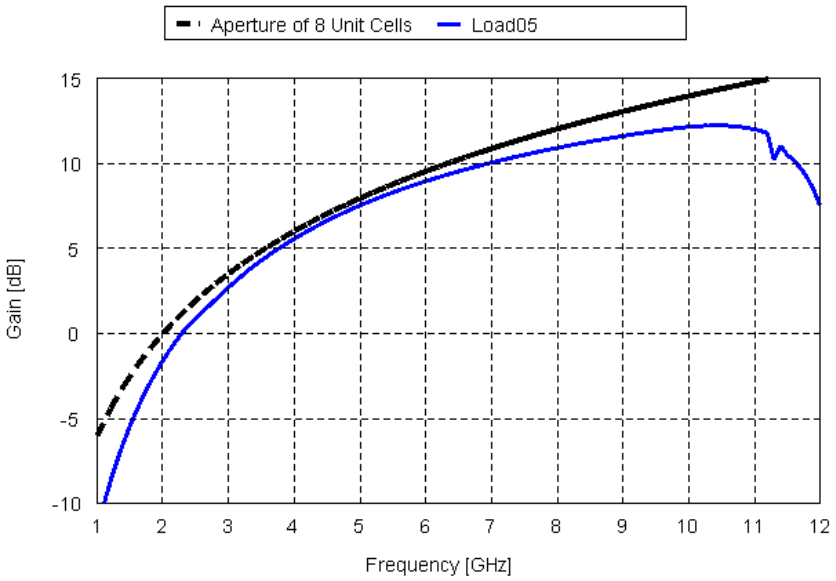

Figure 5-23 – Gain comparison of the eight Rot 9 elements shown in Figure 5-1 using Load05 to the uniform aperture limit

With the array loaded in the finite $\pm\hat{x}$ direction, there is an effective amplitude taper across the array. This amplitude taper effects the pattern shape and the side lobe levels, although the loading has not been implement to impart a specific side lobe level (SLL). The side lobe levels depend on the current distribution across the finite array dimension, and these currents are reduced where the loads are greatest. The loads are also seen directly in the radiation efficiency of the array, which per Figure 5-20 is maximum between 5-6 GHz. Higher amplitude tapers are expected away from these frequencies. The tapers at many frequencies, however, are not as large one would intentionally design to effect a lower side lobe level, such as in a Binomial or Dolph-Chebyshev distribution [6]. This distribution carries forward into finite arrays in two dimensions,

but with similar effects. Figure 5-24 compared the normalized patterns of the *H*-plane finite unloaded Rot 9 array and the Rot 9 array with Load 05. All patterns are computed from only the 1×8 elements shown in Figure 5-1.

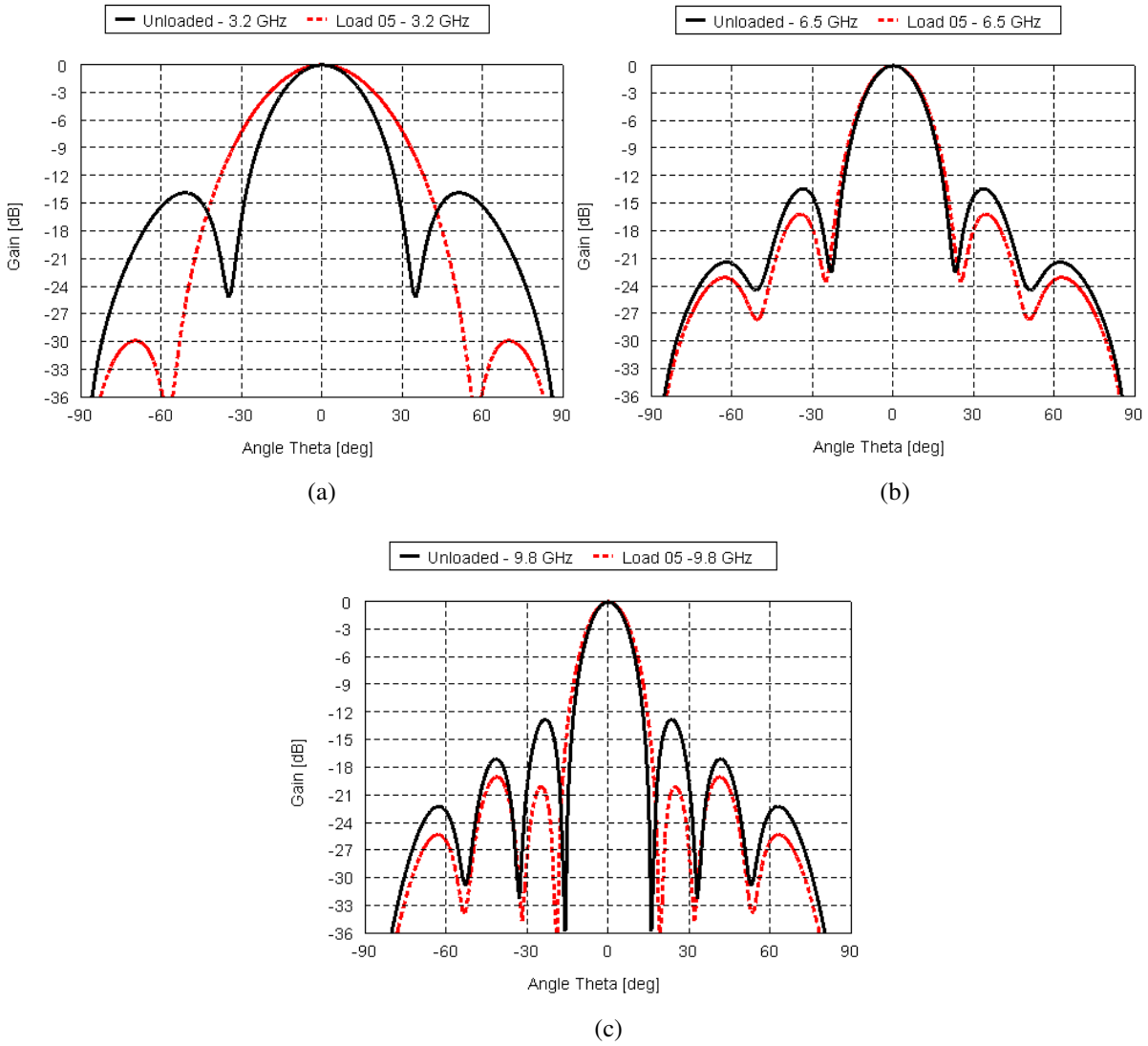

Figure 5-24 – Side lobe level comparison of the eight Rot 9 elements shown in Figure 5-1 when unloaded and loading with the Load05 scheme at (a) 3.2 GHz, (b) 6.5 GHz, and (c) 9.8 GHz

5.3 Rot 9 *E*-Plane Finite Array

Following on the analysis and design of the Rot 9 *H*-plane finite array, this section next addresses the *E*-plane finite array. This array geometry (seen in Figure 5-25) has small gaps exist between each element, although these may not be clearly visible in the figure. All geometric

parameters match the *H*-plane finite array, with the exception of the redefinition of the periodic boundaries. Here it is located at $x = \pm 15$ mm. All elements are PEC surfaces.

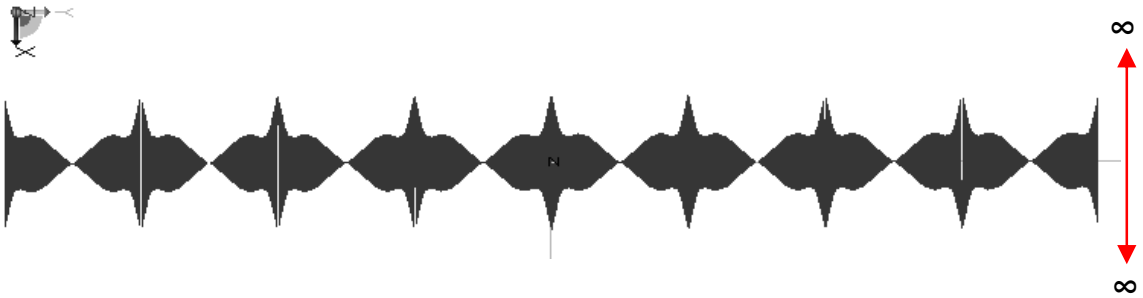

Figure 5-25 – Geometry of the eight-element Rot 9 semi-infinite array (element 1 is on the left, to element 8 on the right)

5.3.1 The Unloaded Array

As with the *H*-plane finite array configuration, the AGSW is present in the *E*-plane configuration. However, here the impact is much more severe, as seen in Figure 5-26, and ranges between approximately 3.5-7.5 GHz on at least one element in the array. This frequency range where present is much larger in the *E*-plane that the *H*-plane (Figure 5-4), which may be indicative of higher mutual coupling in the *E*-plane. Outside this range, the input resistance is a close match to that of the infinite array. The end element, Element 1, shows less deviation in this configuration than in the *H*-plane configuration, as well. The input resistance spikes on Element 4 at the middle of the array (not shown) extend to ± 1500 Ohms; Elements 2 and 3 also show negative input resistance.

These distortions to the input impedance limit the bandwidth substantially, and an S3 bandwidth only appears on all elements between 2.32-3.58 GHz and 7.74-10.67 GHz (Figure 5-27). The upper frequency, as seen in Figure 5-5, is mostly unchanged, but the lower frequency increases from $2.04 \rightarrow 2.32$ GHz. In other words, when combined with the *H*-plane configuration as though the superposition of two semi-infinite arrays to make a finite array, the only usable frequency range exists between 7.74-10.67 GHz. The coupling between configurations is substantially different.

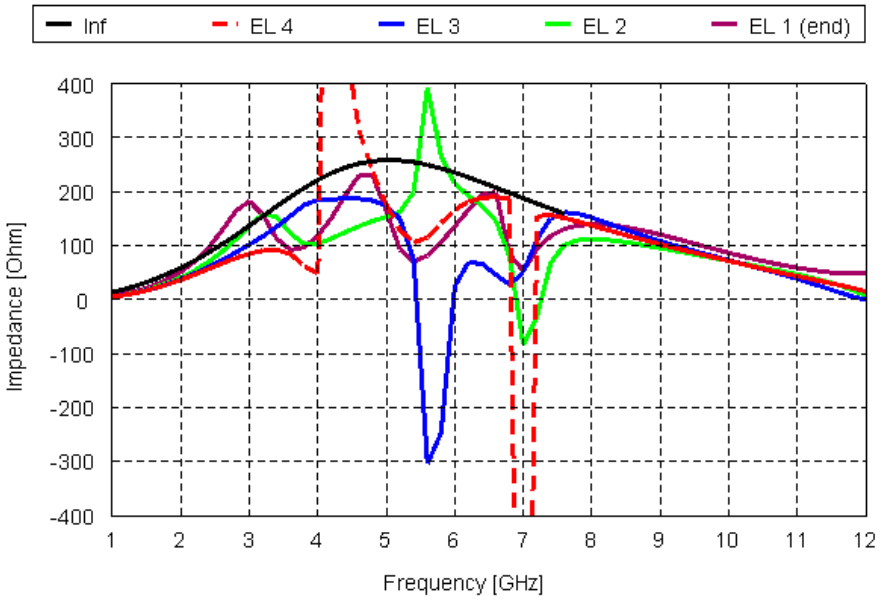

Figure 5-26 – Input resistance at elements 1-4 on the eight-element Rot 9 semi-infinite array, finite in the *E*-plane, unloaded and at broadside scan

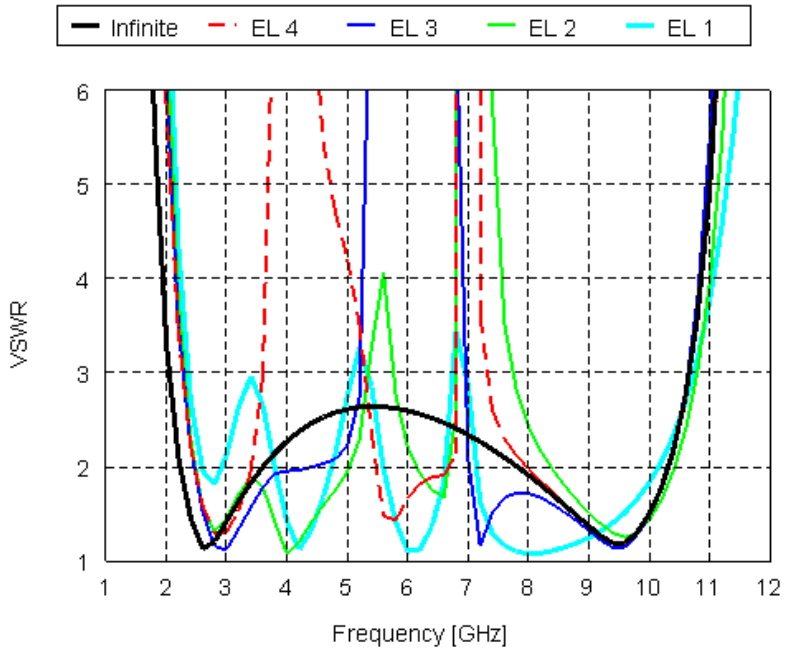

Figure 5-27 – VSWR at elements 1-4 on the eight-element Rot 9 semi-infinite array, finite in the *E*-plane, unloaded and at broadside scan[2]

[2] $Z_o = \{150,100,100,100,100,100,100,150\}$ Ohms on elements 1-8 across the array.

As before, the DFFT allows for the observation of the AGSW at the feeds of elements along the array. Below for the frequencies 3.4, 4.2, 5.4, 7.0, and 10 GHz, Figures 5-26 to 5-35 show the magnitude of the element feed currents and their Fourier transforms, padded for smoothness. The array at these frequencies exhibits some interesting and different properties than seen in the *H*-plane configuration. For documentation and consistency, each frequency section includes the corresponding far-field pattern. Only the eight elements shown determine the far-field pattern.

3.4 GHz

The spatial and spectral domains of the currents at 3.4 GHz are well behaved, but they are beginning to show the development of multiple lobes. Unlike Figure 5-8, however, which has a similar shape, these bulges lie within visible space for the *E*-plane configuration.

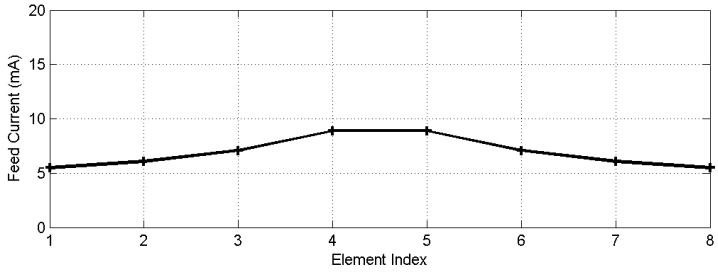

(a) Current magnitudes on element centers

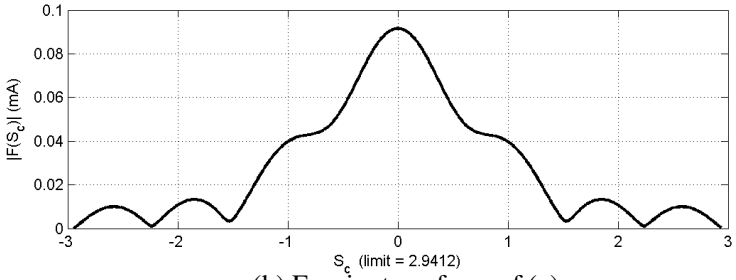

(b) Fourier transform of (a)

Figure 5-28 – Currents on eight-element Rot 9 semi-infinite array at 3.4 GHz

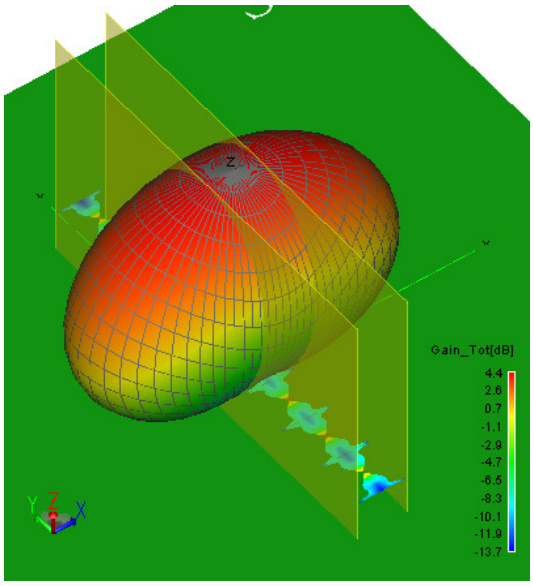

Figure 5-29 – Far-field pattern of the Rot 9 semi-infinite array at 3.4 GHz

4.2 GHz

At 4.2 GHz, there is the appearance of small grating lobes. Current theory of the substrate-guided surface wave (SGSW) does not explain such an occurrence at this frequency, and again, because of the frequency, it may be mistaken for an AGSW. The peaks of the spectral side lobes lie within visible space, but a substantial portion of the current lies outside visible space.

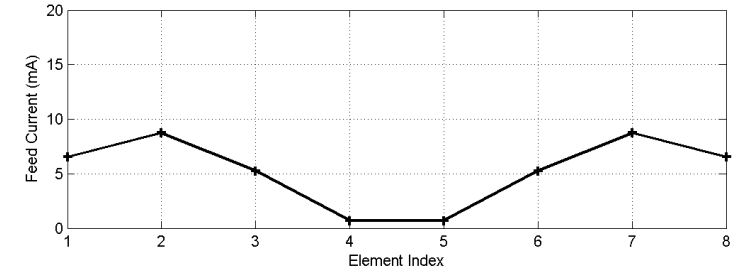

(a) Current magnitudes on element centers

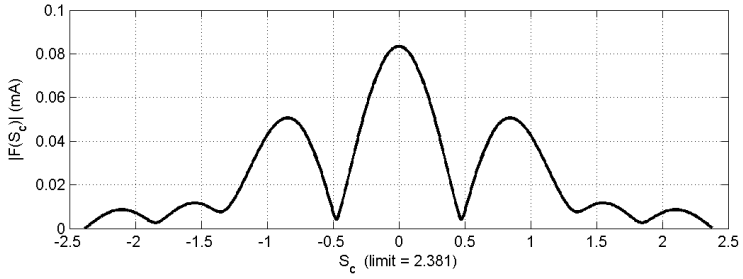

(b) Fourier transform of (a)

Figure 5-30 – Currents on eight-element Rot 9 semi-infinite array at 4.2 GHz

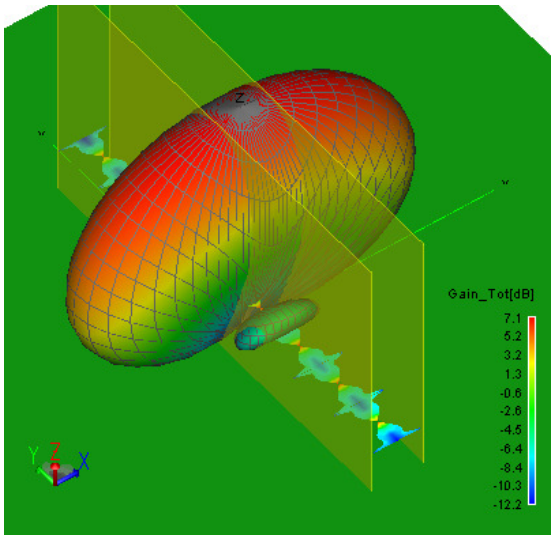

Figure 5-31 – Far-field pattern of the Rot 9 semi-infinite array at 4.2 GHz

5.4 GHz

Like at 4.2 GHz, the spectral current side lobes are both inside and outside visible space at 5.4 GHz, with the peaks slightly outside. The AGSW is certainly more apparent at this frequency, and its impact on the input resistance (Figure 5-26) is detrimental for Elements 2 and 3, in particular.

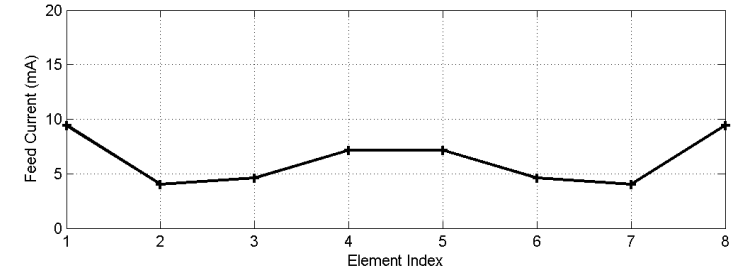

(a) Current magnitudes on element centers

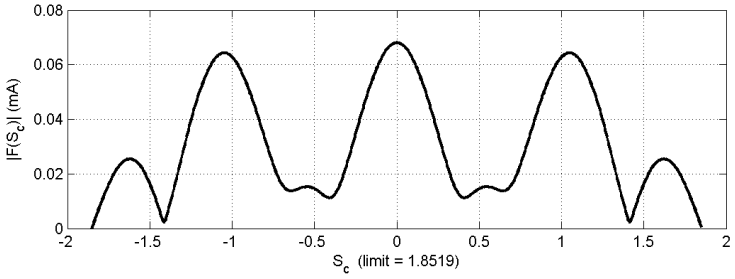

(b) Fourier transform of (a)

Figure 5-32 – Currents on eight-element Rot 9 semi-infinite array at 5.4 GHz

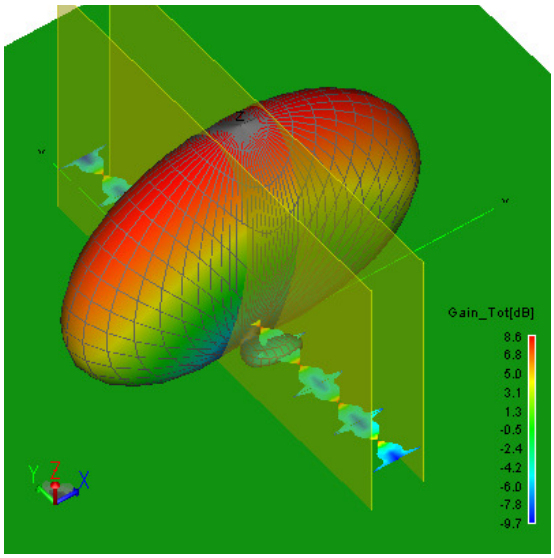

Figure 5-33 – Far-field pattern of the Rot 9 semi-infinite array at 5.4 GHz

7.0 GHz

At 7.0 GHz, the AGSW is very strong and has major lobes outside visible space. The current magnitude on the center two elements is nearly zero; for the same frequency, the element $R_{in} = -1500$ Ohms.

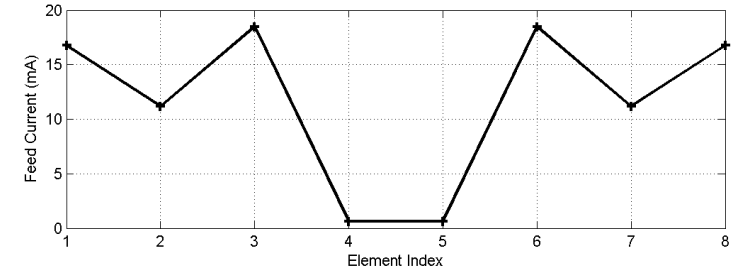

(a) Current magnitudes on element centers

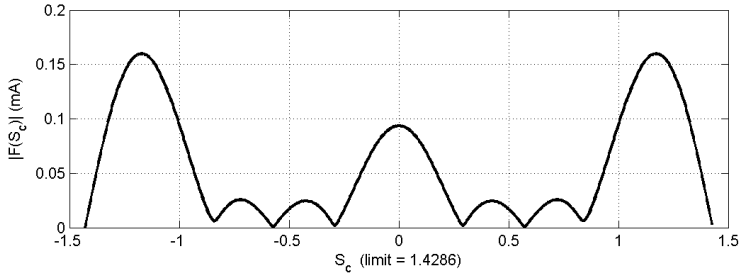

(b) Fourier transform of (a)

Figure 5-34 – Currents on eight-element Rot 9 semi-infinite array at 7.0 GHz

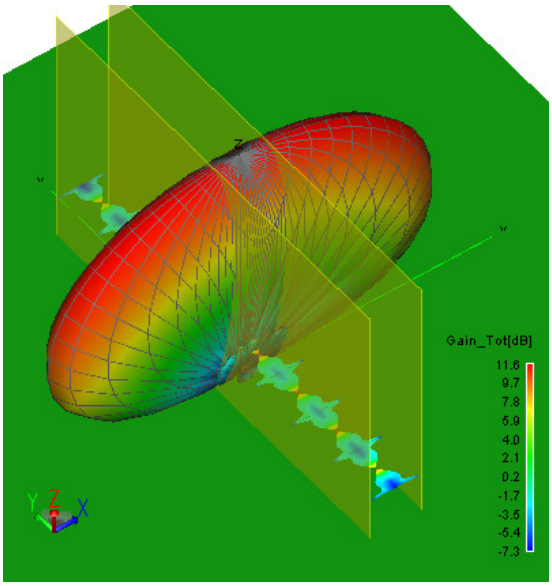

Figure 5-35 – Far-field pattern of the Rot 9 semi-infinite array at 7.0 GHz

10 GHz

The results for 10 GHz are for comparison to the *H*-plane pattern. No evidence of the AGSW is present, but the pattern shows the formation of a larger dip in $+\hat{z}$, stemming from the reflection from the ground plane. The gain is –4.3 dB below maximum found at $\theta = 50^{\circ}$. No true grating lobes form in the frequencies up to 12 GHz.

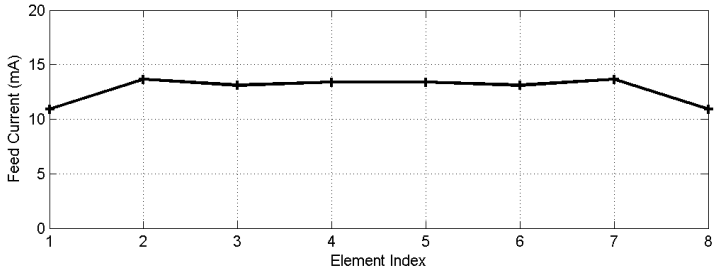

(a) Current magnitudes on element centers

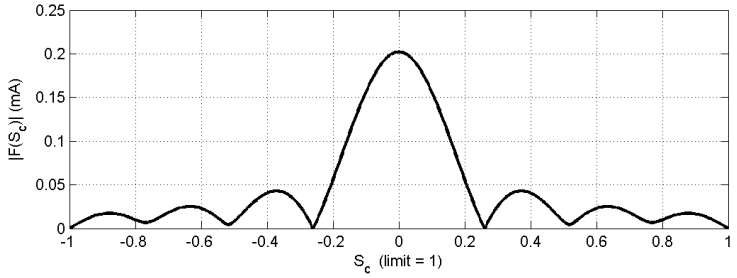

(b) Fourier transform of (a)

Figure 5-36 – Currents on eight-element Rot 9 semi-infinite array at 10 GHz

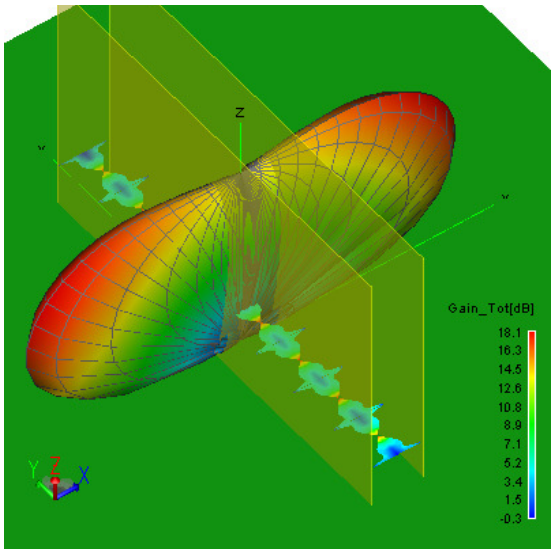

Figure 5-37 – Far-field pattern of the Rot 9 semi-infinite array at 10 GHz

5.3.2 Suppression of the AGSW

Loading pattern Load04 and Load05 shown in Table 5-1 serve as the starting point for suppressing the AGSW in the *E*-plane finite Rot 9 array. In observing the effects of the loads on the input resistance on Element 4 (center), it is clear in Figure 5-38 that the AGSW is suppressed using either Load04 or Load05. The input resistance for the Load05 array appears less well controlled than that of Load 04.

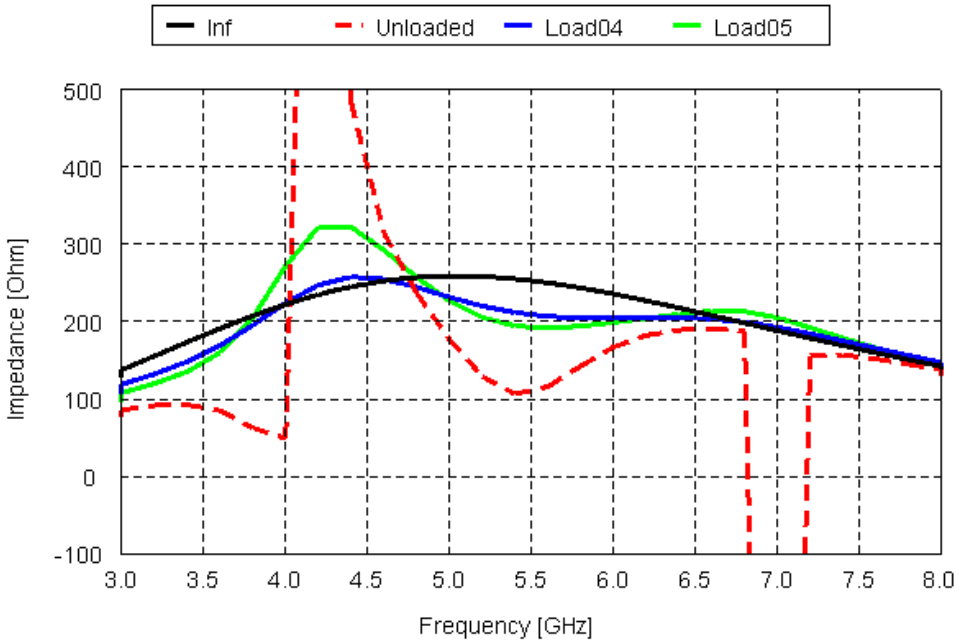

Figure 5-38 – Overlaid spectral domain of unloaded array (top), Load04 array

To complete a quick comparison, the spectral domain currents are overlaid across the region of interest (3-8 GHz) to determine the viability of both methods quickly. From Figure 5-39, Load05 appears a sufficient solution and has little difference from the Load04 array results. With higher spectral currents and less ohmic loss, Load05 has higher efficiency (Figure 5-40).

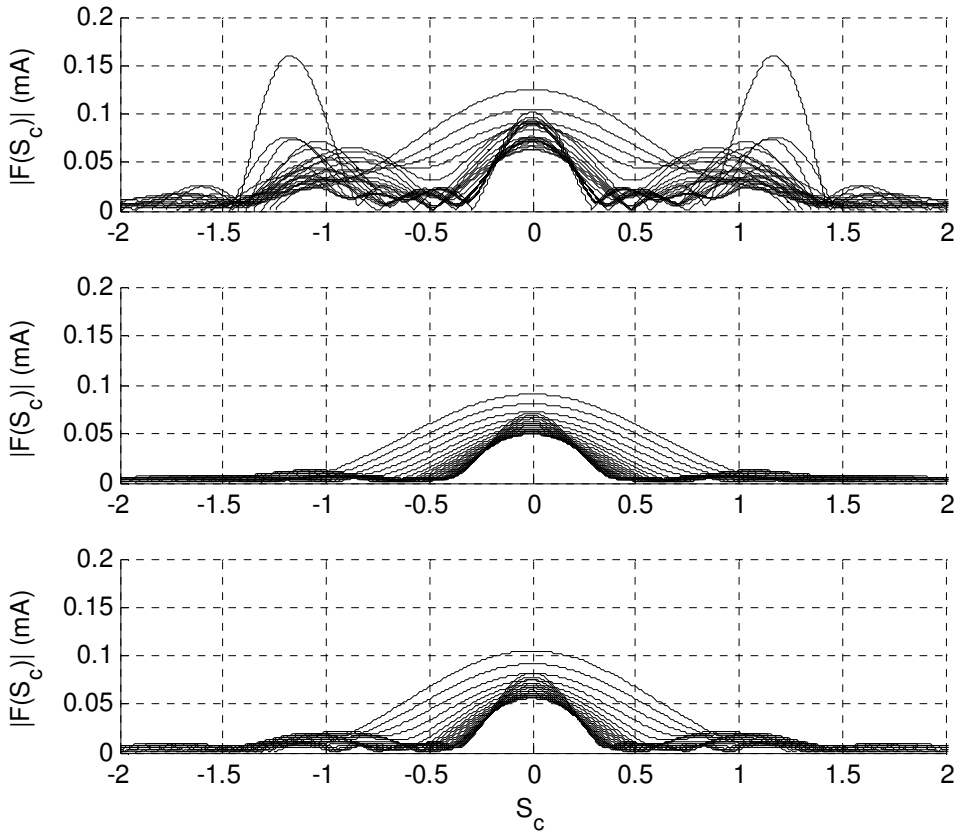

Figure 5-39 – Overlaid spectral domain of unloaded array (top), Load04 array (middle), and Load05 array (bottom) in region of AGSW (3-8 GHz)

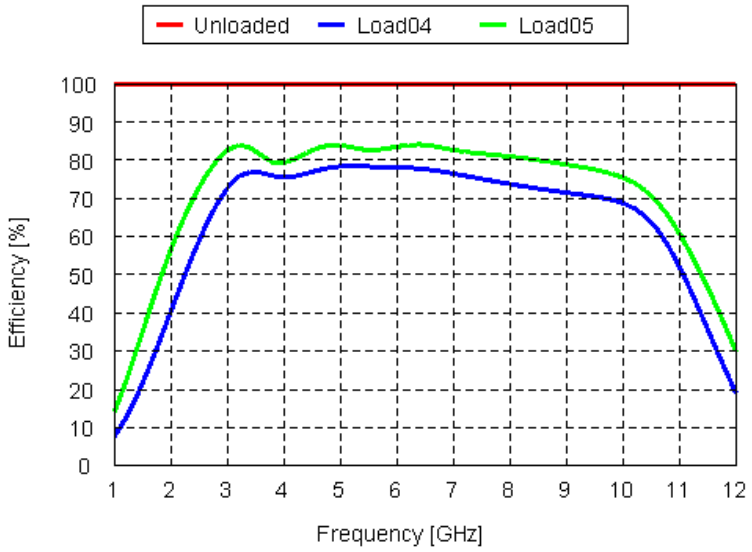

Figure 5-40 – Radiation efficiency of *E*-plane finite Rot 9 arrays for various loadings

While the higher efficiency is good, the achieved VSWR on all elements is not less than three, as is seen in Figure 5-41. Reviewing the loading results again in Figure 5-39, the Load05 results show a larger distribution of spectral currents outside the visible region. In observing the VSWR, Load04 unexpectedly emerges as the better choice of loading. Figure 5-42 shows the VSWR for the Load04 array, which achieves an S3 bandwidth of 4.95:1.

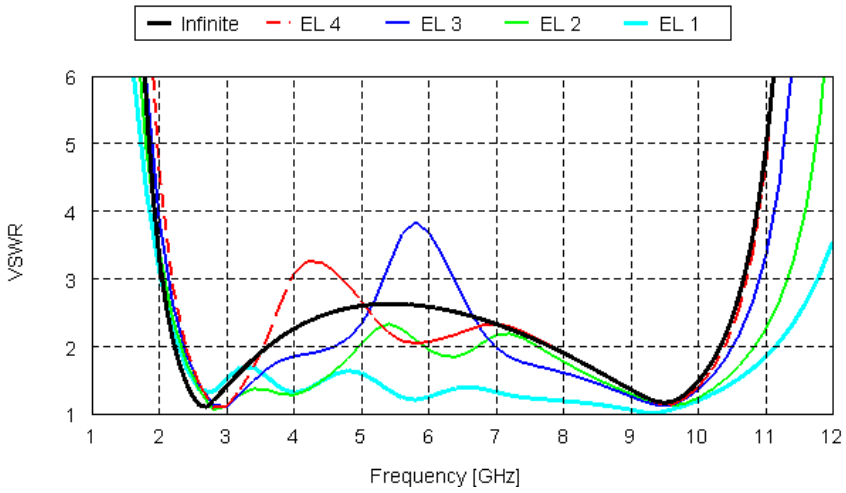

Figure 5-41 – VSWR on elements 1-4 of Load05, *E*-plane finite Rot 9 array[3]

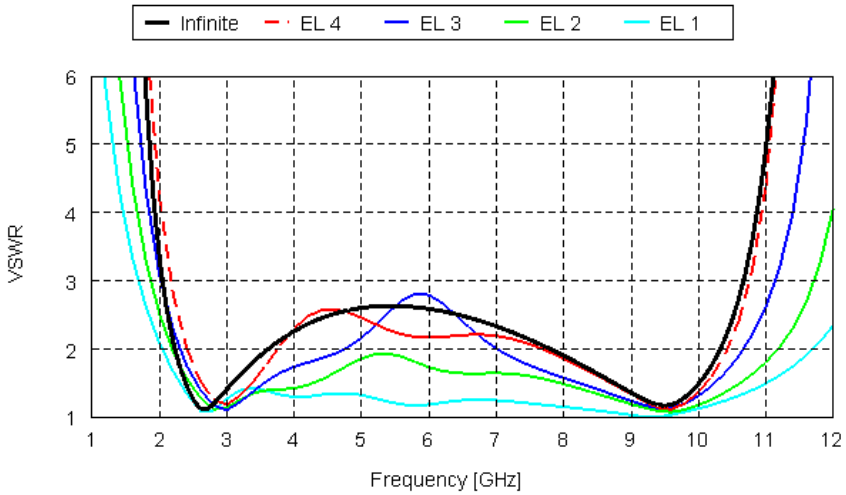

Figure 5-42 – VSWR on elements 1-4 of Load04, *E*-plane finite Rot 9 array[4]

---

[3] $Z_o = \{200,150,125,100,100,125,150,200\}$ Ohms across array.

[4] $Z_o = \{300,200,150,100,100,150,200,300\}$ Ohms across array

Figure 5-43 shows the resulting gain in $+\hat{z}$ for both loading cases. The loss in gain with the additional loading of Load04 is worst near 2 GHz, at 1 dB but is typically 0.4 dB.

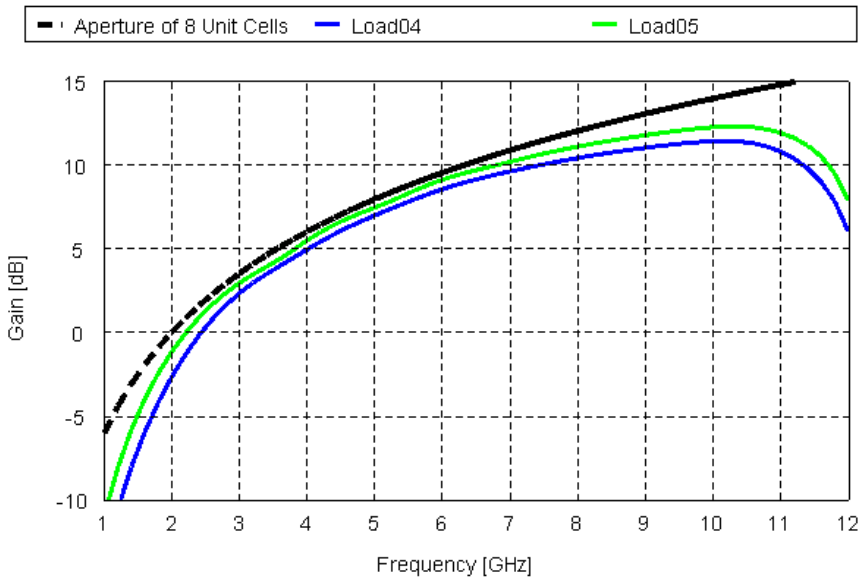

Figure 5-43 – Gain comparison of the eight Rot 9 elements shown in Figure 5-25 using Load04 and Load05 schemes to the uniform aperture limit

5.4 Wrapped Bowtie *H*-Plane Finite Array

Figure 5-44 shows the geometry of the semi-infinite Wrapped Bowtie array, finite in $\hat{x}$ or the *H*-plane. Element numbers are zigzagged from 1 (left) to 15 (right), as labeled. This odd layout, with elements split other than at their edges is required since feeds cannot lie on the periodic boundary in FEKO®. That boundary spacing is 21.21 mm here.

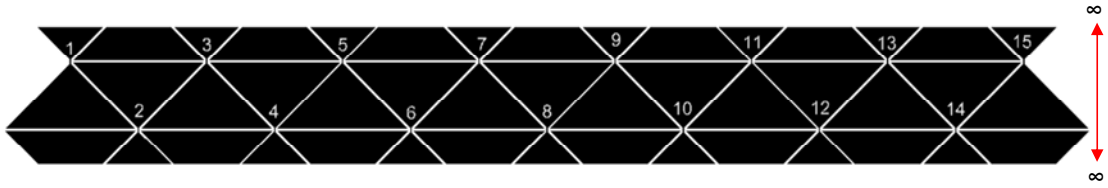

Figure 5-44 – Geometry of 15-element Wrapped Bowtie *H*-plane array

5.4.1 The Unloaded Array

The new geometry and tight interlacing of elements require that 15 ports be modeled to observe rows of seven (even-numbered) and eight (odd-numbered) elements across. For a focus, this section presents only the seven-element row. As before, the AGSW is present as seen in Figure 5-45, and here the frequency range of distortion is concentrated at the lower frequency range of the infinite array. At about 3.6 GHz, it abruptly ends, yet over a 2.5:1 bandwidth remains without any distortions from the AGSW. (The infinite Wrapped Bowtie array displayed a 7.24:1 S3 bandwidth.)

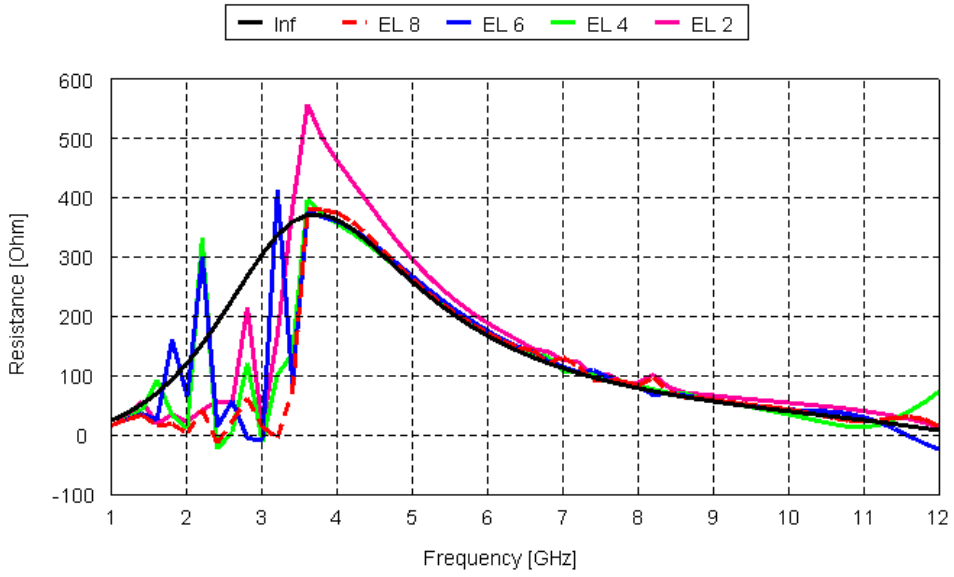

Figure 5-45 – Input resistance at elements 2, 4, 6, & 8 on the Wrapped Bowtie semi-infinite array, finite in *H*-plane, unloaded and at broadside scan

The large bandwidth and tight spatial interlacing of elements in the Wrapped Bowtie array indicate a high level of mutual coupling. If the AGSW was present at 20-30% below resonance in previous work [2-5] with dipoles, perhaps the occurrence AGSW effects over a wider (and separate) frequency range indicates multiple resonances. As with the Rot 9 arrays, the AGSW is observable in the spectral domain using DFFTs. Spectral lobes outside the visible region appear abruptly between 1.4 GHz and 1.6 GHz. At 1.6 GHz, the far-field gain shown in Figure 5-46 shows a sharp dip. The AGSW typically has a minor effect on the far-field pattern, but at this frequency, its effects show. Unlike other arrays analyzed, Figure 5-46 shows limited frequencies where the array gain exceeds the theoretical aperture limit. Of course, these

improvements are minor, and the widely changing input impedance prevents any realization of this gain.

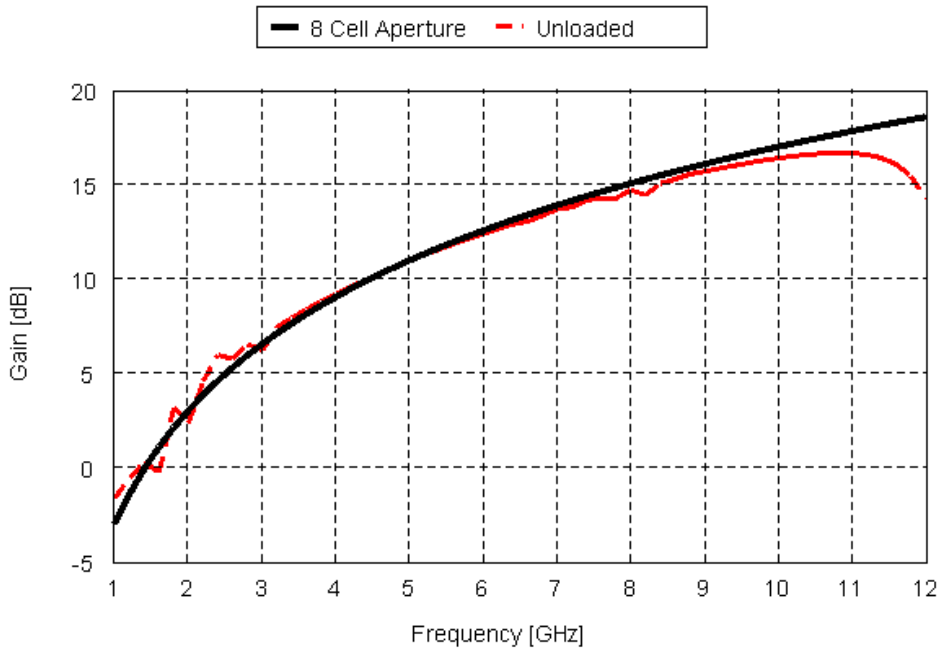

Figure 5-46 – Gain in $+\hat{z}$ for the 8 unloaded, odd numbered Wrapped Bowtie array elements shown in Figure 5-44, finite in *H*-plane, compared to gain from an eight-cell uniform aperture

The effects of the AGSW are evident up through 3.2 GHz, and the 3.4 GHz spectral results appear to be transitional to a well-behaved array. Figures 5-45 to 5-48 show some interesting properties for the 1.6 GHz and 2.4 GHz frequencies. As before, far-field patterns for these frequencies are below. All 15 elements shown determine the far-field patterns. Likewise, traces for both the seven-element row of even-numbered elements and eight-element row of odd-numbered elements are overlaid. Because of differences in array length on each row, the effects of the AGSW change between rows.

1.6 GHz

At 1.6 GHz, the distortions are significantly large as seen in the input resistance. In the spectral domain, there is no distinction between the main, visible lobe and the lobes outside the visible region. In such cases, the integration of currents within the visible region is small compared to the integration of currents outside the visible region.

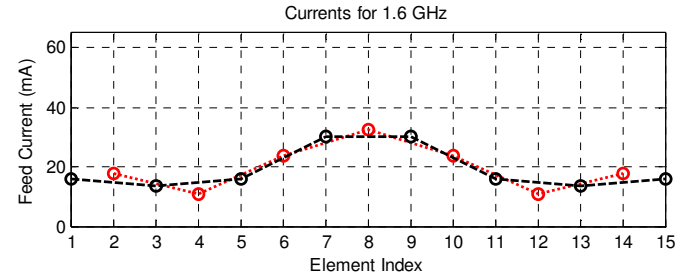

(a) Current magnitudes on element centers

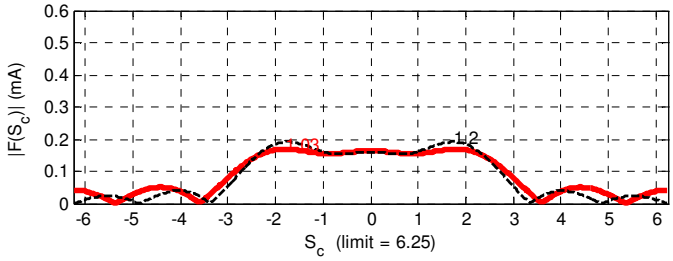

(b) Fourier transform of (a)

Figure 5-47 – Currents on eight-element Rot 9 semi-infinite array at 1.6 GHz

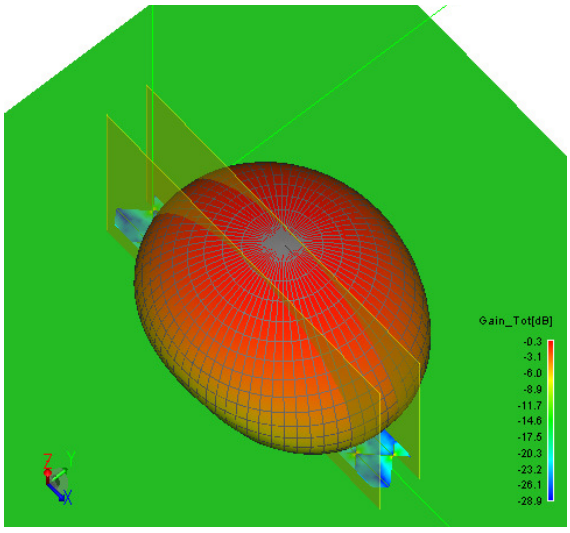

Figure 5-48 – Far-field pattern of the Wrapped Bowtie semi-infinite array at 1.6 GHz

2.4 GHz

Looking again at Figure 5-45, the input resistance on all elements at 2.4 GHz is at a low point for even-numbered elements. The spectral currents show very little within the visible region for these elements, although the adjacent odd-numbered element row has some meaningful lobes in the visible region. In observing the pattern, side lobes are evident and are larger than at 2.2 or 2.6 GHz, as seen in Figure 5-51. These side lobes appear to be from the significant radiation of the AGSW at the edges of the array.

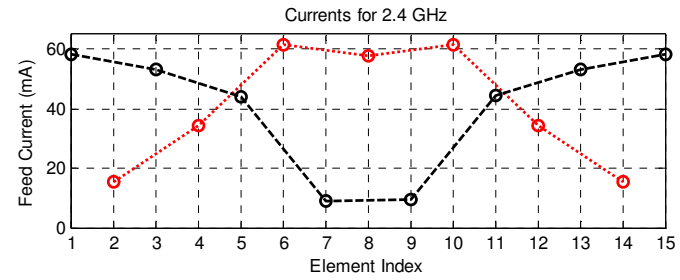

(a) Current magnitudes on element centers

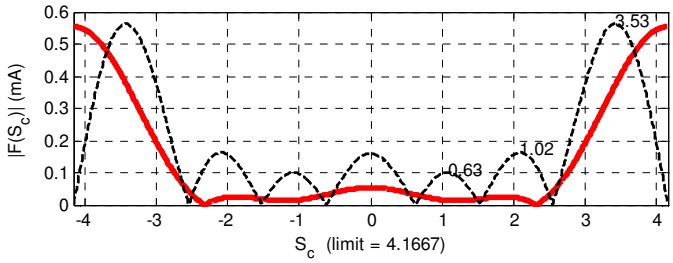

(b) Fourier transform of (a)

Figure 5-49 – Currents across the 7-element Wrapped Bowtie semi-infinite array at 2.4 GHz

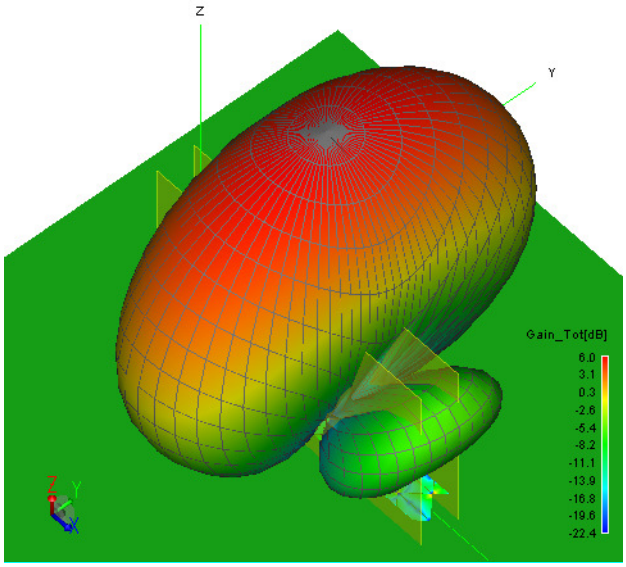

Figure 5-50 – Far-field pattern of the Wrapped Bowtie semi-infinite array at 2.4 GHz

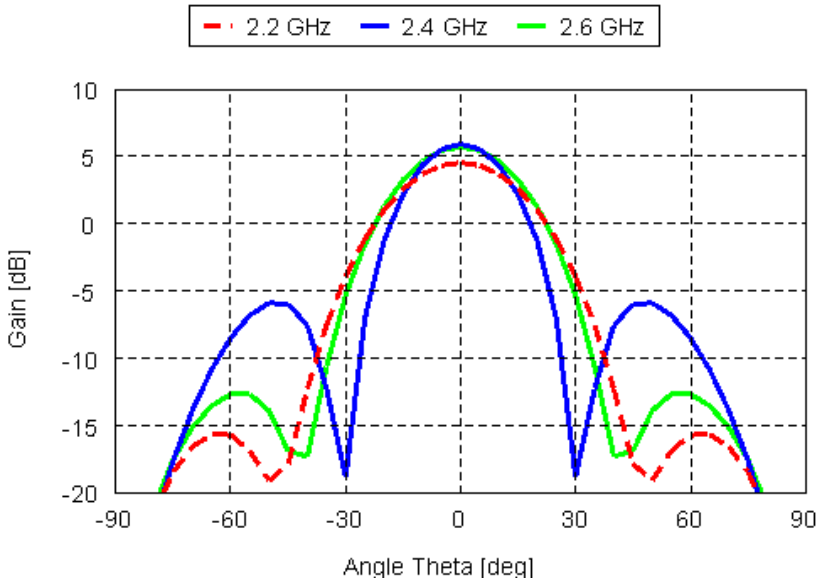

Figure 5-51 – Far-field pattern cut of the Wrapped Bowtie semi-infinite array at 2.2, 2.4, and 2.6 GHz

5.4.2 Suppression of the AGSW

Table 5-2 below presents the loading patterns to control the AGSW. The starting point for this array was the Load04 loading scheme from the Rot9 array; but because of the presences of strong AGSW (or at least the effects), some additional loss is introduced on the center elements.

Since two rows of elements are present in this design, the loads are zigzagged from the center outward in the finite direction.

Table 5-2 – Loadings on the *H*-plane finite Wrapped Bowtie array

Name	R_1	R_3	R_5	R_7	R_9	R_{11}	R_{13}	R_{15}
	R_2	R_4	R_6	R_8	R_{10}	R_{12}	R_{14}	
Unloaded	0	0	0	0	0	0	0	0
	0	0	0	0	0	0	0	
L01	200	100	50	25	25	50	100	200
	200	100	50	25	50	100	200	
L02	200	100	50	50	50	50	100	200
	200	100	50	50	50	100	200	

The loadings in Table 5-2 control the AGSW and smooth out the VSWR to different degrees to have VSWR < 3. Figure 5-52 shows the input impedance of both loading schemes. It is apparent that the L01 scheme (transferred from the Rot 9 array development) sufficiently controls the AGSW and nearly matches the input impedance of the infinite array. Figure 5-53 compares the radiation efficiencies and argues simply for the adoption of the L01 loading scheme, with its marginally higher efficiency. The efficiency directly shows the resulting loss in gain, as compared to the aperture maximum, as shown in Figure 5-54. The maximum gain difference between loading patterns L01 and L02 is under 0.3 dB, and L02 is certainly an acceptable solution.

Figure 5-55 shows the VSWR with the L01 loading scheme for Elements 1-8 on the array, representing the full left side of the array in both rows. Since the row with the odd-numbered elements contains eight elements, while the even-numbered elements are in a row of seven elements, some minor differences emerge. The outer elements, with more loading in place from the center outward, show overall to have wider S3 bandwidths. The limiting bandwidth is the center Element 8, which achieves a 7.41:1 bandwidth over 1.34-9.94 GHz.

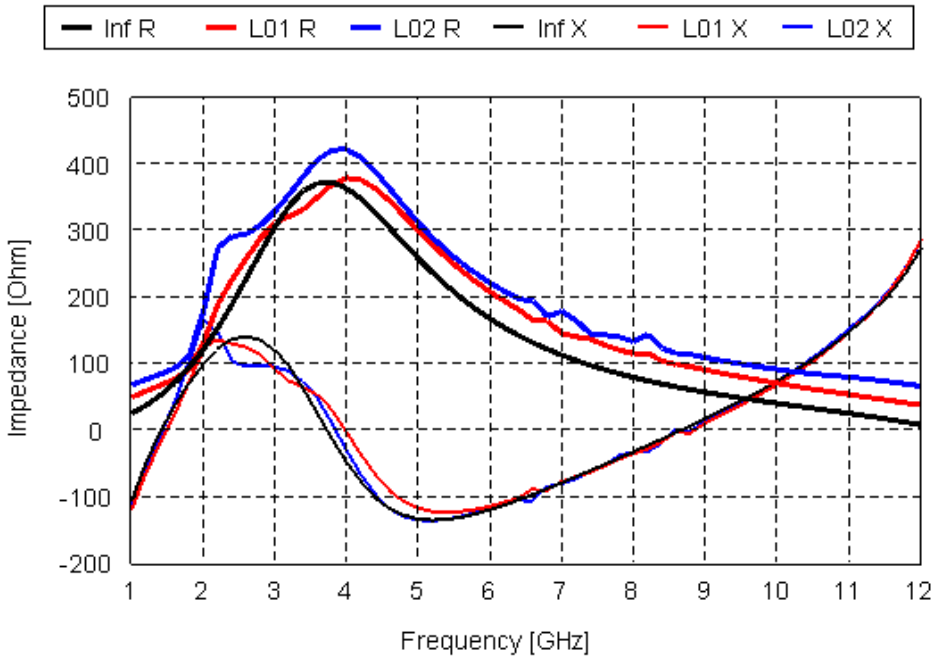

Figure 5-52 – Input impedance for various loads on center element (element 8) of *H*-plane finite Wrapped Bowtie array

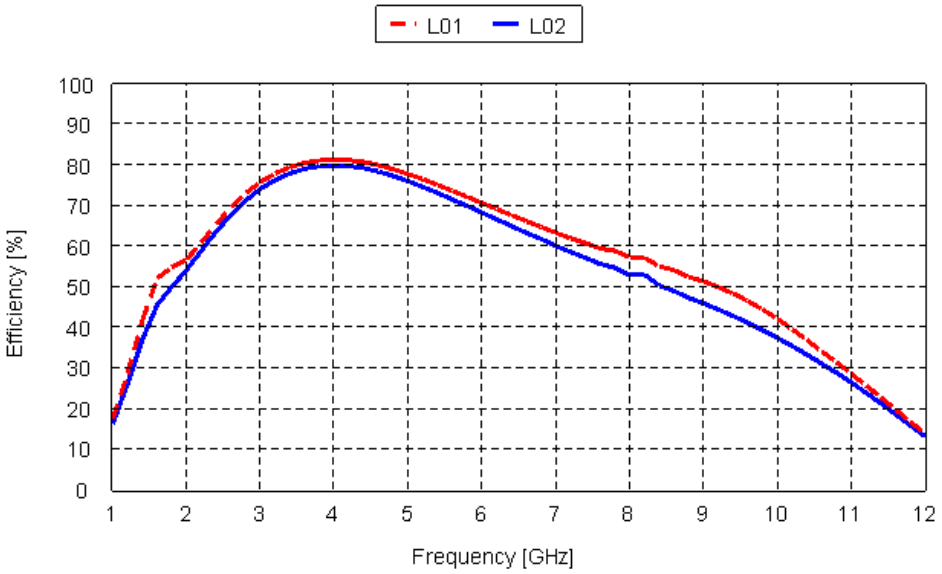

Figure 5-53 – Efficiency of *H*-plane finite Wrapped Bowtie array using various loading patterns

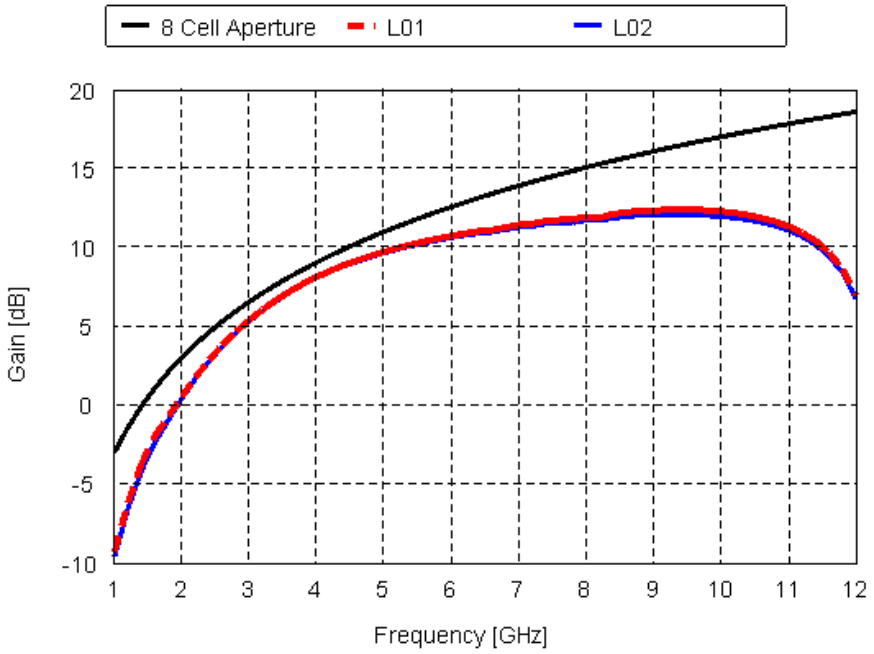

Figure 5-54 – Far-field gain in $+\hat{z}$ for the eight odd-numbered Wrapped Bowtie array elements shown in Figure 5-44, *H*-plane finite and using various loading patterns

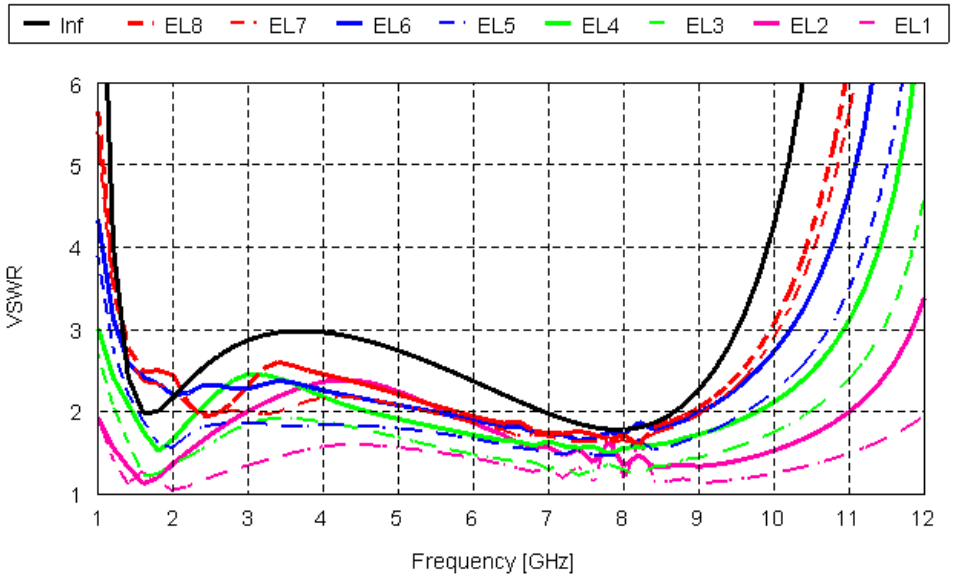

Figure 5-55 – Element VSWR for L01 loading in *H*-plane finite Wrapped Bowtie array[5]

[5] $Z_o = \{300, 300, 250, 250, 200, 200, 175, 175, 175, 200, 200, 250, 250, 300, 300\}$ for elements 1-15.

5.5 Wrapped Bowtie *E*-Plane Finite Array

Figure 5-56 shows the geometry of the semi-infinite Wrapped Bowtie array finite in $\hat{y}$ or the *E*-plane. Sixteen elements are shown with even numbered elements split between the $\pm\hat{x}$ directions. Presented throughout this section are results for the odd-numbered elements. These lie down the middle, with Element 1 at the far left. As before, the square unit cell for this array is 21.21 mm on each side.

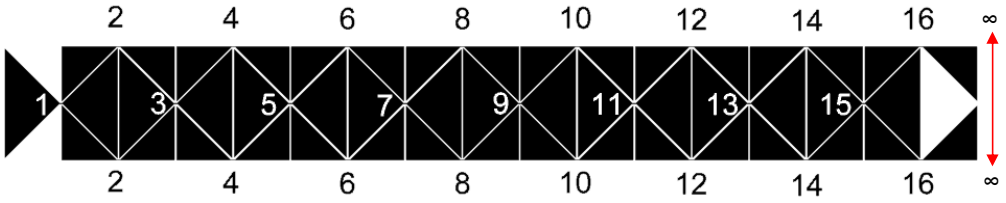

Figure 5-56 – Geometry of 16-element Wrapped Bowtie *E*-plane array

5.5.1 The Unloaded Array

With the rotation of the periodic boundaries, there are now 16 ports in the *E*-plane finite array. Both even-numbered (here, on the outside and split in Figure 5-56 because of its meeting with the periodic boundary) and odd-numbered elements down the center are evaluated. Both "columns" of elements are eight elements in length, but neither is symmetric in the finite direction. This geometry leads to some interesting currents across the array. Again, the distortion from the AGSW affects a substantial portion of the frequency band from about 1.8 to 4.8 GHz. Some other grating lobe distortions occur at 11.5 GHz, which is outside the operating band.

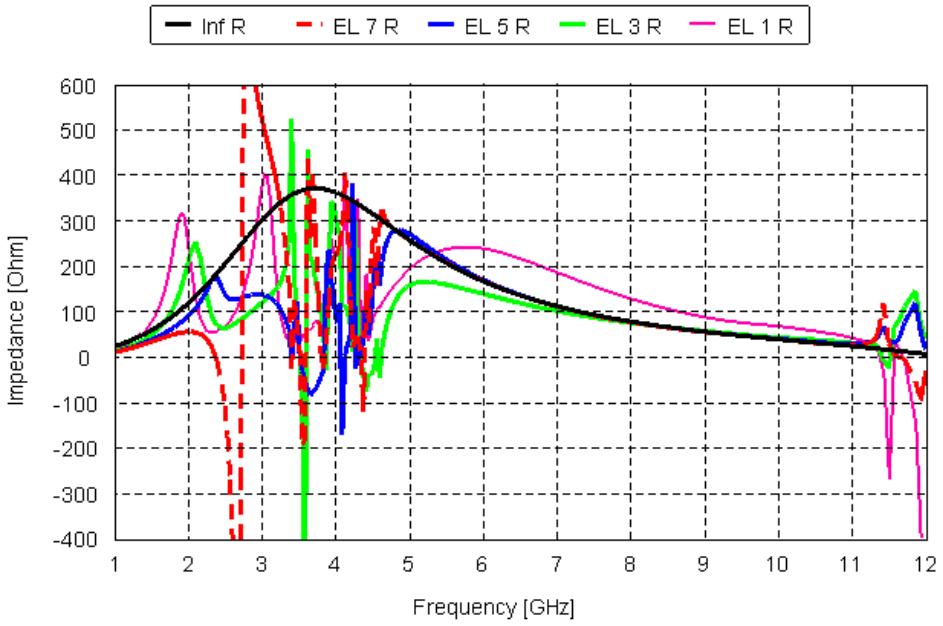

Figure 5-57 – Input resistance at elements 2, 4, 6, & 8 on the Wrapped Bowtie semi-infinite array, finite in *E*-plane, unloaded and at broadside scan

The large bandwidth and tight spatial interlacing of elements in the Wrapped Bowtie array indicate a high level of mutual coupling. Spectral lobes outside the visible region do not appear as with some other semi-infinite array configurations. Here, the main visible lobe becomes rather wide and extends significant spectral currents outside the visible region. As with the *H*-plane finite configuration, Figure 5-58 shows limited frequencies where the array gain exceeds the theoretical aperture limit comprised of 8.5 unit cells. The gain comes from the 16 elements shown in Figure 5-56, and not any form of infinite array. A large dip in gain occurs at 2.3 GHz. Closer examinations of this and another dip at 4.2 GHz are below.

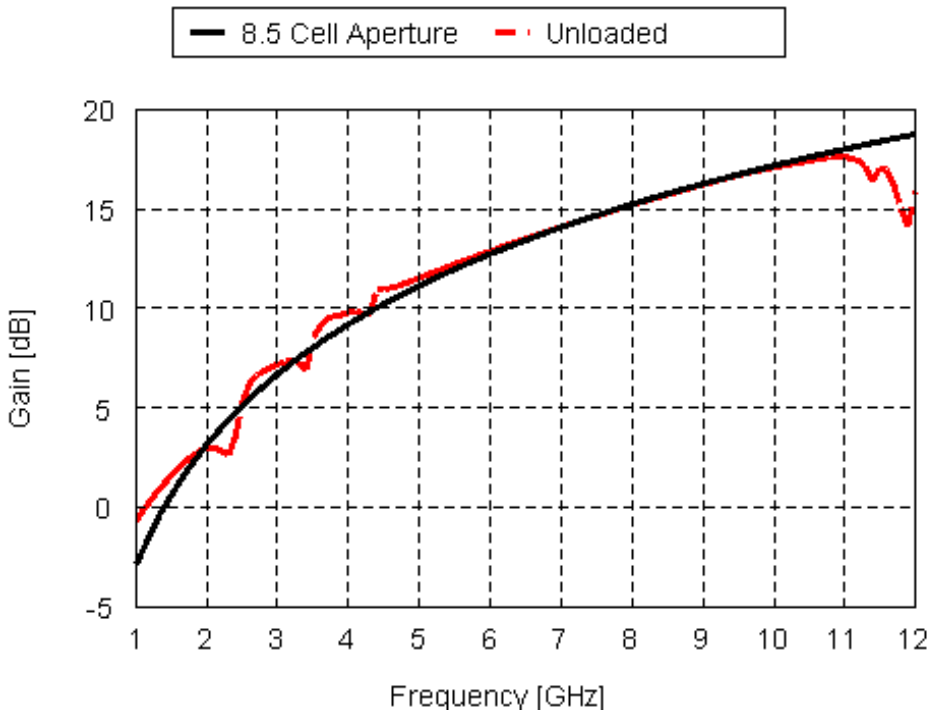

Figure 5-58 – Gain comparison in $+\hat{z}$ for the 16 unloaded Wrapped Bowtie array elements shown in Figure 5-56, finite in *E*-plane, compared to the gain from an 8.5-cell uniform aperture

2.3 GHz

At 2.3 GHz, asymmetries in the spectral currents are evident, as are the main peaks lying outside the visible region. The resulting pattern does not have side lobes, which may be in part to the low frequency and small electrical size of the aperture. At this frequency, however, there is a dip in the far-field gain. This appears to be through a widening of the beam (as compared to nearby frequencies), instead of sidelobes.

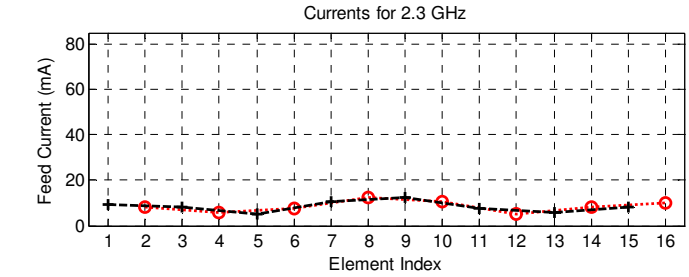

(a) Current magnitudes on element centers

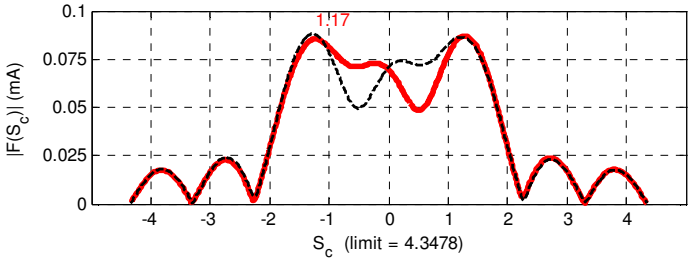

(b) Fourier transform of (a)

Figure 5-59 – Currents on eight-element Rot 9 semi-infinite array at 2.3 GHz

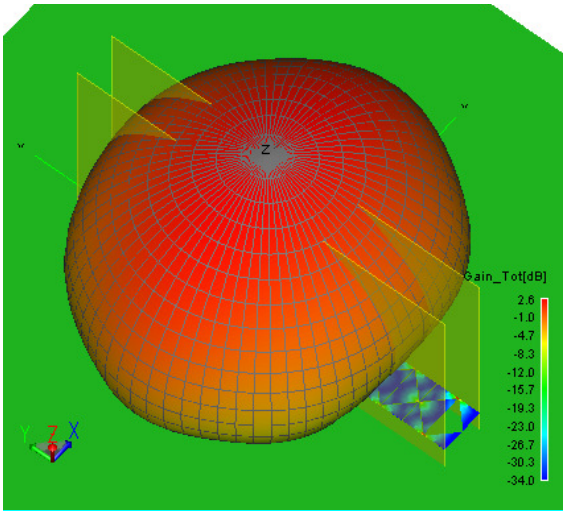

Figure 5-60 – Far-field pattern of the Wrapped Bowtie semi-infinite array at 2.3 GHz

4.2 GHz

At 4.2 GHz, again there are asymmetries, and even not symmetries between the even-numbered and odd-numbered elements in the two columns. The large peaks outside the visible region are, relative to $s_{c,\max}$, farther from the visible region. At 4.2 GHz, side lobes are evident, as contrasted with the array behavior at 2.3 GHz.

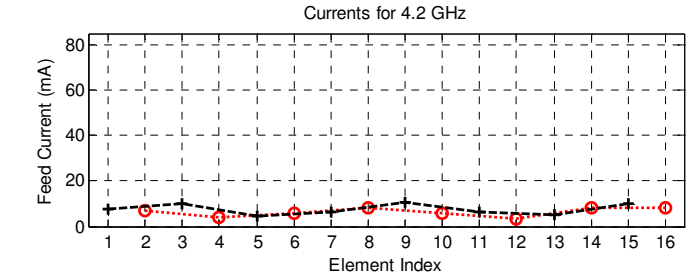

(a) Current magnitudes on element centers

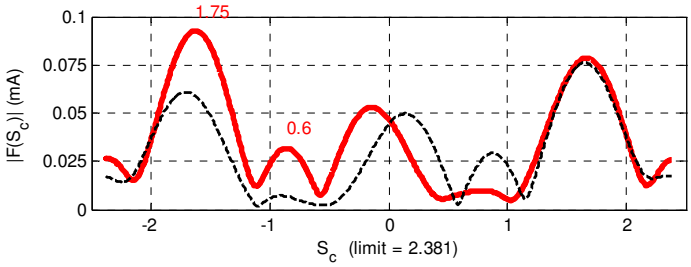

(b) Fourier transform of (a)

Figure 5-61 – Currents on eight-element Rot 9 semi-infinite array at 4.2 GHz

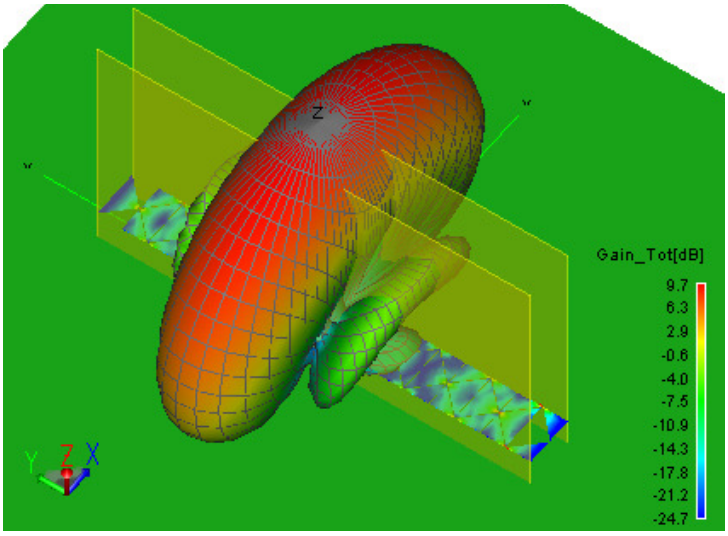

Figure 5-62 – Far-field pattern of the Wrapped Bowtie semi-infinite array at 4.2 GHz

5.5.2 Suppression of the AGSW

Table 5-3 below presents the loading patterns to control the AGSW. (Since two rows of elements are present in this design, the loads are shifted a half-space from the center outward in the finite direction.) The L01 and L02 loading patterns match those for the array finite in $\hat{x}$. Both the L01 and L02 loading schemes have minor VSWR spikes on their center elements around 2.6 GHz, where the input reactance peaks and transitions (see Figure 5-63). With the increased resistive loading, elements require higher reference impedances. Additional adjustments to the reference impedance may lower some VSWR spikes, but this overall limits the bandwidth. Scheme L01 achieves a frequency range from 1.5-9.3 GHz, for a 6.2:1 S3 bandwidth; scheme L02 ranges from 1.6-9.6 GHz for a 6.0:1 bandwidth.

Table 5-3 – Loadings on the *E*-plane finite Wrapped Bowtie array

Name	R_1	R_3	R_5	R_7	R_9	R_{11}	R_{13}	R_{15}	
		R_2	R_4	R_6	R_8	R_{10}	R_{12}	R_{14}	R_{16}
Unloaded	0	0	0	0	0	0	0	0	
		0	0	0	0	0	0	0	0
L01	200	100	50	25	25	50	100	200	
		200	100	50	25	25	50	100	200
L02	200	100	50	50	50	50	100	200	
		200	100	50	50	50	50	100	200
L03	200	150	100	50	50	100	150	200	
		200	150	100	50	50	100	150	200

Scheme L03 includes additional loading. This loading scheme fully suppresses the VSWR spikes and extends the minimum frequency range across all elements from 1.23-10.48 GHz, for an 8.5:1 S3 bandwidth. This bandwidth is substantial and a large increase over even the infinite Wrapped Bowtie array S3 bandwidth of 7.24:1. This increased loading clearly results in lower radiation efficiency (Figure 5-64) and lower gain (Figure 5-65), as compared to the former two loading schemes. Although efficiency drops substantially with the L03 loading across frequency, there is a less than 1.2 dB drop in gain. Figure 5-66 shows the VSWR on all odd-numbered elements using the L03 loading scheme. Unfortunately, while the resistive loading expands the upper frequency range most notably, it clearly comes through a loss in radiation efficiency. Ideally, a frequency-selective resistive loading would work best here.

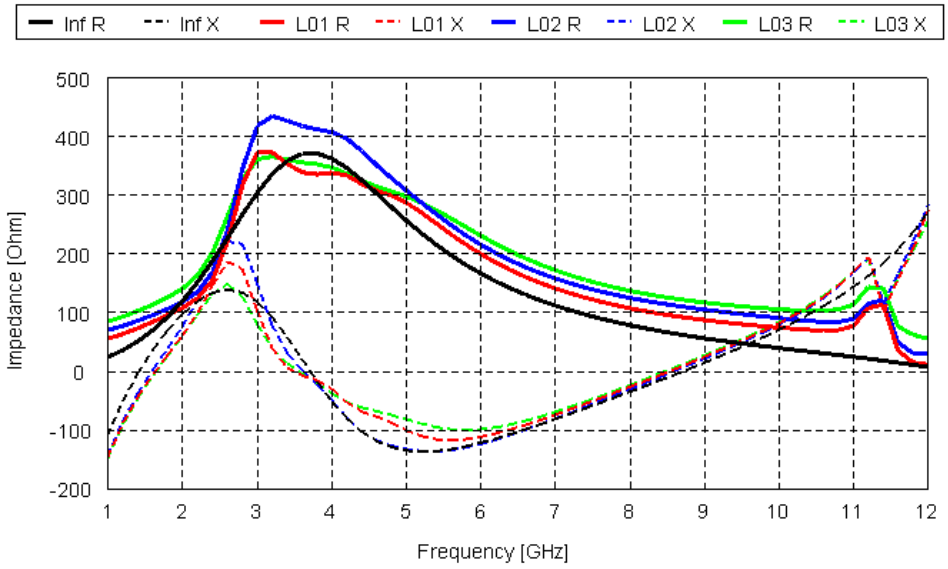

Figure 5-63 – Input impedance for various loads on center element of *E*-plane finite Wrapped Bowtie array

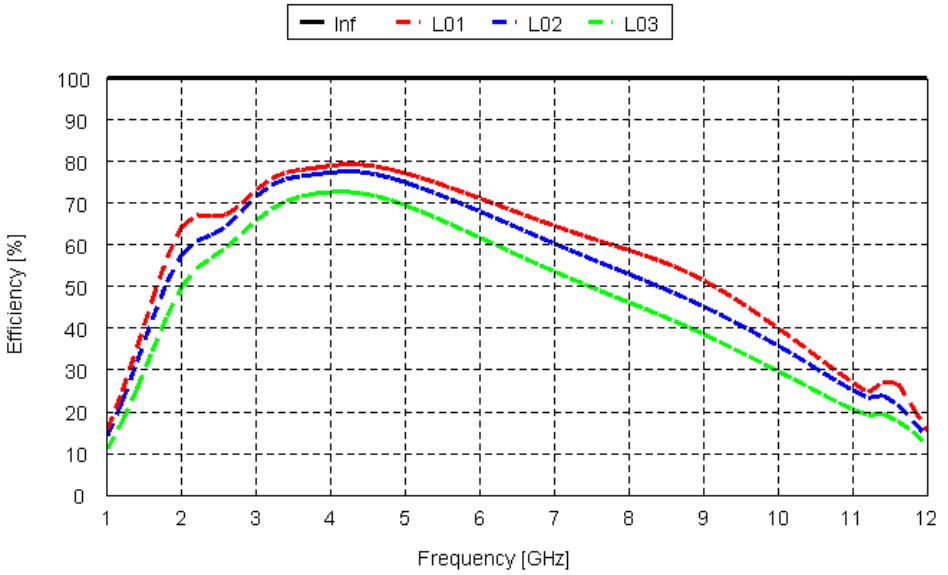

Figure 5-64 – Efficiency of *E*-plane finite Wrapped Bowtie array using various loading patterns

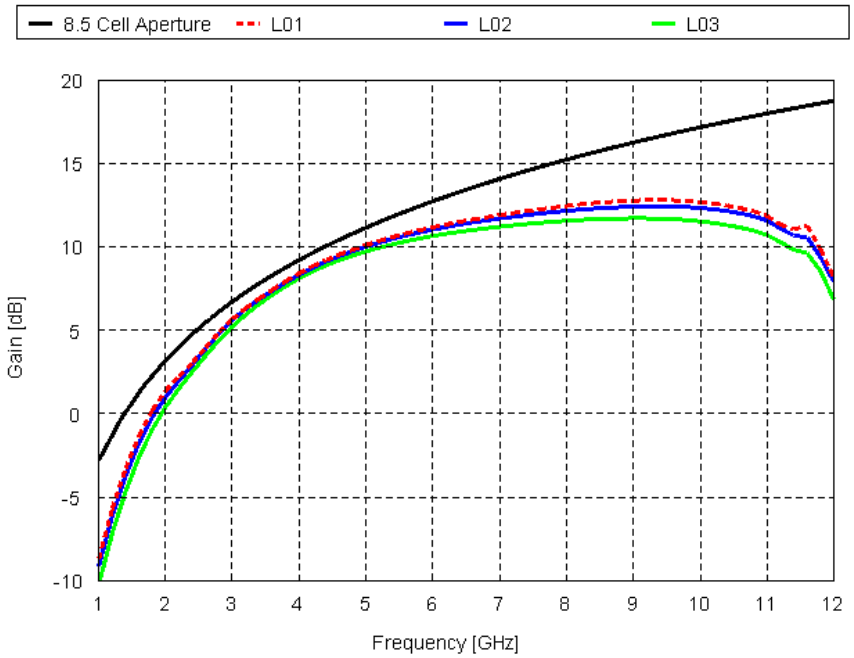

Figure 5-65 – Gain comparison in $+\hat{z}$ for the 16 Wrapped Bowtie array elements shown in Figure 5-56, finite in *E*-plane and using various loading schemes, compared to the gain from an 8.5-cell uniform aperture

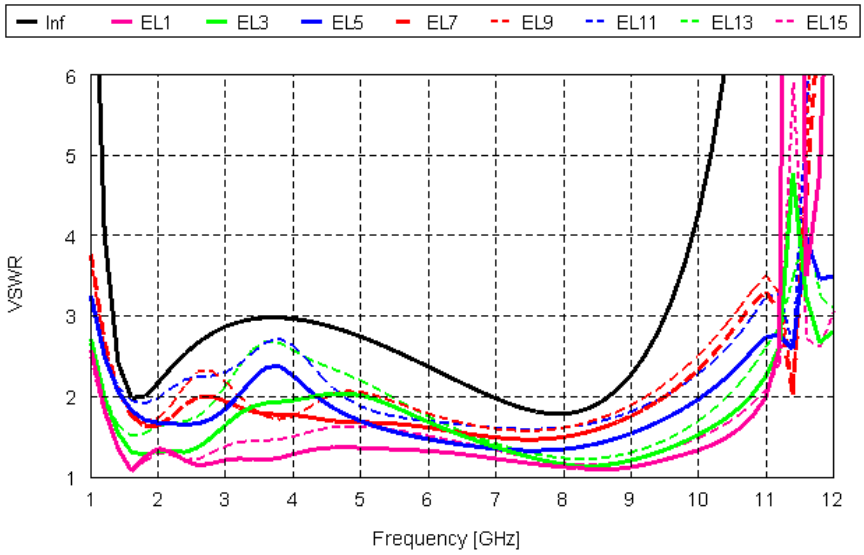

Figure 5-66 – Element VSWR for L03 loading in *H*-plane finite Wrapped Bowtie array [6]

[6] $Z_o = \{300, 250, 250, 200, 200, 250, 250, 300\}$ for odd elements 1-15.

5.6 Array Conforming

After a thorough examination of the unloaded and loaded behavior of the Rot 9 and Wrapped Bowtie arrays in their two semi-infinite forms each, this section investigates the other option to control the AGSW. The conforming of the array plane sheds power from the AGSW and reduces its overall negative effects. As the AGSW travels along the array, minor differential curvatures act as small discontinuities in the otherwise periodic structure and allow power to radiate away from the array; this is comparable to the creeping wave in the UTD scheme. While Munk [4] presents this as an option for frequency selective surfaces (FSS), its value in active arrays is not defined or bounded. There is a paucity of literature on conformal tightly-coupled arrays.

For this study, a cylindrical conformation around the y-axis is implemented. This geometry makes the array (for these less burdensome, semi-infinite simulations) finite in $\hat{x}$ and infinite in $\hat{y}$. The *H*-plane finite Rot 9 array requires the loading scheme Load 05 to suppress the AGSW, and to it, this section compares two cylindrical conforming radii: 86.05 mm (Conf1) and 57.46 mm (Conf2). Conf1 is flatter than Conf2 as seen in Figure 5-67 for Conf1 and Figure 5-68 for Conf2. All elements are at $h = 12\,\text{mm}$ above the conformed ground plane.

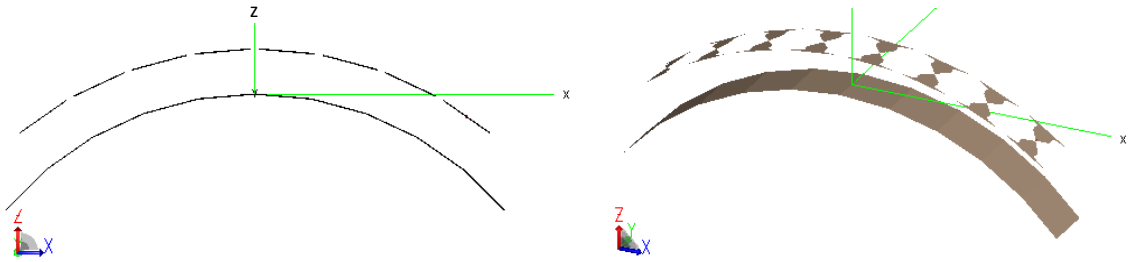

Figure 5-67 – Geometry of one row of the Conf1 semi-infinite array configuration

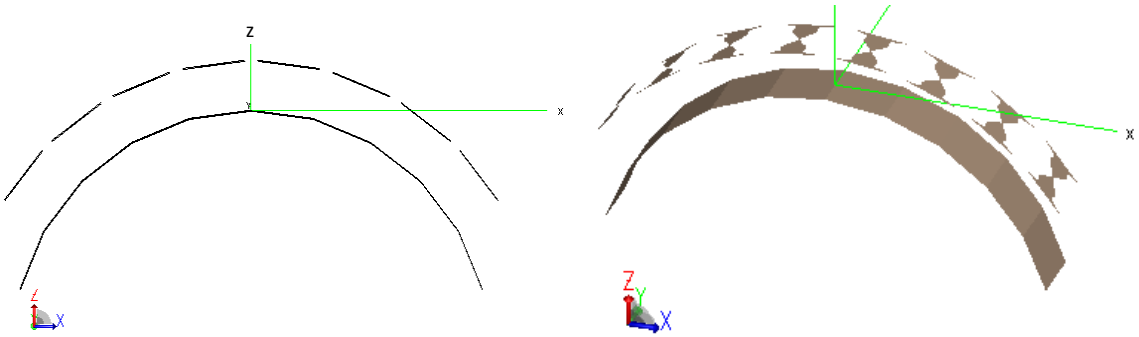

Figure 5-68 – Geometry of one row of Conf2 in a semi-infinite array configuration

The motivations of conforming an antenna array are different than conforming a FSS, although both may be beneficial to reduce the AGSW. For conformed array geometries, there are several characteristics that function concurrently, namely:

1) Less ohmic loading is required, leading to higher radiation efficiency.
2) Less loading will reduce bandwidth[7].
3) A conformed array will have a wider beamwidth[8].
4) The wider beamwidth means a lower directivity.
5) If conforming is applied to the ground plane (as done here), the elements are spread apart slightly, leading to lower mutual coupling.
6) Lower mutual coupling leads to less bandwidth.

This section takes a similar approach with the conformed geometries, within a discrete set of loading options (typically 25-Ohm increments). The loading patterns in Table 5-4 were the minimal amounts needed for AGSW suppression and maximization of radiation efficiency. (Figure 5-70 and Figure 5-71 show how these loading schemes barely control AGSW at around 3 GHz.) Although tighter conformations should result in less loading, Conf2 requires nearly the same loading as Conf1. The lower loading schemes needed with the conformed geometry result in more efficiency of approximately 5-10%, as seen in Figure 5-69.

Table 5-4 – Loadings on the *H*-plane finite Rot 9 array, flat and conformal

Name	R_1	R_2	R_3	R_4	R_5	R_6	R_7	R_8
Flat Load05	100	50	25	0	0	25	50	100
Conf1	100	50	0	0	0	0	50	100
Conf2	100	50	0	0	0	0	50	100

[7] Narrowband antennas follow closely the relationship $BW_{loaded} = BW_{unloaded} / e_r$, which describes increased bandwidth with more loading and reduced radiation efficiency, to the point of an infinite bandwidth. This relationship continues generally for wideband elements, but it does not have such a clear expression.

[8] This assumes the array has no wideband phase control to adjust for phase differences stemming from conformation.

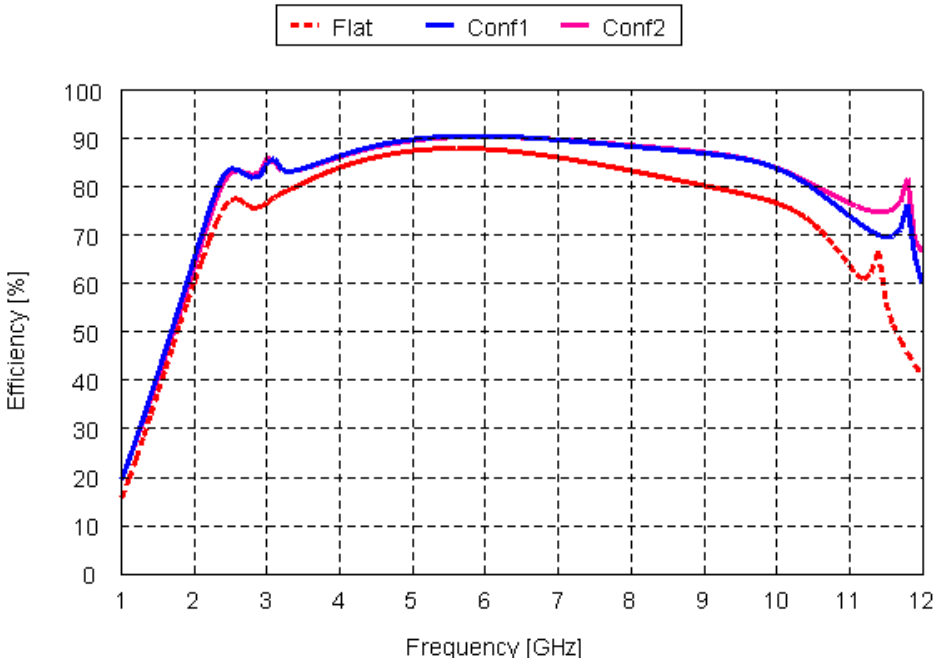

Figure 5-69 – Conformal and Flat Rot 9 array efficiency comparison

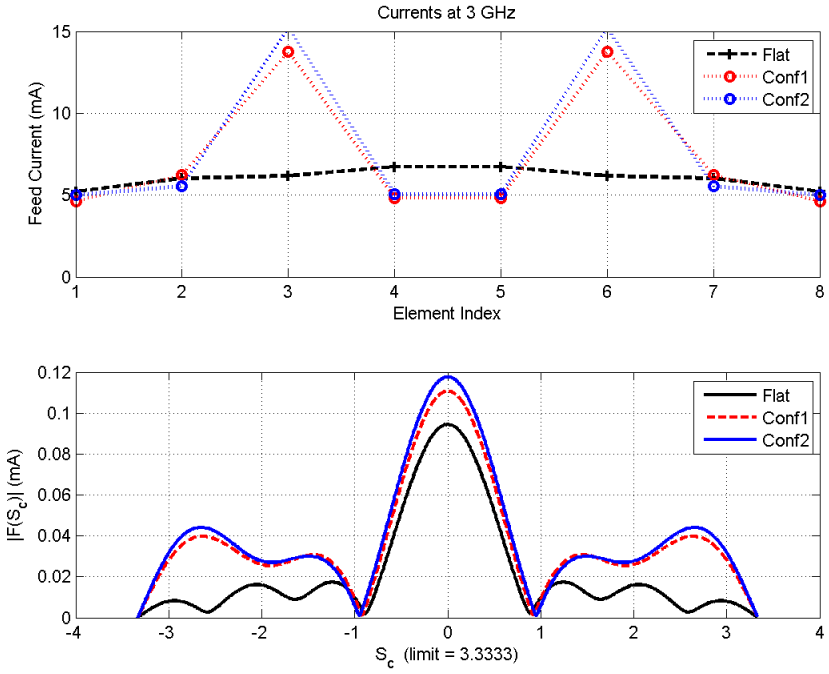

Figure 5-70 – Currents at 3 GHz for the Rot 9 Flat, Conf1, and Conf2 arrays

Both the losses from loading and the spatial separation of elements pursuant with ground plane conformation decrease the overall bandwidth. The difference from loading may not be evident, but the differences from tighter conformations are evident, as seen between the Conf1 and Conf2 geometries. In Figure 5-71, the lower frequencies are nearly the same for all cases. Differences arise at the higher frequencies and, with only the radius of curvature differing between Conf1 and Conf2 (i.e., loading schemes match), the lower mutual coupling is evident in its impact on bandwidth. Table 5-5 shows the S3 bandwidths and frequency limits for infinite, flat, and both conformed arrays.

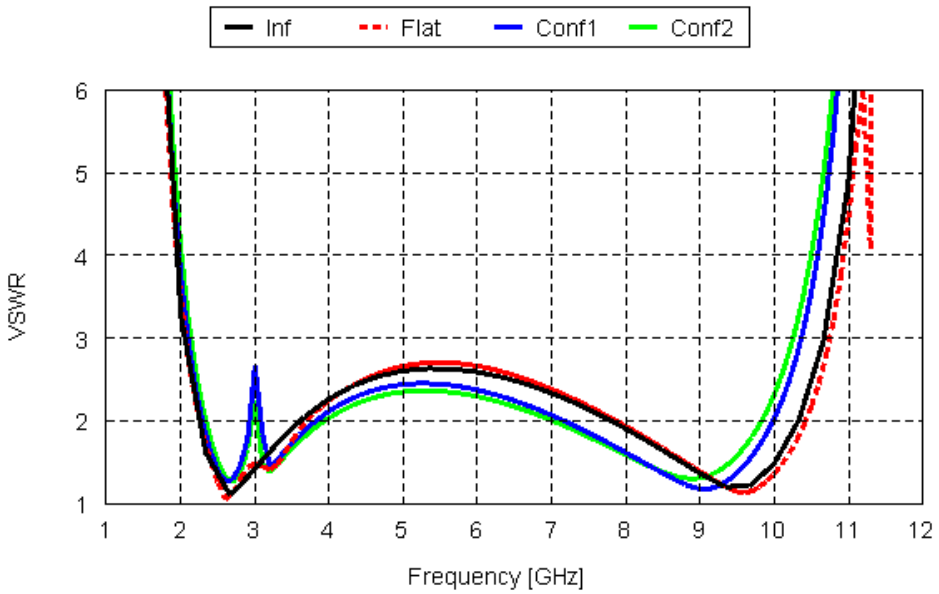

Figure 5-71 – VSWR on center element of Rot 9 Flat, Conf1, and Conf2 arrays[9]

Table 5-5 – Bandwidth results of conformed arrays

Name	S3 Bandwidth	f_L (GHz)	f_u (GHz)
Infinite	5.23	2.04	10.67
Flat Load05	5.22	2.06	10.75
Conf1	4.90	2.11	10.36
Conf2	4.79	2.14	10.25

[9] $Z_o = 100$ Ohms

The last major relationship for conformed arrays is between the gain and beamwidth. Although conforming achieves approximately 5-10% higher efficiencies (as shown), the broadside gain is substantially lower: between 1-4 dB for Conf1 array and between 2.5-7.5 dB for the Conf2 array. This follows a divergence between a beamwidth that narrows for the flat array with increased frequencies, and those of the conformed arrays that are more consistent. The gain reductions may be acceptable for applications where a more consistent beamwidth is warranted, such as in sector coverage of an area.

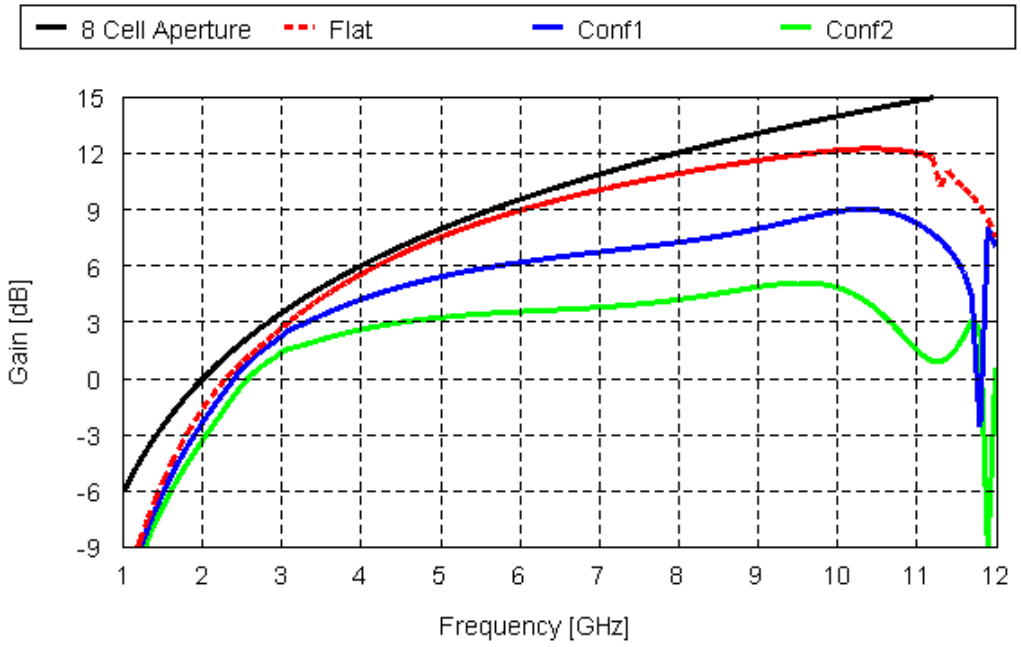

Figure 5-72 – Conformal and Flat Rot 9 array broadside gain comparison with loading schemes as shown in Figure 5-4

Figure 5-6 lists the 3-dB beamwidths for the three arrays. The beamwidth of the flat array gradually narrows. Conf1 stabilizes around about a 40° bandwidth, and Conf2 displays about a 70° beamwidth. Commercially available cellular antennas have, in general, 90°, 65°, and 35° horizontal beamwidths. While such a design may be the goal, conforming is a poor choice solely to reduce the AGSW effects.

Table 5-6 – 3-dB Beamwidths of flat and conformed arrays (in degrees)

Freq (GHz)	Flat	Conf1	Conf2
2	58.6	65.6	84.8
3	41.6	48.0	56.4
4	32.0	39.2	57.8
5	26.0	36.6	71.0
6	22.8	37.2	77.2
7	20.0	42.0	74.0
8	18.2	45.0	70.0
9	16.6	42.2	66.8
10	15.6	37.4	66.4

5.7 Array Scanning

Section 4.8 details the effects on impedance, gain, side-lobe levels, and the presence of scan blindness for scanned infinite arrays. The questions investigated in this section using semi-infinite arrays are how the finite dimension of the array affects performance and how the loading must change to sufficiently suppress the AGSW when the array is scanned off broadside. This section uses the *H*-plane finite Rot9 array of eight elements ($\infty \times 8$) as shown in Figure 5-1. Elements incorporate additional series resistances of $\{100, 50, 25, 0, 0, 25, 50, 100\}$ Ohms across the array at their feeds, which is the Load05 loading scheme outlined in Table 5-1. The Load05 scheme is sufficiently effective in suppressing the AGSW for a broadside scan, but it is less effective when scanning occurs. Even moderate scanning greatly increases the magnitude of the AGSW; this is seen in impedance spikes and as lobes outside the visible region in the spectral domain.

Figure 5-73 and Figure 5-74 shows such an effect in the input impedance. Recall that in the unloaded array, the AGSW was present over a range of 2.4-3.6 GHz per Figure 5-5. When the array is scanned off broadside, the AGSW effects are again visible. Negative impedances are seen on the center element between 3.3-3.6 GHz, depending on the scan angle. This indicates that additional loading is required to suppress such a wave in a scanned array and is likely the result of tighter coupling when the aperture projection in the scan direction is reduced. Although negative resistances are present, it is clear in contrasting these results to the infinite array results of Chapter 4 that no disturbances exist in this 3 GHz frequency range. The AGSW only becomes destructive in array with finite boundaries. Separately, and as with the infinite array scans of

Figure 4-60, the impedance for semi-infinite scans shows the emergence of scan blindness above 11 GHz. Likewise, the input resistance increases with scan angle, but to greater maximums.

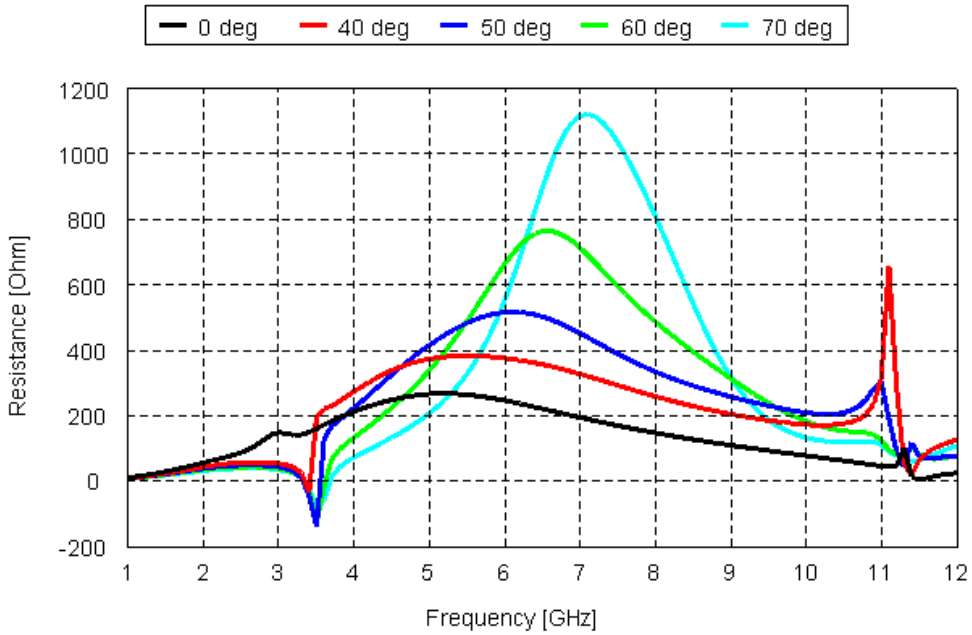

Figure 5-73 – Input resistance on the center element (#4) of Figure 5-1 for arrays with desired scan angles θ_o = 0, 40, 50, 60, and 70 degrees

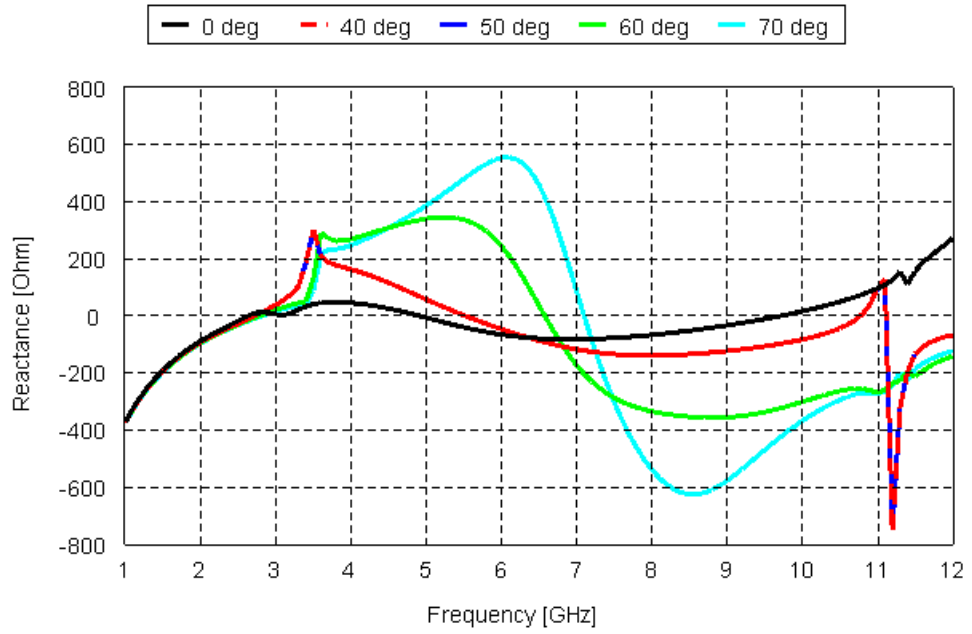

Figure 5-74 – Input reactance on the center element (#4) of Figure 5-1 for arrays with desired scan angles θ_o = 0, 40, 50, 60, and 70 degrees

These changes in the input impedance directly limit the array bandwidth. Again, considering the center elements that typically have the least bandwidth due to their limited loading and a reference impedance $Z_o = 100$ Ohms, *H*-plane scanning is exceptionally detrimental to the bandwidth of this Rot 9 semi-infinite array. Figure 5-75 shows the array bandwidth reduce to be exceptionally narrowband between 2-3 GHz, but otherwise unusable. The alternative is increased loading and a corresponding reduction in radiation efficiency.

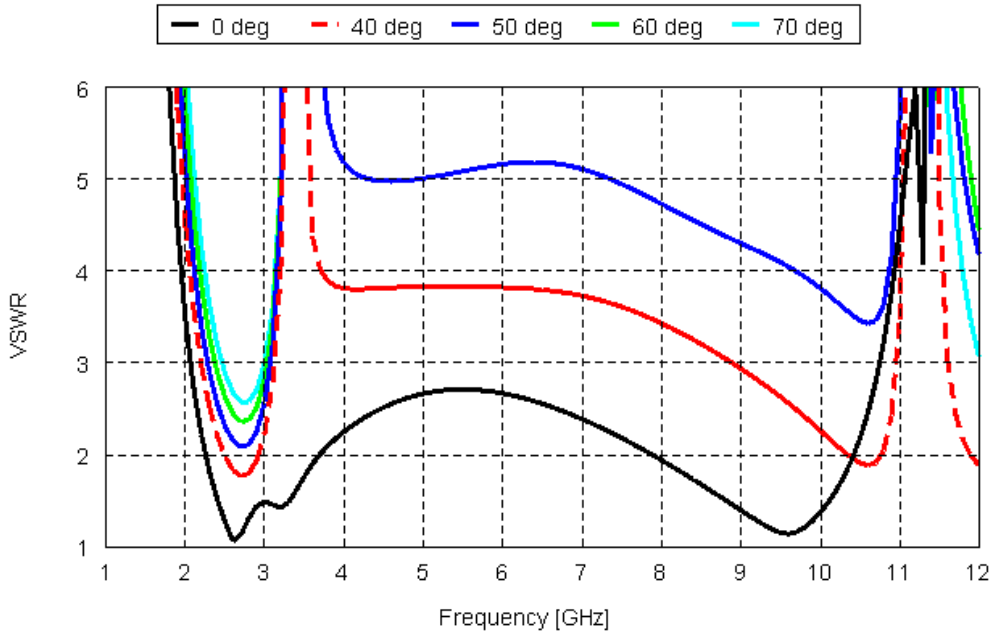

Figure 5-75 – VSWR on the center element (#4) of Figure 5-1 for arrays with desired scan angles θ_o = 0, 40, 50, 60, and 70 degrees; Z_o=100 Ohms for all.

Since scanning is a common function in arrays, the applicability for arrays of only eight elements may be less than ideal indicators of how the array will perform when scanned. Larger arrays will have a similar loading pattern to suppress the AGSW, but this pattern will be limited, as with only eight element arrays, to the out three or four elements. This would apply even if the array were much larger. Therefore, scanned fields would not be as strongly coupled into the adjacent elements that are loaded.

5.8 Summary

This chapter has advanced the designs of the Rot 9 and Wrapped Bowtie arrays, and tightly-coupled arrays in general, using semi-infinite array modeling. This modeling uses FEKO® with a single periodic boundary condition (PBC). This expansion of the problem beyond infinite techniques introduces finite edge effects. Semi-infinite techniques allow modeling of the arrays without the extensive computational burdens needed with finite arrays.

The focus of this chapter has been to identify and mitigate the array-guided surface waves (AGSW) using semi-infinite arrays, with separate finite $\hat{x}$ and $\hat{y}$ directions (or, *H*-plane finite and *E*-plane finite arrays, respectively). Primarily, the designs use resistive loads and tuned designs to control the AGSW, maximize the VSWR < 3 bandwidth, and achieve the highest radiation efficiencies across frequency. Subsequently, cylindrical conformation to the "controlled" Rot 9 array shows its limited value in controlling the AGSW. The addition of conformation allows some AGSW power to radiate away from the array, which then requires less loading for AGSW control. The conformal designs are investigated and compared to the flat arrays, where as before, the loading also seeks to maximize the gain (efficiency) and bandwidth. Array conforming is introduced in the literature as a method to control the AGSW primarily in frequency-selective surfaces (FSS). Although the conformation does reduce the AGSW, conformation by itself does not control the AGSW in tightly-coupled arrays.

Lastly, this chapter presents a brief overview of the effects of array scanning on tightly-coupled arrays. When scanned, such arrays experience significant bandwidth reductions, to the extent the author believes to make array phasing a poor choice for arrays of this size. (Larger arrays would require equivalent loading, but proportionately, these loaded elements would be a smaller percentage of the total array.) Mechanical steering of the array would deliver the wide bandwidths desired of tightly-coupled arrays.

5.9 References

[1] T. R. Vogler and W. Davis, "Parasitic Modifications to the Finite, Foursquare Antenna Array," presented at the USNC-USRI National Radio Science Meeting, Boulder, CO, 2008.

[2] T. R. Vogler and W. Davis, "Surface Waves in Medium-Sized, Tightly Coupled Planar Arrays," presented at the USNC-USRI National Radio Science Meeting, Boulder, CO, 2009.

[3] J. B. Pryor, "Suppression of surface waves on arrays of finite extent," M.S. Thesis, Dept. of Electrical and Computer Engineering, The Ohio State University, Columbus, Ohio, 2000.

[4] B. A. Munk, *Finite Antenna Arrays and FSS*. Hoboken, NJ: Wiley-Interscience, 2003.

[5] D. S. Janning, "Surface Waves in Arrays of Finite Extent," Ph.D. Dissertation, Dept. of Electrical and Computer Engineering, The Ohio State University, Columbus, OH, 2000.

[6] W. Stutzman and G. Thiele, *Antenna Theory and Design*, 2nd ed. New York: John Wiley & Sons, Inc., 1998.

CHAPTER 6

Designs of Finite Tightly-Coupled Arrays

This chapter continues the advancement of the technical details of designs and analysis of tightly-coupled planar arrays. It builds upon the background presented in Chapters 2 and 3 and the designs in Chapters 4 and 5. Chapter 4 presented several methodical steps in designing and tuning infinite array designs for tightly-coupled, and thus wideband, arrays. Chapter 5 advanced the dominant designs, the Rot 9 and Wrapped Bowtie elements, using semi-infinite. The finite dimension in these arrays allows for the formation of the array-guided surface wave (AGSW), which is only detrimental to the active impedance on elements in the array. Chapter 5 described several loading and conformal options to suppress, through absorption or radiation, the power in the AGSW.

Chapters 4 and 5 used infinite and semi-infinite analyses to gain insight into the coupling mechanisms in tightly-coupled arrays because they were much less computationally burdensome than finite simulations. They allowed for the specific development of techniques to mitigate the AGSW, which this chapter will apply to finite arrays. Finite arrays sized around 8×8 elements, with substantial portions of the array aperture covered by conducting surfaces, present a heavy computational burden to analyze over the wide frequency range of their operation. Proper electrical and magnetic symmetry across the mid-lines in the array surface reduce the burden to a tolerable level. In many ways, given the background of Chapters 4 and 5, the results of this chapter are not surprising. However, this chapter also begins to address some issues of construction of such arrays.

Construction details are imperative to the value of any design. If a design is unbuildable, does it have any real value? Perhaps some, in illustrating and conceptualizing design methodologies for tightly-coupled arrays. Construction details, to include the feed network, are substantial and ongoing challenges that this chapter does not solve. If the thickness of the planar array is not to grow substantially, the greatest obstacle is likely the need for a wideband, balanced feed in a small per-element space. Discussions of such issues are at the end of this chapter. Other specifics like substrate types and properties, the needed adjustments to the elements because of the presence of substrates, mechanical supports, power handling, ruggedization, etc. are not. Real construction details may also influence the loading approach taken in Chapter 5 and this chapter. Resistive loads on excited elements increase the reference impedance, and as many as five different feed designs may be required to feed these.

In Chapter 7, beyond summarizing the research of this dissertation and enumerating its contributions, it presents several items for future work, including construction details and research into early design trade-offs that impact construction.

6.1 The Finite Rot 9 Array

This section considers the Rot 9 array in its finite form. Figure 6-1 shows the geometry of an 8×8 element Rot 9 array with the element numbering in Figure 6-2. As in Chapters 4 and 5, an infinite PEC ground plane is located behind this array (in the view shown, below) at a distance $h = 12\,\text{mm}$. The Rot 9 element has a length of $L = 14.9$ mm, leaving a small inter-element gap of $g_{element} = 2g_{cell} = 0.1$ mm between elements, as shown in Figure 4-49 and repeated in Figure 6-2(b). In effect, and as expected, the unit cells used in the infinite and semi-infinite analyses of the previous two chapters are maintained in the finite design.

In Chapter 5, two loading schemes were sufficient to suppress the AGSW in the *E*-plane and *H*-plane finite Rot 9 arrays, each with 8 elements in the finite direction. Table 6-1 repeats these. When expanded to both dimensions, simulations showed that the greater loading scheme, Load04 was necessary to suppress the AGSW in all directions.

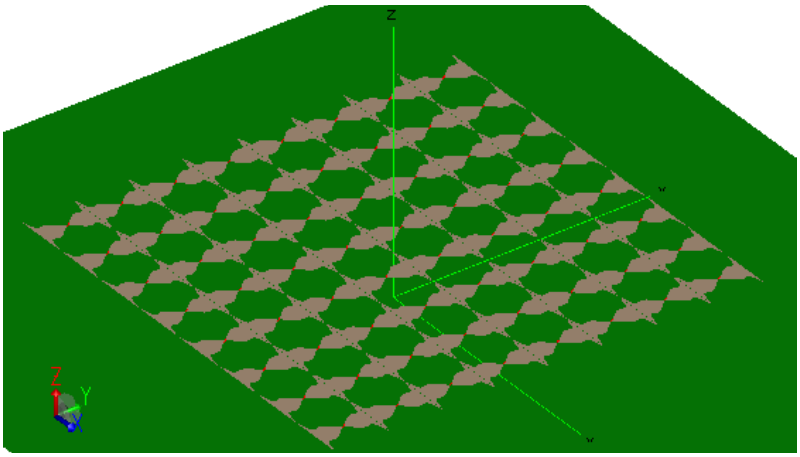

Figure 6-1 – Geometry of an 8x8 element Rot 9 array as seen in PostFEKO®

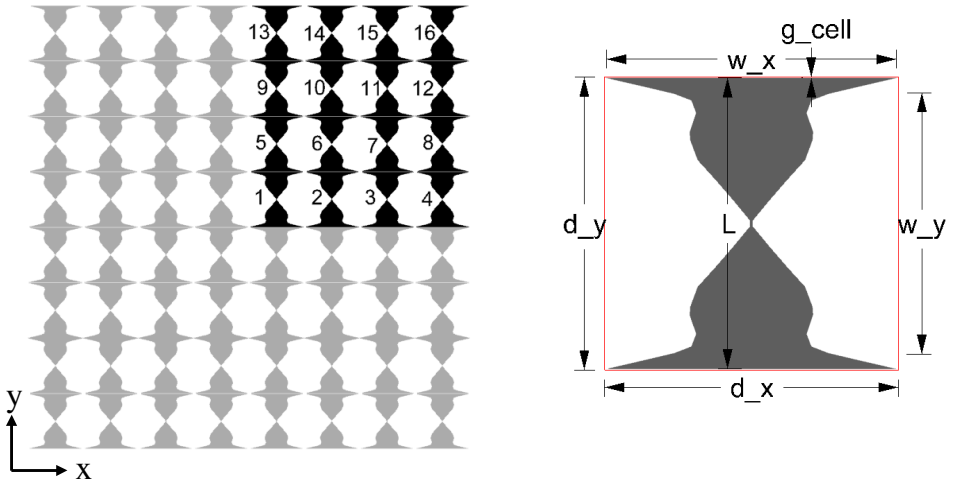

(a) (b)

Figure 6-2 – (a) Numbering of the 8x8 element Rot 9 array elements; and (b) blow-up of an individual element with unit cell (first presented as Figure 4-49)

Table 6-1 – Loadings on the semi-infinite Rot 9 arrays (from Table 5-1)

Name	R_1	R_2	R_3	R_4	R_5	R_6	R_7	R_8	Suitable for Semi-Infinite Array in the
Load04	200	100	50	0	0	50	100	200	*E*-plane
Load05	100	50	25	0	0	25	50	100	*H*-plane

The Load04 loading scheme, expanded in both *E*-plane and *H*-plane directions with larger values selected at conflicts in the diagonal directions, resulted in a scheme that controls the AGSW sufficiently to eliminate losses in impedance bandwidth. (The expanded Load05 scheme

did not.) Table 6-2 shows this 2D loading. With the increased loading, the 100-Ohm reference impedance of the Rot 9 element in the infinite array is increased. Table 6-3 shows the corresponding reference impedances for these resistive loads.

Table 6-2 – Loadings on the finite Rot 9 array of Figure 6-2 (Ohms)

200	200	200	200	200	200	200	200
200	100	100	100	100	100	100	200
200	100	50	50	50	50	100	200
200	100	50	0	0	50	100	200
200	100	50	0	0	50	100	200
200	100	50	50	50	50	100	200
200	100	100	100	100	100	100	200
200	200	200	200	200	200	200	200

y
x

Table 6-3 –Element reference impedances for the Rot 9 array of Figure 6-2 (Ohms)

300	300	300	300	300	300	300	300
300	250	250	250	250	250	250	300
300	250	200	200	200	200	250	300
300	250	200	100	100	200	250	300
300	250	200	100	100	200	250	300
300	250	200	200	200	200	250	300
300	250	250	250	250	250	250	300
300	300	300	300	300	300	300	300

y
x

Figure 6-3 shows the VSWR on each unique element (shown un-shaded in the above tables). Because of its cluttered content, Figure 6-4 shows the VSWR for only the diagonal elements numbers 1, 6, 11, and 16. This view illustrates the expanded bandwidth that comes through additional loading with, of course, reduced radiation efficiency.

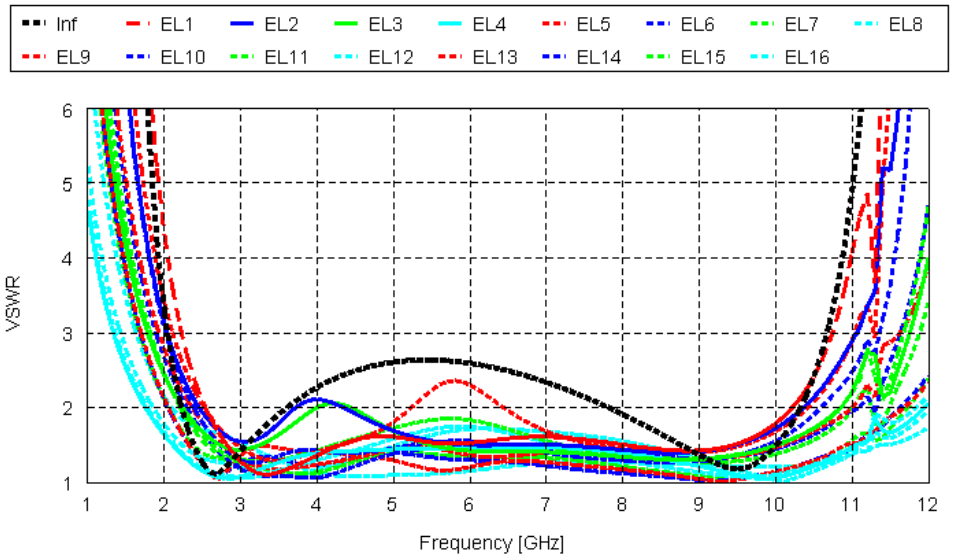

Figure 6-3 – VSWR on elements 1-16 of the finite Rot 9 array of Figure 6-2(a), loaded per Table 6-2 and with reference impedances per Table 6-3

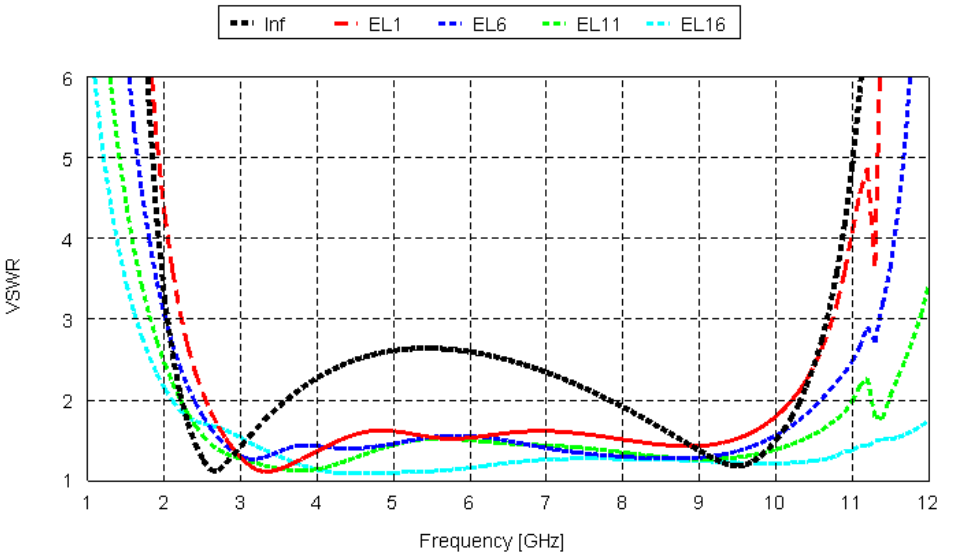

Figure 6-4 – VSWR of diagonal elements 1, 6, 11, and 16 of the finite Rot 9 array of Figure 6-2(a), loaded per Table 6-2 and with reference impedances per Table 6-3

This loading pattern results in a S3 bandwidth[1] that nearly matches the infinite S3 bandwidth, ranging from 2.06-10.75 GHz for a 5.22:1 bandwidth. The unloaded center elements had the narrowest bandwidth, with reductions at the lower frequency range. The elements with

[1] The "S3 bandwidth" is the short form for an impedance bandwidth with VSWR < 3.

the four narrowest bandwidths are (from worst to best) numbers 1, 5, 2, and 6. The overall S3 bandwidth for the 8×8 finite Rot 9 array is 4.79:1, ranging from 2.24-10.74 GHz on the worst element (Element #1). Applying additional resistive loads of 25 Ohms to these center elements would achieve a slightly wider bandwidth. A small reduction in efficiency would occur, but be limited, because of the small resistor values.

The loading in both directions produces an overall lower radiation efficiency than observed with either form of semi-infinite array. Comparing the outer columns of the array to the center ones may help the reader understand this observation. In the *E*-plane finite array, only the center columns are present. The resulting finite array efficiency (Figure 6-5) is slightly better than the multiplication of the efficiency of both semi-infinite arrays with the Load04 loading scheme. This observation is worth noting as a rule of thumb for developing finite arrays from less computationally burdensome semi-infinite simulations. Although the resulting efficiency is not high, across the frequency range it is better than 25%. If a design used a simpler loading scheme with two outer rings of elements terminated for AGSW suppression, only the 16 center elements would be active. Assuming no mutual coupling losses from these fed elements, such an array can achieve a maximum radiation efficiency[2] of 25%. Admittedly, larger arrays would see a corresponding increase in efficiency if they need only a fixed number of terminated outer rings. However, loading schemes like Load04, where all elements are active, would also show a comparable increase in radiation efficiency as the array grows.

This drop in efficiency affects the array gain directly, which Figure 6-6 compares to the aperture limit ($A = (8\times8)\times(15\times15)$ mm^2). Since most impedance matches are under a VSWR = 2, the realized gain would be reduced by approximately another 0.5 dB. At the low frequencies, the lower efficiency is the cause of the divergence from aperture gain; at the higher frequencies, the pattern distortion stemming from the ground plane reflection comes into play. Over a large extent of the frequency range, the difference from maximum is within 3 dB.

[2] Depending on the viewpoint, aperture efficiency may be a better term here than radiation efficiency.

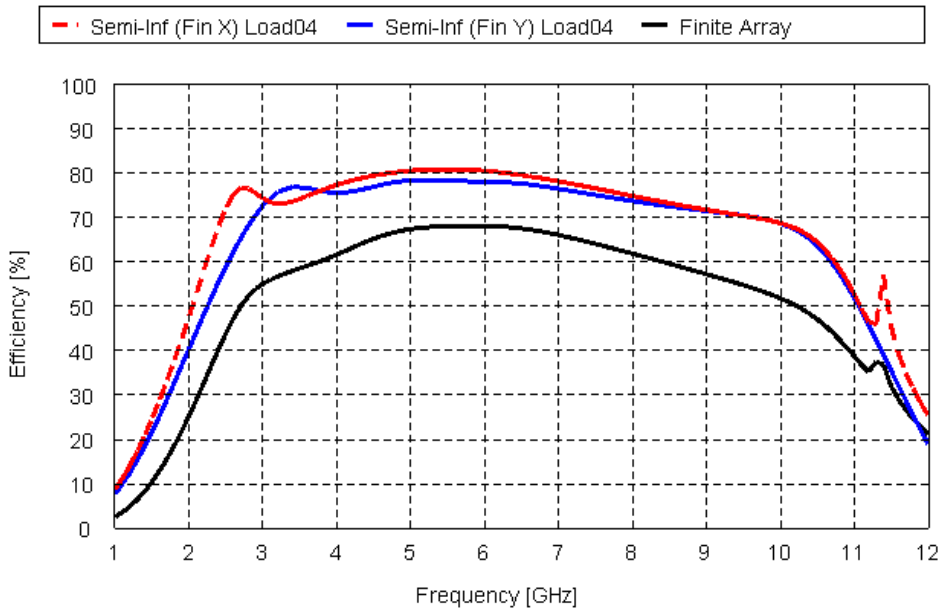

Figure 6-5 – Comparison of radiation efficiencies of the finite Rot 9 array, of Figure 6-2(a) and loaded per Table 6-2, and both semi-infinite Rot 9 arrays of Figure 5-1 and 5-24, respectively, loaded per Table 6-1

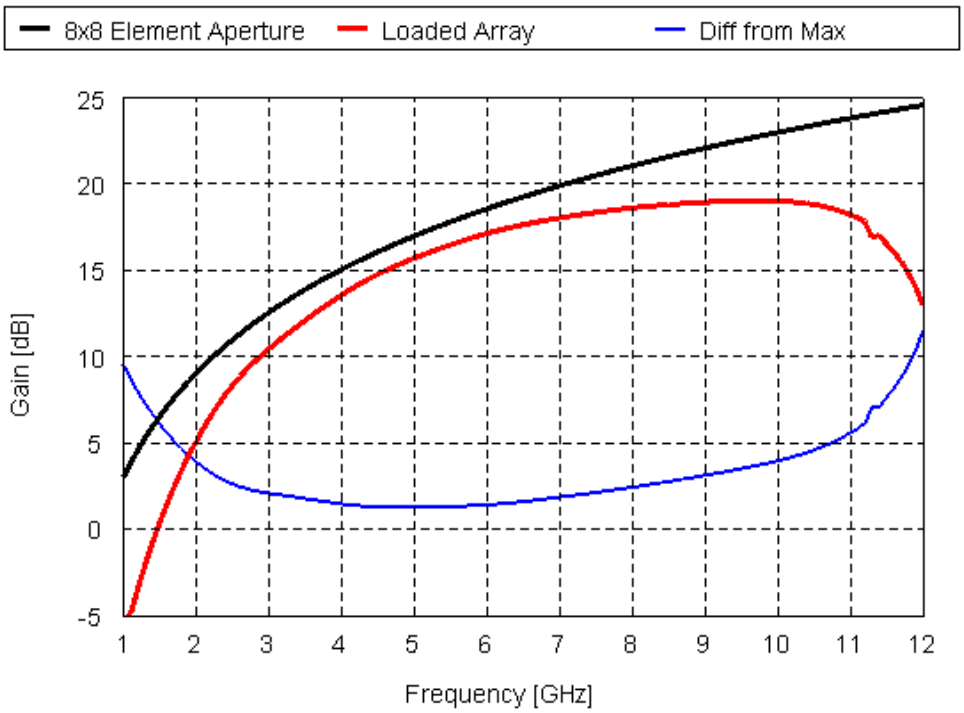

Figure 6-6 – Comparison of finite Rot 9 array gain of Figure 6-2(a) and loaded per Table 6-2, to a uniform aperture of 64 unit cells

6.2 The Wrapped Bowtie Array

Following the Rot 9 array design, this section considers the Wrapped Bowtie element in a finite array of nearly comparable size. Figure 6-7 shows the geometry and element numbering of the finite array, with element numbers located to the left of the feeds. This array contains 120 elements, of which 64 are unique given the array symmetry.

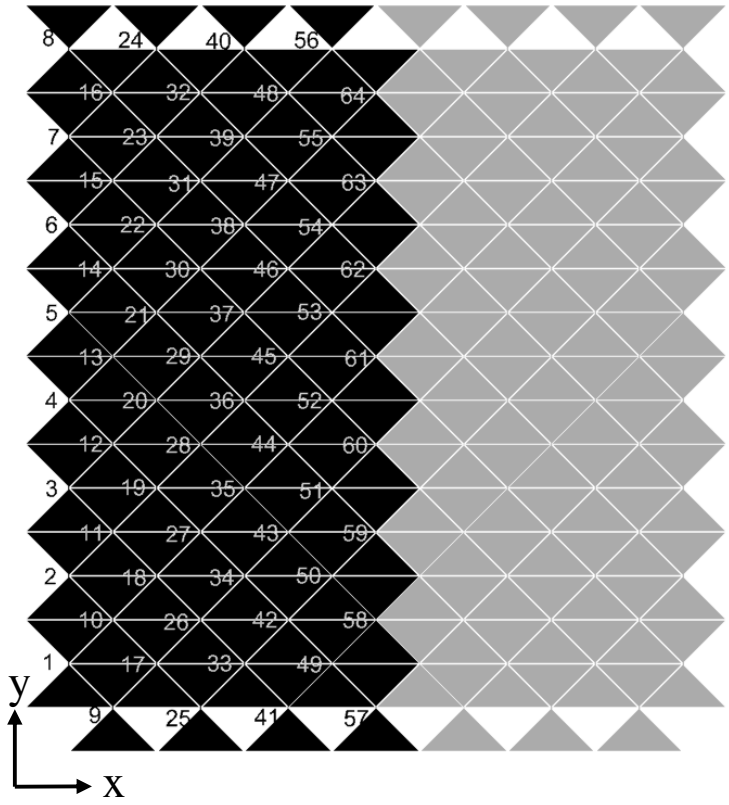

Figure 6-7 – Geometry of the 120-element Wrapped Bowtie array; element labels are located left of first 64 element feeds

While an analysis of the unloaded finite wrapped Bowtie array in the spectral domain may verify the presence of the AGSW, as with its semi-infinite forms, perhaps a better view is simply to consider the surface currents visually. These make an impressive view of the distortions caused by the AGSW. At those frequencies where the AGSW are present, current distortions are evident across all directions and not just the orthogonal ($\pm\hat{x}$ and $\pm\hat{y}$) ones.

In well-behaved currents at 10 GHz (Figure 6-8), it is easy to see the repetitive currents on the interior of the array. Equation (45) of Chapter 2 describes these as Floquet currents. Small

distortions near the edges, and especially the corners, show the inclusion of the end currents described in that same equation.

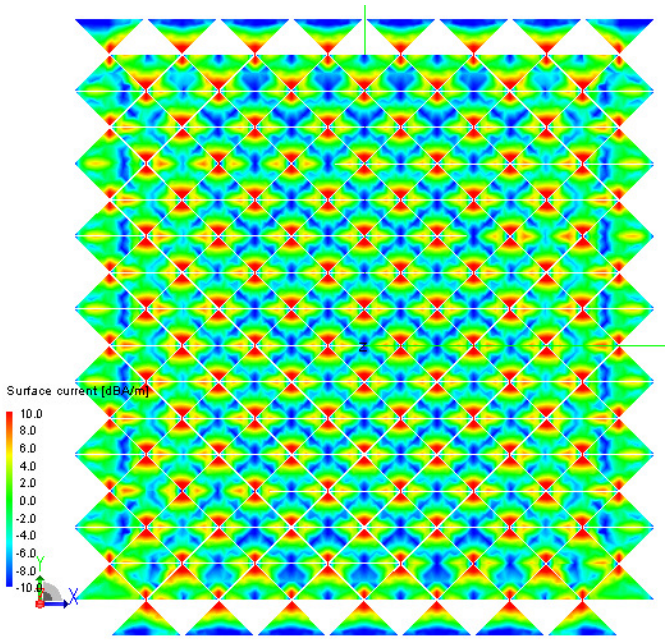

Figure 6-8 – Currents on the unloaded Wrapped Bowtie array at 10.0 GHz, within frequency range where the AGSW is not present

Contrast these to the currents at frequencies where the AGSW is present. At these frequencies, periodicities across multiple elements are evident, and the currents on each element are no longer consistent, with minor allowances for changes at the edges. Figure 6-9 shows distortions of about 2-3 wavelengths across the array face, in either the $\hat{x}$ or $\hat{y}$ directions. Figure 6-10 shows only one such period.

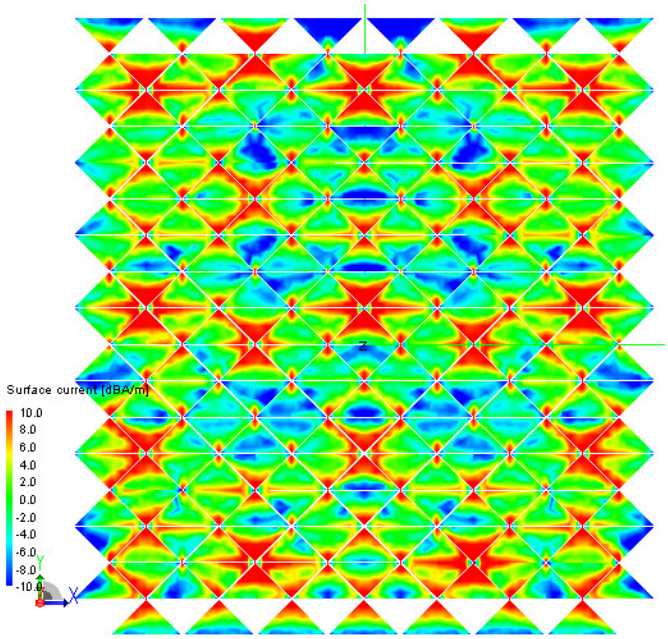

Figure 6-9 – Currents on the unloaded Wrapped Bowtie array at 3.6 GHz, within the frequency range where AGSW are present

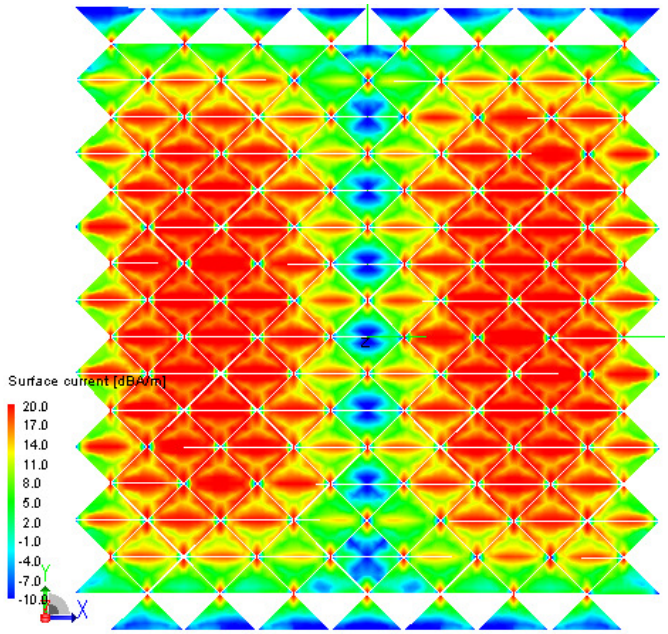

Figure 6-10 – Currents on the unloaded Wrapped Bowtie array at 8.8 GHz, within frequency range where input impedance ripples

The L03 loading pattern from the *E*-plane finite Wrapped Bowtie array (Table 5-3) controlled the AGSW completely, although the heavy loading decreases radiation efficiency

substantially. When expanded into two dimensions, with allocations for the half steps of the Wrapped Bowtie geometry, the loading pattern of Table 6-4 develops. As with the Rot 9 array, the additional loading requires corresponding increases in the reference impedances. Table 6-5 shows these. The reference impedances do not match exactly to the increased resistive loads. This array has very high mutual coupling and the response to resistive loading seems to be more temperamental and sensitive than in the Rot 9 array. Certainly, the Wrapped Bowtie array required higher resistive loads for AGSW control than the Rot 9 array.

Table 6-4 – Loadings for the Wrapped Bowtie array of Figure 6-7 (Ohms)

200		200		200		200		200		200		200		200
	200		200		200		200		200		200		200	
200		150		150		150		150		150		150		200
	200		150		150		150		150		150		200	
200		150		100		100		100		100		150		200
	200		150		100		100		100		150		200	
200		150		100		50		50		100		150		200
	200		150		100		50		100		150		200	
200		150		100		50		50		100		150		200
	200		150		100		50		100		150		200	
200		150		100		100		100		100		150		200
	200		150		100		100		100		150		200	
200		150		150		150		150		150		150		200
	200		150		150		150		150		150		200	
200		200		200		200		200		200		200		200
	200		200		200		200		200		200		200	

y
x

Table 6-5 – Element reference impedances for the Wrapped Bowtie array of Figure 6-7 (Ohms)

400		400		400		400		400		400		400		400
	400		400		400		400		400		400		400	
400		400		300		300		300		300		400		400
	400		400		300		300		300		400		400	
400		400		300		250		250		300		400		400
	400		400		300		250		300		400		400	
400		400		300		200		200		300		400		400
	400		400		300		200		300		400		400	
400		400		300		200		200		300		400		400
	400		400		300		200		300		400		400	
400		400		300		250		250		300		400		400
	400		400		300		250		300		400		400	
400		400		300		300		300		300		400		400
	400		400		300		300		300		400		400	
400		400		400		400		400		400		400		400
	400		400		400		400		400		400		400	

y
x

Figure 6-11 and Figure 6-12 (divided due to software instabilities in PostFFKO®) show the VSWR on each unique element, shown un-shaded in the above tables. Element numbers 1 through 32 have either 150-Ohm or 200-Ohm loads. A substantial increase in the impedance bandwidth over the infinite Wrapped Bowtie array input impedance is evident, with increases at both the upper and lower frequency ends. Element numbers 1 through 32 have an S3 bandwidth from 1.04-11.2 GHz, or 10.77:1.

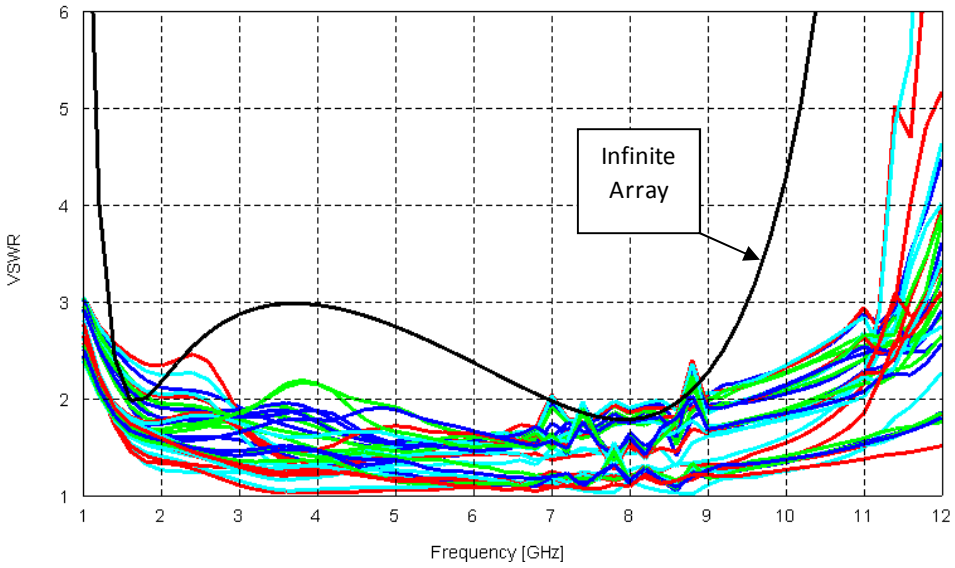

Figure 6-11 – Element VSWR for the Wrapped Bowtie array of Figure 6-7: elements 1-32, loaded per Table 6-4 and with reference impedances per Table 6-5

Figure 6-12 shows the VSWR for the more interior and less loaded elements. These loads range from 50-200 Ohms, but overall the bandwidth on these elements is wider than the infinite array. Still, in both figures, it is apparent that some disruptions still occur in the 7-9 GHz range. Based on the experience of loading throughout this research, this indicates that the loading is close to minimal. Element numbers 33 through 64, being the remainder of the unique elements, have an S3 frequency range that is slightly more limited to 1.19-10.54 GHz, or 8.85:1. These figures are comparable to the infinite Wrapped Bowtie array S3 bandwidth of 7.24:1 for a $Z_o = 125\Omega$.

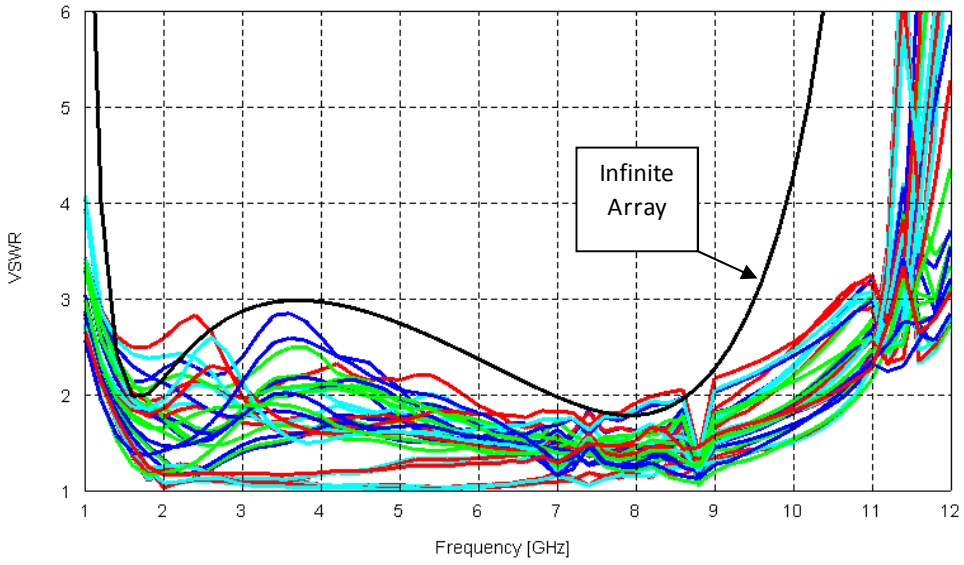

Figure 6-12 – Element VSWR for the Wrapped Bowtie array of Figure 6-7: elements 33-64, loaded per Table 6-4 and with reference impedances per Table 6-5

The loading in both directions produces a lower radiation efficiency than observed with either form of semi-infinite array of the same Wrapped Bowtie elements. Figure 6-13 compares the resulting finite array efficiency to the L02 and L03 loading schemes of Table 5-3, for the finite *H*-plane and finite *E*-plane arrays, respectively. (Chapter 5 never considered the Loading L03 scheme on the *H*-plane finite array because the L02 scheme sufficiently suppressed the AGSW effects.) The resulting efficiency is on average below 50% and it is lower than the Rot 9 array efficiency of Figure 6-5. While the Rot 9 array efficiency is somewhat level across most frequencies, with only drop-offs in efficiency at the upper and lower frequencies, the Wrapped Bowtie array has pronounced reductions in efficiency from its maximum of 4.4 GHz. The ability to apply resistive loading only on frequencies selectively would offer a large increase to the overall efficiencies of realized, well-behaved tightly-coupled arrays.

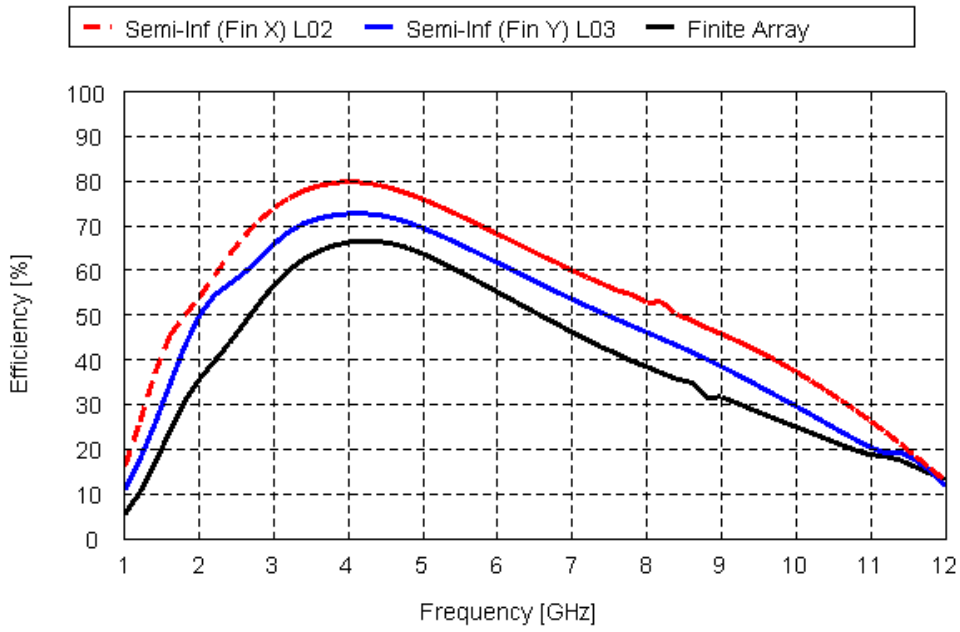

Figure 6-13 – Radiation efficiency of the Wrapped Bowtie array of Figure 6-7, loaded per Table 6-4, compared to the two semi-infinite arrays of Figure 5-43 and 5-55, loaded per Table 5-3

This drop in efficiency affects the array gain directly. Figure 6-14 compares gain to the aperture limit, where the largest rectangular extents of the array define the area to be 30384 mm^2. With most impedance matches under a VSWR = 2, the realized gain would be approximately 0.5 dB lower, with some additional decreases at the upper and lower frequency ends. The differences from the aperture limit increase with frequency, but overall another nice effect occurs, namely a consistent gain from 5.5 to 10.5 GHz of 19 dBi. Again, some ability to apply resistive loads on specific frequencies would substantially increase the radiation efficiency and gain.

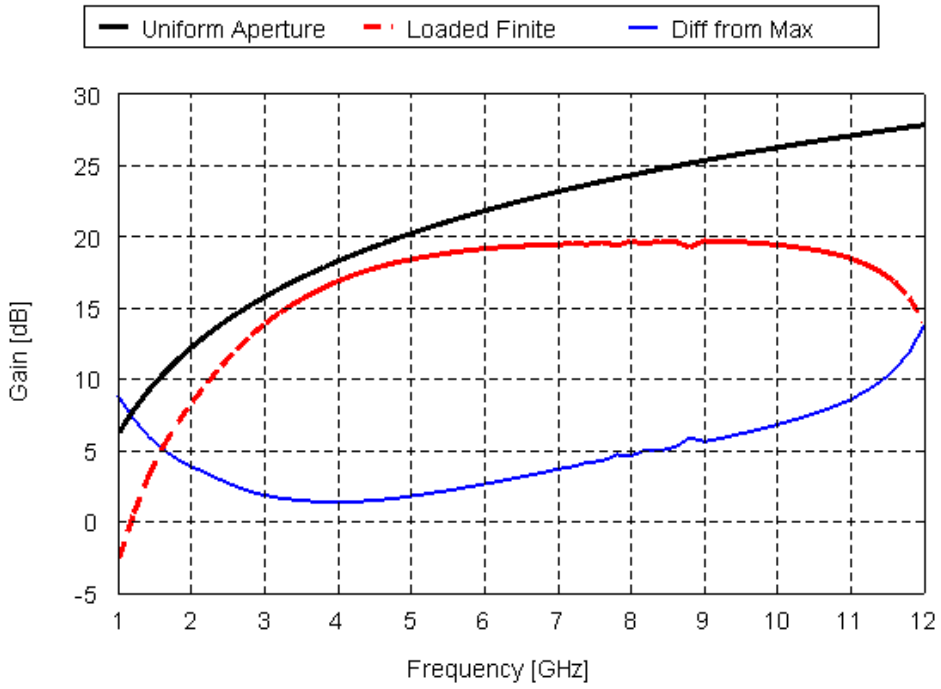

Figure 6-14 – Far-field gain in $+\hat{z}$ for the Wrapped Bowtie array, loaded per Table 6-4

6.3 Array Conforming

Research is ongoing within the software-defined and cognitive radio communities to develop a single radio solution for a wide range of multiple public-safety frequency ranges. Providing such a radio solution for complete interoperability among the myriad of law enforcement and public safety organizations is a vision of the future. One limitation to the implementation of such a radio system is the antenna to support all frequencies. These frequencies range from 45 to 869 MHz and would require an antenna to have a staggering 19:1 bandwidth. Eliminating the lowest sub-band (commonly called VHF low band), the frequency range decreases to 138 to 869 MHz, for a 6.3:1 bandwidth. The Wrapped Bowtie array shows bandwidths in this range. Additionally, wideband antennas in such a public-safety radio system need to maintain the gains typical in base-station/tower antennas for each individual sub-band. Without a clear achievement of comparable antenna gains, these radio networks would require substantial reconfiguration, with additional coverage sites likely.

The coverage patterns of base-station antennas for public safety applications are typically omnidirectional in azimuth and have a narrow vertical beamwidth. These base station antennas

are normally a collinear array of exposed folded dipoles. A fully omnidirectional tightly coupled array may later be designed (it is detailed in Chapter 7 on future work), but the concept of sectoral coverage may also be employed to achieve an omnidirectional pattern. If the array is rotated and conformed cylindrically about the *z*-axis, three arrays with beamwidths of about 60° will produce a good coverage pattern in a terrestrial propagation environment. As detailed in Section 5.6, the conformation allows the array to be less loaded to control the AGSW. This increases the radiation efficiency, but the conformation also widens the beamwidth and reduces the gain as a result. A sectoral, public-safety base-station antenna needs this exact effect.

6.3.1 The Conformal, Finite Array of Rot 9 Elements

This section considers the Rot 9 array in a cylindrically conformal configuration. This geometry is an expansion of the Conf2 geometry detailed in Section 5.6, and Figure 6-15 shows it in the finite array form. The radius of curvature is 57.46 mm as applied to the ground plane. Conforming at the ground plane expands the separation between antennas in the *H*-plane. The separation from ground remains $h = 12\,\text{mm}$, however. Although the 8×8 Rot 9 array does not achieve the full 6.3:1 bandwidth described in the previous section, its non-wrapped geometry is easier to work with in a conformed geometry and to determine some guidelines. Several additional design steps consider additional radii of curvature, inter-element spacings when conformed, possible changes to ground plane separation, etc., without mentioning feed network designs in such a geometry with less volumetric space behind the ground plane.

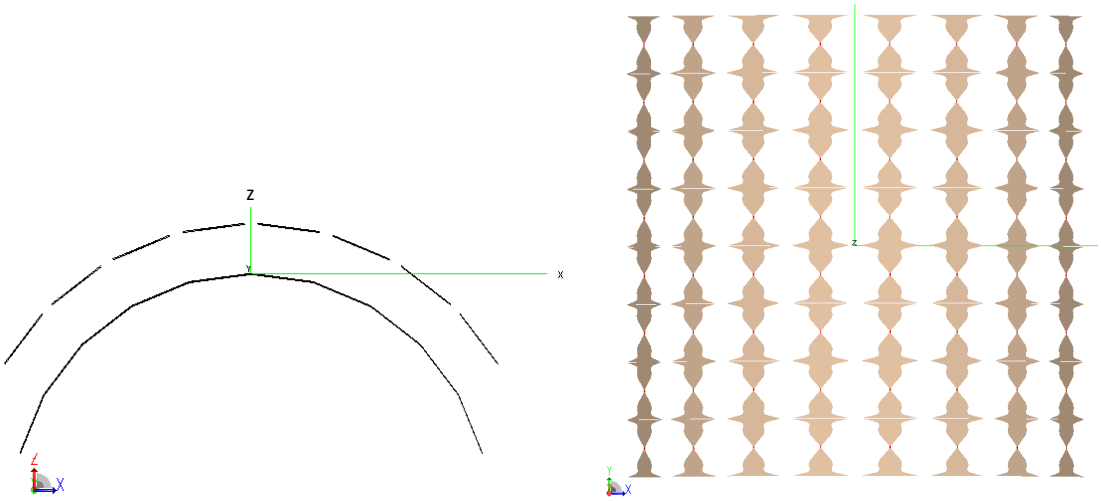

(a) (b)

Figure 6-15 – Geometry of the conformal 8x8 Rot 9 array: (a) end view; and (b) top-down view with ground hidden

Similar effects appear with the finite conformed array as with the semi-infinite array. The radiation efficiency is less due to the two-dimensional loading, but the same trends and mechanisms apply as detailed in Section 5.6. Table 6-6 shows the combination of the conformal semi-infinite loading pattern and the Load04 loading scheme. Table 6-7 shows the corresponding reference impedances. These loads and reference impedances control the AGSW adequately. Figure 6-16 shows the resulting VSWR on the 16 elements in the upper right quadrant.

Table 6-6 – Loadings on the conformal Rot 9 array of Figure 6-15

200	200	200	200	200	200	200	200
200	100	100	100	100	100	100	200
200	50	50	50	50	50	50	200
100	50	0	0	0	0	50	100
100	50	0	0	0	0	50	100
200	50	50	50	50	50	50	200
200	100	100	100	100	100	100	200
200	200	200	200	200	200	200	200

y
x

Table 6-7 –Element reference impedances on the conformal Rot 9 array of Figure 6-15

300	300	300	300	300	300	300	300
250	250	250	250	250	250	250	250
250	200	200	200	200	200	200	250
200	150	100	100	100	100	150	200
200	150	100	100	100	100	150	200
250	200	200	200	200	200	200	250
250	250	250	250	250	250	250	250
300	300	300	300	300	300	300	300

y

x

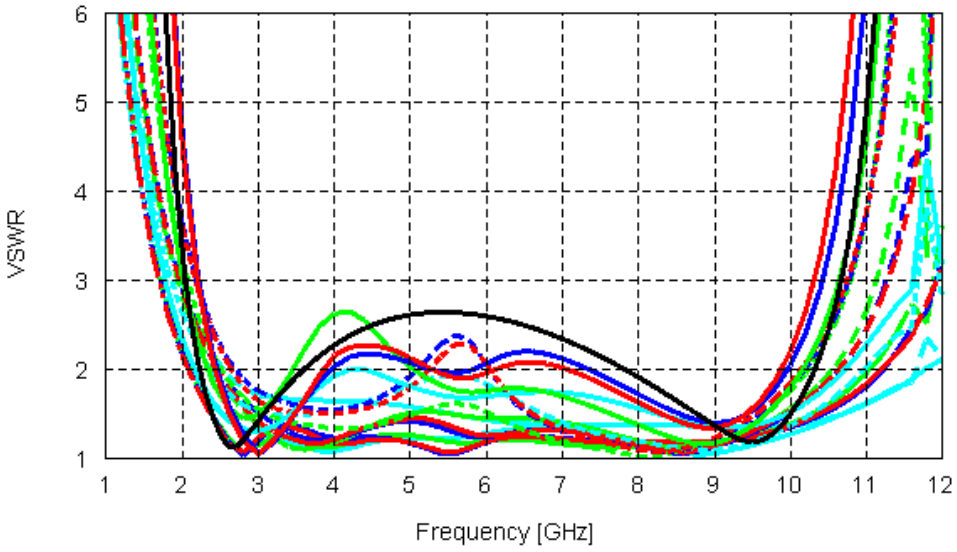

Figure 6-16 – VSWR on elements 1-16 of the conformal Rot 9 array of Figure 6-15, with loadings and reference impedances of Table 6-6 and Table 6-7, respectively

The loading and the spatial separation of elements pursuant with ground plane conformation together decrease the overall bandwidth. The lower mutual coupling is evident in its impact on bandwidth. Table 6-8 presents the S3 bandwidths and frequency limits for infinite, flat, and conformal Rot 9 arrays.

Table 6-8 – Comparison of Rot 9 array bandwidths

Name	Shown in	S3 Bandwidth	f_L (GHz)	f_u (GHz)
Infinite (flat, unloaded)	Figure 6-2(b)	5.23	2.04	10.67
Flat Loaded 8x8	Figure 6-1	4.79	2.24	10.73
Conformal Loaded 8x8	Figure 6-15	4.68	2.20	10.30

The improvements in efficiency that stem from lower resistive loads are minimal and should not be the main method to control the AGSW. Figure 6-17 shows minimal improvements mostly at the upper frequencies. The gain from conforming, however, results in a nearly constant gain around 10 dBi above 3.5 GHz upwards, as Figure 6-18 shows. Additional gain is available by lengthening the array in the non-conformed direction.

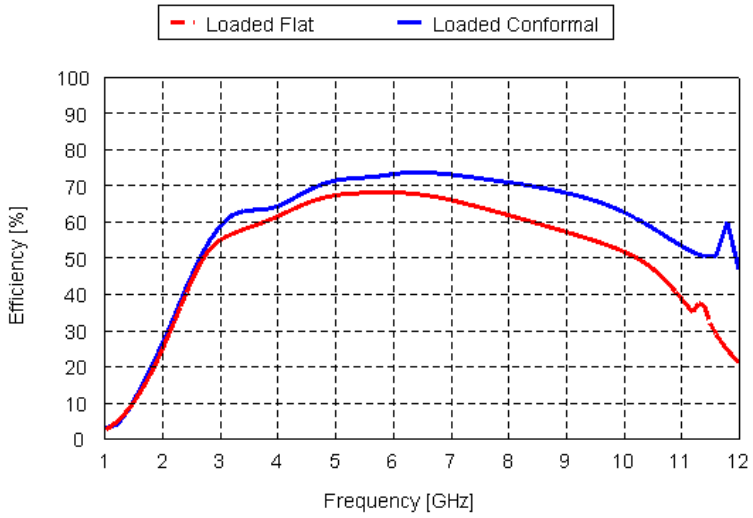

Figure 6-17 – Radiation efficiencies for the conformal loaded and flat loaded 8x8 Rot 9 arrays

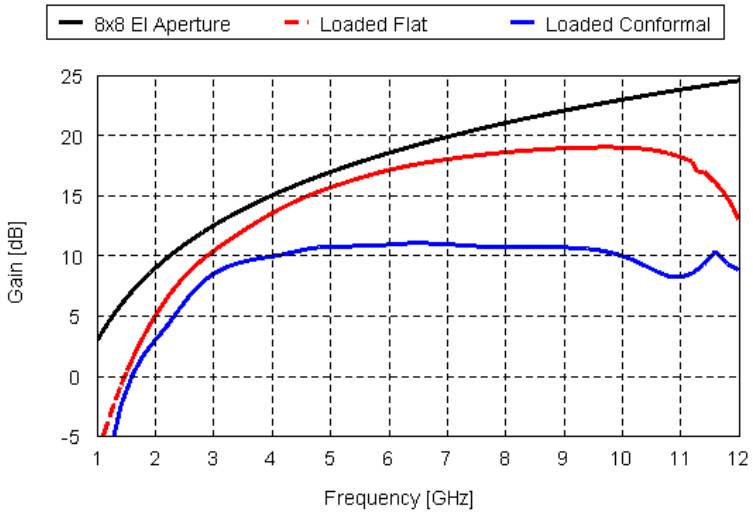

Figure 6-18 – Broadside gain for the conformal loaded and flat loaded 8x8 Rot 9 arrays to the directivity of a 8x8 unit cell uniform aperture

Table 6-9 lists beamwidth and gain performance across frequency. Maintaining the *H*-plane beamwidth at a nearly constant $75-80^{\circ}$ across much of the frequency range keeps the

gain from rising. The *E*-plane beamwidth narrows with increased frequency, as the electrical size of the aperture grows. Figure 6-19 and Figure 6-20, respectively, show these 2D pattern cuts at increments from 2 to 10 GHz. Starting near 6 GHz, a dip begins to form in the vertical ($+\hat{z}$) direction, which increases with frequency. The design needs some optimization to keep this null from growing beyond -3 dB across the impedance frequency range.

Table 6-9 – 3-dB beamwidths of flat and conformed Rot 9 arrays of Figure 6-1 and Figure 6-15, respectively (in degrees)

Freq (GHz)	Flat *H*-plane $\phi = 90^\circ$	Flat *E*-plane $\phi = 0^\circ$	Conformal *H*-plane $\phi = 90^\circ$	Difference from G_{max} at $(\phi.\theta) = (0,0)$	Conformal *E*-plane $\phi = 0^\circ$	G_{max} (dBi)
2	58.0	50.0	68.2	-	62.4	3.1
3	43.7	41.3	56.2	-	47.3	8.6
4	31.8	30.8	63.6	-	35.8	10.0
5	25.5	24.8	80.3	-	28.7	10.8
6	21.9	21.2	82.9	-0.3	24.1	11.3
7	19.4	18.6	78.4	-1.3	20.9	12.3
8	17.0	16.2	77.0	-2.2	19.3	12.9
9	15.5	14.8	76.6	-2.6	16.6	13.4
10	14.6	13.8	75.1	-3.5	16.3	13.5

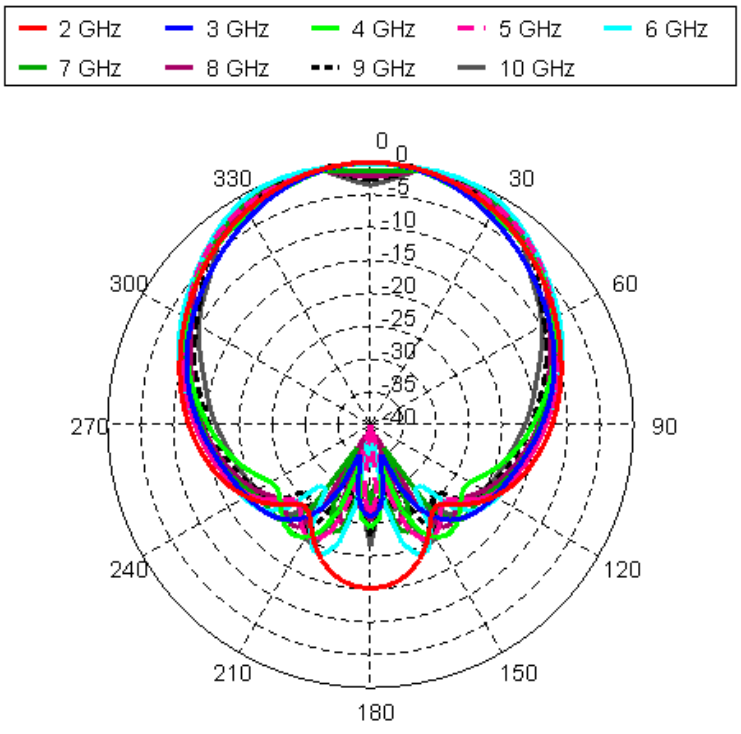

Figure 6-19 – Normalized *H*-plane far-field pattern at $\phi = 0^\circ, 180^\circ$ for the conformal 8x8 Rot 9 array of Figure 6-15

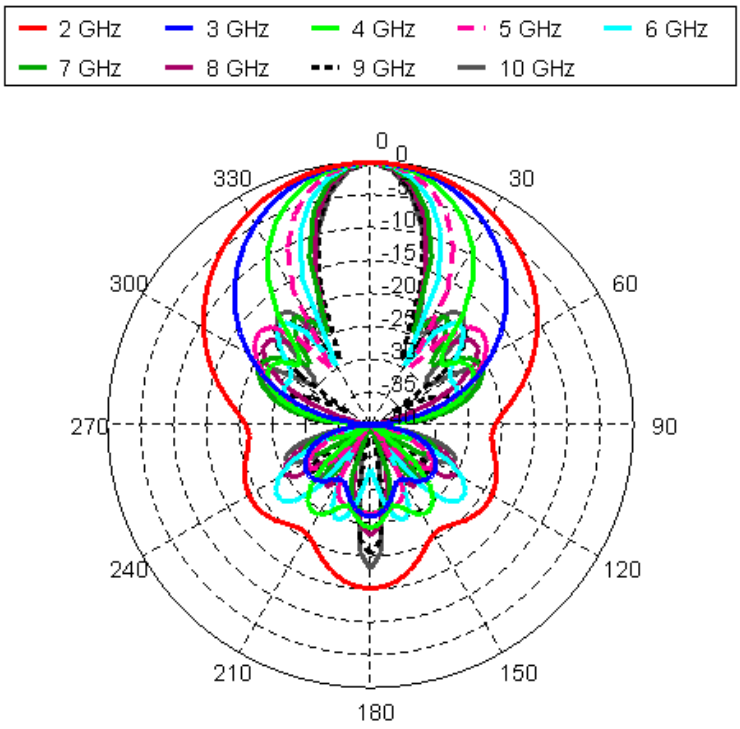

Figure 6-20 – Normalized *E*-plane far-field pattern at $\phi = 90^{\circ}, 270^{\circ}$ for the conformal 8x8 Rot 9 array of Figure 6-15

6.4 Array Feeding

The feeding of the array introduces another set of design issues and concerns, but they are necessary to advance an array design to the building stage. All element designs within this research are balanced antennas, which appears to dictate the need for balanced feed lines. Balanced feed lines require the currents on one side of the transmission line to be 180° out of phase with those on the other half of the transmission line. The currents on both lines, with their close parallel spacing to one another, nearly cancel any radiation from the feed lines. The low level of radiation from differential-mode (or push-pull) radiation contrasts with the common-mode (or push-push) radiation.

Without a source device like an MMIC[3] with a balanced output port, a balun is quite likely required. A balun transforms a balanced port to an unbalanced port. With the array viewed in a receive configuration, once an unbalanced transmission line is reached, the lines from each

[3] Monolithic Microwave Integrated Circuit

element can be combined until one output port is reached. Within such a design, generally of a corporate feed type, impedance transformations and magnitude adjustments can be included[4]. The input impedance looking into the source or receiver should be included as part of the resistive loading on the elements needed to control the AGSW, but design specifics will certainly emerge.

The following sections describe designs with balanced and unbalanced sources. The sections address each separately because of the differences in their feed types, although some design issues are common to both.

6.4.1 Design Issues with Balanced Sources

The simplest solution with this type of balanced antenna element and small inter-element spacing is to feed each element with an independent source, preferably of an MMIC type. MMICs commonly have balanced outputs, which is ideal for feeding these balanced antennas with the addition of twin lead transmission lines. MMICs are good power amplifiers and frequency mixers, and although they are not exceptionally powerful, the sheer number of elements may meet the total needed output power. MMICs typically have the standard 50-Ohm reference impedance on their output terminals.

As shown below, the resistive loading necessary to suppress the AGSW changes the input impedance of the element. Likewise, the inclusion and translation of the impedance reference point from the element terminal to behind the ground plane will alter the input impedance. This alteration follows (1), as expected, where $\beta = 2\pi / \lambda$, and l is the length of the transmission line.

$$Z_{in}(l) = Z_o \frac{Z_L + jZ_o \tan(\beta l)}{Z_o + jZ_L \tan(\beta l)} \tag{1}$$

Parallel twin lead feeds were calculated and tested in simulation using terminated loads of 100, 150, 200, and 300 Ohms, respectively, for the four loading conditions in the Rot 9 array. These cables have line radii of 0.1 mm and center-center separations of 0.106, 0.122, 0.25, and

[4] These additions would allow for matching outer array elements that have higher input impedances due to their resistive loading. The amplitude adjustments, although not addressed in this research, is typically the method of controlling sidelobes. Some level of amplitude taper is already included in these finite array designs because of the increased loading toward the outside of the array. This chapter does not address exact parallels and comparisons, however.

0.60 mm, respectively. Figure 6-21 shows the model for the unloaded element. If MMICs have 50-Ohm impedance references, the translation of the input impedance using (1) for the Rot 9 array works well but not for the Wrapped Bowtie array, as seen in Figure 6-22 and Figure 6-23, respectively. Of course, the translated VSWR would match the element VSWR exactly if the same reference impedance were kept at the end of the feed line.

With feed lines included in the infinite array models, Figure 6-24 presents the VSWRs simulated for sources on the backside of the ground plane. Each line contains half the resistive load just below the element. For example with the 100-Ohm load, the top of each parallel line incorporates a 50-Ohm series resistor. The unloaded VSWR (red dashed) in Figure 6-24 is close to the results of the analytical impedance translation illustrated in Figure 6-22.

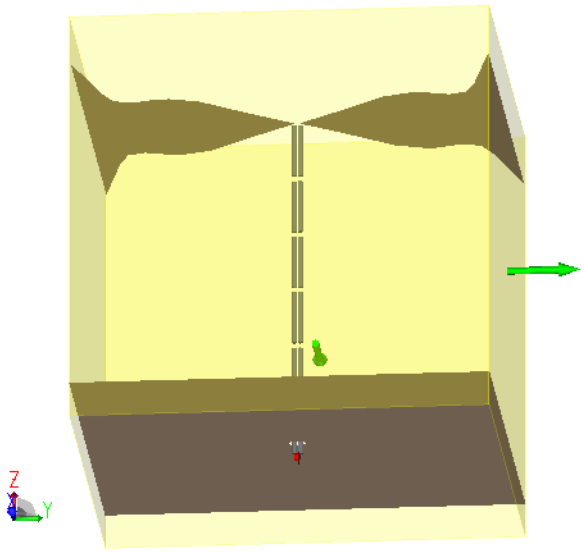

Figure 6-21 – Model of twin lead, balanced feed for the infinite Rot 9 array

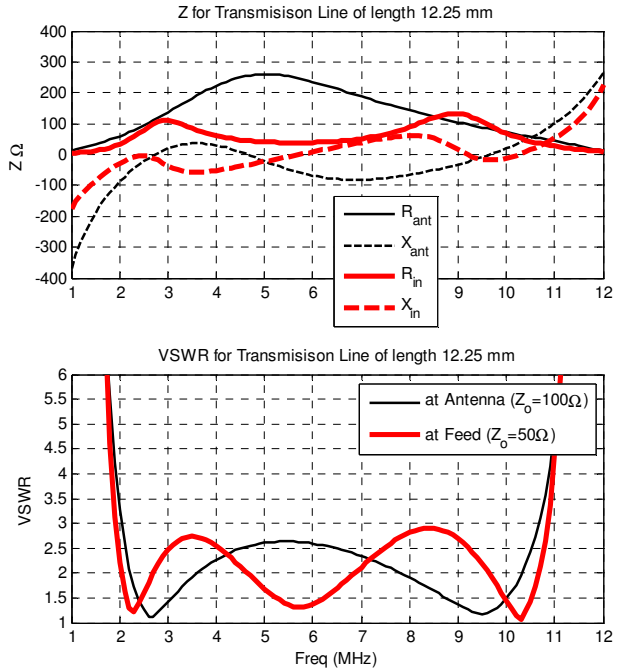

Figure 6-22 – Analytical impedance transformation on the Rot 9 infinite array element where $l = h$ = 12.25 mm

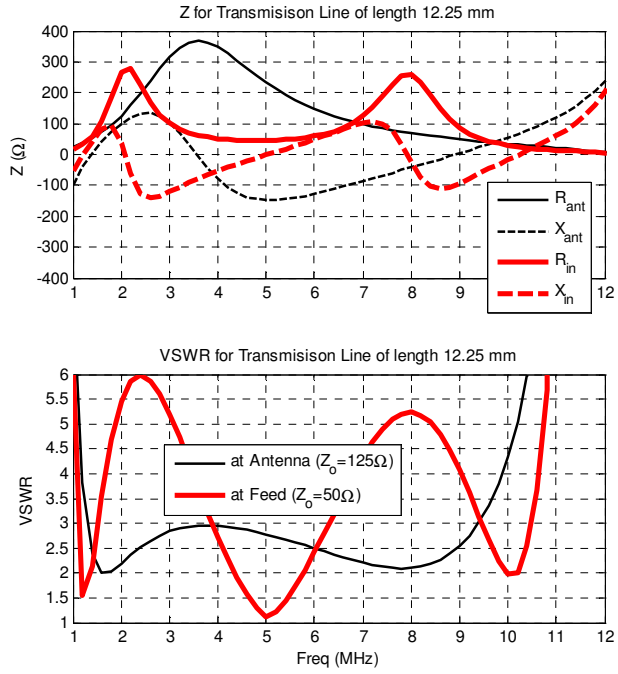

Figure 6-23 – Analytical impedance transformation on the Wrapped Bowtie infinite array element where $l = h$ = 12.25 mm

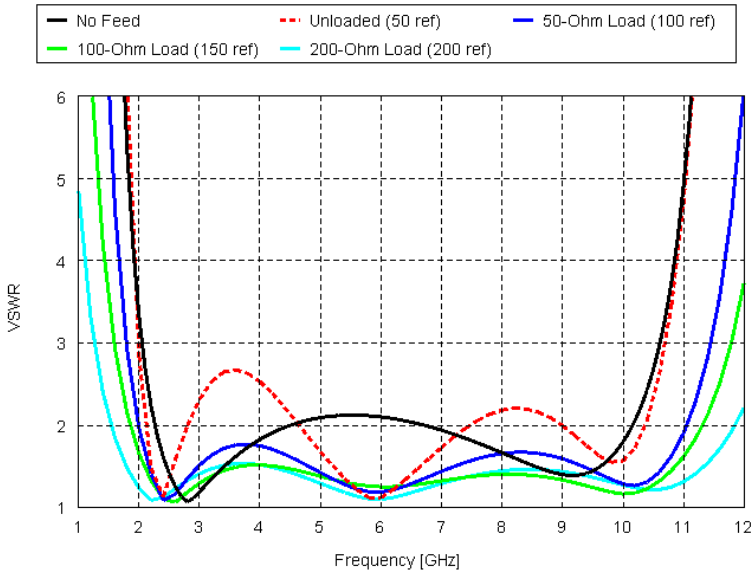

Figure 6-24 – VSWRs at twin line feeds of length *l* = 12.25 mm with reference impedances as indicated

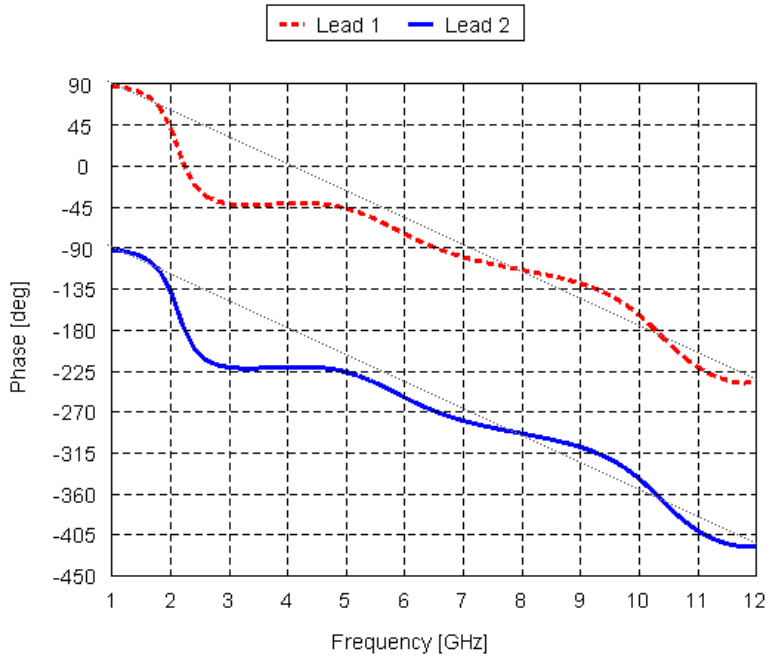

Figure 6-25 – Current phases at lower end of twin line feeds of length *l* = 12.25 mm

The phases on the lowest section of both feed lines are 180° out of phase across the frequency range. They are not linear, however, which may introduce difficulties if this array is to support wideband signals. (The cause of this non-linearity is unknown at this time and is

enumerated for future work.) Some small differences in gain emerge between the unloaded infinite array with an ideal feed ("no feed") and the unloaded infinite array with a twin-line feed. Additional loading further reduces the gain.

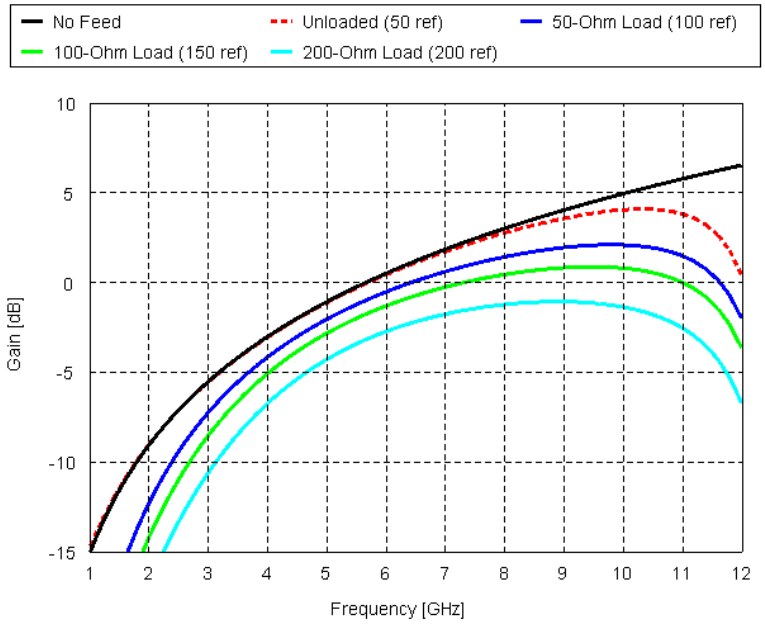

Figure 6-26 – Active element gain for various loading conditions & feed lines

With the need for additional loading to suppress the AGSW, the engineer should address and balance the issues regarding the loading approach and the required impedance transformations to higher reference impedances. In many ways, these difficulties argue for only exciting unloaded elements and terminating a ring of unexcited elements around the outside of the array with only resistive loads. (The outer ring(s) of elements are not excited.) However, as discussed in Section 6.1, rings of terminated-only elements drives down the aperture efficiency substantially. At some level, the loading approach depends on the number of elements in the array. Medium-sized arrays, such as an 8×8 element array, would benefit from feeding all elements. Exact comparisons and trade-offs were not explored in this research.

6.4.1.1 Common-Mode Radiation

When a planar array radiates to broadside $\left(+\hat{z}\right)$, its currents are very nearly limited to the $xy-$plane of the antenna. If the array is conformal, or the array scans away from the normal direction, electric fields will develop in $\hat{z}$. From these, currents can develop on the outside of

transmission lines, whether the transmission line is balanced or unbalanced, because of their close proximity to the antenna. If parallel (balanced) lines are used, the impressed currents on the transmission line will be in a common direction. Without the out-of-phase cancellation of currents as with balanced feed lines, both lines will have *common-mode* (or push-push mode) radiation.

In an unphased planar array, the need to prevent common mode radiation on balanced feed lines is not a major concern. The impressed currents from multiple elements are equivalent and have a manner of cancelling common-mode radiation within each element. With scanned arrays, asymmetries form in the fields behind the element along the feed lines, and common-mode radiation occurs. Often, balanced feed lines are constructed of small coaxial lines, and the two center conductors act as the balanced feed lines. The outer conductors of both coaxial cables are soldered together, or otherwise electrically connected, but they are separated from the element. This outer shielding then can act much like the outside of the outer conductor in an unbalanced feed line.

Since the outer conductors are not connected to the antenna (and would end on the underside of the antenna support substrate), common-mode are induced on the outside of the cables. If these are not very short electrically, they act as parasitic monopole antennas that are spatially orthogonal to the array. The array structure over the top of these cable, although not directly connected, act as top-hat loads [1], which reduces the length requirements of the cable to become resonant. As the element become more electrically resonant (if grounded, at a length $\lambda/4$, and if ungrounded, at a length around $\lambda/2$), the induced currents increase and begin to dominate. This leads to the development of a monopole antenna pattern.

The need is to make the parasitic "antennas" into extremely poor radiators by reducing the ungrounded length of the "antenna" or adding loss. The *feed organizer* by Harris is one structure that accomplishes this (Figure 6-27). It grounds the extent of the coaxial cable along $+\hat{z}$ to the ground plane, thereby reducing the length of the parasitic monopole to close to zero.

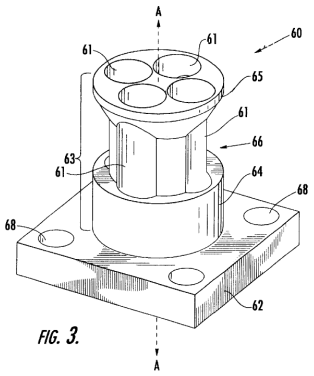

FIG. 3.

Figure 6-27 – Harris element feed organizer (Figure 3 of [2])

6.4.2 Design Issues with Unbalanced Sources

Unbalanced sources are typical transmitters or receivers of a super-heterodyne nature with coaxial input/output ports. These units are certainly the common form in base stations for cellular and land-mobile radio applications, as well as mobile (vehicular) transceivers. Unlike a balanced twin-lead transmission line, a coaxial cable has three structures that can support currents: the center conductor, the inside of the outer shielding, and the outside of the outer shielding. Properly designed, the first two support the desired TEM mode on the line. However, currents can develop on the outer structure of the coaxial cable because of its presence in an environment with radiofrequency energy. If the coaxial cable connects two components and has proper connectors, the outside of the outer shielding is grounded at each end. The coaxial cable is appealing for its flexibility and ease of installation in a number of environments, as little radiation external for the transmission line occurs.

Unfortunately, once it reaches the antenna, other problems develop since the connection at the antenna end is not grounded. Currents developed on the outside of the cable, and this structure becomes part of the radiating structure. The antenna element effectively grows, although some orthogonality exists, but the extension is asymmetric since the outer conductor is normally only attached to the negative side of a balanced antenna. This asymmetry distorts the antenna pattern and can act to move the antenna feed to be off-center.

Unfortunately, the unbalanced feed line is not a good way to feed a balanced antenna or array element, such as those designed in this research. A balun connects balanced and unbalanced feed lines or sources to prevent unintentional radiation. The balun can also serve as

impedance transformer, which appears to be necessary with the finite Rot 9 and Wrapped Bowtie designs. Although many different balun designs exist, options for wideband baluns are limited. Also, these typically employ gradual transitions that are several wavelengths in length [3, 4], such as with the tapered microstrip balun. Tapered baluns for their bandwidth, and in their first impression, one might consider extended lines from one element (or unit cell) to the next to achieve the required transitions. However, three wavelengths at 10 GHz would be six cells long (across the square direction) and 30 cells long at 2 GHz. Spatial limitations with the Wrapped Bowtie array would be even tighter due to the tight element overlaps. Arranging feed lines across six element cells would be very difficult, and 30 cells would be impossible, *if a generally planar structure is to remain*. This last requirement appears throughout the literature and is a major obstacle to any such tightly-coupled array.

Connecting the coaxial cable to a location on the element where currents are minimal across frequency forms a type of natural balun. Such a balun was possible for Manteghi [5] because the Vivaldi element feeds on the IRA antenna are electrically large. (One can also consider a ground plane with a monopole antenna to be a natural balun.) Unfortunately, with the high levels of mutual coupling, electrically small element size, and wide frequency range, no region on the element has minimum currents across its operating band.

Likewise, Dyson baluns [6, 7] are a poor choice with tightly-coupled array designs. Dyson baluns require the currents to dissipate via radiation from the feed before they reach back to end of the element arm (typically a spiral antenna), where the unbalanced transmission line is attached. Because the radiation regions in tightly-coupled arrays extend to the ends of the array across all frequencies, derivatives of the Dyson balun are not optimal.

One balun type that can fit within the small unit cell of the array element is the Marchand balun, if adapted to this limited size. Here again, without further modifications, the bandwidth of the balun is typically 3:1 [8] and well below the needed bandwidths of the Rot 9 and Wrapped Bowtie designs, especially when resistively loaded. A Marchand balun can fit within the size of the unit cell. One implementation requires two spirals on opposite sides of the ground plane, essentially requiring a multi-layer ground substrate. This design is a physical wrapping of the design in [8], but it is not fully realized yet and remains an area for future work.

In the case of planar arrays, two coaxial cables can feed a single antenna element, but additional mechanical support probably needs to reinforce the center conductors. The outer

conductor is not connected at the antenna. If the cables are grounded together via soldering, this is similar to a twin-lead line. Although the line impedance effects are different, the structure is physically symmetrical, and the outer conductor confines the line fields. Both coaxial cables are then connected on the backside of the ground plane. The simplest wideband solution behind the ground plane is to connect the two sides with a 4-port 180° hybrid combiner, which McLean [9] describes in detail in terms of *S*-parameters. Hybrid combiners also served as the method of choice for, at least, early work in feeding the Harris tightly-coupled array designs [10].

6.4.2.1 No Balun?

The underlying requirement of any balun is to keep the currents on opposite sides of the feed to be out of phase. If this is successful within meaningful radiation regions but relaxed elsewhere, one might ask if an explicit balun is necessary. Important regions are include between the element and ground plane but behind the ground plane is less important.

The simplest way not to avoid a balun is to connect the coaxial cable directly to the element. Currents form on the outside of the coaxial cable, but not all frequencies have significant currents as illustrated by Figure 6-28(a) for currents at 5.4 GHz. The worst frequencies are from 5 to 6 GHz, where the $\lambda/4$-length is between 12.5 and 15.0 mm. Since the vertical coaxial line is nearly 12 mm, it becomes a resonant structure, with something of a top-hat load from the array element. With such currents, the pattern is no longer the desired hemispherical pattern; instead, the pattern is nearly one of a monopole antenna. Altering the length through the application of a sleeve around the vertical coaxial section will alter the frequencies where these strong currents appear. However, with the wide bandwidth, a sleeve-type balun cannot move the disturbances to outside the impedance bandwidth.

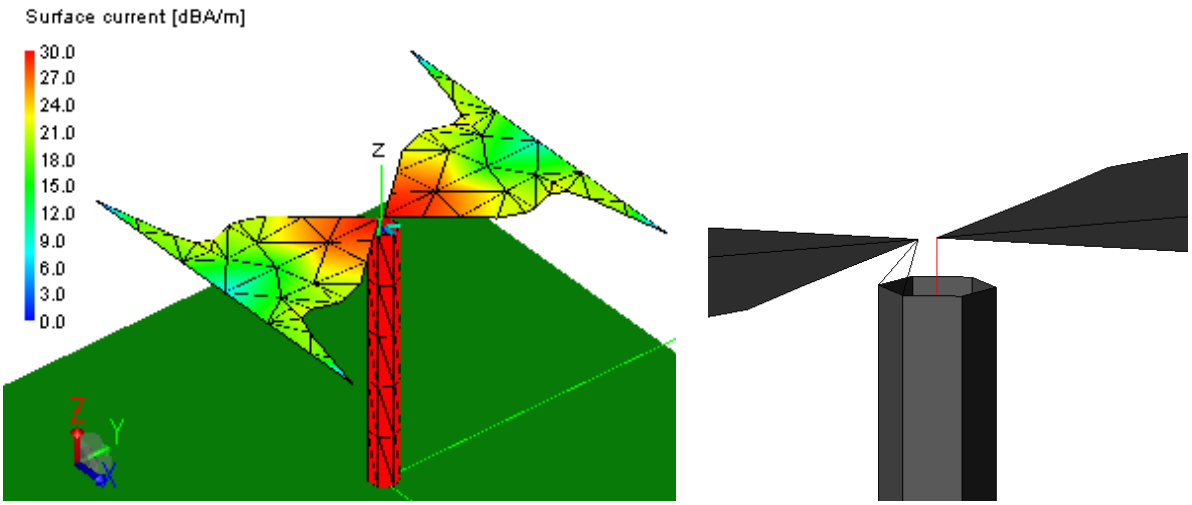

(a) (b)

Figure 6-28 –(a) Currents on coaxial (unbalanced) feed for the Rot 9 infinite array at 5.4 GHz, with (b) a blow-up of the feed region and connections

When using 180° hybrid combiners as baluns, the center conductors of two ports oftentimes feed the balanced antenna. The outer conductors on these coaxial lines are soldered together to maintain an equal potential for both lines. The outer shielding extends to close to the array element, but it is not connected. In many ways, such a design is comparable to the Harris feed organizer described previously. Alterations to the input impedance, referenced below the ground plane, are comparable to the unshielded twin lead performance (and adjustments can achieve closer solutions). This design does not develop a monopole pattern. Across frequency, its patterns nearly match those of the Rot 9 infinite array when fed by an edge voltage at the element center (as done throughout the designs presented prior to this Section 6.4).

The above design still requires or assumes a balanced feed, just below the ground plane. Further design details become a trade-off between maintaining the low thickness of the array and developing a suitable balun, if an unbalanced feed is used. Once the impedances between the balanced feed lines above the ground plane and the coaxial cable behind match, full power transfers to the antenna element. If necessary, absorber may surround the coaxial cables behind the ground plane to reduce coupling between the cables of each element. Still, such reduction of radiation does not guarantee equal amplitudes on each feed line. The conclusion is that either a balanced source or a balun is required. It may be possible, however, to have only one balun at the single feed of the array and to design a corporate (and likely unphased) feed system using balanced transmission lines.

6.5 Summary

This chapter has advanced the designs of the Rot 9 and Wrapped Bowtie arrays, and tightly coupled arrays, in general, using finite array modeling. Such simulations are computationally the most demanding, and therefore they are resource limited. The expansion of the problem from infinite (Chapter 4) to semi-infinite (Chapter 5) and then to finite designs (here) introduced and doubled the finite edge effects. The array-guided surface wave (AGSW) travels in multiple directions in the *xy*-plane in tightly-coupled finite planar arrays, requiring loading in both dimensions and their intermediate transitions for control.

Chapter 5 developed guidance on controlling the AGSW whether by loading or array conforming. The focus of work in this chapter has been to expand that loading to both dimensions concurrently, identify the overall impacts to efficiency and bandwidth. The efficiencies seen in finite arrays are lower than semi-infinite arrays, by something slightly better than the square of the semi-infinite array efficiencies (or the multiplication of two orthogonal semi-infinite array efficiencies). That the finite array efficiency is lower than the semi-infinite array efficiency makes sense; over the two-dimensional extents of the array, more loading is required, which leads to lower radiation efficiencies.

The lower efficiencies tend to extend the bandwidth on all elements within the array. The least affected, however, are the unloaded center elements, and when considering the smallest bandwidths on any element as the limiter, the center elements tend to have the smallest bandwidths. For the Rot 9 element design, the loading reduces the S3 bandwidth from 5.23:1 in the infinite array to 4.79:1 in an 8×8 finite array. The loss of bandwidth is at the lower frequencies. The Wrapped Bowtie array shows an increased S3 bandwidth from 7.24:1 in its infinite form to 8.85:1 in an 120-element finite array. More loading is required to control the AGSW in the Wrapped Bowtie design, as it exhibits higher levels of mutual coupling.

Next, the tighter cylindrical conformation from Chapter 5, labeled Conf2, modifies the "controlled" 8×8 Rot 9 array. Conformation allows for some of the AGSW power to radiate away from the array, which then requires less loading for AGSW control. The improved efficiency is marginal, and thus, the main benefit of conformation is to control the beamwidth in the direction of conformation. The finite conformed Rot 9 array achieves a nearly constant gain of 11 dBi toward the array normal ($+\hat{z}$) from 4-10 GHz, with an *H*-plane 3-dB beamwidth of

typically $+75^{\circ}$; see Figure 6-19. If the issues with the feed network can be solved, especially within a volumetrically reduced space behind a conformed ground plane, such a design would have a place in several wide or multiband cellular/land-mobile radio systems.

Throughout this chapter and the previous, loading to suppress the AGSW has been on active elements only. This results in an amplitude taper across the array surface and leads to lower sidelobe levels. The intention of the loading, however, was never to manipulate or optimize the sidelobe level. A separate common technique to control the AGSW with tightly-coupled arrays is to load a number of outer rings of elements and not feed them at all. There is value in addressing and complimenting this other approach. Using multiple reference impedances adds several complexities to the design, even if limited to four reference impedances. Whether a balanced or unbalanced transmission line connects to the element, the design requires four different reference impedances and four different transmission line designs. Looking farther back into the feed system, if the design uses balanced feed lines, some impedance transformation is required from the source generator or to be built into a corporate feed. Some (future) allowance or possibility may exist for purchasing MMICs with distinct balanced output impedances, but this is not certain.

Real and practical design issues emerge when one begins to consider the construction of these arrays. Although the elements and their heights over ground are scalable with frequency, dielectric substrates, resistive lumped loads, existing transmission lines, etc. are not. The sizing of the unit cell throughout this research has put the inter-element spacing of $d = \lambda / 2$ at 10 GHz. The next step for future work is to define very specific specifications for bandwidth, frequency, sidelobes, and gain, and to continue designs to meet them. While this chapter has advanced many aspects of the designs of tightly-coupled arrays, it has also illustrated several construction and feeding details remaining to bring such arrays into full fruition.

6.6 References

[1] B. A. Munk, *Finite Antenna Arrays and FSS*. Hoboken, NJ: Wiley-Interscience, 2003.

[2] J. J. Rawnick*, et al.*, "Patch dipole array antenna including a feed line organizer body and related methods," US Patent #6483464, 2002.

[3] W. Stutzman and G. Thiele, *Antenna Theory and Design*, 2nd ed. New York: John Wiley & Sons, Inc., 1998.

[4] E. Channabasappa, "Balanced antenna arrays for 24 GHz automotive UWB radar sensors," in *IEEE Antennas and Propagation Society International Symposium*, 2007, pp. 785-788.

[5] M. Manteghi and Y. Rahmat-Samii, "A novel UWB feeding mechanism for the TEM horn antenna, reflector IRA, and the Vivaldi antenna," *IEEE Antennas and Propagation Magazine,* vol. 46, pp. 81-87, 2004.

[6] G. H. Huff and T. L. Roach, "Stripline-based spiral antennas with integrated feed structure, impedance transformer, and dyson-style balun," in *IEEE Antennas and Propagation International Symposium*, 2007, pp. 2698-2701.

[7] J. Dyson, "The equiangular spiral antenna," *Antennas and Propagation, IRE Transactions on,* vol. 7, pp. 181-187, 1959.

[8] J. G. Padilla, "Ultra-wideband Planar Coupled Spiral Balun," US Patent #6683510, 2004.

[9] J. S. McLean, "Balancing networks for symmetric antennas. I - Classification and fundamental operation," *Electromagnetic Compatibility, IEEE Transactions on,* vol. 44, pp. 503-514, 2002.

[10] M. Jones and J. Rawnick, "A New Approach to Broadband Array Design using Tightly Coupled Elements," in *IEEE Military Communications Conference*, 2007, pp. 1-7.

CHAPTER 7

Conclusions

This dissertation has advanced several designs and processes pertaining to tightly-coupled wideband planar arrays. This chapter summarizes the work of this dissertation, articulates the contributions it makes to the body of technical knowledge, and outlines several tasks for future research.

7.1 Summary

Chapter 1 introduced the research in this dissertation and articulated the need for the work. Chapters 2 and 3 together formed the review of the literature. Chapter 2 explained primarily the physical phenomenon of coupling between elements in arrays, and Chapter 3 reviewed past work of computational and asymptotic techniques for characterizing these large problems. Chapter 2 covered coupling characteristics, aperture theory, power flow between elements, infinite vs. finite array coupling, and surface waves. Although no significant computational code emerged from this research, the methods of other engineers found in Chapter 3 described many of the underlying physical properties in tightly-coupled arrays.

Chapter 4 reviewed the past designs of tightly-coupled planar arrays and began the development of several designs using different inspirations with infinite array techniques. From this wandering design process, the Rot 9 and Wrapped Bowtie element designs emerged. The latter part of Chapter 4 presented the infinite array behavior of these designs without ground

planes and as isolated elements. It also included a brief consideration of the Rot 9 element in an infinite scanned array.

Chapter 5 and Chapter 6 advanced only these two aforementioned designs. Chapter 5 used semi-infinite techniques (the 1D periodic boundary condition within FEKO®) to develop the resistive loading schemes needed for suppression of the array-guided surface wave (AGSW). First, though, Chapter 5 documented the effects of the AGSW on the input impedance and included representations of the surface currents in the spectral domain. Chapter 5 put forth the designs of each element design separately for *H*-plane and *E*-plane finite arrays. Chapter 5 considered the effects and overall value of conforming the *H*-plane finite Rot 9 array. Different conformations and reduced loading patterns showed how conforming the array introduces aperiodicities and sheds some power from the AGSW. Lastly, Chapter 5 presented the performance limitations of *H*-plane scanning in an eight-element semi-infinite Rot 9 array.

Chapter 6 extended the loading schemes from Chapter 5 to finite arrays. The effects of loading in multiple directions showed reduction in radiation efficiency, to the level that one may begin to consider trade-offs between radiation efficiency and aperture efficiency. Chapter 6 presented simulation results for the cylindrically conformed Rot 9 array and articulated an application for it as a wideband, base-station antenna. The remainder of Chapter 6 considered the real and challenging issues of feeding these arrays.

7.2 Contributions

The first contribution of this research is the defense of the process of designing elements for tightly-coupled arrays. When done at the antenna feed, the application of loading to suppress the array-guided surface wave (AGSW) can be a step subsequent to the element design completed using infinite array techniques. Most impedance tuning involves adjusting the input reactance to achieve a wide bandwidth. The addition of resistive loading serves to improve bandwidth, as well, since it increases the reference impedance. Designers should use infinite array techniques for the first stages of designing elements for tightly-coupled arrays. This approach offers a simplified problem space compared to either semi-infinite or finite array simulations. This approach is counter to a classical view where a designer simply drops a properly designed antenna into an array layout. Likewise, since the AGSW makes an impact even in semi-infinite

array simulations, semi-infinite techniques are likely more valuable than finite array techniques for advancing many design details. Particularly if any conformation is one dimensional, semi-infinite analyses are nearly sufficient and much less computationally burdensome than finite array analyses.

Within the infinite array context, one contribution is in the tuning of elements in tightly-coupled arrays. Because of their electrically small size, the engineer often pursues ways to increase the capacitance by extending, interweaving, or overlapping element edges. It is a new observation to view the input impedance as distributed, parallel capacitors. These distributed capacitors exist between the element edges and between the two sides of the feed. Adjustments to the feed region were necessary to achieve the wider bandwidth elements akin to the Rot 9 element designed. Such details are electrically small when only one element is considered. However, since that detail extends to all elements in a uniform array, the effects become meaningful. This finding explains some of the performance limitations of the Foursquare array.

Another contribution is the appraisal of using conformal arrays as an alternative means of suppressing the AGSW. A qualitative trade-off of the efficiency improvements against beamwidth alterations had not been previously made. The research here, using semi-infinite techniques, showed conforming the array to suppress the AGSW to have little value in tightly-coupled transmit or receive arrays because of the associated widening of the beamwidth and loss of gain. This gain loss alternatively occurs through higher loading levels in non-conformed arrays. The value of conforming for frequency-selective surfaces may be otherwise.

The last contribution is the development of the Wrapped Bowtie array. Many antenna engineers revere the concept and definition of a 10:1 bandwidth. While such statements usually include impedance, pattern, and gain bandwidths, engineers rarely strictly define their aperture and/or radiation efficiency. The finite Wrapped Bowtie array developed in this dissertation has a ground plane underneath and comes very close to the 10:1 bandwidth. A VSWR < 3 bandwidth of 10.77:1 exists on the more loaded, outer elements; and a VSWR < 3 bandwidth of 8.85:1 exists overall. The Wrapped Bowtie array achieves this bandwidth at the expense of resistive loading, which reduces the radiation efficiency. Other than conforming or, in general, increasing aperiodicities in the array structure, loading is thus far the only effective way to control the AGSW. The Wrapped Bowtie design emerged through infinite array techniques (as advocated above), but its tuning is distinctly different from others. This design is new and differs

substantially from other tightly-coupled array designs of Harris/Munk[1], Nealy[2], and Tzanidis most recently[3][1].

7.3 Future Work

The author and other researchers may consider the following tasks to expand the research detailed in this dissertation:

1. Design a full, cylindrically conformal array to provide omnidirectional coverage. Optimize this design and investigate trade-offs between beam shaping with inter-element coupling and bandwidth.
2. Likewise, advance and optimize the concept of using three sectoral wideband arrays to complete a quasi-omnidirectional coverage. Determine the strength and extent of coupling effects between sectors.
3. Develop alternate ground shapes, whether sloped per element or concave across the array. Investigate the impacts on element tuning and on the array-guided surface wave (AGSW) in finite arrays.
4. Develop a comprehensive, field- or currents-based explanation for the wideband performance of the Wrapped Bowtie array. Consider embedded currents to explain its performance.
5. Determine the cause and mechanisms that lead to feed-line phase non-linearity in the Rot 9 array (Figure 6-25).
6. Seek alternative locations to place resistive loads on the array elements. Determine if distributing the loads to regions with lower current densities can increase the radiation efficiency and still control the AGSW.
7. Investigate microwave circuit and filtering options to implement frequency-selective resistive loading as a means of increasing radiation efficiency at frequencies where the AGSW is not present.
8. Likewise, investigate the value and implantation hurdles of non-linear resistive loading and complex loading schemes to control the AGSW.

[1] This paper won first place in the student paper competition at the IEEE APS 2010 conference.

9. Consider a solution to mitigate the AGSW currents through adaptive cancellation; purposefully generate an out-of-phase AGSW to cancel the naturally occurring one.
10. Complete a trade-off study between using outer rings of terminated elements as compared to an excited but tapered loading of elements. Compare the designs to aperture efficiency as a function of array size.
11. Correlate loading for the AGSW control to amplitude tapering in the array design to control sidelobes. Consider the overall array size in these analyses.
12. Investigate the effects of noise coupling found in tightly-coupled arrays, especially with resistive loads present.
13. Develop wideband (to ultra-wideband) baluns to feed such arrays. Carefully focus to minimize the balun size, especially with the Wrapped Bowtie design.
14. Fully research feed options and alternatives for balanced-line corporate feed structures.
15. Fully research and judge the MMIC options for feeding each element independently. Determine real viability and limitations of implementing MMIC sources.
16. Construct and test the expanded designs of these arrays, as unknown obstacles will undoubtedly appear.

7.4 References

[1] R. C. Taylor, *et al.*, "Wideband phased array antenna and associated methods," US Patent #6512487, 2003.

[2] J. R. Nealy, "Foursquare antenna radiating element," US Patent #5926137, 1999.

[3] I. Tzanidis, *et al.*, "An Interweaved Spiral Array (ISPA) Providing a 10:1 Bandwidth Over a Ground Plane," in *IEEE Antennas and Propagation Society International Symposium*, 2010.